This electronic thesis or dissertation has been downloaded from Explore Bristol Research, http://research-information.bristol.ac.uk

Author:
Hong, Dongxiao

Title:
Using symmetry to understand nonlinear modal interactions

General rights
Access to the thesis is subject to the Creative Commons Attribution - NonCommercial-No Derivatives 4.0 International Public License. A copy of this may be found at https://creativecommons.org/licenses/by-nc-nd/4.0/legalcode This license sets out your rights and the restrictions that apply to your access to the thesis so it is important you read this before proceeding.

Take down policy
Some pages of this thesis may have been removed for copyright restrictions prior to having it been deposited in Explore Bristol Research. However, if you have discovered material within the thesis that you consider to be unlawful e.g. breaches of copyright (either yours or that of a third party) or any other law, including but not limited to those relating to patent, trademark, confidentiality, data protection, obscenity, defamation, libel, then please contact collections-metadata@bristol.ac.uk and include the following information in your message:

- Your contact details
- Bibliographic details for the item, including a URL
- An outline nature of the complaint

Your claim will be investigated and, where appropriate, the item in question will be removed from public view as soon as possible.

Using Symmetry to Understand Nonlinear Modal Interactions

Dongxiao Hong

Department of Mechanical Engineering
University of Bristol

A dissertation submitted to the University of Bristol in accordance with the requirements for award of the degree of Doctor of Philosophy in the Faculty of Engineering.

October 2022

Word count: 85000 (approx.)

Abstract

With the drive for more efficent slender structures, nonlinear dynamic phenomena are increasingly being observed in, and sometimes designed into, engineering systems. The objective of this thesis is to develop a better theoretical understanding of nonlinear systems that manifest internal resonance and provides practical insights into the exploitation of such nonlinear behaviours in engineering practice. To achieve this, an analytical approach is employed, that is based on nonlinear normal mode, or backbone curve, analysis.

The geometry, i.e. synchronicity and asynchronicity, of internal resonances is investigated using conceptually simple, two-mode systems. Special dynamic behaviours that emerge from internal resonance are studied, including isolated backbone curves and backbone solutions where the phases of modal coordinates vary. The underpinning mechanisms that govern their existence are analytically derived and demonstrated using relevant engineering systems. These geometric features are generalised to account for arbitrary types of internal resonances for two-mode interactions with arbitrary eigenfrequency ratios; an analytical technique is proposed for the efficient and robust determination of internal resonances.

The research scope is then extended to forced-damped scenarios. By employing an energy-based method, the relationships between backbone curves and forced periodic responses are established. A semi-analytical, energy balancing method is formulated by combining the energy balancing principle across multiple harmonics with quadrature criteria. With known NNM solutions, it allows for efficient prediction of forced responses with the applicability and accuracy estimated via harmonic phase-shifts.

Based on the concept of resonant capture, backbone curves are used to interpret damped transient responses with applications of Targeted Energy Transfer (TET). The required backbone curves for realising TET are identified from a symmetry-breaking perspective. Using these insights, an analytical method is presented for parameter selection of a nonlinear energy sink; the effectiveness of this is demonstrated via a beam system.

Author's declaration

I declare that the work in this dissertation was carried out in accordance with the requirements of the University's Regulations and Code of Practice for Research Degree Programmes and that it has not been submitted for any other academic award. Except where indicated by specific reference in the text, the work is the candidate's own work. Work done in collaboration with, or with the assistance of, others, is indicated as such. Any views expressed in the dissertation are those of the author.

SIGNED:

DATE:

Acknowledgements

First of all, I would like to express my gratitude to my supervisors, Dr. Tom Hill and Prof. Simon Neild, for their continuous guidance, patience, and enthusiasm during my doctoral studies. Tom Hill has been a supportive and inspiring supervisor throughout. He was always open to discussions to any level of details like mathematical derivations and code debugs; in the meantime, he also encouraged me to seek my ideas independently and offered research directions when I came across difficulties. His infectious passion and positive attitude made every meeting or catch-up an enjoyable experience. Simon Neild is an insightful and brilliant supervisor with a wealth of knowledge. In discussions with him, he frequently showed things from a different perspective and inspired me to find the inner connections of seemingly scattered details. In my research adventure, their complementary roles were a great fortune and kept me aware of the importance of seeing the bigger picture whilst taking care of every detail. I would also like to thank them for their encouragement and for providing opportunities in attending conferences and group seminars.

Working with talented colleagues has also brought many joys and completed my research experience. I would like to express my gratitude to all of them, including Alice Brown, Evangelia Nicolaidou, Wasi Ahmadi, Gang Shen, Yiyuan Li, Ruiwei Feng, Haifei Wang, and Xiao Xiao. Particularly, I would like to thank Evangelia Nicolaidou for her valuable help and interesting discussions on reduced-order modelling and the outstanding work during our collaborations. In addition, thanks to Gang Shen for his constant support and friendship. I would also like to thank all the colleagues in the Dynamics & Control Research Group for organising a series of engaging seminars and providing a platform for discussions and knowledge sharing.

I want to express my deepest gratitude to my family, especially my parents for their encouragement and support. Finally, I would like to thank my girlfriend, Xiaoyu Xu, for her unconditional love and support during the whole journey. Life would not have been so amazing without her by my side.

Publications

Journal publications

- D. Hong, T. L. Hill, S. A. Neild, 2019. Conditions for the existence of isolated backbone curves, *Proceedings of the Royal Society A: Mathematical, Physical and Engineering Sciences* 475 (2232) 20190374.
- D. Hong, E. Nicolaidou, T. L. Hill, S. A. Neild, 2020. Identifying phase-varying periodic behaviour in conservative nonlinear systems, *Proceedings of the Royal Society A: Mathematical, Physical and Engineering Sciences* 476 (2237) 20200028.
- D. Hong, T. L. Hill, S. A. Neild, 2021. Understanding targeted energy transfer from a symmetry breaking perspective, *Proceedings of the Royal Society A: Mathematical, Physical and Engineering Sciences*, 477(2251) 20210045.
- D. Hong, T. L. Hill, S. A. Neild, 2022. Existence and location of internal resonance of two-mode nonlinear conservative oscillators, *Proceedings of the Royal Society A: Mathematical, Physical and Engineering Sciences* 478 (2260) 20210659.
- D. Hong, T. L. Hill, S. A. Neild, 2022. Efficient Energy Balancing Across Multiple Harmonics of Nonlinear Normal Modes, *Nonlinear Dynamics.*

Conference publications

- T. L. Hill, D. Hong, S. A. Neild, 2020. Uncovering hidden responses using isolated backbone curves, 14th *WCCM & ECCOMAS Congress.*
- D. Hong, E. Nicolaidou, T. L. Hill, S. A. Neild, 2021. Identifying phase-varying periodic behaviours in a conservative cable model, 2nd *International Nonlinear Dynamics Conference.*

Contents

List of figures

List of tables

Nomenclature

N	Number of degrees-of-freedom
t	Time
q_i	The i^{th} linear modal coordinate
$u_{i,j}$	The j^{th} harmonic of the i^{th} mode
ω_{ni}	The i^{th} natural frequency
d_i	The i^{th} linear modal damping
P_i	The i^{th} external modal forcing amplitude
Ω	The excitation frequency
$\mathit{\Xi}_i$	The coefficients of the quadratic nonlinear terms in the modal domain
$\mathit{\Psi}_i$	The coefficients of the cubic nonlinear terms in the modal domain
$\dot{\bullet}$	The first derivative with respect to time
$\ddot{\bullet}$	The second derivative with respect to time
U_i	The response amplitude of the fundamental component of the i^{th} mode
ω_i	The response frequency of the fundamental component of the i^{th} mode
θ_i	The phase of the fundamental component of the i^{th} mode
θ_d	The phase difference between the fundamental components of two linear modal coordinates
$\phi_{i,j}$	The linear modeshape
$\mathbf{q}$	An $\{N \times 1\}$ vector of modal displacements
$\mathbf{\Phi}$	An $\{N \times N\}$ modeshape matrix
$\mathbf{\Lambda}$	An $\{N \times N\}$ diagonal matrix of natural frequencies
$\mathbf{D}$	An $\{N \times N\}$ linear modal damping matrix
$\mathbf{N_q}$	An $\{N \times 1\}$ vector of nonlinear terms in the modal domain
x_i	The i^{th} horizontal physical coordinate
y_i	The i^{th} vertical physical coordinate
m_i	The i^{th} mass value
c_i	The i^{th} damping coefficient
k_i	The i^{th} linear stiffness coefficient

F_i	The i^{th} external forcing amplitude
L_i	The unstretched length of the i^{th} linear spring
α_i	The i^{th} nonlinear stiffness coefficient
β_i	The i^{th} coefficient of quadratic nonlinear terms in the physical domain
γ_i	The i^{th} coefficient of cubic nonlinear terms in the physical domain
$\mathbf{x}$	An $\{N \times 1\}$ vector of physical displacements
$\mathbf{M}$	An $\{N \times N\}$ mass matrix
$\mathbf{C}$	An $\{N \times N\}$ damping coefficient matrix
$\mathbf{K}$	An $\{N \times N\}$ stiffness matrix
$\mathbf{N_x}$	An $\{N \times 1\}$ vector of nonlinear terms in the physical domain
δ	The angle between the elastic support and the $x-$axis, see Figs. 4.2 and 4.6
ρ	The uniform density
E	The Yong's modules
d	The diameter of the cable in Fig. 4.6
L_0	The unstretched cable length
T	The static pre-tension applied to the cable
w	The transverse displacement of the beam system
I	The second moment of area of the beam system
A	The cross-sectional area of the beam system
$\mathcal{B}_{\mathcal{R},n}, \mathcal{B}_{\mathcal{C},n}$	The stability boundaries of Fourier-real and Fourier-complex backbone curves
$\mathcal{A}_{\mathcal{R},n}, \mathcal{A}_{\mathcal{C},n}$	The asymptotic values of stability boundaries
E_D	The damping energy transfer to the system
E_P	The forcing energy transfer to the system
E_{Di}	The damping energy transfer to the i^{th} mode
E_{Pi}	The forcing energy transfer to the i^{th} mode
E_{Ni}	The nonlinear energy transfer to the i^{th} mode
$E_{Di,j}$	The damping energy transfer to the j^{th} harmonic of the i^{th} mode
$E_{Pi,j}$	The forcing energy transfer to the j^{th} harmonic of the i^{th} mode
$E_{Ni,j}$	The nonlinear energy transfer to the j^{th} harmonic of the i^{th} mode
$\mathcal{H}_i$	The set of harmonics in the i^{th} mode
$\hat{\theta}_{i,j}$	The phase-shift of the j^{th} harmonic of the i^{th} mode
$R_{\mathcal{H}}$	The total number of harmonics considered in the energy balancing analysis
$R_{\mathcal{F}}$	The total number of forcing considered in the energy balancing analysis
$E_{\text{ins,NES}}$	The instantaneous energy ratio in the NES
$E_{d,\text{NES}}$	The total energy dissipated by the NES over the response
$E_{\text{initial,NES}}$	The initial energy ratio in the NES scaled by the total energy in the system

Chapter 1

Introduction

The rapid development of the engineering industry has been accompanied by dealing with dynamic problems and exploiting dynamic resources. For example, to ensure the safety of life in the presence of earthquakes, the performance-based seismic design is extensively considered in civil structures; to mitigate unwanted vibrations, dynamic vibration absorbers are widely used in engineering systems.

To quantify and analyse dynamic behaviours, a great number of tools have been developed, many of which are established via the concept of Linear Normal Modes (LNMs). A LNM represents a vibration pattern in which all components of the system oscillate at the same eigenfrequency with a fixed phase relationship. One useful mathematical property of LNMs lies in their orthogonal relations. The orthogonality of LNMs indicates that any response initiated in a specific LNM will remain in it for all time without influence on other LNMs (this is also termed the invariance feature). Therefore, the superposition principle can be applied, i.e. any free or forced response can be viewed as a linear combination of LNMs. Based on these features, a direct application of LNMs is that a high-dimensional physical system can be decoupled as a lower-order modal model. With such a powerful methodology, the computational cost is greatly reduced, and this makes analysis of complex dynamical systems feasible. To date, the application of linear modal analysis has witnessed significant evolutions for dynamical systems such as damping devices, civil structures, and aerospace systems. In many engineering fields, the linear modal theory is still extensively used in the design, construction, and monitoring processes.

Over recent decades, the demand for high-performance engineering structures has been continually growing. Meeting this demand often requires extending the performance envelope of structures to regions where nonlinearity must be considered – it brings about a variety of advantageous applications; nonetheless, it also gives rise to numerous challenges in modelling, analysis, and tests of nonlinear systems. For example, lightweight and flexible aircraft wings can show more efficient aerodynamic performance, yet the flexibility, in turn, can lead to significant nonlinear behaviours that are challenging to predict. Another example is the nonlinear tuned mass damper, which can outperform linear damping devices in showing a broader band performance; however, the use of nonlinear tuned mass damper can lead to complex dynamic behaviours such as the existence of isolas – this makes it difficult to guarantee a robust and reliable performance.

In the presence of nonlinearity, dynamical systems can manifest a number of nonlinear behaviours such as modal interactions, bifurcations, and instability, which have no counterpart in linear systems. In this case, applying the linear methodology in the dynamic analysis cannot reliably predict these nonlinear behaviours, as such, it usually results in suboptimal designs where the nonlinearity is not fully exploited. The complexity of nonlinear behaviours, combined with the limitations of linear methodologies, have presented technical challenges in understanding and exploiting nonlinear behaviours. Therefore, seeking a nonlinear extension to linear modal analysis attracts much research effort. In this context, the concept of Nonlinear Normal Modes (NNMs) provides a mathematically rigorous methodology in understanding and analysing nonlinear behaviours. Unlike their linear counterpart (i.e. LNMs), NNMs are able to capture the intrinsic mechanisms of nonlinear phenomena. However, similar to LNMs, NNMs possess the invariance property and thus offer an analysis framework that allows the complex, large-scale nonlinear systems to be exactly interpreted via a simpler, reduced-order model. Owing to these useful features, the NNM analysis can assist in overcoming the bottleneck of nonlinear modelling and designs, and in exploring advantageous nonlinear resources. To date, the NNM analysis has been widely considered in a variety of nonlinear systems from microelectromechanical systems to large-scale aerospace systems.

With tools suited to dealing with nonlinearity in dynamical systems, the desire also grows: how to incorporate beneficial nonlinear properties in designs whilst eliminating or reliably accounting for unfavorable features? The NNM-related methodology has shown its power in handling nonlinear dynamic problems, however, NNM solutions can show complex topologies in the presence of modal interactions and bifurcations – this makes the interpretation of nonlinear behaviours a challenging task. Furthermore, how the simpler modal properties of NNMs are related to more complex, yet more practical, forced-damped responses is to be explored. Addressing these problems requires a further study of the NNM properties and extending the framework to more general scenarios.

Achieving this can help gain an in-depth understanding of nonlinear phenomena and ease the bottleneck of exploiting nonlinearity in practical engineering structures.

This thesis aims to develop a better understanding of nonlinear behaviours and gain insights into practical applications. Specifically, the NNM-based nonlinear modal analysis is employed to study nonlinear dynamic phenomena in the presence of modal interactions. By exploring the theoretical mechanisms that underpin intricate modal interactions, a methodology is provided for the interpretation and determination of modal interactions. The NNM-based framework is then further extended to account for nonlinear systems in forced-damped scenarios. The relationships between NNMs and forced-damped responses are established, and an NNM-based methodology is developed to interpret forced-damped responses.

In addition to theoretical studies, a number of engineering-related examples will be considered for demonstration such as cable and beam dynamics. Particularly, practical applications related to vibration suppressions will be discussed, which include the existence of isolated backbone curves in the application of nonlinear tuned mass dampers and the identification and realisation of targeted energy transfer.

Chapter 2

Literature review

Over the last few decades, extensive research on and applications of nonlinear dynamics have been carried out in the fields of applied science and engineering. This is, to some degree, in response to the urgent need of handling and exploiting nonlinear phenomena in practice.

Due to objective reality such as intricate environments and natural disasters, nonlinear phenomena have been continually observed in engineering systems. For example, underwater vehicles, designed for monitoring, exploration, and military applications, can experience complex nonlinear ocean disturbances [1, 2]; subject to earthquakes, civil structures can suffer large-amplitude nonlinear vibrations, which threaten the security of both structures and people [3]. Additionally, the requirements for more environmentally friendly and highly efficient engineering facilities/structures have been calling for deliberate exploitation of nonlinear phenomena. For example, harnessing the energy from ocean waves via wave energy converters is a promising renewable energy solution [4, 5]; to protect structures from large deformations imposed by earthquakes, nonlinear damping devices can outperform their linear counterparts [6, 7]. In practice, the boundary between dealing with undesirable nonlinear problems and exploiting advantageous nonlinearity can blur as they are indeed interconnected rather than separated as two facets. One example is the application of high-aspect-ratio wings of aircraft – their slender geometry results in higher efficiency due to lower drag coefficient, in turn, it also brings about challenges in modelling the nonlinear behaviours [8]. To some extent, the advances of green and efficient engineering technology are always accompanied by solving nonlinear problems and harnessing nonlinear phenomena.

2.1 Nonlinear dynamic phenomena

To better handle the undesirable nonlinear phenomena, observed in practice, and potentially even exploit nonlinearity, the causes of nonlinear phenomena and their characteristics should be understood beforehand.

2.1.1 Causes of nonlinear phenomena

A number of physical sources may lead to nonlinear dynamic phenomena. An overview of some typical sources are given below.

Material properties

The material property reflects the response of a material due to external stimuli; it can be expressed by the constitutive law between strain and stress, or displacement and force. Typically, the constitutive relationship consists of a linear region followed by a nonlinear region where the material exhibits plastic behaviours. In addition, damage, wear and environmental factors (e.g. temperature) can also lead to nonlinear constitutive laws [9]. In this case, nonlinear behaviours such as hysteresis [10, 11] and rate dependence [12] can be observed.

Constraints and external forces

Many engineering problems involve constraints between two or more entities that do not allow them to move freely in all directions. In some cases, these constraints may cause problematic nonlinear behaviours and need to be mitigated. For example, due to degradation and manufacture tolerance, freeplay, or backlash, between components can lead to repeated impacts, termed vibro-impact motions. Such nonlinear motions can be observed in many engineering systems, e.g. aircraft [13, 14]. Another example is the friction that occurs along the contact surface between two components of assembled structures, of which the caused repeated stick and slip cycles can significantly affect the performance, e.g. turbomachinery systems [15, 16]. In other cases, they can be exploited in designs to offer advantageous applications such as vibro-impact dampers [17, 18] and frictional dampers [19].

External forces acting on structures can also cause nonlinear behaviours. For instance, when an elastic structure is subjected to a fluid flow, the structure can interact with the aerodynamic forces – an important topic termed aeroelasticity [20]. For micro-scale systems, e.g. micro-electromechanical systems (MEMs), inter-molecular forces also play an important role in governing the dynamic behaviours [21].

Geometric nonlinearity

Geometric nonlinearity refers to the nonlinear effect arising from the geometric change of systems, which can be expressed by a nonlinear strain-displacement relationship. Such a nonlinear effect has been widely encountered in many engineering systems as a consequence of the extensively used slender structures that aim for high efficiency and performance. For example, the flexible nature of aircraft wings can exhibit significant geometric nonlinearity when vibrating at large amplitudes [22]. One important exploitation of geometric nonlinearity can be found in MEMs, where their large-amplitude vibrations have been considered in energy harvesting [23], filters [24] and sensors [25].

To complicate matters, in practice, engineering systems can exhibit even more complex dynamic behaviours that are attributed to combinations of the aforementioned sources. For example, the dynamic behaviours of rotorcrafts can be significantly affected by the coexistence of geometric nonlinearity, induced by large deflections, and contact nonlinearity, caused by freeplay [26]. In [22], geometric nonlinearities have shown significant effect on the aeroelastic characteristics of a high-aspect-ratio wing.

In reviewing the causes of nonlinear behaviours, it shows the extensiveness of engineering systems that may experience nonlinear behaviours during operation; it also highlights the importance of an in-depth understanding of their underpinning mechanism in order to make full exploitation of them. The following discussions present an overview of the characteristics of nonlinear phenomena before introducing the nonlinear modal analysis that rigorously and efficiently captures these nonlinear features.

2.1.2 Characteristics of nonlinear phenomena

The sources leading to nonlinear phenomena are relatively well-studied; whilst they can result in rich and complex nonlinear dynamic phenomena that have no counterpart in linear systems, for instance, internal resonance, bifurcations, and instability [27–32]. Note that the following discussions focus on nonlinear features of periodic responses, as they represent typical operational states of many mechanical systems; whilst other responses such as transient, quasi-periodic, and chaotic responses will be briefly discussed for completeness. Even though periodic motions are only a subset of the full dynamics of nonlinear systems, an in-depth understanding of them can still reveal the mechanisms that underpin the rich nonlinear phenomena; consequently, periodic responses have been extensively considered in the analysis and design of nonlinear systems.

Modal interaction

Modal interactions denote the phenomenon that, during a general motion, the energy can exchange between two or more modal components of a nonlinear system because of the nonlinear effect [33, 31]. Therefore, due to energy transferred from other modes, a mode that is not directly forced may exhibit significant contributions to the overall responses. This nonlinear behaviour is governed by equations of motion where nonlinear terms couple different modal coordinates and can be defined by referring to the commensurate relationships between nonlinear response frequencies [33, 34]. For example, two interacting modes with a periodic response frequency commensurate match of $1:3$ is termed the $1:3$ internal resonance.

Regarding the underpinning mechanism and geometric features of modal interactions, they will be detailed in §2.2.2; here, some examples are given for a brief introduction. Modal interactions have been extensively studied in a wide range of mechanical systems, e.g. cables [35], beams [36–38], plates [39, 40] and shells [41, 42]. Exploiting the accompanying energy exchange, they also receive considerable attention in vibration mitigation devices, e.g. Nonlinear Tuned Mass Dampers (NLTMDs) [43, 44] and Nonlinear Energy Sinks (NESs) [45, 46].

Bifurcations and instability

A bifurcation of a dynamical system occurs when the perturbation of parameter values, termed bifurcation parameters, leads to a qualitative, or topological, change in its behaviours. In vibration analysis of dynamical systems, the frequency and amplitude of the excitation are often used to characterise steady-state responses; therefore, they are typically considered as bifurcation parameters, yet other parameters can also be used. In this case, bifurcations of a nonlinear system may result in more periodic solutions than the number of its degrees of freedom [47, 31], a special scenario that cannot be observed in linear systems.

Another feature of nonlinear responses lies in that they can be either stable or unstable. Indeed, the instabilities are correlated to bifurcations as the change of stability occurs through a bifurcation [31]. In determining the stability of a periodic response, the Floquet theory can be used – it can be formulated either in the time domain by computing the monodromy matrix to find Floquet multipliers [48], or in the frequency domain by constructing the Hill's matrix (through harmonic balancing) to find its eigenvalues, termed Floquet exponents [49–52].

Localisation

Localisation can occur and lead to the spatial confinement of energy to subcomponents of nonlinear dynamical systems. Indeed, localisation can also be observed in linear systems, which, however, is limited to weak coupling between subcomponents and structural irregularity, or disorder [53–56]. Nonlinear systems do not have such prerequisites to exhibit localisation because the amplitude-dependent frequency can act as a mistuning parameter [47, 46]. One important example that exploits this feature is the Targeted Energy Transfer (TET) via applications of the NES. By attaching a NES to a primary structure, the energy input to the primary structure can be irreversibly transferred to and localised in the NES where the energy is dissipated [46]. Owing to this promising feature, NES systems have been widely considered in vibration mitigation and isolation [57–59].

In addition to these features, nonlinear systems can also exhibit quasi-periodic motions where the response contains two or more incommensurate frequency components [60, 61]; and chaos where the behaviours of a dynamical system are highly sensitive to initial conditions [62, 29].

Observing that nonlinear systems can exhibit intricate behaviours due to nonlinear sources highlights the importance of rigorous and robust tools to interpret and quantify these nonlinear phenomena.

2.2 Understanding nonlinear behaviours using modal analysis

To interpret and quantify behaviours of dynamical systems, there is a great number of tools [63, 28, 64, 30, 65–67], among which modal analysis has been extensively used in literature and engineering practice. Here, an overview of modal analysis is provided.

One important modal theory is the concept of Linear Normal Modes (LNMs) [68, 69], as introduced in Chapter 1. Owing to orthogonal relations between LNMs, they bring about useful mathematical properties of invariance and superposition principle, based on which linear modal analysis has become an integral part of many well-established techniques and engineering practices. To date, LNMs are still extensively used in the fields of, for example, reduced-order modelling [70], structural health monitoring [71] and experimental modal analysis [72].

The applicability of linear modal analysis requires the system to be linear. However, linearity is an idealised condition whilst nonlinearity is the frequently observed scenario [32, 31, 66]; as demonstrated in §2.1.1 and §2.1.2, a great number of physical sources can lead to intricate nonlinear behaviours in practice. For nonlinear dynamical systems, the useful properties of LNMs break down, and the direct application of LNMs to nonlinear systems can never be guaranteed to yield accurate and robust results. In this context, seeking a nonlinear extension of a LNM is needed for the interpretation and quantification of rich nonlinear behaviours; this attracts much research effort in developing the nonlinear modal analysis.

2.2.1 Concepts of nonlinear normal modes

The early attempts to derive a nonlinear mode were carried out by Rosenberg in [73, 74], where the concept of a Nonlinear Normal Mode (NNM) is defined as a synchronous periodic motion of a conservative nonlinear system. Synchronicity requires that *all* system components reach their extrema and equilibrium simultaneously. In this case, an oscillation in an NNM is characterised by a line, termed a modal line, passing through the origin in the configuration space. In the geometric sense, this can be viewed as an extension of a LNM, a vibration in which is depicted by a straight line (which also passes through the origin) in the configuration space due to linearly related coordinates. Following a similar approach, the construction of NNMs has been further investigated by Rand [75, 76] and Vakakis [77–79].

Later, Shaw and Pierre proposed a generalisation of Rosenberg's definition for a damped nonlinear system via the theory of invariant manifolds [80–83]. In this series of works, an NNM is defined as a two-dimensional invariant manifold that is tangent to the underlying linear modal subspace at the equilibrium point. This definition also extends the invariant, or orthogonal, property of a LNM to the nonlinear context, namely, an arbitrary damped motion that starts on an invariant manifold remains on it over time. In the case of an undamped conservative system, the relationship between Rosenberg's and Shaw-Pierre's definitions can be established by the subcenter-manifold theorem [84]. Adopting a complex invariant manifold formulation, a further extension of the Shaw-Pierre-type NNM was proposed in [85], which shows an improved computational efficiency.

An alternative extension to the Rosenberg's NNM definition was proposed in [31], where an NNM is defined as a periodic response (not necessarily synchronous) of a nonlinear conservative system. Based on this periodic definition, a damped Nonlinear Normal Mode (dNNM) was defined for a non-conservative nonlinear system in [86], where an artificial damping is added to the system in order to compensate for the non-conservative effects.

Recently, the definition of an NNM is relaxed as a set of small-amplitude recurrent motions (i.e. fixed points, periodic and quasi-periodic responses) of damped nonlinear systems [87]. In this context, the smoothest invariant manifold asymptotic to an NNM is termed a spectral submanifold (SSM). The existence, uniqueness, and persistence of SSMs are also derived to provide a mathematically rigorous methodology in nonlinear modal analysis. Building on invariant manifold theory and defined as recurrent motions, the SSM establishes the connections between the Shaw-Pierre-type and Rosenberg's NNMs in dissipasive nonlinear systems.

Additionally, there are other generalisations of nonlinear modes. For example, in [88], a nonlinear mode is defined as a periodic response when phase quadrature takes place, termed a phase resonance nonlinear mode (PRNM). Established based on harmonic forcing, a PRNM represents an actual periodic oscillation on the forced response curve; therefore, it is directly connected to experimental modal testing results, for instance, obtained via force appropriation [89, 90] and control-based continuations [91, 92].

In computations of nonlinear modes, a large body of early studies employed analytical frameworks based on methods that include, for example, the harmonic balance technique [93, 94], perturbation techniques [95, 77], normal form theory [65] and invariant manifold theory [80, 84]. Many of these methods depend on perturbative expansions of the dynamic solutions, combined with truncations up to the first few leading-order terms. With analytical expressions of NNMs, these methods lend themselves to uncover the mechanisms that underpin nonlinear behaviours such as internal resonance, bifurcations, and instability [36, 77, 96].

With the advances of engineering technologies, the last few decades have witnessed a growing need for nonlinear analysis of complex high-dimensional structures. This demand is, to some extent, fulfilled with the development of computational power and algorithms, for example, continuation algorithms [97–99]. Therefore, with the aid of numerical computational techniques [100, 99, 67], the concept of NNMs is progressively considered in the analysis of full-scale nonlinear systems [101–104].

An alternative strategy in response to the computational need is making use of the invariance property of NNMs to derive reduced-order models (ROMs) [105–111]. This idea is especially attractive when dealing with complex engineering systems that are modelled via finite element (FE) discretisation, in which case the nonlinear analysis is computationally infeasible based on the high-dimensional FE model. The appropriately derived ROMs, taking the form of a lower-order nonlinear system, can considerably reduce the computational effort; consequently, the aforementioned analytical and numerical methods can be employed to interpret and quantify nonlinear behaviours based on ROMs.

To derive a ROM from a FE model, the methods can be categorised as intrusive and non-intrusive methods – the non-intrusive method builts ROMs based on the outputs of a FE model without the requirement to analyse the fundamental equations of motion; in contrast, the intrusive method relies on manipulation of the coefficients of full-order model. In this context, the non-intrusive methods mainly include the stiffness evaluation procedure (STEP) [112–114, 107, 115, 110], implicit condensation and expansion (ICE) [102, 107, 116, 109, 117] and quadratic manifold method with static modal derivative [118, 119]; whilst intrusive methods include the quadratic manifold method with modal derivative [119] and invariant manifold methods [80, 87, 120, 121]. Note that, for methods that are based on invariant manifolds, recent developments overcome the requirement for direct manipulation of nonlinear coupling coefficients and give rise to non-intrusive implementations, for example, explicit SSM reduction method [122] and direct normal form reduction method [123, 124]. These methods have been successfully implemented in a variety of nonlinear systems, for example, beam systems [107, 119, 117], flat structures [119], micro-electromechanical systems [124]. Comparison studies between these methods have been carried out in [125, 126], highlighting their advantages and limitations. For a detailed review of these methods, the interested reader is directed to [111].

One could observe that the concepts of NNMs rigorously suit different scenarios (e.g. undamped and damped systems) with different generalisations (e.g. periodic motions and invariant manifolds); therefore, they lend themselves as a versatile tool in the analysis of nonlinear systems.

2.2.2 Characteristics of NNMs

As briefly discussed above, NNMs can significantly simplify the analysis of complex nonlinear systems due to their invariance property. In addition, due to the nonlinear basis they build upon, they provide a rigorous and robust tool in interpreting and quantifying nonlinear behaviours such as internal resonance and bifurcations, in contrast to the LNMs, which cannot capture the nonlinear phenomena. Note that, in this thesis, the term *mode* is used to refer to a mode of the underlying linear model of the system, whereas an NNM denotes a periodic response of the conservative nonlinear system and a backbone curve represents an NNM branch, i.e. a family of periodic motions. [31]. In the following, it is discussed how the concept of NNM captures those nonlinear phenomena, demonstrated in §2.1, along with its applications in nonlinear engineering systems.

NNMs and modal interactions

As briefly mentioned in §2.1.2, modal interactions, or internal resonances, are characterised by energy exchange between modal coordinates during oscillations. This phenomenon can be described by a mixed-mode NNM (i.e. an NNM with multiple linear modal components) where interactions between its modal components can be observed. In this case, the presence of internal resonance is connected to the commensurability between *nonlinear response frequencies* of these modal components. The associated modal interaction may be termed $m : n$ internal resonances [33, 34] with m and n denoting the commensurate frequency match. In practice, when the nonlinear system is vibrating at small to moderate amplitudes, estimating the types of internal resonance can be achieved by approximately referring to the commensurate *eigenfrequency* relationships of the interacting modes in an NNM [33, 111]. This particular scenario can be justified when the nonlinearity-induced frequency detuning (from the eigenfrequency) is small. Therefore, a system with an eigenfrequency ratio of 3 is expected to exhibit $1 : 3$ internal resonance, e.g. in nonlinear beam models [36, 94]. A large body of literature has concentrated on specific types of internal resonances that can be found in a broad range of engineering systems [36, 127, 41, 128]. However, modal interactions become more complex when dynamical systems are vibrating at large amplitudes. In this case, the small frequency detuning condition cannot be satisfied because the response frequency is amplitude-dependent. Therefore, access to the nonlinear response frequency becomes necessary in determining the existence of internal resonances. In addition, multiple commensurate relationships may be satisfied even for a simple two-mode system – this indicates the existence of multiple internal resonances. Owing to these features, determining internal resonance for systems that vibrate at large amplitude is challenging, and usually relies on computationally expensive numerical simulations [31, 104, 52].

Additionally, the concept of NNMs provides a geometric perspective to describe modal interactions. Indeed, many definitions of an NNM are built upon its geometric features, e.g. synchronous/asynchronous periodic responses [73, 74, 31] and an invariant manifold tangent to the equilibrium of a linear modal subspace [80], to name a few. Here, based on the synchronous/asynchronous classification, it is demonstrated how it captures geometric features of modal interactions. For a mixed-mode synchronous NNM, the modal components reach their extrema and equilibrium at the same time over a period of response. Such a periodic motion is characterised by a *modal line* passing through the origin in the configuration space [77]. In contrast, a mixed-mode asynchronous NNM has modal components that *do not* reach their extrema and equilibrium simultaneously. In this case, the NNM is described by a *modal loop* that does not pass through the origin in the configuration space. One example of the latter case is the whirling motions of nonlinear cable systems where the in-plane and out-of-plane modes exhibit $1:1$ modal interactions [129].

NNMs with bifurcations and instability

As discussed in §2.1.2, nonlinear systems can exhibit bifurcations and lead to multiple solutions. Likewise, due to the presence of bifurcations, there can be more NNM solutions than degrees of freedom of the system [77, 31]. One case is the bifurcation that emerges from modal interactions, which may lead to an internally resonant region of NNMs and stability change. This is a topic that attracts a vast amount of research, for example, based on the normal form method, the parameter values leading to bifurcations and $1:1$ internal resonances have been identified in [130]; the general bifurcation scenario, emerging from $1:1$ internal resonance, has been studied theoretically and experimentally in [128]. Another important feature of NNMs that arises from bifurcations is the isolated NNM branch, which, as indicated by its terminology, is isolated from the primary branches that emerge from eigenfrequencies. Due to the geometric feature of being isolated, detecting the existence of isolated NNM branches is of great challenge as initial solutions on that branch are difficult to determine, which are typically required in order to find the full branch. In addition, such an isolated branch can be related to large-amplitude isolated forced responses, termed isolas [131, 132], which have a significant impact on the performance of engineering devices, for example, the vibration mitigation performance of NLTMD systems [43, 133]. Regarding this special feature of NLTMD applications, it will be discussed in detail in §2.3.1.

NNMs with energy localisation

The energy localisation, i.e. energy confinement to subcomponents of a dynamical system, can also be interpreted by the modal compositions of a subset of NNMs. This feature has been demonstrated in many nonlinear systems, for example, flexible systems with smooth nonlinearities [134–137] and non-smooth nonlinearities [138]. As discussed in §2.1.2, one important application that exploits energy localisation is the NES. The irreversiable energy transfer and eventual localisation in the NES device are also captured by the localised NNMs [136]. Another example was demonstrated in [137], where the symmetry breaking induced nonlinear modal veering leads to energy localisations of NNMs for a beam system. In this example, low-amplitude and large-amplitude vibrations are captured by NNM subsets that are localised in bending and torsion modes respectively.

2.2.3 Relationships between NNMs and forced damped responses

Even though NNMs represent the underlying conservative (unforced and undamped) dynamics[1], the relationships between NNMs and forced damped responses can be established.

The connections between NNMs and *forced periodic responses* can be established by the energy balancing analysis [139]. By viewing the forced resonant motions as phase-shift perturbations from NNM solutions, this methodology considers the energy balancing of each modal component during periodic oscillations – the net energy transfer in and out of any mode must be zero. Alternatively, their relationships can be established via the Melnikov analysis in [140]; the Melnikov function (that determines such relationships) is revealed to be equivalent to the leading-order terms of the energy balancing principle.

Using the energy balancing method, NNMs can be used to interpret forced responses, for example, in predicting the existence of isolas [107, 141, 142] – i.e. forced response curves that are separated from the primary branches; and identifying the relative significance of NNMs in forced responses [143]. In addition, the energy balancing method can also aid experimental tests in finding the appropriate number of excitations and their locations in order to accurately extract NNMs experimetally [144]. This technique has later been extended to account for non-conservative nonlinearity based on a numerical framework [145], where it was shown to yield accurate resonance predictions for full-scale dynamical systems with friction nonlinearity.

One advantage of the energy balancing technique, proposed in [139], lies in its highly efficient computation due to analytical formulation based on a single-harmonic assumption. However, such an assumption may also lead to errors when multiple harmonics show

---

[1] Indeed, some nonlinear modal theories derive NNMs based on the forced damped context, for example, Shaw-Pierre-type NNMs [80–83], SSMs [87] and PRNMs [88]; here, the conservative formulation, i.e. the Rosenberg's type [73, 74] and its generalisation in [31], is considered.

significant contributions. Such a limitation was demonstrated in [142], where significant errors can be observed during the emergence of an isola to the primary forced response curve.

In addition to the connections between NNMs and forced periodic motions, the relationships between NNMs and *damped transient responses* can be established via the concept of resonant capture – the damped responses can be locked in the neighbourhood of NNMs for nonlinear oscillators that are weakly coupled [57, 146]. By referring to the frequency commensurate relationships of the NNMs (where the transient motions are locked), such relationships can be characterised as $m : n$ resonant capture [45], similar to the definition of periodic internal resonance. In [45, 147, 148], the NNM-based method was used to interpret the transient targeted energy transfer. The damped transient oscillations, which manifest irreversible energy transfer from one component to the other, were accurately captured by the underlying energy localisation features of NNMs. Regarding the use of NNMs in understanding the targeted energy transfer of NES systems, it will be discussed in §2.3.1.

Based on the relationships between NNMs and forced damped responses, the conceptually simpler NNMs can be used to interpret complex forced damped responses, as discussed above. Conversely, forced damped responses can be used to identify NNMs, an important application of which is the experimental NNM identification, detailed in the following.

2.2.4 Experimental modal analysis

Even though the advanced mathematical tools and increasingly powerful computational techniques have made great contributions to nonlinear analysis of complex engineering systems, experimental modal analysis still has an important role in both verification and validation of numerical/analytical results and recognition of new or unsolved problems.

Experimental modal analysis for linear structures is a well-matured field that has been extensively used in engineering practice. This can be achieved by applying impact hammer testing, shaker testing, and ambient vibration testing [149–153]. From the testing data, modal parameters, namely eigenfrequencies, modeshapes and modal damping ratios, can then be identified by techniques, for example, eigensystem realisation algorithm [154], polyreference least-squares complex frequency-domain technique [155] and stochastic subspace identification technique [156].

However, in the nonlinear context, dynamical systems can exhibit rich nonlinear behaviours (as discussed in §2.1) that significantly complexify experimental tests in identifying modal properties such as that presented in §2.2.2. The past few decades have witnessed a large amount of research effort devoted to nonlinear modal testing techniques; for a complete survey, the interested reader is directed to [64, 66]; here, an overview is given of the NNM-based experimental techniques.

The nonlinear resonant decay method was proposed in [157] for identification of nonlinear systems. Firstly, a burst is applied to the system at eigenfrequencies of linear modes to excite responses that exhibit modal coupling due to nonlinear terms. A curve fitting based on the restoring force surface method is then employed to identify modal parameters and NNMs. This experimental technique has been implemented in many mechanical systems, for example, a wing structure [158] and an aircraft [159].

A nonlinear extension of linear force appropriation was proposed in [89] to extract NNM branches via experimental tests. The idea is to seek a set of excitations in order for the system to exhibit responses of a single NNM. This is achieved by adapting the multi-point multi-harmonic excitations to satisfy quadrature criterion – the excitations are 90° phase-lagged to all harmonics of displaments at the excitation points. Once the NNM approparation is achieved, the frequency-amplitude relationship of an NNM can be determined from the transient motions, termed resonant decay [90], via time-frequency analysis methods such as Wavelet transfrom [160] and Hilbert transfrom [161]. Successful implementations of the force appropriation technique were demonstrated in many studies in combinations with, for example, control-based continuation technique [91, 92] and phase-locked loop [162, 163]. These studies show that, for most scenarios, even a single excitation is sufficient to accurately identify an NNM branch. However, numerical and experimental studies in [144] show that significant errors can arise due to insufficient compensation between mono-point excitation and distributed damping.

Nonlinear modal analysis can also be realised by control-based continuation (CBC), which was first introduced in [164] as an experimental technique that aims to track nonlinear steady-state oscillations with varied parameters. It relies on a feedback controller whose control target acts as a proxy for the system state and ensures non-intrusive implementations, i.e. the observed solutions in the controlled system are also solutions for the uncontrolled system. In addition, the controller stabilises the system and therefore, it allows for tracking of unstable solutions experimentally. This technique has been implemented in identifying NNM branches [91, 92]; capturing softening-hardening features [165] and modal interactions [166].

2.3 Exploiting nonlinear phenomena

Some nonlinear phenomena can be problematic – they not only pose challenges to analysis and designs of engineering systems but also significantly affect the performance of structures/facilities, as detailed in §2.1. For example, inferior machining quality caused by chatter instability during turning process of cutting machines [167]; limit cycle oscillations of the aircraft caused by nonlinear interactions of the structural and aerodynamic forces [168]; vibrations of civil structures caused by earthquake, burst and wind loads [3]. Conversely, other nonlinear phenomena are of great potential, and a large body of studies seek to exploit their features in engineering practice. The main families of applications include vibration suppression [47, 169, 136, 170–172] and energy harvesting [173, 174].

2.3.1 Vibration suppression

Linear dampers have been extensively used in engineering practice due to their simple concepts in the field of vibration suppression; nonetheless, they are sensitive to the variation of the system parameters and external environments. For example, the vibration mitigation performance of a linear tuned mass damper may severely be weakened due to the mistuning effect that arises from such as the natural frequency shift of the primary system [175]. Active control has been proposed to address this limitation when using linear dampers [175–177]; however, several problems, for example, the high requirement for robust control algorithms and relatively high costs, may complicate and limit the design and application.

Nonlinear dampers have received increasing attention over the last few decades due to their wider frequency bandwidth and higher robustness in-service when compared with linear dampers. A great number of studies can be found on different nonlinear dampers, which, according to the nonlinear characteristic, can be categorised into the following classes [178]: the *nonlinear stiffness dampers*, for instance, the NLTMD and NES [47, 131]; the *nonlinear damping dampers*, e.g. the fluid viscous damper [3, 179], magneto-rheological damper [180–182], friction damper [183], etc; and *nonlinear stiffness and damping dampers* such as vibro-impact dampers [17, 18].

Among these applications, the nonlinear stiffness dampers are further discussed in the following, as this type of damping devices has been widely considered in engineering practice and literature [184, 46, 43, 44]; in these studies, the nonlinear modal analysis (the topic of this thesis) was shown to be an accurate and efficient tool in interpretation, quantification, and optimisation.

Nonlinear Tuned Mass Damper

To suppress structural vibration, the dynamic vibration absorber, or the tuned mass vibration absorber, was proposed in 1911 by [185]. Such a device consists of a mass and a linear spring and is attached to the primary system to ameliorate the dynamic behaviour of the primary system. With properly selected mass and spring parameters, attaching the device to the system can redistribute the vibration energy by transferring energy from the primary system to the absorber. Afterward, Den Hartog introduced a damping component to the absorber and generated the concept of the linear tuned mass damper (LTMD) in 1956 [68], where a corresponding optimisation methodology, termed the equal-peak method, was proposed to achieve the best vibration suppression performance. Since then, the LTMD has received extensive studies and applications [186–188]. Nonetheless, as a linear damper, it is subject to the limitations mentioned previously, namely, it can only achieve sufficient suppression performance within a narrow bandwidth. Even though several measures can be adopted to address this limitation, e.g. combining the tuned mass damper with active or semi-active control strategies [176], and implementing multiple tuned mass dampers [189], several problems such as the high cost and power supply still need to be solved in practical use.

An alternative strategy to address the limitations of a LTMD is integrating nonlinear components to generate the concept of a NLTMD. A nonlinear generalisation of the equal-peak method was introduced in [43] for optimising a NLTMD; its vibration suppression performance was compared with that of a LTMD. In [44], the main advantage of introducing nonlinearity is highlighted as the improvement of the performance bandwidth. The NLTMD has, for example, been utilised to control a supercritical Hopf-bifurcation of aerofoil flutter [190]; suppress machining chatter, and improve machining stability [191]; and suppress limit cycle oscillations of mechanical systems [192].

Besides these favorable properties, the use of a NLTMD also brings about some undesirable dynamic behaviours that may limit, even severely weaken, its performance. One of such undesirable phenomena is the existence of isolas, i.e. forced responses that are detached from the primary response branches. Predicting the existence of isolas is challenging; and furthermore, these isolated branches may be associated with large-amplitude responses [131, 132, 43, 133]. Early study of isolas in engineering systems was carried out by Abramson [193]; later, extensive works have focused on the mechanism of their creation, such as discontinuity [194, 195], internal resonances [196] and symmetry breaking [197, 141].

Numerous approaches have been used to detect and trace isolas. One method is numerical continuation which uses special points, such as fold bifurcations and extremum points, to trace the evolution of isolas by varying specific parameters [198, 199]. In combination with continuation methods, singularity theory can be used to provide complementary information in the prediction and identification of isolas [200–202]. Methods based on continuation can efficiently find isolas; however, they require a good understanding of the system, and its responses, to select the appropriate continuation parameters. Another numerical method is global analysis, which may detect an isola by finding initial conditions which are within the basin of attraction of that isola [203]. This approach requires a large number of simulations of initial conditions, making it computationally expensive and thus unsuitable for large systems. An alternative approach is making use of backbone curves in isola prediction via the energy balancing analysis [139, 198, 141]. This approach reduces the isola-finding problem to an analytical and computationally simpler one; however, it requires that the backbone curves are known.

Nonlinear Energy Sink

To work efficiently, the natural frequency of a NLTMD, similar to a LTMD, is usually tuned with respect to a particular mode of the primary system based on resonant responses [43]. Even though the NLTMD has already shown an improved bandwidth performance when compared to a LTMD, it still exhibits a suboptimal performance when the excitation frequency is not in the vicinity of the target mode. One way of overcoming the band-limited nature of the vibration suppression device is to employ multiple dampers targeting different modes [204].

The effective bandwidth of vibration suppression can be further extended by exploiting the nonlinearity in the form of a NES. As with a NLTMD, a NES is composed of a small-sized device with a small mass value but is now attached to the primary system by a nonlinearisable spring (i.e. one lacking a linear stiffness component) [46]. Without a resonant frequency, the NES is able to interact resonantly with numerous modes of the primary system, and hence exhibits a broad frequency bandwidth performance [57, 205, 146]. In addition, one promising feature seen in applications of the NES is the TET phenomenon [57, 146, 206] – with an initial energy (above a critical level) in the primary system, the energy can be transferred in an irreversible manner from the primary system to the NES (or energy receiver), where the energy is dissipated. Due to these advantages, a variety of NES schemes have been proposed, e.g. a device with cubic nonlinearity [58, 207], a nonlinear rotator [208, 209], a vibro-impact oscillator [210, 211], a tuned bistable NES [212] and a lever-type NES [213]. The NES has been utilised to suppress the building structure vibrations caused by earthquake and shock loadings [210, 214, 59], suppress the aeroelastic instability of a long-span bridge due to coupled flutter [58], and attenuate the vibration of a railway bridge caused by traffic loads [215].

The mechanism underpinning the phenomenon of TET has been investigated by numerous studies, where the concept of NNMs [31], were frequently used to interpret the forced and damped responses [216, 45, 46]. These NNM-based frameworks revealed that the resonant capture (as introduced in §2.2.3) governs the strong energy transfer from the primary system to the NES [57, 146]. In [216], the bifurcations and energy localisation features of NNM branches were used in combination with numerical wavelet transforms to consider the time evolution of harmonic responses to evaluate the energy transfer between modes. In [45], three mechanisms were identified to realise TET, namely, fundamental, or 1 : 1, resonant capture; subharmonic resonant capture; and resonant capture triggered by nonlinear beating. Later, experimental investigations on the resonant capture were performed in [169, 136]. Focusing on the fundamental resonant capture, the conditions of the system and external forcing that are required to exhibit efficient or optimal TET are quantified in [147, 148]. To understand TET, the dynamics of the system can also be approximated as a partition of slow and fast dynamics; as such, the phenomena of TET are captured by the evolutions of the slow-flow dynamics [45, 148].

2.3.2 Other applications

Besides vibration suppression, which is the main application considered in this thesis, other applications that exploit nonlinear behaviours are also widely considered in research and engineering practice. One major field is the energy harvesting, an overview of which is briefly given here, whilst the interested reader is referred to [217, 218] for a survey.

The frequent use of small-scale mobile devices in engineering practice, e.g. the wearable devices, the field test, structural health monitoring, etc., has made device powering an open problem [219, 220]. One potentially viable solution, ambient vibration harvesting has received much research effort. Early works on vibration harvesting were mostly based on linear oscillators that convert vibration to electricity via capacitive, inductive or piezoelectric methods with the natural frequency of the oscillators tuned in the spectral region where most energy can be exploited [221, 222]. Nonetheless, the ambient vibrations are usually caused by wind loading, seismic noise and traffic loading, which exhibit nonstationary and wide spectral band properties. This makes the linear oscillators insufficient for the harvesters as it can only extract a limited amount of energy within a narrow band [223].

To overcome the limitations of linear energy harvesters, the exploitation of nonlinearity is extensively considered. To date, a vast number of studies were conducted to explore the application of nonlinear energy harvesters, mostly in the forms of monostable Duffing [224, 225], impact [226] and bistable oscillators [227]. Benefiting from nonlinearity and damping of the oscillator, the monostable harvester exhibits a broadening resonant effect, and thus it has a widen bandwidth. The impact harvester is a device in which a lower-frequency ambient vibration impacts a higher-frequency energy harvester through the mechanism of frequency up-conversion, leading to energy harvesting at the coupled frequency. The bistable harvesters, with a unique double-well potential, has three distinct dynamic operation regimes, namely low-energy intrawell vibrations, aperiodic or chaotic vibrations between two wells and periodic interwell oscillations, which strongly depends on the amplitude of the excitation. Having higher mass velocity during the periodic interwell oscillations, the bistable harvester has favourable electrical output performance. For an overview of the applications of bistable energy harvesters, the interested reader can refer to [227] for a survey.

In addition to energy harvesting, nonlinear phenomena have also been closely exploited in signal processing [228, 229], micro-electromechanical devices [230, 25, 170] and filters [231, 24], to name a few.

2.4 Research motivations

In §2.1, it was presented that, with commonly observed nonlinear sources, engineering systems can experience rich nonlinear phenomena. These nonlinear behaviours can present numerous challenges in analysis and design of dynamical systems, yet they also bring about advantageous applications.

To overcome challenges and develop applications, a great number of tools can be used for nonlinear analysis. Specifically, in §2.2.1, it was demonstrated that nonlinear modal theory, using the concept of NNMs, or backbone curves, can provide a tool for efficient interpretation and quantification of nonlinear behaviours.

Due to the invariance property of NNMs, reduced-order modelling methods can be employed to construct computationally cheap, low-dimensional models that capture the salient dynamics of computationally expensive, high-dimensional systems. In addition, due to the nonlinear basis they build on, NNMs can rigorously and robustly capture nonlinear behaviours such as modal interactions, bifurcations, and instabilities, as discussed in §2.2.2.

Even though NNMs and backbone curves represent the underlying conservative dynamics, their connections to forced periodic responses can be established via the energy balancing analysis; likewise, the relationships between backbone curves and damped transient responses are underpinned by the concept of resonant capture, shown in §2.2.3. Therefore, backbone curves can be used to interpret and predict forced damped responses; or conversely, using forced damped responses to identify backbone curves during experimental tests, as demonstrated in §2.2.4.

As a versatile analysis tool, backbone curve analysis is extensively used in designs, optimisations and validations of nonlinear engineering applications, some examples of which were introduced in §2.3.1. Specifically, discussions were given on the applications in vibration suppression using nonlinear damping devices such as a NLTMD and a NES.

It was noted in §2.2.1 that the primary advantages of using backbone curves for dynamic analysis include the simplified computations that are required, as well as the capability to rigorously interpret the mechanisms that underpin nonlinear dynamic behaviours. However, due to the complexity of nonlinear phenomena, backbone curves can also exhibit intricate features that are difficult to quantify, especially in the presence of modal interactions. Synchronous backbone curves, where the modal components oscillate either in-phase or anti-phase, are commonly observed in engineering systems. However, they can be transformed into isolated backbone curves, the existence of which can pose challenges to the computations as a prior knowledge (extra initial solutions) of these isolated branches is required. In addition, they can be associated with high-amplitude responses that have a significant impact on the performance of engineering systems, for example, the NLTMD systems that were introduced in §2.3.1. Therefore, an objective of the research is to provide an analytical study of isolated backbone curves in order to gain insights into the mechanisms that govern their existence. In addition, considering their significant impact on applications of a NLTMD, how these isolated backbone curves can be reliably eliminated must be investigated. This will also help account for these nonlinear features more easily when designing other nonlinear systems.

Another nonlinear feature, arising from modal interactions, of backbone curves lies in the existence of asynchronous motions, for example, whirling motions of cables and rotor-shaft systems. In contrast to synchronous motions, the asynchronous motions represent cases where the phase relationships between modal coordinates are arbitrary values. As such, they represent a large family of nonlinear responses, however, they have received less investigations in literature. The study of asynchronous backbone curves can further the theoretical understanding of whirling-like motions and gain insights into practical designs of engineering systems such as cables to better account for this nonlinear behaviour. By comparing the definitions of synchronous and asynchronous motions, it is the phase relationship between modal coordinates that governs their differences. Therefore, the study looks in-depth into the phase relationships to uncover the underpinning mechanism that distinguishes between synchronous and asynchronous backbone curves. Interestingly, it will be shown how the phase relationships of asynchronous backbone curves can exhibit amplitude-frequency dependency – a new class of nonlinear behaviours. This uncovered mechanism also reveals the significance of accounting for phases in nonlinear modal analysis.

As demonstrated in §2.2.2, the picture becomes more complex when dynamical systems vibrate at large amplitudes in the presence of internal resonances between *nonlinear frequencies*. In this context, determining the existence of internal resonances is challenging because of the required access to nonlinear frequencies as well as the fact that multiple internal resonances can exist. As such, many studies employed case-by-case studies, or computationally expensive simulations to determine specific types of internal resonances. To address the challenges, an analytical approach is employed to study the existence and locations of internal resonances for two-mode interactions with an arbitrary eigenfrequency ratio when vibrating at large amplitudes. In this general context, the underlying relationships between synchronous and asynchronous backbone curves will be explored to generalise the insights gained during separate studies of them. In addition, the study aims to derive explicit formulas that reveal the relationships between physical properties and internal resonances that may occur. A method will be provided for efficient determination of internal resonances, which can aid practical designs when specific types of internal resonances are exploited, or to be eliminated.

In §2.2.3, it was shown that the relationships between backbone curves and forced periodic responses can be established via the energy balancing principle. Based on this mechanism, one can use backbone curves to interpret forced periodic oscillations, or conversely use forced responses to identify backbone curves. One advantage of the energy balancing method, proposed in [139], lies in the analytical formulation that lends itself to efficient prediction of forced responses; however, it also brings about an inherent limitation that it may yield unrobust and even incorrect predictions due to neglecting harmonic contributions. Furthermore, it also prevents a direct analytical extension that accounts for multiple harmonics, instead, it results in a numerical scheme that is of a high computational cost. Therefore, another objective of this thesis is to propose an energy balancing method that overcomes the unrobust and inaccurate limitations whilst preserving the computational efficiency. This is achieved by employing a semi-analytical framework to account for multi-harmonic energy-transfer balancing. A criterion will also be presented which evaluates the applicability, as well as monitoring the accuracy, of the proposed method. As such, this method will allow a robust and accurate use of backbone curves to interpret forced responses. In addition, it will also aid experimental backbone curve identification, for example, in designing an appropriate number of excitation points and their arrangements in order for accurate identification.

In §2.2.3, it was also demonstrated that the relationships between backbone curves and damped transient responses are underpinned by the concept of resonant capture. With this mechanism, the backbone curve can be used to interpret TET in applications of the NES, as discussed in §2.3.1. Indeed, TET is governed by the energy localisation properties of the underlying conservative backbone curve, and the irreversible energy transfer is realised via resonant decays that are locked in the neighbourhood of such a backbone curve. However, how the energy localisation features are realised and how they can be identified in other mechanical systems, has not been explored fully. Therefore, the final objective of this thesis is to explore the underpinning mechanism that governs the essential backbone curves to gain insights into the realisation of TET. These insights must allow such a nonlinear phenomenon to be better accounted for and more easily exploited in practical designs of NES systems. Furthermore, a more general understanding of TET (not necessarily limited to NES systems) will also facilitate the identification of TET in other mechanical systems.

Based on the observations, this thesis has the following main objectives:

1. *To investigate internal resonances using backbone curves.*

   To achieve this, an analytical approach is employed that is based on backbone curve analysis. Firstly, some special geometric features (with significant engineering application relevance) of nonlinear normal modes are explored, including how synchronous backbone curves are transformed into isolated backbone curves, and what mechanism underpins the features of asynchronous backbone curves. These concepts will then be generalised in a broader scope to account for arbitrary types of internal resonances for arbitrary two-mode interactions. The connections and differences between synchronous and asynchronous backbone curves will be analytically investigated; this will allow their existence to be reliably and efficiently determined.

2. *To investigate the relationships between backbone curves and forced-damped responses.*

   To establish the relationships between backbone curves and forced periodic responses, an energy-based method is employed to account for energy balancing across multiple harmonics in an NNM. This provides a robust and accurate method to interpret and predict forced responses using backbone curves; in addition, it will also aid the experimental designs for backbone curve identification. Whilst, based on the relationships between backbone curves and damped transient responses, the required backbone curves for the realisation of TET are explored. The gained insights allow TET to be better accounted for and more easily exploited in NES systems; furthermore, they can also aid in identifying the realisation of TET in other engineering systems.

To better motivate the research of this thesis, a motivating example is provided before presenting the thesis outline.

2.5 Motivating example

In this section, an example case is presented to demonstrate modal interactions in nonlinear dynamical systems and motivate the studies of this thesis. In literature, the majority of works on modal interactions are based on two-mode interactions, see Refs. [33, 130, 251, 263, 142], although other cases such as three-mode interactions have been reported in [41]. In line with much literature, a two-mode nonlinear system is considered in this section. Such a two-mode system may be seen as representative of many mechanical systems with two interacting modes, e.g. a primary system with a vibration absorber attached [46, 131, 43], cable systems [232, 129] or nonlinear beam systems [233, 36, 52].

In the linear modal domain, the equations of motion for the two-mode system with a cubic nonlinearity under periodic excitations are given by

$$\ddot{q}_1 + d_1\dot{q}_1 + \omega_{n1}^2 q_1 + \Psi_4 q_1^3 + 3\,\Psi_1 q_1^2 q_2 + \Psi_3 q_1 q_2^2 + \Psi_2 q_2^3 = P_1 \cos(\Omega t)\ , \tag{2.1a}$$

$$\ddot{q}_2 + d_2\dot{q}_2 + \omega_{n2}^2 q_2 + \Psi_1 q_1^3 + \Psi_3 q_1^2 q_2 + 3\,\Psi_2 q_1 q_2^2 + \Psi_5 q_2^3 = P_2 \cos(\Omega t)\ , \tag{2.1b}$$

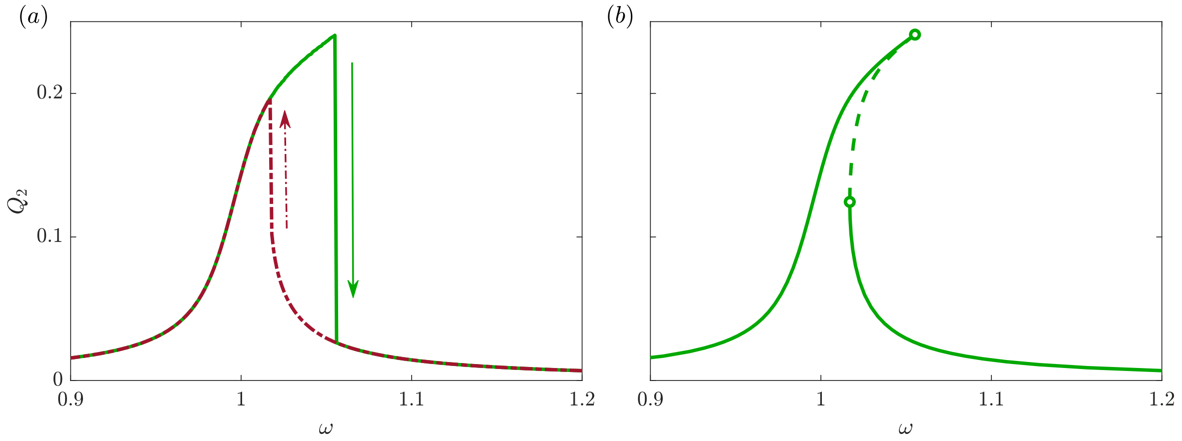

Fig. 2.1 Forced response curves (FRCs) of the example system with forcing amplitude $P_2 = 0.003$. Both panels show the FRCs in the projection of the response frequency, ω, against the maximum response amplitude of the second mode, Q_2. (*a*) The FRCs obtained via forward and backward frequency sweeps, denoted by solid and dot-dashed lines respectively, where the arrows denote the jump phenomena. (*b*) The FRCs, obtained via numerical continuations, where the stable and unstable segments are denoted by solid and dashed lines respectively with bifurcation points marked by dots.

Table 2.1 Parameters of the motivating example system.

ω_{n1}	ω_{n2}	d_1	d_2	Ψ_1	Ψ_2	Ψ_3	Ψ_4	Ψ_5
0.9	1	0.01	0.01	0.5	0.5	5	1	1

where q_i, $\dot{q}_i$, and $\ddot{q}_i$ are the i^{th} linear modal displacement, velocity, and acceleration respectively. d_i denotes the i^{th} linear modal damping. It should be noted that the linear modal damping is reflective of a significant number of engineering systems with geometric nonlinearity where the damping may be assumed small when compared to external forcing and nonlinear stiffness [234, 30, 31, 144, 117]. ω_{ni} is the i^{th} linear natural frequency. $\Psi_1, \ldots, \Psi_5$ are coefficients of the nonlinear terms, and P_i is the amplitude of i^{th} modal excitation with forcing frequency Ω. In this example case, only the cubic nonlinearity is considered for demonstrating the rich dynamics in nonlinear systems. In practice, other forms of nonlinearity such as quadratic nonlinearity can also be relevant [228, 246].

Here, an example system, with parameters given in Table 2.1, is considered. Note that the parameters of the example system are considered for an illustrative purpose rather than a case study of any practical engineering systems[2]. However, a number of practical examples will be given in accordance with the related applications in the following chapters.

For a given system, the Forced Response Curves (FRCs) are solution branches of forced periodic responses. They reveal rich nonlinear behaviours, e.g. modal interactions, bifurcations, and instability that emerge from nonlinear coupling mechanism; therefore, FRCs are widely used for analysis and design of nonlinear systems [235, 31, 30]. Here, to study the nonlinear responses, a periodic forcing with amplitude $P_2 = 0.003$, is applied to the second mode, q_2. The simplist way to compute the FRCs of the example system is arguably via direct numerical integration by performing frequency forward and backward sweep simulations. This may be performed using inbuilt solvers such as Matlab's `ode45` [236]. The forward and backward FRCs are shown as solid and dot-dashed curves respectively in Fig. 2.1*a* in the projection of the response frequency, ω, against the maximum displacement amplitude of the second mode, Q_2. As this technique relies on integration of steady-state responses, it only captures the stable solutions. The bifurcations from stable to unstable responses are characterised by jump phenomena, denoted by arrows in Fig. 2.1*a*. To locate unstable solutions, one can employ the shooting method, where an initial value problem is formulated. The initial state of the system is iteratively updated to meet the periodicity condition of a forced response.

Alternatively, one can avoid numerical integration in finding periodic solutions by employing the harmonic balance method and the collocation method [235, 30, 67]. The harmonic balance method is a frequency domain method where the periodic solution of the nonlinear dynamical system is approximated by a series of harmonic components with unknown Fourier coefficients. By substituting the assumed solution to the equations of motion, and balancing the harmonic components, finding periodic solutions leads to solving a set of nonlinear algebraic equations. Whilst, the collocation method is a time domain method where the periodic solution is divided into mesh time intervals; at each interval, the solution is approximated by a Lagrange polynomial function. To find the periodic solution, the equations of motion are satisfied at a given set of nodes termed collocation points. These two methods have been frequently incorporated in numerical continuation techniques to find periodic solutions of nonlinear dynamical systems, see references [31, 100, 99].

---

[2] Note that, when considering practical systems, the coefficients of the nonlinear terms, Ψ_i, may be seen as functions of the physical parameters, e.g., linear stiffness and nonlinear stiffness. In that case, additional constraints should be imposed to define positive-definite strain energy.

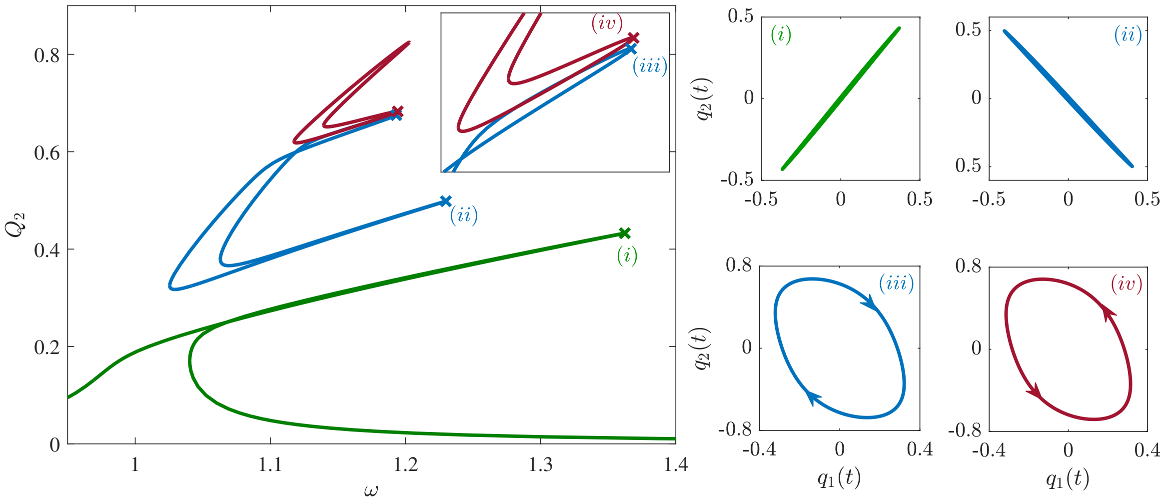

Fig. 2.2 Forced responses of the example system with forcing amplitude $P_2 = 0.01$. The left panel shows the FRCs in the projection of the response frequency, ω, against the maximum response amplitude of the second mode, Q_2. For simplicity, the stability of the responses is not presented here. On FRCs, four example resonant responses are denoted by '×' and labelled $(i) \rightarrow (iv)$, the time-parameterised responses of which are shown in the right panels in the configuration space. The arrows in panels (iii) and (iv) denote clockwise and anticlockwise asynchronous responses.

Here, the Matlab-based continuation software COCO is used to compute FRCs of the example system. It should be noted that the `po`-toolbox of COCO makes use of the collocation method to discretise the problem and continuation is performed to obtain periodic solutions [99]. The computed results are shown in Fig. 2.1*b*, where the stable and unstable segments are represented by solid and dashed lines respectively with bifurcations denoted by hollow dots. A typical nonlinear hardening feature can also be observed as the response curve bends to higher response frequency as amplitude increases.

To complicate matters, as the external forcing amplitude increases, more complex nonlinear phenomena may be observed. Here, to demonstrate the complexity, the forcing amplitude is increased from $P_2 = 0.003$ to $P_2 = 0.01$. The FRCs are computed via numerical continuations and shown in the left panel of Fig. 2.2; note that, for simplicity, the stabilities of the responses are not shown.

In this figure, besides the primary forced response curve (green line), two isolas, i.e. regions of forced responses that are separated from the primary branch, can also be observed – they are represented by red and blue lines. Due to this isolated feature, the existence of isolas can be difficult to determine; in addition, these isolated solutions may represent significant, high-amplitude responses, which are of great importance for practical engineering systems, as discussed in §2.3.1. Note that the direct numerical integration is not favourable in quantifying these features as stable solutions on these isolas are required to initiate the frequency sweep – it must be performed very carefully at a computationally expensive cost; hence the results from numerical integration are not shown here. In contrast, numerical continuations can effectively stabilise the responses (see Fig. 2.1*b*) and thus, it allows the full dynamics to be found if an appropriate number of initial solutions are provided.

Another feature of the larger-amplitude forcing case lies in the existence of intricate modal interactions, or internal resonances. By definition, the internal resonance denotes a periodic response where the interacting modes exhibit frequency commensurate matches. Here, four example periodic responses at phase resonances[3] on FRCs (labelled $(i) \to (iv)$ in the left panel of Fig. 2.2) are considered; and they are mapped to the configuration space in the right panels. From the configuration mappings, one can observe that, for every period of q_1 response, q_2 also oscillates for one period. As such, these two modes vibrate with a $1:1$ frequency relationship, denoting $1:1$ internal resonance. Even though these responses are dominated by the same frequency, they show different geometric features in the configuration space. In panels (i) and (ii), q_1 and q_2 vibrate in-phase and anti-phase respectively, in another word, these two periodic responses exhibit synchronous, or in-unison, resonance – a line passes through the origin in the configuration space. In contrast, in panels (iii) and (iv), the responses exhibit asynchronous features, characterised by a loop in the configuration space. The two isolas, combined with geometrically intricate internal resonances, make it challenging to fully characterise the nonlinear behaviours of the example system, despite its apparent simplicity.

One method to account for these features is to consider the concept of nonlinear normal modes (NNMs), i.e. undamped and unforced periodic responses of the nonlinear system [31]. The NNM branches, or backbone curves, provide a simpler topology than the FRCs, nonetheless they still capture the essential nonlinear behaviours. To compute the backbone curves of the example system, the damping and forcing terms of Eqs. (2.1) are removed (regarding the conservative NNM definition). Using numerical continuations, the backbone curves are found and shown as solid black lines in Fig. 2.3; whilst the FRCs are shown as thin lines for comparison. One can observe that the FRCs envelope the backbone curves, with phase resonances captured by the backbone curves. Four time-parameterised responses with respect to the labelled signs on backbone curves, near

---

[3] Note that, at these labelled responses, the external forcing exhibits 90° phase-lagged to the modal displacement, as such, they are termed phase resonances [88].

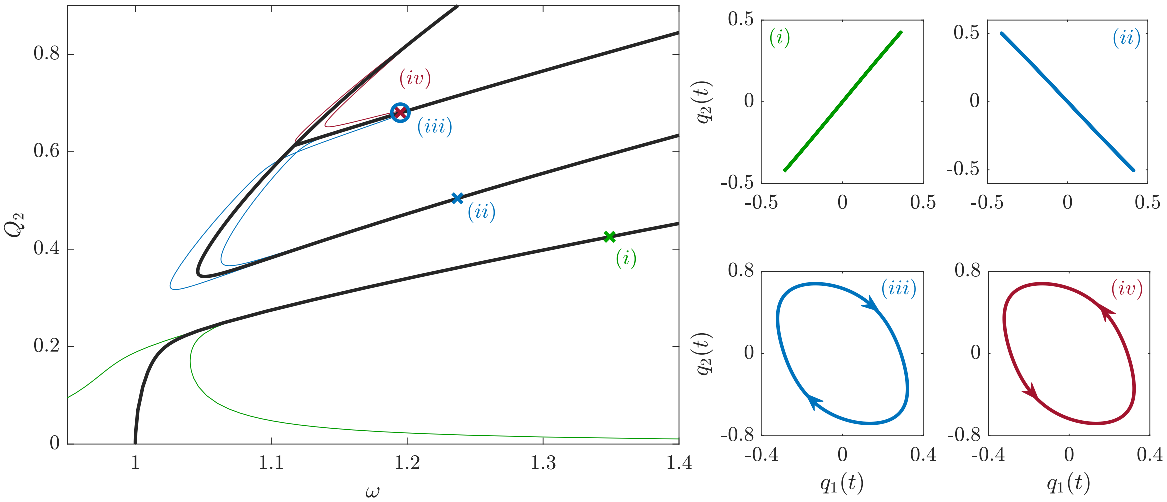

Fig. 2.3 Backbone curves of the motivating example system. The left panel shows the backbone curves in the projection of the response frequency, ω, against the maximum response amplitude of the second mode, Q_2. For comparison, the FRCs for $P_2 = 0.01$, presented in Fig. 2.2, are shown as thin lines. On these *backbone curves*, four example NNM solutions are labelled $(i) \to (iv)$, the time-parameterised responses of which are shown in the right panels in the configuration space. Note that these NNM solutions are in the neighbourhood of the resonant responses on FRCs.

the phase resonances on the FRCs, are shown in the right panels of Fig. 2.3. These four unforced, undamped responses show strong similarity to that of the forced cases in Fig. 2.2.

Up to this point, it has been shown that the backbone curves, i.e. the underlying unforced undamped dynamics, provide a *qualitative* interpretation of the forced-damped responses. To further establish a *quantitative* relationships between the backbone curves and forced periodic responses, one can consider the energy balancing technique, proposed in [139]. The energy principle used by this technique is that the net energy transfer in and out of the system must be zero over a period of response. The conservative stiffness does not lead to energy transfer in and out of the system; as such, the only parameters that allow energy transfer are damping and external forcing. Across all modes of the system, the energy balancing principle is given by

$$\sum_{i=1}^{N} (E_{Di} + E_{Pi}) = 0 \,, \tag{2.2}$$

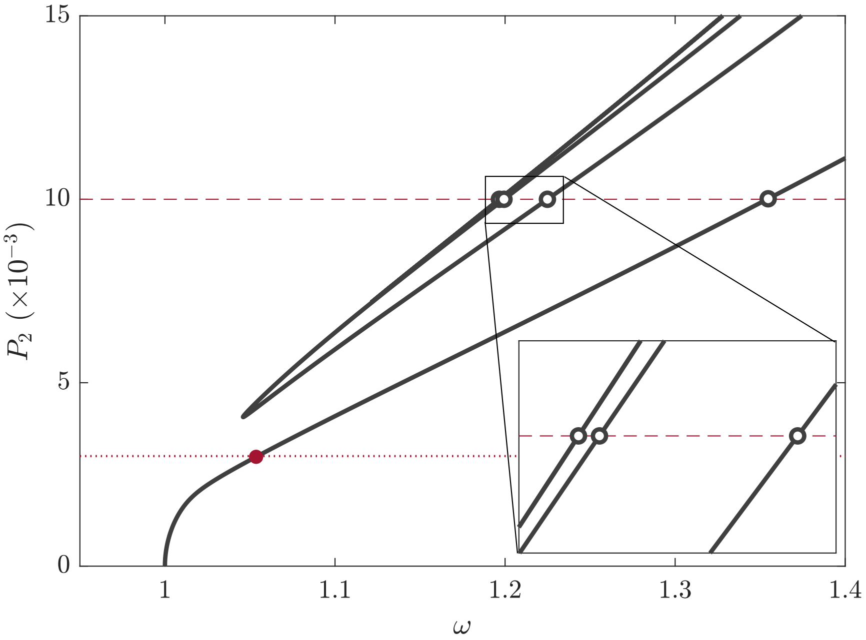

Fig. 2.4 Energy balancing analysis of the motivating example system. The solid lines represent the required forcing amplitudes, P_2, in order to have intersections between forced responses and backbone curves at response frequency ω. The dashed line represents the case with a forcing amplitude of $P_2 = 0.01$, where four crossing points on the backbone curves are identified and shown as hollow dots; whilst the dotted line represents the case with a forcing amplitude of $P_2 = 0.003$, where the identified resonant crossing point is denoted by a solid dot. The two forcing cases are associated with the forced responses shown in Figs. 2.1 and 2.2.

where E_{Di} and E_{Pi} denote the i^{th} modal damping and forcing energy-transfer terms respectively, and N is the total number of modes of the system. As given in [139], E_{Di} and E_{Pi} can be computed using

$$E_{Di} = \int_0^T [d_i \dot{q}_i] \, \dot{q}_i \mathrm{d}t \, , \tag{2.3a}$$

$$E_{Pi} = -\int_0^T [p_i(t)] \, \dot{q}_i \mathrm{d}t \, , \tag{2.3b}$$

where T is the period of the response of the system considering all modes, and $p_i(t)$ is the periodic forcing applied to the i^{th} mode, i.e. $p_i(t) = P_i \cos(\omega t)$ for the case considered here.

Using energy balancing to establish the relationships between backbone curves and forced periodic responses, it is assumed that they share intersections, called *resonant*

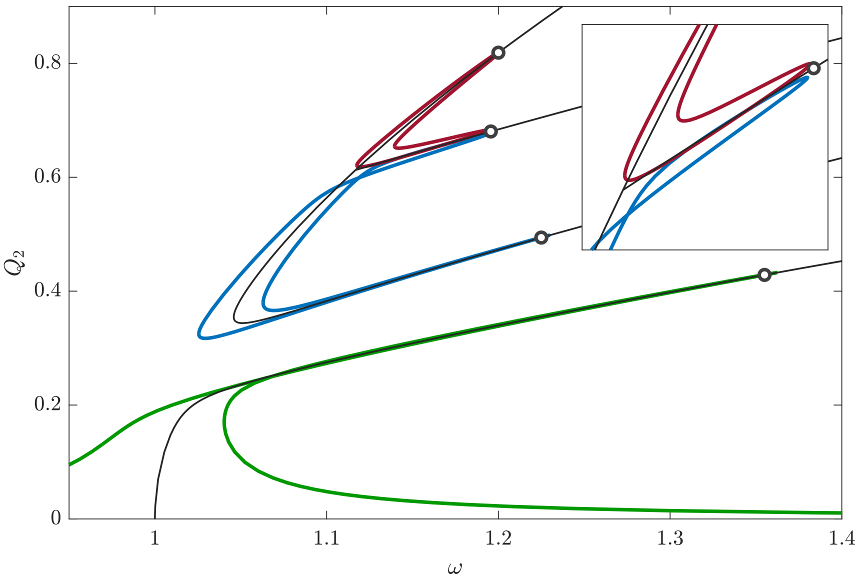

Fig. 2.5 Interpretating forced responses using backbone curves. Backbone curves of the system are shown as thin black lines; whilst the FRCs are denoted by thick solid lines. The relationships between forced responses and backbone curves are identified using the energy balancing analysis (see Fig. 2.4). Four intersectins between the forced responses and backbone curves are identified and shown as hollow dots in this figure.

crossing points. As such, the backbone curves may be seen as loci of potential forced responses; then at resonant crossing points, the energy balancing mechanism for periodic forced responses also holds for backbone curves. Note that, in constructing the energy balancing analysis, the backbone curves are viewed as known parameters whilst the forcing amplitude, P_i, are unknowns and to be computed via Eqs. (2.2) and (2.3). Consequently, based on energy balancing, the backbone curves can be used to predict/interpret forced responses.

To demonstrate this, the same system parameters are considered, given in Table 2.1; whilst the forcing amplitude of the second mode, P_2, is assumed as an unknown parameter to be computed. The results are shown in Fig. 2.4 – the forcing amplitude required for the forced responses to share solutions with the backbone curves at response frequency ω. For any given forcing amplitude, i.e. a horizontal line in this projection, the energy balancing technique identifies the crossing points on backbone curves at corresponding response frequencies. For example, the forcing case where $P_2 = 0.01$ is represented by a dashed line in Fig. 2.4, and the energy balancing analysis identifies four crossing points, denoted by hollow dots. To verify the predicted results, the backbone curves, forced responses and identified resonant crossing points are shown in Fig. 2.5 for comparison.

One can observe that these identified points on backbone curves capture the forced resonances with an excellent agreement. Likewise, one may recall the first example case in Fig. 2.1, where the forcing amplitude is $P_2 = 0.003$. Such a forcing amplitude is denoted by a dotted line in Fig. 2.4, where only one intersection (a solid dot) is identified at response frequency $\omega \approx 1.05$, indicating a single resonance on the FRC. This again is in line with the results shown in Fig. 2.1*b* where only the primary FRC (whose resonance is at $\omega \approx 1.05$) is found without the existence of isolas.

It can be concluded that using backbone curves, combined with the energy balancing technique, offers a tool for nonlinear modal analysis, which significantly simplifies the challenging and computationally expensive numerical simulations. However, there still are some challenges and unaddressed issues when using backbone curves in nonlinear modal analysis, namely in

- **Characterising the features of backbone curves.**

  Even though backbone curves already exhibit a much simpler topology than forced responses, they may exhibit intricate features arising from modal interactions. One of these features is the existence of *isolated backbone curves*, an example of which is shown in Fig. 2.3. Their existence makes determining backbone curves a challenging task (arguably as difficult as finding isolas for forced systems), and complicates the use of backbone curves in nonlinear modal analysis.

  Another complexity that arises from modal interactions lies in the geometric features (synchronous and asynchronous oscillations). Shown in Figs. 2.2 and 2.3, the 1 : 1 internal resonance is captured by two geometrically different responses. One type is related to the commonly observed synchronous responses, where the phase relationship between the interacting modes is either in-phase or anti-phase. Additionally, the less explored asynchronous responses, where the phase relationship may assume any value, can also be found. As a generalisation of NNMs in terms of phase relationships, the asynchronous response represents an important class of nonlinear responses. However, further investigation is still needed on what governs their existence and what is the mechanism that underpins their connections to, and differences from, synchronous motions.

- **Determining the existence and locations of internal resonances.**

  In contrast to the low-amplitude forcing case, the large-amplitude case exhibits multiple mixed-mode backbone curves that emerge from internal resonances, see Figs. 2.2 and 2.3. This is not the unique case where a nonlinear system shows intricate topologies of internal resonance when vibrating at large amplitudes. Indeed, as discussed in §2.2.2, even a simple mechanical system may show similar intricacy and the picture can further complexify when other frequency commensurate relationships are satisfied (in the presence of $m : n$ internal resonance). In practice, determining internal resonance is typically associated with computationally expensive numerical simulations. To overcome this challenge, a robust method is needed for efficient determination of internal resonances for an arbitrary system, regardless of the response frequency range.

- **Relationships between backbone curves and forced damped responses.**

  The relationships between backbone curves and *forced periodic responses* can be established via the energy balancing analysis, proposed in [139]. Using a single harmonic as the representative of the modal response, this technique permits predictions of resonances in a computationally cheap analytical framework. In the motivating example, it was revealed that this method accurately predicted the resonances on both the primary branch and isolated branches, see results in Figs. 2.4 and 2.5. However, it can also lead to unrobust and even erroneous results when the response has multiple significant harmonics, as discussed in §2.2.3. In addition, a direct extension of the method to consider multiple harmonics can only result in a numerical framework that loses the advantages of high efficiency. To overcome this single-harmonic limitation, whilst preserving the computational efficiency, an alternative formulation is required.

  In addition, as discussed in §2.2.3, the relationships between backbone curves and *damped transient responses* are underpinned by the concept of resonant capture – the free damped responses can be locked in the neighbourhood of backbone curves. This indicates that conceptually simpler backbone curves can be used to interpret intricate transient oscillations. In this case, it is of great interest to make use of this connection to further the understanding of and even optimise engineering systems that exploit transient responses, e.g. the targeted energy transfer.

In addition to these challenges and unaddressed issues, applications of such an NNM-based nonlinear modal analysis framework in practical scenarios are also within the consideration of this thesis. Particularly, the focus is on the fields of nonlinear oscillations and vibration suppression of engineering systems. Throughout this thesis, a number of applications will be presented, for example, the existence of isolated backbone curves in applications of a NLTMD, the whirling motions in cable systems, and the realisation of TET in applications of a NES and beam systems.

Based on the observations in §2.4 and §2.5, the thesis outline is presented as follows.

2.6 Thesis Outline

An outline of the research, broken down chapter by chapter is now presented. The relationships between the chapters are also discussed at the end of the section using Fig. 2.6.

Chapter 3 – Isolated backbone curves

As previously discussed, based on geometric features, the concept of NNMs, or backbone curves, can be categorised as either synchronous or asynchronous responses. An important feature of synchronous responses is the existence of isolated backbone curves that are separate from the primary branch; as such, their existence is challenging to predict and compute.

In Chapter 3, the conditions for the existence of isolated backbone curves are explored from a symmetry-breaking perspective. A symmetric two-mass chain oscillator is firstly studied which, as observed in literature, exhibits a bifurcation between its backbone curves. As the symmetry is broken, the bifurcation splits to form an isolated backbone curve. Here, it is demonstrated that this bifurcation, indicative of a symmetric structure, may be preserved when the symmetry is broken under certain conditions; these are derived analytically. This generalises the effect of symmetry breaking on the existence of isolated backbone curves. Using these insights, an asymmetric model – a single-mode nonlinear structure with a NLTMD – is then considered. The evolution of backbone curves is investigated in the nonlinear parameter space. It is found that this space can be divided into several regions, within which the backbone curves share similar topological features; whilst those topological boundaries define the emergence and annihilation of isolated backbone curves. Analytical formulas that govern the existence of isolated backbone curves are derived, which allow these features to be more efficiently accounted for, or eliminated, when designing relevant nonlinear facilities.

Chapter 4 – Phase-varying backbone curves

In contrast to the synchronous NNMs that are studied in Chapter 3, asynchronous NNMs have also been reported in the literature, taking the special form of out-of-unison motions, where the two underlying linear modes exhibit a phase difference of 90°. Chapter 4 extends the special out-of-unison concept to account for *general* *asynchronous* NNMs, where the modes exhibit a phase difference that can be an arbitrary value (not necessarily 90°). A single-mass, two-mode model is firstly used to demonstrate the symmetry-breaking mechanism that transforms the out-of-unison NNMs into general asynchronous NNMs. Additionally, analytical derivations reveal that, along with the breaking of the symmetric layout, the out-of-unison backbone curves evolve into branches that exhibit amplitude-dependent phase relationships. This means that the phase relationships between modes can vary along the backbone curve as frequency or amplitude varies. As such, these NNM branches are introduced here and termed *phase-varying backbone curves*. To explore this further, a cable model, with an additional support near one cable end, is used to demonstrate the existence of phase-varying backbone curves (and corresponding general asynchronous NNMs) in a common engineering structure. The objective of this chapter is to study the general asynchronous motions in nonlinear conservative systems. A new class of nonlinear phenomena, namely the phase-varing behaviour, is analytically derived and demonstrated using example systems. The significance of considering phase relationships between modes in nonlinear response analysis is also discussed.

Chapter 5 – Topological Mapping of Internal Resonances

The synchronous and asynchronous backbone curves, studied in Chapters 3 and 4, are special cases where the two modes exhibit a 1 : 1 frequency commensurate relationship, or 1 : 1 modal interactions. In Chapter 5, these concepts are further extended to a general case where the interacting modes have an arbitrary frequency commensurate match, namely, $m : n$ internal resonance. This is achieved by investigating the backbone curves of a conservative system with arbitrary modal parameters when vibrating at large amplitudes from a symmetry-breaking perspective.

Firstly, the symmetric case is considered, where the internal resonances are shown to be approximately captured by the Mathieu equation. It is revealed that the backbone curves (emerging from internal resonance) exist in pairs; and for each pair, the interacting modes exhibit the same response frequency commensurate relationships but with different phase relationships (in line with the concepts introduced in Chapters 3 and 4). To study the topological features of internal resonances and to determine their existence and locations, the divergence and convergence for pairs of backbone curves are then considered. Analytical formulas show that the existence of internal resonances is determined by the eigenfrequency ratio and nonlinear parameter ratio. Using these insights, a graphical method is proposed for the efficient determination of internal resonances in arbitrary two-mode interactions. Lastly, by extending to asymmetric cases, the asymmetric evolutions of internal resonance are shown to be captured by a non-homogeneous extended Mathieu equation, where the asymmetry-induced bifurcation splitting is governed by the non-homogeneous terms. This chapter aims to explore the mechanism underpinning internal resonances and quantify their topologies by extending the cases, considered in Chapters 3 and 4, to a general case. Analytical formulas and a graphical method are presented to aid the determination and interpretation of internal resonance.

Chapter 6 – Multi-harmonic energy balancing analysis using backbone curves

Previous chapters will be focused on using NNMs, i.e. unforced and undamped periodic responses, in studies of internal resonances and their relevant applications. Chapter 6 extends the scope to forced-damped scenarios by establishing the relationships between NNMs and forced damped periodic responses from an energy-based perspective.

In this chapter, an overview is given of the energy balancing mechanism at the system level, and then at the modal level and harmonic level. Using this mechanism, the relationships between NNMs and forced responses are established via the energy balancing analysis. For the energy balancing analysis based on a single-harmonic representative, its applicability and accuracy are investigated – it can bring about unrobust and even incorrect predictions when multiple harmonics show significant contributions. To address this, a semi-analytical framework is employed to formulate the multi-harmonic energy balancing analysis which combines the energy balancing mechanism and quadrature constraints. With known inputs of NNM solutions, the forcing amplitude and required perturbations, i.e. harmonic phase-shifts, to establish the connections between backbone curves and forced responses, can be computed. This allows for using backbone curves to interpret forced responses with the applicability and accuracy estimated via phase-shifts. The proposed method is then applied via a number of examples with comparison to numerical force appropriation to demonstrate how it can aid experimental tests. Lastly, this technique is adopted in isola prediction, which shows an improved accuracy and robustness when compared with the single-harmonic formulation. The objective of this chapter is to formulate the energy balancing analysis across multiple harmonics to provide an accurate and robust method to interpret forced responses using backbone curves.

Chapter 7 – Understanding targeted energy transfer using backbone curves

In Chapter 6, the connections between backbone curves and forced periodic responses are established by the energy balancing principle. Indeed, the relationships between backbone curves and damped transient responses are underpinned by the mechanism of resonant capture. Based on this mechanism, Chapter 7 studies TET using backbone curves.

TET represents the phenomenon where energy in one component is irreversibly transferred to another one when the initial energy is above a critical level. An important engineering application of TET is the NES, attached to the primary system to allow the energy to flow to and dissipated in the NES. There is a natural asymmetry in the system due to the desire for the NES to be much smaller than the primary structure it is protecting. This asymmetry is also essential from an energy-transfer perspective. To explore how the essential asymmetry is related to TET, the realisation of TET is interpreted from a symmetry-breaking perspective. This is achieved by introducing a symmetrised model with respect to the generically asymmetric original system. Firstly a classic example, where the system consists of a linear primary system and a nonlinearisable NES, is studied. The backbone curve topology that is necessary to realise TET is explored and it is demonstrated how this topology evolves from the symmetric case. This example is then extended to a more general case, accounting for nonlinearity in the primary system and linear stiffness in the NES. Exploring the symmetry-breaking effect on the backbone curve topologies enables the parameters of the NES to be identified, which give rise to TET. Lastly, the uncovered symmetry-breaking mechanism in the realisation of TET is demonstrated using a nonlinear beam model. The objective of this chapter is to understand the phenomenon of TET using backbone curves based on the mechanism of resonant capture. This phenomenon is interpreted from a symmetry-breaking perspective with the necessary backbone curve topologies identified. The proposed technique can aid the parameter designs of systems with an NES and others without a peripheral device in order to realise TET.

Chapter 8 – Conclusions and future work

The conlusions of the achievements are drawn in Chapter 8; discussions are also given on the potential future research.

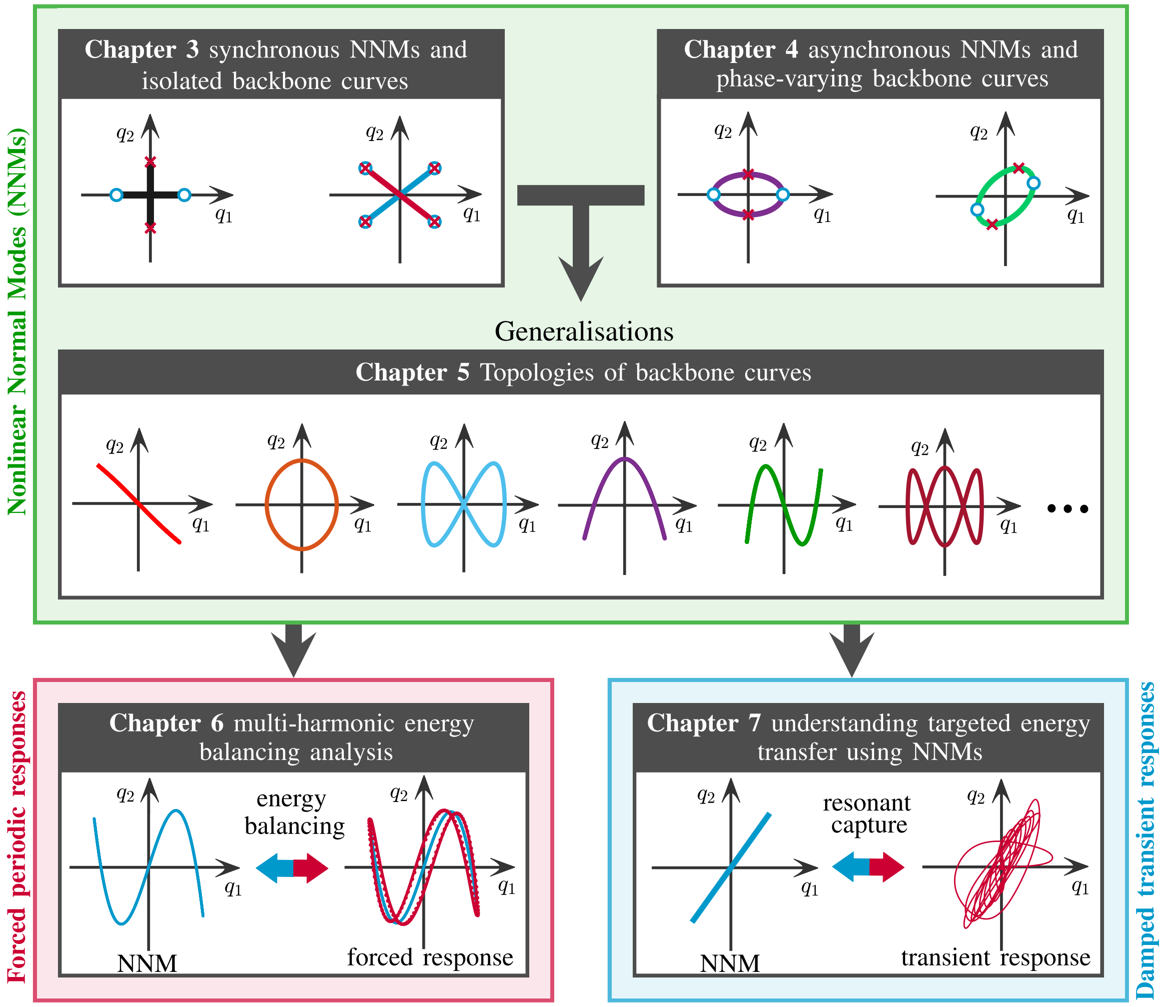

Fig. 2.6 A schematic diagram of the thesis outline.

To summarise the focus of and connections between each chapter, a schematic diagram of the thesis outline is presented in Fig. 2.6 using the featured nonlinear oscillations (in each chapter) in the configuration space for a two-mode system $(q_1,\ q_2)$. Chapters 3 to 5 focus on the use of NNMs to study nonlinear modal interactions from a geometric perspective. In Chapter 3, the synchronous NNMs and their correlated isolated backbone curves are studied; whilst Chapter 4 investigates the counterpart, namely the asynchronous NNMs and the uncovered new set of nonlinear phenomenon – phase-varying behaviours. Results in Chapters 3 and 4 are then generalised in Chapter 5 to account for $m : n$ internal resonance for systems with arbitrary modal parameters. In Chapter 6, the relationships between backbone curves and forced periodic responses are established via the energy balancing analysis. In Chapter 7, based on the mechanism of resonant capture, backbone curves are used to interpret and understand transient TET.

Chapter 3

Isolated backbone curves

In this chapter:

- Analytical expressions of backbone curves are derived for a general two-mode system with a cubic nonlinearity. Two example systems, in the form of two-mass oscillators, are used for analysis and demonstration.
- Features of synchronous backbone curves are characterised, and shown how they can be isolated from the primary curve due to symmetry breaking.
- Conditions for the existence of isolated backbone curves are quantified by exploring the topological evolutions of backbone curves for an asymmetric system.
- Results are demonstrated using the application of a Nonlinear Tuned Mass Damper (NTMD) to account for, or eliminate, the existence of isolated backbone curves in design.

Publications related to this work

- D. Hong, T. L. Hill, S. A. Neild, 2019. Conditions for the existence of isolated backbone curves, *Proceedings of the Royal Society A: Mathematical, Physical and Engineering Sciences* 475 (2232) 20190374.
- T. L. Hill, D. Hong, S. A. Neild, 2020. Uncovering hidden responses using isolated backbone curves, 14th *WCCM & ECCOMAS Congress.*

3.1 Introduction

Forced response curves (FRCs) are extensively used in the dynamic analysis of nonlinear systems [235, 31, 30]. However, nonlinear forced responses can be challenging to quantify and interpret; one example of particular interest is the existence of isolas, i.e. FRCs that are separated from the primary branch [131]. The existence of isolas has been identified in many nonlinear systems, e.g. the motivating example in §2.5 and Refs. [131, 132, 43, 133]. In these studies, the isolas can be associated with significant, high-amplitude responses that must be accounted for, or eliminated; nonetheless, due to the isolated characteristics, their existence is difficult to determine. In practice, this is often achieved via case-by-case studies, or computationally expensive simulations via, for example, numerical continuation of special points [198, 199, 203] and global analysis [203].

To interpret the complex forced responses, the concept of NNMs [31], or backbone curves, can be employed, which exhibit a simpler topology, yet still capture the essential nonlinear features, as discussed in §2.2.2. The relationships between forced responses and backbone curves can be established using the energy balancing analysis [139, 198, 141]. As such, the isola-finding problem can be reduced to an analytical and computationally simpler scheme, provided that the backbone curves are known. One example of using backbone curve to identify isolas can be found in the motivating case in §2.5.

To complicated matters, like the FRCs, backbone curves can be isolated, e.g. the isolated backbone curve for the motivating example system shown in Fig. 2.3. Without *a priori* knowledge of their existence, the associated isolas may go undetected and pose a risk of unexpected, high amplitude responses. One mechanism for the emergence of isolated backbone curves has been demonstrated in [139], where their creation is related to symmetry breaking. This mechanism has been verified via experimental studies in a cross-beam system [237]. In practice, a significant number of systems are asymmetric, e.g. a primary structure with a damping device attached for vibration suppression [43, 133]. A desirable design usually requires the damping device to be much smaller in size compared to the system it is protecting – this formulating an essentially asymmetric configuration. In such cases, the existence of isolas, as well as isolated backbone curves, can show a particularly significant impact on the performance of the damping device, as demonstrated in §2.3.1. However, a general methodology, establishing the relationship between symmetry and the existence of isolated backbone curves, has not been explored fully. This chapter aims to understand this relationship, and provides a method that ensures these isolated features are reliably predicted when designing nonlinear devices and systems. To this end, the rest of this chapter is organised as follows.

In §3.2, a brief overview of NNMs is given by considering their geometric features – either synchronous or asynchronous periodic motions. Such features are demonstrated using two methods, namely, the geometry in the configuration space, and phase relationships between modal coordinates. Specifically, the synchronous response is the focus of this chapter, and the evolution of synchronous backbone curves to isolated branches will be demonstrated and quantified.

In §3.3, the backbone curves for a two-mode system with a symmetric configuration are firstly revisited. For such a symmetric case, one can observe a typical backbone curve topology – two single-mode backbone curves with one pitchfork bifurcation leading to mixed-mode synchronous backbone curves. The effect of symmetry breaking on backbone curves is then considered – it can split the bifurcation and lead to the existence of isolated synchronous backbone curves, as with Refs. [139, 237]. In contrast, here, it will also be shown that the backbone curve topology for symmetric cases can hold for asymmetry if parameters are properly selected. This highlights the shared features between symmetric and asymmetric systems – an asymmetric system can exhibit the same dynamic features as a symmetric system.

In §3.4, an asymmetric system is considered, taking the form of a primary system with a NLTMD attached. Using the insights from §3.3, the parameter conditions to achieve two single-mode backbone curves with one bifurcation are analytically derived – when this asymmetric system shows similar dynamics as a symmetric system. Optimising the NLTMD parameters (to achieve best vibration mitigation performance) breaks these conditions and leads to the split of bifurcation and the existence of isolated backbone curves. The evolution of backbone curves in the parameter space is then considered to track the *emergence* of isolated backbone curves, conditions of which are analytically derived.

In §3.5, additional conditions are identified when the isolated backbone curves *annihilate* with infinite response frequency and amplitude. Combined with those derived in §3.4, conditions for the emergence and annihilation of isolated backbone curves are obtained. In addition to defining the existence of isolated backbone curves, these conditions serve as topological boundaries that distinguish topological features of backbone curves in the parameter space.

Lastly, this chapter is closed with summary given in §3.6.

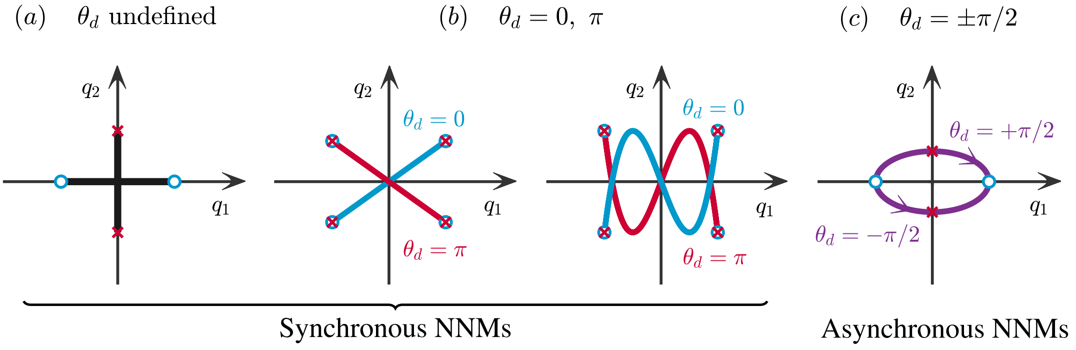

Fig. 3.1 Schematic representations of NNMs for a two-mode system. The responses are illustrated in the modal configuration space, i.e. the projection of the first and second linear modal coordinates, $q_1(t)$ and $q_2(t)$, parameterised in time. (a) The single-mode NNMs. (b) The in-phase ($\theta_d = 0$) and anti-phase ($\theta_d = \pi$) NNMs. (c) The out-of-unison ($\theta_d = \pm\pi/2$) NNMs.

3.2 Synchronous NNMs of a two-mode system

In this section, an overview of the concept of NNMs, i.e. periodic responses of a conservative system [31, 100], for a two-mode system is given. Such a two-mode system is composed of two linear mods, q_1 and q_2, and those two modes are coupled by an arbitrary nonlinearity, for example, a cubic nonlinearity. Considering the geometric features, NNMs can be categorised as either synchronous or asynchronous motions [73, 31]. The synchronous NNMs denote periodic motions where the system components *all* reach their extrema and equilibria simultaneously [73]; whilst the counterpart, asynchronous NNMs, are cases where the system componants *do not* reach their extrema and equilibria simultaneously [31].

To illustrate the features of NNMs, one can consider the responses in the configuration space with modal coordinates parameterised in time, i.e. the $(q_1(t),\ q_2(t))$ space. Some examples of NNMs are shown in Fig. 3.1 where the lines, termed modal lines [77], denote oscillations of the system over time, and where the extrema of q_1 and q_2 are marked by '$\circ$' and '$\times$' respectively. Regarding the definition of a synchronous motion, it requires '$\circ$' and '$\times$' to be overlapping, as shown in panels (a) and (b). In these two panels, two types of synchronous motions are shown, they can be described respectively as

1) panel (a) represents the simplest type of NNM solution – *single-mode* synchronous NNMs that contain contributions from only q_1 or q_2, illustrated by modal lines on the axes in the configuration space, $(q_1(t),\ q_2(t))$.

2) panel (b) shows the *mixed-mode* synchronous NNMs which, in contrast to the single-mode NNMs in panel (a), arise from modal interactions and consist of contributions from both linear modal coordinates, q_1 and q_2; such motions are denoted as lines passing through the origin in the configuration space.

An alternative, nonetheless equivalent, method to differentiate between synchronous NNMs in panels (a) and (b) is referring to the phase relationship between the components. For the single-mode motions in panel (a), the phase relationship is undefined; whilst for the mixed-mode cases, the phase difference between two modal components, θ_d, can be either in-phase ($\theta_d = 0$) or anti-phase ($\theta_d = \pi$). In panel (b), the in-phase and anti-phase motions are denoted by blue and red lines respectively. To further distinguish between cases presented in panel (b), one can account for the response frequency commensurate relationships. In the left plot of panel (b), for every period of response of q_1, q_2 also oscillates for a period, as such, the response frequency ratio is one. In this case, the NNM motions are emerging from $1:1$ internal resonance, where the ratio denotes the frequency commensurate match. Likewise, the NNM motions in the right plot of panel (b) emerge from $1:3$ internal resonance as for a period of q_1 response, q_2 vibrates for three periods.

In panel (c), one example of the asynchronous NNMs is presented, where it clearly shows that the responses of the two modes do not reach extrema and equilibrium simultaneously (‘$\circ$’ and ‘$\times$’ are separate). In this example, the two modes are oscillating out-of-unison, or with $\pm\pi/2$ phase differences, where $+$ and $-$ denote clockwise and anticlockwise motions respectively. In addition, the two modes exhibit a $1:1$ frequency commensurate match, namely, $1:1$ internal resonance. Note that, in this chapter, the discussion is constrainted on the synchronous NNMs; whilst asynchronous NNMs will only be briefly discussed whenever necessary. Instead, detailed investigations on asynchronous NNMs will be given in Chapter 4.

Synchronous motions can be observed in a variety of nonlinear systems – see examples in Refs. [238, 130, 203, 129, 139, 144, 237] and the following discussions. A particular case of interest is the correlated isolated NNM branch, or isolated backbone curve, which is the topic of this chapter. In the following studies, conditions for the existence of isolated backbone curves will be derived from a symmetry-breaking perspective and based on the case of $1:1$ internal resonance. Whilst, extensions to general $m:n$ internal resonances will be discussed in Chapter 5.

3.3 Symmetry breaking of nonlinear two-mode systems

In this section, modal interactions of a general conservative system with cubic nonlinearities are considered. Such a nonlinear system is characterised by two interacting modes, whose Lagrangian may be written

$$\mathcal{L} = \frac{1}{2}\dot{q}_1^2 + \frac{1}{2}\dot{q}_2^2 - \frac{1}{2}\omega_{n1}^2 q_1^2 - \frac{1}{2}\omega_{n2}^2 q_2^2 - \frac{1}{4}\mathit{\Psi}_4 q_1^4 - \mathit{\Psi}_1 q_1^3 q_2 - \frac{1}{2}\mathit{\Psi}_3 q_1^2 q_2^2 - \mathit{\Psi}_2 q_1 q_2^3 - \frac{1}{4}\mathit{\Psi}_5 q_2^4 \,, \quad (3.1)$$

where q_i, $\dot{q}_i$ and ω_{ni} are the i^{th} linear modal coordinate, modal velocity, and natural frequency respectively, and $\mathit{\Psi}_1, \ldots, \mathit{\Psi}_5$ denote the coefficients[1] of nonlinear terms. Applying the Euler-Lagrange equation then leads to the following equations of motion

$$\ddot{q}_1 + \omega_{n1}^2 q_1 + \mathit{\Psi}_4 q_1^3 + 3\mathit{\Psi}_1 q_1^2 q_2 + \mathit{\Psi}_3 q_1 q_2^2 + \mathit{\Psi}_2 q_2^3 = 0 \,, \quad (3.2a)$$

$$\ddot{q}_2 + \omega_{n2}^2 q_2 + \mathit{\Psi}_1 q_1^3 + \mathit{\Psi}_3 q_1^2 q_2 + 3\mathit{\Psi}_2 q_1 q_2^2 + \mathit{\Psi}_5 q_2^3 = 0 \,, \quad (3.2b)$$

where $\ddot{q}_i$ is the i^{th} modal acceleration. To study modal interactions, the concept of NNMs, i.e. the periodic solutions of the conservative system (3.2), is used. For most cases, one can find responses composed of both modal components, capturing modal interactions, due to the nonlinear coupling terms; whilst, special solution branches, where the modal oscillations are decoupled, can only be found when the system processes symmetries. From Eq. (3.2b), when the coefficient of q_1^3 equals 0, i.e. when $\mathit{\Psi}_1 = 0$, one solution set is related to $q_2 = 0$. With $q_2 = 0$, nontrivial solutions of the system (3.2) give the single-mode solutions, which consist of only the first linear modal coordinate, q_1; the related periodic solution branch represents a single-mode backbone curve that can be solved from

$$\ddot{q}_1 + \omega_{n1}^2 q_1 + \mathit{\Psi}_4 q_1^3 = 0 \,. \quad (3.3)$$

Likewise, when the coefficient of q_2^3 in Eq. (3.2a), $\mathit{\Psi}_2$, equals to 0, one can find the single-mode backbone curve that consists of only the second linear modal coordinate, q_2, from

$$\ddot{q}_2 + \omega_{n2}^2 q_2 + \mathit{\Psi}_5 q_2^3 = 0 \,. \quad (3.4)$$

---

[1] The nonlinear coefficients are defined in this order for simplicity in later discussions.

Otherwise, when both $\Psi_1 \neq 0$ and $\Psi_2 \neq 0$, the system *only* has periodic solutions containing both linear modal coordinates, termed mixed-mode backbone curves.

To find the expressions of backbone curves of the general two-mode system, the harmonic balance technique[2] is used, firstly by assuming that the modal displacements may be written as

$$q_i \approx u_i = U_i \cos\left(\omega_{ri} t - \theta_i\right) , \tag{3.5}$$

where q_i is approximated by its fundamental component u_i, or the leading-order component; and where U_i, ω_{ri}, and θ_i are amplitude, response frequency, and phase of u_i respectively. Here, it is further assumed that the response frequencies of the fundamental components of the two modes are equal ($\omega_{r1} = \omega_{r2} = \omega$), namely the system exhibits $1:1$ internal resonance. Note that the more general case, where the system exhibits $m:n$ internal resonances ($m,\ n \in \mathbb{Z}^+$), will be considered in Chapter 5. With substitution of the assumed solution (3.5) into the equations of motion (3.2), and the removal of non-resonant terms, i.e. terms that do not resonate at response frequency ω, one can obtain

$$\begin{aligned}
&4\left(\omega_{n1}^2 - \omega^2\right) U_1 \cos\left(\omega t - \theta_1\right) + \left(3\,\Psi_4 U_1^2 + 2\,\Psi_3 U_2^2\right) U_1 \cos\left(\omega t - \theta_1\right) + \Psi_3 U_1 U_2^2 \cos\left(\omega t + \theta_1 - 2\theta_2\right)\\
&\qquad +3\left(2\,\Psi_1 U_1^2 + \Psi_2 U_2^2\right) U_2 \cos\left(\omega t - \theta_2\right) + 3\,\Psi_1 U_1^2 U_2 \cos\left(\omega t - 2\theta_1 + \theta_2\right) = 0\,, \qquad (3.6a)\\
&4\left(\omega_{n2}^2 - \omega^2\right) U_2 \cos\left(\omega t - \theta_2\right) + \left(2\,\Psi_3 U_1^2 + 3\,\Psi_5 U_2^2\right) U_2 \cos\left(\omega t - \theta_2\right) + \Psi_3 U_1^2 U_2 \cos\left(\omega t - 2\theta_1 + \theta_2\right)\\
&\qquad +3\left(\Psi_1 U_1^2 + 2\,\Psi_2 U_2^2\right) U_1 \cos\left(\omega t - \theta_1\right) + 3\,\Psi_2 U_1 U_2^2 \cos\left(\omega t + \theta_1 - 2\theta_2\right) = 0\,. \qquad (3.6b)
\end{aligned}$$

After some algebraic manipulation, Eq. (3.6) can be rearranged as

$$\begin{aligned}
&\left\{4\left(\omega_{n1}^2 - \omega^2\right) U_1 + 3\,\Psi_4 U_1^3 + \Psi_3 U_1 U_2^2 \left[1 + 2\cos^2\left(\theta_d\right)\right] + 3\left(\Psi_2 U_2^3 + 3\,\Psi_1 U_1^2 U_2\right) \cos\left(\theta_d\right)\right\} \cos\left(\omega t - \theta_1\right)\\
&\qquad - \left[2\,\Psi_3 U_1 U_2 \cos\left(\theta_d\right) + 3\,\Psi_1 U_1^2 + 3\,\Psi_2 U_2^2\right] U_2 \sin\left(\theta_d\right) \sin\left(\omega t - \theta_1\right) = 0\,, \qquad (3.7a)\\
&\left\{4\left(\omega_{n2}^2 - \omega^2\right) U_2 + 3\,\Psi_5 U_2^3 + \Psi_3 U_1^2 U_2 \left[1 + 2\cos^2\left(\theta_d\right)\right] + 3\left(\Psi_1 U_1^3 + 3\,\Psi_2 U_1 U_2^2\right) \cos\left(\theta_d\right)\right\} \cos\left(\omega t - \theta_2\right)\\
&\qquad - \left[2\,\Psi_3 U_1 U_2 \cos\left(\theta_d\right) + 3\,\Psi_1 U_1^2 + 3\,\Psi_2 U_2^2\right] U_1 \sin\left(\theta_d\right) \sin\left(\omega t - \theta_2\right) = 0\,, \qquad (3.7b)
\end{aligned}$$

where $\theta_d = \theta_1 - \theta_2$, i.e. the phase difference between two modal coordinates. Eq. (3.7) can be satisfied when

$$4\left(\omega_{n1}^2 - \omega^2\right) U_1 + 3\,\Psi_4 U_1^3 + \Psi_3 U_1 U_2^2 \left[1 + 2\cos^2\left(\theta_d\right)\right] + 3\left(\Psi_2 U_2^3 + 3\,\Psi_1 U_1^2 U_2\right) \cos\left(\theta_d\right) = 0\,, \tag{3.8a}$$

---

[2] Other methods, such as the normal form technique [239], the multiple-scales method [240], or the numerical continuation [97–99], could alternatively be used.

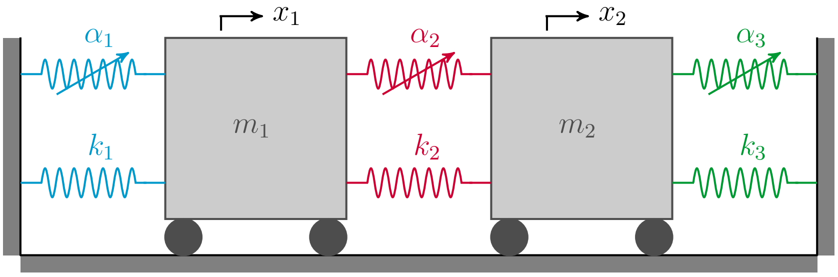

Fig. 3.2 A schematic diagram of a two-mode system in the form of a two-mass oscillator. Two masses, with mass values m_1 and m_2, have displacements x_1 and x_2 respectively, whilst linear and nonlinear cubic springs have coefficients k_i and α_i respectively, where $i = 1, 2, 3$.

$$4\left(\omega_{n2}^2 - \omega^2\right) U_2 + 3\,\Psi_5 U_2^3 + \Psi_3 U_1^2 U_2 \left[1 + 2\cos^2(\theta_d)\right] + 3\left(\Psi_1 U_1^3 + 3\,\Psi_2 U_1 U_2^2\right)\cos(\theta_d) = 0\,, \tag{3.8b}$$

$$\left[2\,\Psi_3 U_1 U_2 \cos(\theta_d) + 3\,\Psi_1 U_1^2 + 3\,\Psi_2 U_2^2\right]\sin(\theta_d) = 0\,. \tag{3.8c}$$

These equations can then be used to compute the backbone curves of the general two-mode system. It should be noted that employing the harmonic balance method (as derived above) results in the same formula, Eq. (3.8), to that obtrained via the second-order normal form method of a first-order accuracy [30, 239]. Again, seen from Eqs. (3.8), when $\Psi_1 = 0$, or $\Psi_2 = 0$, one can find single-mode backbone curves that consist of only U_1 or U_2; otherwise one can only find mixed-mode solutions, containing both U_1 and U_2.

3.3.1 Backbone curves of a symmetric two-mass oscillator

The derivations above show that having $\Psi_1 = 0$, or $\Psi_2 = 0$, plays a critical role in obtaining single-mode solutions. In the following, it is demonstrated how these conditions are related to the breaking of symmetric configurations to set the stage for discussions on the existence of isolated backbone curves. To this end, a specific two-mode system, taking the configuration of the two-mass oscillator (schematically shown in Fig. 3.2), is now used. The system consists of two masses with mass values m_1 and m_2; three linear springs with coefficients k_1, k_2, and k_3; and three nonlinear springs with coefficients α_1, α_2, and α_3. The physical symmetry of the system is divided into two parts: Linear Symmetry (LS), when the underlying linear system is symmetric, i.e. $m_1 = m_2$ and $k_1 = k_3$; and likewise, Nonlinear Symmetry (NS), when $\alpha_1 = \alpha_3$. For this two-mass oscillator, the governing dynamics is given by the equation of motion, i.e.

$$\mathbf{M}\ddot{\mathbf{x}} + \mathbf{K}\mathbf{x} + \mathbf{N}_{\mathbf{x}} = \mathbf{0}\,, \tag{3.9}$$

where $\mathbf{M}$ and $\mathbf{K}$ are mass and linear stiffness matrices respectively, $\mathbf{N}_{\mathbf{x}}$ is a vector of nonlinear stiffness terms, and $\mathbf{x}$ is a vector denoting displacements of the two masses. They are defined as

$$\begin{aligned} \mathbf{M} &= \begin{bmatrix} m_1 & 0 \\ 0 & m_2 \end{bmatrix}, \quad \mathbf{K} = \begin{bmatrix} k_1+k_2 & -k_2 \\ -k_2 & k_2+k_3 \end{bmatrix}, \\ \mathbf{N}_{\mathbf{x}} &= \begin{pmatrix} \alpha_1 x_1^3 + \alpha_2 \left(x_1 - x_2\right)^3 \\ \alpha_2 \left(x_2 - x_1\right)^3 + \alpha_3 x_2^3 \end{pmatrix}, \quad \mathbf{x} = \begin{pmatrix} x_1 \\ x_2 \end{pmatrix}. \end{aligned} \tag{3.10}$$

The system can be transformed into the linear modal space by introducing linear modal transform $\mathbf{x} = \boldsymbol{\Phi}\mathbf{q}$, given by

$$\mathbf{x} = \boldsymbol{\Phi}\mathbf{q} = \begin{bmatrix} \phi_{11} & \phi_{12} \\ \phi_{21} & \phi_{22} \end{bmatrix} \begin{pmatrix} q_1 \\ q_2 \end{pmatrix}, \tag{3.11}$$

where $\mathbf{q}$ is the vector of linear modal coordinates and $\boldsymbol{\Phi}$ is the linear modeshape matrix, whose first and second columns, i.e. $[\phi_{11}\ \phi_{21}]^\top$ and $[\phi_{12}\ \phi_{22}]^\top$, denote the modeshapes of the first and second linear modes respectively; they are given by

$$\phi_{11}^2 = \frac{k_2^2}{\left(k_1+k_2-m_1\omega_{n1}^2\right)^2 m_2 + m_1 k_2^2}, \quad \phi_{12}^2 = \frac{k_2^2}{\left(k_1+k_2-m_1\omega_{n2}^2\right)^2 m_2 + m_1 k_2^2}, \tag{3.12a}$$

$$\phi_{21}^2 = \frac{\left(k_1+k_2-m_1\omega_{n1}^2\right)^2}{\left(k_1+k_2-m_1\omega_{n1}^2\right)^2 m_2 + m_1 k_2^2}, \quad \phi_{22}^2 = \frac{\left(k_1+k_2-m_1\omega_{n2}^2\right)^2}{\left(k_1+k_2-m_1\omega_{n2}^2\right)^2 m_2 + m_1 k_2^2}. \tag{3.12b}$$

After the linear modal transform and some algebraic manipulation, one can obtain the equations of motion taking the same form as Eqs. (3.2) with coefficients of nonlinear terms, $\Psi_1, \ldots, \Psi_5$, given by

$$\begin{aligned} \Psi_1 &= \phi_{11}^3\phi_{12}\alpha_1 + \left(\phi_{11}-\phi_{21}\right)^3\left(\phi_{12}-\phi_{22}\right)\alpha_2 + \phi_{21}^3\phi_{22}\alpha_3, \\ \Psi_2 &= \phi_{11}\phi_{12}^3\alpha_1 + \left(\phi_{11}-\phi_{21}\right)\left(\phi_{12}-\phi_{22}\right)^3\alpha_2 + \phi_{21}\phi_{22}^3\alpha_3, \\ \Psi_3 &= 3\left[\phi_{11}^2\phi_{12}^2\alpha_1 + \left(\phi_{11}-\phi_{21}\right)^2\left(\phi_{12}-\phi_{22}\right)^2\alpha_2 + \phi_{21}^2\phi_{22}^2\alpha_3\right], \\ \Psi_4 &= \phi_{11}^4\alpha_1 + \left(\phi_{11}-\phi_{21}\right)^4\alpha_2 + \phi_{21}^4\alpha_3, \\ \Psi_5 &= \phi_{12}^4\alpha_1 + \left(\phi_{12}-\phi_{22}\right)^4\alpha_2 + \phi_{22}^4\alpha_3. \end{aligned} \tag{3.13}$$

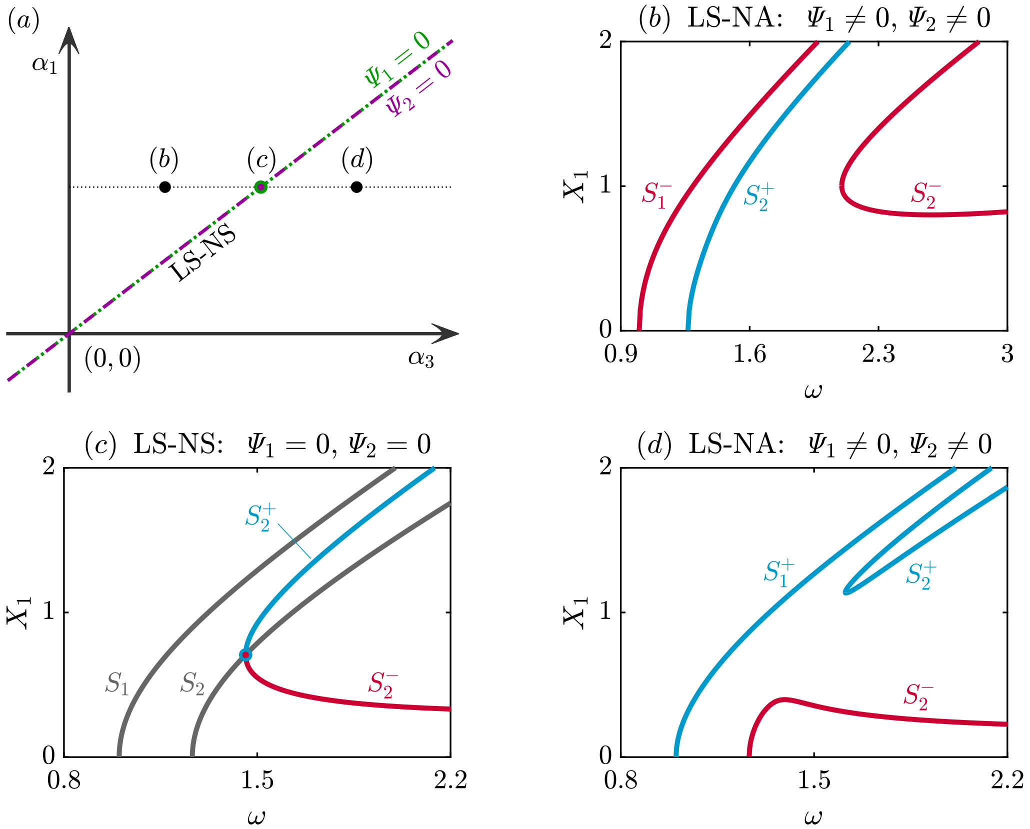

Fig. 3.3 The effect of nonlinear symmetry (NS) breaking, namely, breaking the parameter condition $\alpha_1 = \alpha_3$, for a system with linear symmetry (LS), i.e. $m_1 = m_2$ and $k_1 = k_3$. (a) The nonlinear parameter space, $(\alpha_1,\ \alpha_3)$, for the system with LS when $m_1 = m_2 = 1, k_1 = k_3 = 1,\ k_2 = 0.3$ and $\alpha_2 = 0.025$. The α_1 and α_3 values that lead to $\mathit{\Psi}_1 = 0$ and $\mathit{\Psi}_2 = 0$ are shown as a dotted green line and a dashed purple line respectively. Panels $(b) \to (d)$ are backbone curves shown in the projection of the response frequency, ω, against the amplitude of the first mass, X_1, for systems, labelled $(b) \to (d)$ in panel (a), respectively. (b) A system with linear symmetry and nonlinear asymmetry (NA) when $\alpha_1 = 1,\ \alpha_3 = 0.5$. (c) A LS-NS system with $\alpha_1 = \alpha_3 = 1$; (d) A LS-NA system with $\alpha_1 = 1, \alpha_3 = 1.5$.

With modal equations of motion (3.2) and coeffieicnts of nonlinear terms (3.13), the backbone curves can be computed via Eqs. (3.8) when the system exhibits $1:1$ internal resonance.

Firstly, the case where the system has both LS and NS, is considered. The backbone curves for such a symmetric case have been investigated in detail in [130, 139, 141]; here, they are briefly revisited. With $m_1 = m_2 = 1$, $k_1 = k_3 = 1$, $k_2 = 0.3$, $\alpha_1 = \alpha_3 = 1$ and $\alpha_2 = 0.025$, this LS-NS system can be described in the parameter space $(\alpha_1,\ \alpha_3)$ – see

Fig. 3.3*a*, where the system is mapped as the solid dot, labelled (*c*), on overlapping lines $\varPsi_1 = 0$ and $\varPsi_2 = 0$. Alternatively, it can be analytically found via Eqs. (3.13) that the physical symmetry of the system results in $\varPsi_1 = 0$ and $\varPsi_2 = 0$.

As previously discussed, $\varPsi_1 = \varPsi_2 = 0$ leads to the existence of two single-mode backbone curves. For the example system, the backbone curves are shown in Fig. 3.3*c* in the projection of the response frequency, ω, against the displacement amplitude of the first mass, X_1. In this plot, S_1 and S_2 represent single-mode backbone curves emerging from the linear natural frequencies, ω_{n1} and ω_{n2}, respectively; whilst two mixed-mode backbone curves, S_2^+ and S_2^-, emerge from S_2 via a Bifurcation Point (BP). Note that the subscripts of S_2^+ and S_2^- indicate the backbone curve from which they bifurcate (i.e. from S_2 in this case), and the superscripts $\bullet^+$ and $\bullet^-$ denote in-phase and anti-phase synchronous responses between the linear modal coordinates respectively. Note that, as the system exhibits $1:1$ internal resonance, the in-phase and anti-phase responses can be represented via blue and red lines respectively in the left plot of Fig. 3.1*b* in the configuration space.

Backbone curves with the features of a LS-NS system are here termed as having *dynamic symmetry*[3], and are characterised by the following two features:

1. Having two single-mode backbone curves, S_1 and S_2.
2. Having two mixed-mode backbone curves; either $S_2^\pm$, emerging from a BP on S_2, or $S_1^\pm$, emerging from a BP on S_1.

Seen from Eq. (3.13), $\varPsi_1$ and $\varPsi_2$ may be seen as *linear functions* of nonlinear parameters, α_1, α_2, and α_3, with coefficients governed by the modeshapes, or the underlying linear system. This means that, in the nonlinear parameter space $(\alpha_1,\ \alpha_3)$,[4] the orientation of $\varPsi_1 = 0$ and $\varPsi_2 = 0$ is determined by the underlying linear system. In addition, any system can be mapped as a point in this space, for example, the previously discussed symmetric case is mapped as a solid dot, labelled (*c*), in Fig. 3.3*a*. Consequently, whether the given system has dynamic symmetry or not, can then be directly determined by the relationships between the mapped point and $\varPsi_1 = 0$ and $\varPsi_2 = 0$, for example, the solid dot, on overlapping $\varPsi_1 = 0$ and $\varPsi_2 = 0$ in Fig. 3.3*a*, denotes a case with dynamic symmetry. In the following, how having dynamic symmetry, i.e. $\varPsi_1 = 0$ and $\varPsi_2 = 0$, relates to the physical symmetry, i.e. LS and NS, and its breaking is discussed.

---

[3] Note that, in comparison to the concept of dynamic symmetry, the symmetry in physical configuration is termed physical symmetry.

[4] Here, as α_2 does not affect the symmetry of the system, the nonlinear parameter subspace $(\alpha_1,\ \alpha_3)$ is used to track the information of NS, for example in Fig. 3.3*a*.

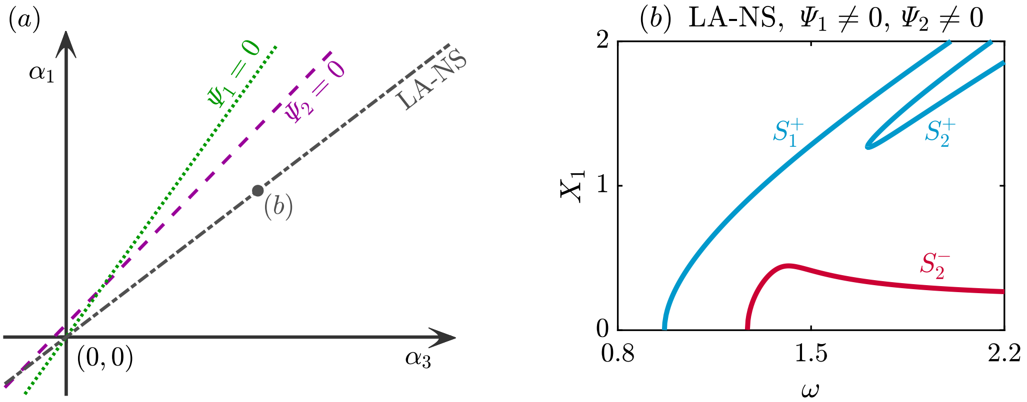

Fig. 3.4 The effect of NS breaking on backbone curves for a system with linear asymmetry (LA). (*a*) The nonlinear parameter space for the system with LA when $m_1 = 1, m_2 = 0.8, k_1 = 1, k_3 = 0.7$, $k_2 = 0.3$ and $\alpha_2 = 0.025$. The α_1 and α_3 values that lead to $\Psi_1 = 0$ and $\Psi_2 = 0$ are shown as a dotted green line and a dashed purple line respectively, and parameters leading to NS are shown as a dash-dotted grey line. (*b*) Backbone curves for a LA-NS system with $\alpha_1 = 1, \alpha_3 = 1$ (the dot labelled (*b*) in panel (*a*)).

3.3.2 Breaking either the nonlinear or the linear symmetry

With the symmetry of the underlying linear system retained, the orientations of $\Psi_1 = 0$ and $\Psi_2 = 0$ also remain overlapping in the $(\alpha_1,\ \alpha_3)$ space, and they denote $\alpha_1 = \alpha_3$, i.e. having NS. As such, with nonlinear parameters perturbed from its symmetric case to give nonlinear asymmetry (NA), i.e. $\alpha_1 \neq \alpha_3$, the system in the nonlinear parameter space $(\alpha_1,\ \alpha_3)$ is perturbed from having $\Psi_1 = \Psi_2 = 0$, which breaks the conditions required for dynamic symmetry. Two example cases are shown as solid dots, labelled (*b*) and (*d*), in Fig. 3.3*a* with respect to NS breaking in direction $\alpha_1 > \alpha_3$ and $\alpha_1 < \alpha_3$. Whilst the effect of symmetry breaking on backbone curves are shown in Figs. 3.3*b* and 3.3*d* for these two cases respectively. This turns the single-mode backbone curves into mixed-mode ones, splits the bifurcation, and generates an isolated backbone curve, the same as that discussed in [141]. For more general cases, a system with LS and NA cannot exhibit dynamic symmetry as in this case $\Psi_1 \neq 0$ and $\Psi_2 \neq 0$, see Eqs. (3.13).

Similarly, breaking the LS, whilst retaining the NS, can also break the conditions required for dynamic symmetry. With the breaking of the LS, the orientations of $\Psi_1 = 0$ and $\Psi_2 = 0$ are changed, and no longer overlapping, as shown in the $(\alpha_1,\ \alpha_3)$ space in Fig. 3.4*a* for a system with $m_2 = 0.8m_1$ and $k_3 = 0.7k_1$. If the NS is retained, i.e. $\alpha_1 = \alpha_3$ (depicted by the grey line in Fig. 3.4*a*), the backbone curves, shown in Fig. 3.4*b*, are similar in topology to the ones for the LS-NA system in Fig. 3.3*d*, i.e. having one isolated backbone

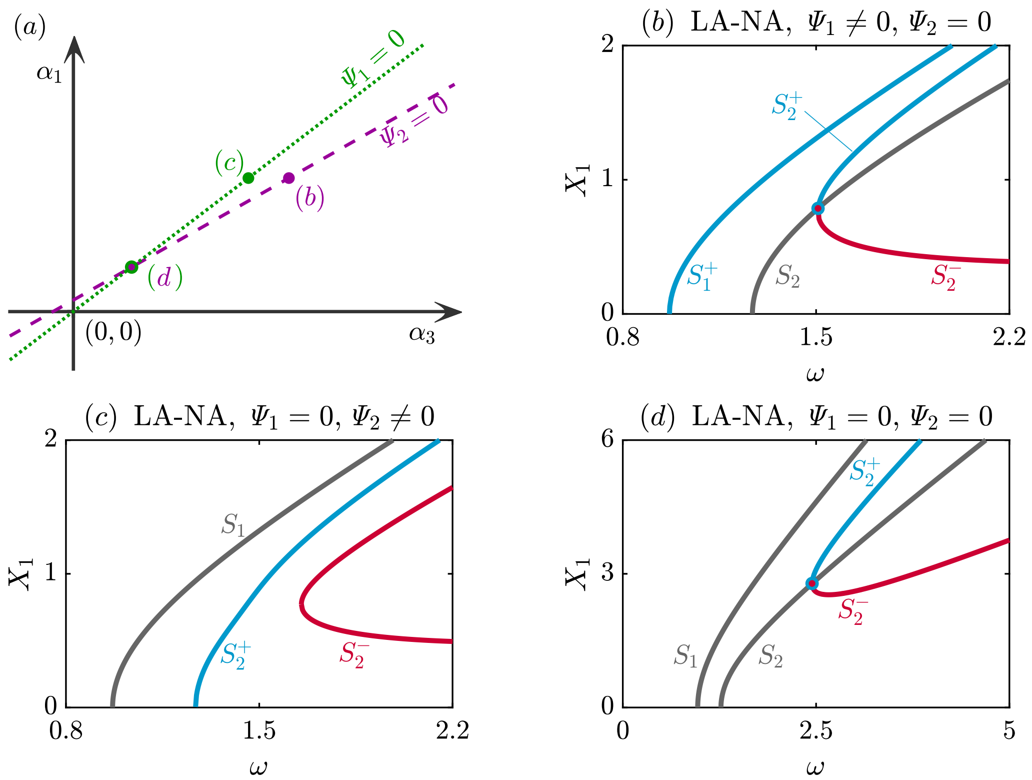

Fig. 3.5 Obtaining dynamic symmetry for a LA-NA system. (*a*) The nonlinear parameter space for a system with LA (linear parameters and α_2 are equal to those considered in Fig. 3.4). The α_1 and α_3 values that lead to $\Psi_1 = 0$ and $\Psi_2 = 0$ are shown as dotted green and dashed purple lines respectively. Panels (*b*) → (*d*) are backbone curves shown in the projection of the response frequency, ω, against the amplitude of the first mass, X_1, for systems, labelled (*b*) → (*d*) in panel (*a*), respectively. (*b*) A LA-NA system with $\alpha_1 = 1, \alpha_3 \approx 0.6785$. (*c*) A LA-NA system with $\alpha_1 = 1, \alpha_3 \approx 0.5510$. (*d*) A LA-NA system with $\alpha_1 \approx 0.3333, \alpha_3 \approx 0.1833$.

curve and two primary mixed-mode backbone curves. The LA-NS system considered here, like a LS-NA system, cannot have dynamic symmetry since the intersection of $\Psi_1 = 0$ and $\Psi_2 = 0$, where one can find two single-mode backbone curves, is not on the line representing $\alpha_1 = \alpha_3$ (i.e. the point at which the green and purple lines in Fig. 3.4*a* cross does not correspond to the grey line).

3.3.3 Breaking both the linear and nonlinear symmetry

Following from the LA-NS system considered in §3.3.2, the NS is also broken to give $\alpha_1 \neq \alpha_3$ to investigate the backbone curves of a LA-NA system (a fully asymmetric system). Firstly, by reducing α_3 from the NS-case (labelled (*b*) in Fig. 3.4*a*) to the point where $\varPsi_2 = 0$, labelled (b) in Fig. 3.5*a*, the obtained backbone curves are shown in Fig. 3.5*b*. As expected, this leads to a single-mode backbone curve S_2; however, as $\varPsi_1 \neq 0$, the first primary backbone curve, S_1^+, contains a component of the second mode with in-phase vibrations. As such, this is not a dynamically symmetric case, despite sharing some characteristics, such as the existence of backbone curves S_2^+ and S_2^-, which emerge from S_2. Further reducing α_3 leads to the point where $\varPsi_1 = 0$ (labelled (c) in Fig. 3.5*a*), of which the backbone curves are shown in Fig. 3.5*c*. These exhibit a single-mode backbone curve S_1 (as predicted by the $\varPsi_1 = 0$ condition) but with a primary and an isolated backbone curve, S_2^+ and S_2^-. Besides these two cases for LA-NA systems, as seen in Fig. 3.5*a*, $\varPsi_1 = \varPsi_2 = 0$ may still be satisfied for this case if α_1 and α_3 are on the intersection of $\varPsi_1 = 0$ and $\varPsi_2 = 0$. Dynamic symmetry can therefore be obtained for such a LA-NA system, as can be seen from the backbone curves in Fig. 3.5*d*.

As previously discussed, the concept of dynamic symmetry is defined as having similar characteristics to a LS-NS system; nonetheless, such a dynamic behaviour can be observed in a LA-NA system, if parameters are appropriately selected, for example, the asymmetric case presented in Fig. 3.5*d*. This indicates that an asymmetric system can exhibit the same dynamic characteristics as a symmetric system. In addition, defining conditions for the existence of single-mode solutions, expressions $\varPsi_1 = 0$ and $\varPsi_2 = 0$ also serve as critical boundaries, which divide the parameter space into several regions (see examples in Figs. 3.3*a*, 3.4*a* and 3.5*a*), within which the backbone curves share similar topological features. These regions, in the parameter space, allow the changes in the fundamental dynamic behaviours to be identified and predicted, as detailed in the following discussions.

3.4 Backbone curves of a NLTMD-inspired two-mode system

In §3.3, the case study showed that the dynamic symmetry breaking leads to bifurcation splitting and results in the existence of isolated backbone curves. This generalises the condition for the existence of isolated backbone curve in [141], where the mechanism of physical symmetry breaking was considered. Using these observations, the existence of isolated backbone curves is further investigated in an asymmetric system (i.e. a LA-NA system) in this section.

To motivate the study, the two-mass system, depicted in Fig. 3.6, is considered. This system is equivalent to that shown in Fig. 3.2, but with the springs grounding the second mass removed. Such a system is extensively considered in the vibration suppression

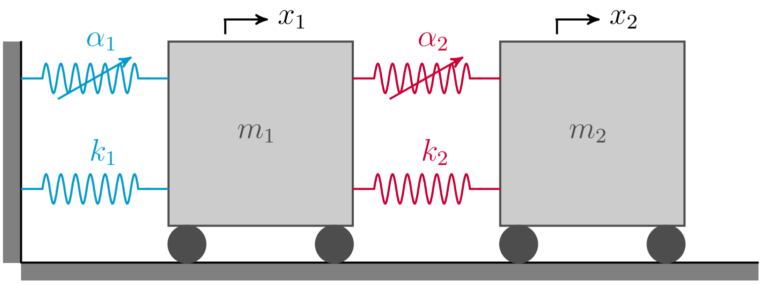

Fig. 3.6 A schematic diagram of a two-mode asymmetric system, representative of a nonlinear structure with a nonlinear tuned-mass damper (NLTMD).

context [131, 43, 133], where the primary structure (being protected) is modelled as the first mass-spring oscillator that captures the target mode of the full system; whilst the NLTMD is modelled as the second mass, being attached to the primary system through a nonlinear spring with a cubic nonlinearity to absorb the primary system's vibrations. Motivated by the likely design requirement, the NLTMD is much smaller in size when compared to the primary system it is protecting – this formulates an essentially asymmetric configuration.

Isolated backbone curves represent particularly undesirable features in a NLTMD device [131, 43, 133], due to the difficulty of predicting them, and their correlated high-amplitude dynamic responses, as discussed in §2.3.1. As such, it is of great importance to have a method that accounts for their features and provides guidance in eliminating them during practical design of such vibration absorbers. To achieve this, firstly the parameter conditions required for *dynamic symmetry* are found for the NLTMD-inspired system in this section. However, in practice, the performance-oriented optimisation of a NLTMD usually cannot satisfy such conditions, leading to the existence of isolated backbone curves. Based on this optimised device (a given set of optimised linear parameters), the evolution of backbone curves is then explored in the nonlinear parameter space to determine the conditions for the existence of isolated backbone curves.

3.4.1 Obtaining dynamic symmetry for an asymmetric system

As discussed in §3.3, a LA-NA system can exhibit dynamic symmetry if the parameters are selected appropriately. One feature of dynamic symmetry is having two single-mode solutions, S_1 and S_2, which requires that both $\Psi_1 = 0$ and $\Psi_2 = 0$ in the equations of motion. Here, the NLTMD-inspired system may be seen as a special case (with $k_3 = 0$ and $\alpha_3 = 0$) of the two-mass chain system, whose equations of motion are given by Eqs. (3.2) with coefficients of nonlinear terms defined by Eqs. (3.13). The expressions of

$\mathit{\Psi}_1$ and $\mathit{\Psi}_2$ may be written in matrix form as

$$\begin{pmatrix} \mathit{\Psi}_1 \\ \mathit{\Psi}_2 \end{pmatrix} = \begin{bmatrix} \phi_{11}^3\phi_{12} & \left(\phi_{11}-\phi_{21}\right)^3\left(\phi_{12}-\phi_{22}\right) \\ \phi_{11}\phi_{12}^3 & \left(\phi_{11}-\phi_{21}\right)\left(\phi_{12}-\phi_{22}\right)^3 \end{bmatrix} \begin{pmatrix} \alpha_1 \\ \alpha_2 \end{pmatrix}, \tag{3.14}$$

where $\alpha_3 = 0$ has been substituted (i.e. no nonlinear spring grounding the second mass) and where ϕ_{ij} are elements of the linear modeshape matrix $\mathbf{\Phi}$, defined in Eq. (3.12). In order to satisfy both $\mathit{\Psi}_1 = 0$ and $\mathit{\Psi}_2 = 0$, Eq. (3.14) reveals two solution sets, given by

1) trivial cases: $\alpha_1 = \alpha_2 = 0$, when the system degenerates to a linear one.

2) nontrivial cases: the determinant of the matrix in Eq. (3.14) must be zero.

The later case is considered and the zero determinant is given by

$$\phi_{11}^3\phi_{12}\left(\phi_{11}-\phi_{21}\right)\left(\phi_{12}-\phi_{22}\right)^3 - \phi_{11}\phi_{12}^3\left(\phi_{11}-\phi_{21}\right)^3\left(\phi_{12}-\phi_{22}\right) = 0\,. \tag{3.15}$$

Note that for a system with an asymmetric configuration, ϕ_{12} and ϕ_{21} are non-zero, and $\phi_{11} \neq \phi_{21}$ and $\phi_{12} \neq \phi_{22}$. Therefore, Eq. (3.15) can be rearranged to give

$$\frac{\phi_{11}^2\left(\phi_{12}-\phi_{22}\right)^2}{\phi_{12}^2\left(\phi_{11}-\phi_{21}\right)^2} = 1\,, \tag{3.16}$$

which is satisfied with the following conditions

$$\frac{\phi_{11}\left(\phi_{12}-\phi_{22}\right)}{\phi_{12}\left(\phi_{11}-\phi_{21}\right)} = 1: \quad \frac{\phi_{11}}{\phi_{21}} - \frac{\phi_{12}}{\phi_{22}} = 0\,, \tag{3.17a}$$

$$\frac{\phi_{11}\left(\phi_{12}-\phi_{22}\right)}{\phi_{12}\left(\phi_{11}-\phi_{21}\right)} = -1: \quad \frac{\phi_{21}}{\phi_{11}} + \frac{\phi_{22}}{\phi_{12}} = 2\,. \tag{3.17b}$$

Condition (3.17a) cannot be achieved in the physical context as it requires the first and second modeshapes to be the same; therefore, dynamic symmetry, i.e. having $\mathit{\Psi}_1 = \mathit{\Psi}_2 = 0$, can only be achieved when condition (3.17b) is satisfied. Interpreting the modeshape coefficients, ϕ_{ij}, using linear physical parameters via Eq. (3.12), the modal parameter condition (3.17b) can be translated into a physical parameter condition, given by

$$\frac{k_1}{k_2} = \frac{m_1 + m_2}{m_2}\,. \tag{3.18}$$

As well as this condition for the linear parameters, the required condition between the nonlinear parameters may be established by substituting expressions (3.18) back to

Eq. (3.14), leading to

$$\frac{\alpha_1}{\alpha_2}=\frac{(\phi_{12}-\phi_{22})^4}{\phi_{12}^4}=\frac{(\phi_{11}-\phi_{21})^4}{\phi_{11}^4}=\left(\frac{m_1+m_2}{m_2}\right)^2 . \tag{3.19}$$

This demonstrates that, in order for the NLTMD-inspired system to exhibit dynamic symmetry, the linear and nonlinear stiffness coefficients must obey the ratio described by Eqs. (3.18) and (3.19) respectively.

For a given mass ratio between the NLTMD and the primary system, for instance, $m_2 = 0.05m_1$, Fig. 3.7*a* shows the the required conditions for dynamic symmetry, i.e. $\varPsi_1 = 0$ and $\varPsi_2 = 0$, in the nonlinear parameter space, $(\alpha_1,\ \alpha_2)$. In this case, $k_1/k_2 = 21$, which satisfies the linear parameter condition (3.18); whilst $\alpha_1/\alpha_2 = 441$, satisfying the nonlinear parameter condition (3.19). Despite being a linearly asymmetric (LA) system, the system exhibits strong similarities in nonlinear parameter space to a linearly symmetric (LS) system in Fig. 3.3*a* – there are *multiple* nonlinear parameter combinations (resulting from overlapping $\varPsi_1 = 0$ and $\varPsi_2 = 0$) leading to dynamic symmetry. When the parameter relationships (3.18) and (3.19) are satisfied, expressions for coefficients of nonlinear terms, $\varPsi_1, \dots, \varPsi_5$, of the NLTMD-inspired system can be further simplified, given by

$$\varPsi_1 = 0\,, \quad \varPsi_2 = 0\,, \quad \varPsi_3 = 6\phi_{11}^2\phi_{12}^2\alpha_1\,, \quad \varPsi_4 = 2\phi_{11}^4\alpha_1\,, \quad \varPsi_5 = 2\phi_{12}^4\alpha_1\,. \tag{3.20}$$

The backbone curves of the dynamically symmetric NLTMD-inspired system can then be computed via expressions (3.8) with coefficients (3.20), which can be reduced to

$$\left\{4\left(\omega_{n1}^2-\omega^2\right)+3\,\varPsi_4U_1^2+\varPsi_3U_2^2\left[1+2\cos^2\left(\theta_d\right)\right]\right\}U_1=0\,, \tag{3.21a}$$

$$\left\{4\left(\omega_{n2}^2-\omega^2\right)+3\,\varPsi_5U_2^2+\varPsi_3U_1^2\left[1+2\cos^2\left(\theta_d\right)\right]\right\}U_2=0\,, \tag{3.21b}$$

$$2\,\varPsi_3U_1U_2\cos\left(\theta_d\right)\sin\left(\theta_d\right)=0\,. \tag{3.21c}$$

Trivial solutions can be found when $U_1 = 0$ and $U_2 = 0$, which denotes a stationary system. For nontrivial cases, two sets of single-mode solutions, denoted S_1 and S_2, can be found with frequency-amplitude relationships described as

$$S_1(\omega,\ U_1):\quad U_2=0,\quad \omega^2=\omega_{n1}^2+\frac{3}{4}\varPsi_4U_1^2\,, \tag{3.22}$$

$$S_2(\omega,\ U_2):\quad U_1=0,\quad \omega^2=\omega_{n2}^2+\frac{3}{4}\varPsi_5U_2^2\,, \tag{3.23}$$

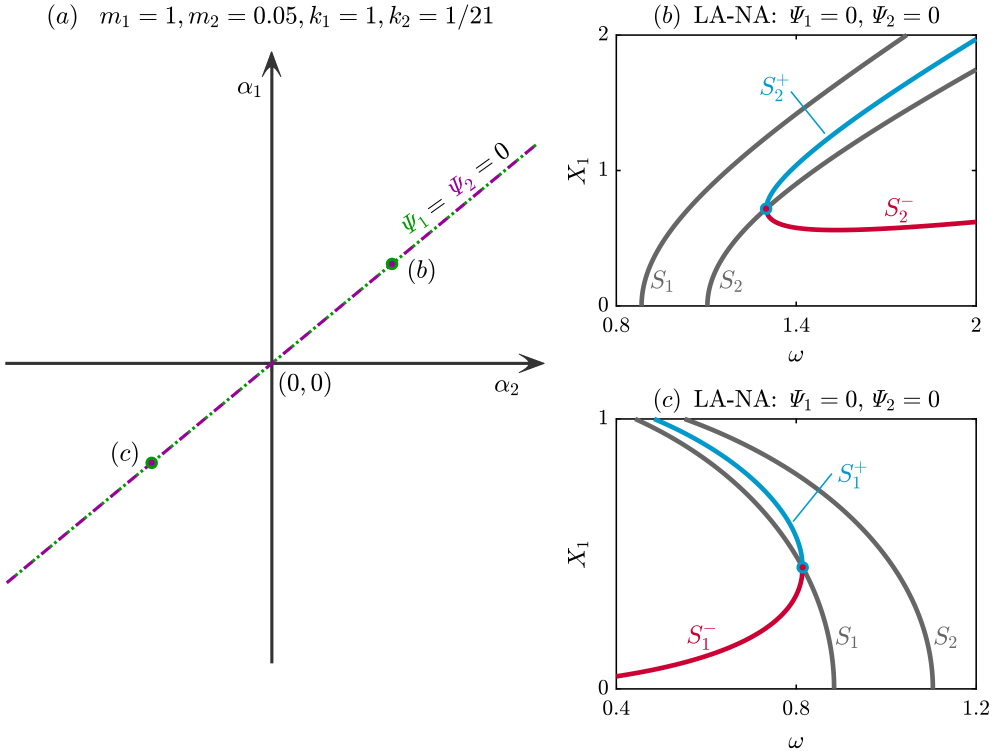

Fig. 3.7 Dynamic symmetry for a NLTMD-inspired system. (a) The nonlinear parameter space, α_1 against α_2, for a system with LA, i.e. $m_1 = 1$, $m_2 = 0.05$, $k_1 = 1$ and $k_2 = 1/21$, where $\Psi_1 = 0$ and $\Psi_2 = 0$ are two overlapping lines. (b) Backbone curves with dynamic symmetry for a hardening LA-NA system when $\alpha_1 = 1$ and $\alpha_2 = 1/441$ (the solid dot labelled (b) in panel (a)). (c) Backbone curves with dynamic symmetry for a softening LA-NA system when $\alpha_1 = -1$ and $\alpha_2 = -1/441$ (the solid dot labelled (c) in panel (a)).

where the parameters in the parentheses denote variables of the backbone curves, namely, the response frequency and modal displacement amplitudes. The other nontrivial solution set is related to mixed-mode backbone curves, whose responses are composed of both modal coordinates. To compute these, the phase relationship, θ_d, between the fundamental components of the two modal coordinates, u_1 and u_2, needs to be determined first. From Eq. (3.21c), this can be satisfied when $\theta_d = n\pi/2$, with $n \in \mathbb{Z}$. The case where n is even, satisfying $\sin(\theta_d) = 0$, represents solutions where the two modes are vibrating in-phase or anti-phase, or alternatively termed synchronous responses [73, 74, 31], as discussed in §3.2. The other case where n is odd, satisfying $\cos(\theta_d) = 0$, denotes solutions where the two modes are vibrating ±90° out-of-phase; this represents the counterpart of a synchronous response, i.e. an asynchronous response [31]. Examples of such asynchronous responses are whirling motions, schematically shown in Fig. 3.1*c*, which have been studied in cable systems [129], rotor systems [238] and the motivating example in §2.5.

The in-phase solutions, with $\theta_d = 0$, are denoted S_1^+ and S_2^+; whilst the anti-phase solutions, with $\theta_d = \pi$, are denoted S_1^- and S_2^- ($S_{1,2}^\pm$ is used to denote all of them). For the dynamically-symmetric case, these backbone curves all share the same frequency-amplitude relationship, given by

$$S_{1,2}^{\pm}(\omega,\ U_1,\ U_2): \quad U_1^2 = \frac{4\left(\omega_{n2}^2 - \omega_{n1}^2\right) + 3\left(\varPsi_5 - \varPsi_3\right)U_2^2}{3\left(\varPsi_4 - \varPsi_3\right)}, \tag{3.24a}$$

$$\omega^2 = \frac{4\left(\varPsi_4\omega_{n2}^2 - \varPsi_3\omega_{n1}^2\right) + 3\left(\varPsi_4\varPsi_5 - \varPsi_3^2\right)U_2^2}{4\left(\varPsi_4 - \varPsi_3\right)}. \tag{3.24b}$$

Likewise, the ±90° out-of-phase asynchronous solutions are labelled $S_{1,2}^{\pm 90}$ where the superscripts, $\bullet^{+90}$ and $\bullet^{-90}$, denote clockwise and anticlockwise motions respectively – see the arrows in Fig. 3.1*c*. With the substitution of out-of-unison phase relationship, i.e. $\cos(\theta_d) = 0$ into Eqs. (3.21a) and (3.21b), the frequency-amplitude relationship of $S_{1,2}^{\pm 90}$ is governed by

$$S_{1,2}^{\pm 90}(\omega,\ U_1,\ U_2): \quad U_1^2 = \frac{4\left(\omega_{n2}^2 - \omega_{n1}^2\right) + \left(3\varPsi_5 - \varPsi_3\right)U_2^2}{3\varPsi_4 - \varPsi_3}, \tag{3.25a}$$

$$\omega^2 = \frac{4\left(3\varPsi_4\omega_{n2}^2 - \varPsi_3\omega_{n1}^2\right) + \left(9\varPsi_4\varPsi_5 - \varPsi_3^2\right)U_2^2}{4\left(3\varPsi_4 - \varPsi_3\right)}. \tag{3.25b}$$

In addition, with parameter conditions required for dynamic symmetry, i.e. expressions from (3.18) to (3.20), substituted into Eq. (3.25b), it is found that the asynchronous responses, in this case, are always related to a zero response frequency – this indicates asynchronous responses cannot exist for the considered system. As the counterpart of synchronous responses, and less commonly observed nonlinear responses, asynchronous responses will be studied in detail in Chapter 4. Here, even though the non-existence of asynchronous responses is particular to the NLTMD-inspired system, it should be noted that bifurcations leading to asynchronous backbone curves *cannot* split due to symmetry breaking, and *no* correlated isolated asynchronous backbone curves may be observed. This will be revisted in Chapter 5, where analytical proof and discussions are considered for more general cases of modal interactions. Hence, the following discussions will only focus on synchronous responses and the correlated isolated backbone curves.

Discussions above presented the conditions for having two single-mode backbone curves, S_1 and S_2, and two mixed-mode in-phase and anti-phase branches, $S^{\pm}_{1,2}$. As well as these conditions, dynamic symmetry also requires to have either $S^{\pm}_1$ bifurcating from S_1, or $S^{\pm}_2$ bifurcating from S_2. To quantify these bifurcation scenarios, one can observe that the amplitude of the first modal coordinate reduces to zero, i.e. $U_1 = 0$, for the BP on S_2; likewise, the second modal amplitude $U_2 = 0$ for the BP on S_1. Using these conditions, the amplitude and response frequency of these two bifurcations can be obtained via Eqs. (3.24); they are given by

$$\text{BP on } S_1\text{:} \quad U_1^2 = \frac{4\left(\omega_{n2}^2 - \omega_{n1}^2\right)}{3\left(\Psi_4 - \Psi_3\right)}, \quad \omega^2 = \frac{\Psi_4\omega_{n2}^2 - \Psi_3\omega_{n1}^2}{\Psi_4 - \Psi_3}, \tag{3.26a}$$

$$\text{BP on } S_2\text{:} \quad U_2^2 = \frac{4\left(\omega_{n2}^2 - \omega_{n1}^2\right)}{3\left(\Psi_3 - \Psi_5\right)}, \quad \omega^2 = \frac{\Psi_3\omega_{n2}^2 - \Psi_5\omega_{n1}^2}{\Psi_3 - \Psi_5}. \tag{3.26b}$$

where, by definition, $\omega_{n2} > \omega_{n1}$. To obtain physically meaningful bifurcations, positive solutions are required, i.e. positive amplitude and frequency, given by

$$\text{existence of a BP on } S_1\text{:} \quad \Psi_4 - \Psi_3 > 0, \quad \Psi_4\omega_{n2}^2 - \Psi_3\omega_{n1}^2 > 0, \tag{3.27a}$$

$$\text{existence of a BP on } S_2\text{:} \quad \Psi_3 - \Psi_5 > 0, \quad \Psi_3\omega_{n2}^2 - \Psi_5\omega_{n1}^2 > 0. \tag{3.27b}$$

Note that conditions (3.27) are valid for any system with cubic nonlinearity that exhibits a 1 : 1 resonance between two modes, rather than specific for the NLTMD-inspired system. To relate these modal coefficient conditions to physical parameter relationships of the NLTMD system, the expressions for modeshape elements (3.12), and the nonlinear parameter relationship (3.20) are substituted into the inequalities (3.27). This reveals

$$\text{existence of a BP on } S_1\text{:} \quad \alpha_1 < 0 \quad \text{and} \quad \alpha_2 < 0, \tag{3.28a}$$

$$\text{existence of a BP on } S_2\text{:} \quad \alpha_1 > 0, \quad \alpha_2 > 0 \quad \text{and} \quad m_2 < m_1/3. \tag{3.28b}$$

This means that a BP on S_1 can exist only for systems with softening nonlinear springs; whilst a BP on S_2 can be observed only for systems with hardening nonlinear springs, combined with a relatively smaller m_2 (this is likely to be satisfied in the practical scenarios where the vibration absorbers are designed much smaller than the structure it is protecting). Besides, any other combinations of one softening and one hardening nonlinear springs result in the non-existence of BPs, and the non-existence of the correlated mixed-mode backbone curves. Figures 3.7*b* and 3.7*c* show the backbone curves with dynamic symmetry, i.e. satisfying parameter conditions (3.18), (3.19) and (3.28) for systems with hardening and softening parameters respectively (labelled (b) and (c) respectively in Fig. 3.7a).

3.4.2 Evolutions of backbone curve topologies

The previous discussions focus on whether the physically asymmetric NLTMD-inspired system can exhibit dynamic symmetry; the required parameter conditions were derived, given by Eqs. (3.18), (3.19) and (3.28). However, the optimisation of the NLTMD regarding the vibration suppression performance was not considered. In this section, linear parameters of the NLTMD are tuned to achieve optimal vibration mitigation performance, which in turn breaks the conditions for having dynamic symmetry. The evolutions of backbone curves are studied for this dynamic-symmetry-broken system to account for the existence of isolated backbone curves.

Firstly, the optimisation of the damping device is considered. The classical approach for optimising the linear parameters of a Tuned Mass Damper (TMD) is known as the fixed-points method, proposed in [68]. Instead of imposing two fixed points, using H_∞ optimisation, a closed-form exact solution to obtain equal peaks in receptance curves of the underlying linear system was discussed in [241], where the linear stiffness of the NLTMD can be optimised analytically using

$$k_2^{\mathrm{opt}} = \frac{8\mu k_1 \left[16 + 23\mu + 9\mu^2 + 2\left(2+\mu\right)\sqrt{4+3\mu}\right]}{3\left(1+\mu\right)^2\left(64 + 80\mu + 27\mu^2\right)}\,, \tag{3.29}$$

and where $\mu = m_2/m_1$ denotes the mass ratio and k_2^{opt} is the optimised linear spring coefficient of the NLTMD. This cannot satisfy the linear parameter relationship (3.18), and hence dynamic symmetry cannot be achieved, i.e. Ψ_1 and Ψ_2 cannot simultaneously be zero. In this case, similar to the asymmetric example considered in §3.3.3, the nonlinear parameters can still be selected on *either* $\Psi_1 = 0$ *or* $\Psi_2 = 0$ to obtain a single-mode backbone curve, S_1 or S_2. To find how the modal coefficient condition, i.e. $\Psi_1 = 0$ or $\Psi_2 = 0$, maps to physical parameter condition, the modeshape expressions (3.12) are substituted into the expressions of Ψ_i, given by Eqs. (3.13) (with $\alpha_3 = 0$); letting $\Psi_1 = 0$ and $\Psi_2 = 0$ respectively, one has

$$\Psi_1 = 0: \quad \frac{\alpha_1}{\alpha_2} = -\frac{\left(-\omega_{n1}^2 m_1 + k_1\right)^3\left(-\omega_{n2}^2 m_1 + k_1\right)}{k_2^4}\,, \tag{3.30a}$$

$$\Psi_2 = 0: \quad \frac{\alpha_1}{\alpha_2} = -\frac{\left(-\omega_{n1}^2 m_1 + k_1\right)\left(-\omega_{n2}^2 m_1 + k_1\right)^3}{k_2^4}\,. \tag{3.30b}$$

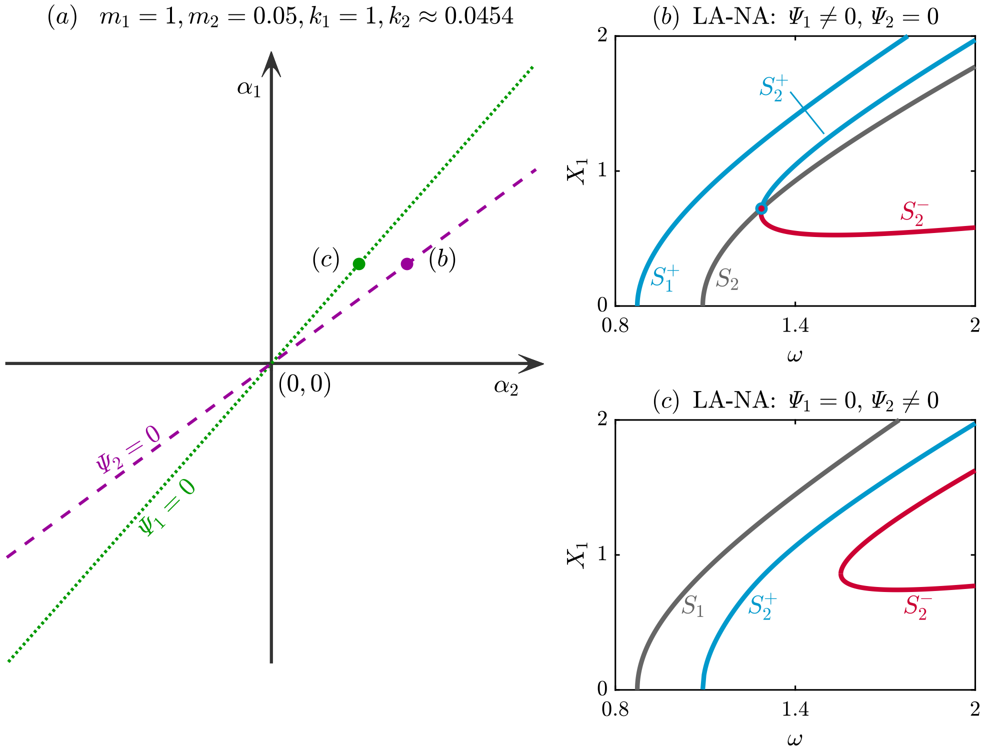

Fig. 3.8 Dynamic symmetry breaking for a NLTMD-inspired system due to optimised linear parameters of the NLTMD. (*a*) Nonlinear parameter space, α_1 against α_2, for a system with LA, i.e. $m_1 = 1$, $m_2 = 0.05$, $k_1 = 1$ and $k_2 = k_2^{\text{opt}} \approx 0.0454$. The α_1 and α_2 values that lead to $\Psi_1 = 0$ and $\Psi_2 = 0$ are shown as a dotted green line and a dashed purple line respectively; here, $\Psi_1 = 0$ and $\Psi_2 = 0$ are intersecting at the origin. (*b*) Backbone curves with the single-mode solution S_2 for the LA-NA system when $\alpha_1 = 1$ and $\alpha_2 \approx 0.00256$ (the purple dot labelled (*b*) in panel (*a*)). (*c*) Backbone curves with the single-mode backbone curve S_1 for the LA-NA system when $\alpha_1 = 1$ and $\alpha_2 \approx 0.00166$ (the green dot labelled (*c*) in panel (*a*)).

When parameter condition (3.30*a*) is satisfied, the single-mode backbone curves, S_1, can be found, given by amplitude-frequency relationships (3.22); likewise, S_2 can be found via Eq. (3.23) when condition (3.30*b*) is satisfied.

Figure 3.8*a* shows the nonlinear parameter space, $(\alpha_1,\ \alpha_2)$, for the NLTMD system with optimised linear parameters. This may be seen as an evolution of that in Fig. 3.7*a* due to linear-symmetry breaking – it leads to the orientation changes of lines $\Psi_1 = 0$ and $\Psi_2 = 0$, which intersect at the origin (where the system degenerates to a linear one). Two example cases, with either $\Psi_1 = 0$ or $\Psi_2 = 0$, are denoted by dots, labelled (*b*) and (*c*). Panel (*c*) shows the backbone curves for the system with $\Psi_1 = 0$ and $\Psi_2 \neq 0$;

the backbone curve topology is similar to that shown in Fig. 3.5*c*, where a single-mode backbone curve S_1 is also present. Whilst, panel (*b*) shows the backbone curves for the system with $\varPsi_2 = 0$ and $\varPsi_1 \neq 0$, which exhibit similarity to Fig. 3.5*b*.

Otherwise, systems with nonlinear parameters that lie on neither $\varPsi_1 = 0$ nor $\varPsi_2 = 0$ only have mixed-mode backbone curves. As previously discussed on the symmetric case in §3.4.1, to compute these mixed-mode backbone curves, the phase relationship between the two modal coordinates needs to be determined first, which is governed by Eq. (3.8c). The expression is satisfied with non-zero solutions when $\sin(\theta_d) = 0$, corresponding to synchronous relationships between two modes, $\theta_d = \theta_1 - \theta_2 = n\pi$, where even and odd n values denote in-phase and anti-phase relationships respectively. Further defining the phase parameter, p, as

$$p = \cos(\theta_d) = \cos(n\pi) = \begin{cases} +1 & \text{for even } n \\ -1 & \text{for odd } n \end{cases}, \tag{3.31}$$

it allows the equations that govern the amplitudes and response freuquencies of mixed-mode backbone curves, given by Eqs. (7.9a) and (7.9b), to be written

$$4\left(\omega_{n1}^2 - \omega^2\right) U_1 + 3\left[\varPsi_4 U_1^3 + \varPsi_3 U_1 U_2^2 + p\left(\varPsi_2 U_2^3 + 3\varPsi_1 U_1^2 U_2\right)\right] = 0\,, \tag{3.32a}$$

$$4\left(\omega_{n2}^2 - \omega^2\right) U_2 + 3\left[\varPsi_5 U_2^3 + \varPsi_3 U_1^2 U_2 + p\left(\varPsi_1 U_1^3 + 3\varPsi_2 U_1 U_2^2\right)\right] = 0\,. \tag{3.32b}$$

Rearranging these two equations gives the frequency-amplitude relationships of the mixed-mode backbone curves for a dynamically asymmetric case

$$S^{\pm}_{1,2}(\omega, U_1, U_2): \quad \omega^2 = \omega_{n1}^2 + \frac{3}{4}\left[\varPsi_4 U_1^3 + \varPsi_3 U_2^2 U_1 + p\left(\varPsi_2 U_2^3 + 3\varPsi_1 U_1^2 U_2\right)\right] U_1^{-1}\,, \tag{3.33a}$$

$$\begin{aligned} 0 =& \left(-3p\varPsi_2 U_1^{-1}\right) U_2^4 + 3\left(\varPsi_5 - \varPsi_3\right) U_2^3 + \left[9p\left(\varPsi_2 - \varPsi_1\right) U_1\right] U_2^2 + \\ & \left[4\omega_{n2}^2 - 4\omega_{n1}^2 + 3\left(\varPsi_3 - \varPsi_4\right) U_1^2\right] U_2 + 3p\varPsi_1 U_1^3\,. \end{aligned} \tag{3.33b}$$

Therefore, for dynamically asymmetric systems, those with $\varPsi_1 = 0$ or $\varPsi_2 = 0$ exhibit a single-mode backbone curve, S_1 or S_2, for example, Figs. 3.8*b* and 3.8*c*; whilst other systems only exhibit mixed-mode backbone curves, defined by Eq. (3.33).

Figure 3.9 presents the topological evolutions of mixed-mode backbone curves in the nonlinear parameter space, $(\alpha_1,\ \alpha_2)$, for a given system with optimised linear parameters $m_1 = 1, m_2 = 0.05, k_1 = 1, k_2 = k_2^{\text{opt}} \approx 0.0454$. Backbone curves for systems on $\varPsi_1 = 0$ and $\varPsi_2 = 0$, are topologically equivalent as those shown in Figs. 3.8*c* and 3.8*b* respectively.

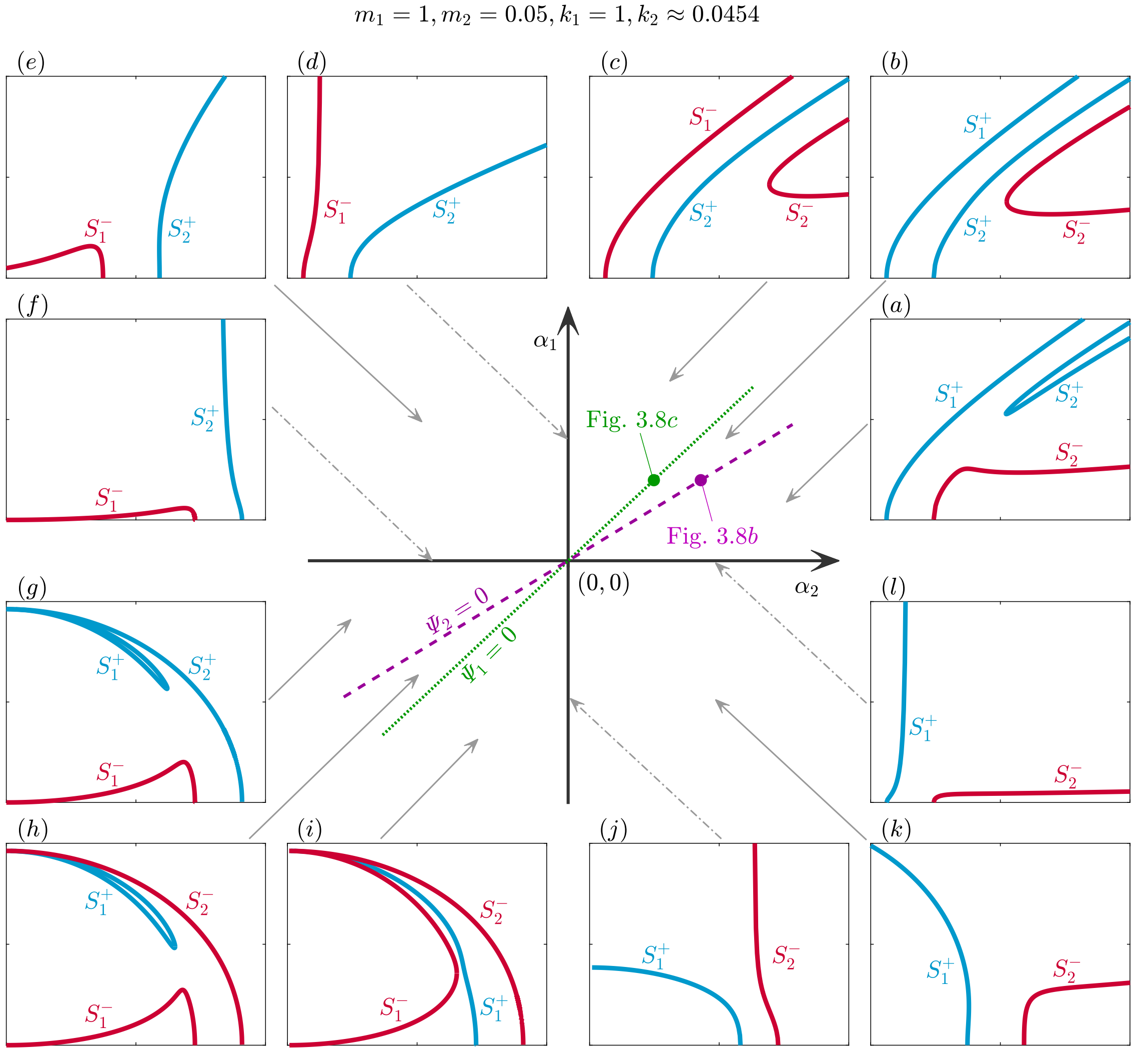

Fig. 3.9 Topological evolution of backbone curves in the nonlinear parameter space, α_1 against α_2, for a system with LA, i.e. $m_1 = 1, m_2 = 0.05, k_1 = 1$ and $k_2 = k_2^{\mathrm{opt}} \approx 0.0454$. The α_1 and α_2 values that lead to $\mathit{\Psi}_1 = 0$ and $\mathit{\Psi}_2 = 0$ are shown as a dotted green line and a dashed purple line respectively. The panels around the main figure show backbone curve topologies for the nonlinear regions in terms of response frequency and displacement amplitude of the first mass. Panels (a, b, c, e, g, h, i, k) are topologies in regions indicated by the solid-grey arrows. Panels (d, f, j, l) are topologies corresponding to α_1 and α_2 axes, as indicated by the dash-dotted grey arrows.

Here, this parameter space is divided by the axes $\alpha_1 = 0$ and $\alpha_2 = 0$ into the following four classes of system:

1. **a hardening system (the first quadrant)**
   For a system on $\varPsi_2 = 0$ (the backbone curves are shown in Fig. 3.8*c*), perturbing the nonlinear parameters clockwise in the $(\alpha_1,\ \alpha_2)$ space splits the BP on S_2 – this generates one isolated backbone curve, S_2^+, between two primary backbone curves, S_2^- and S_1^+,[5] shown in Fig. 3.9*a*. Likewise, if nonlinear parameters are perturbed anticlockwise from $\varPsi_2 = 0$, the BP on S_2 splits in a different direction, resulting in one isolated backbone curve, S_2^-, below two primary backbone curves, depicted in Fig. 3.9*b*.
   Further varying the nonlinear parameters in the anticlockwise direction towards $\varPsi_1 = 0$, the contribution of the second modal coordinate, U_2, to the mixed-mode in-phase backbone curve, S_1^+, gradually decreases to zero. This results in a single-mode backbone curve S_1, seen from the evolution of backbone curves from Fig. 3.9*b* to Fig. 3.8*c*. Finally, perturbing anticlockwise from $\varPsi_1 = 0$, the U_2 component of S_1 increases, leading to a mixed-mode anti-phase backbone curve, S_1^-, as shown in Fig. 3.9*c*.

2. **a hardening structure with a softening attachment (the second quadrant)**
   Further decreasing α_2 until $\alpha_2 < 0$ results in the second quadrant and leads the backbone curve, S_1^-, to bend leftward to a lower response freuqency, as depicted in Fig. 3.9*e*. Note that no isolated backbone curve is predicted for systems in the second quadrant.

3. **a softening system (the third quadrant)**
   Crossing from the second into the third quadrant causes S_2^+ to show a lower response freuqency, ω, with an increasing amplitude, shown in Figs. 3.9*f* and 3.9*g*. Continuing anticlockwise, from above $\varPsi_2 = 0$ to below it, leads to a similar behaviour to the hardening system (the first quadrant) as it crosses $\varPsi_1 = 0$. The contribution from U_1 to the mixed-mode in-phase backbone curve, S_2^+, gradually decreases, reaching zero when the system is on $\varPsi_2 = 0$, leading to a single-mode backbone curve S_2. The contribution from U_1 then increases from zero, giving rise to a mixed-mode anti-phase backbone curve S_2^-. Such an evolution is captured in Figs. 3.9*g* and 3.9*h*. Simultaneously, the isolated backbone curve, S_1^+, emerges from zero frequency and develops closer to the primary backbone curve S_1^-.
   Further varying the nonlinear parameters anticlockwise towards $\varPsi_1 = 0$, the isolated backbone curves, S_1^+ merges to the primary backbone curve, S_1^-, and formulates a single-mode backbone curve, S_1, with a BP leading to mixed-mode backbone

---

[5] Note that in other projections, e.g. ω against X_2, the relative amplitudes of these backbone curves may differ.

curves. Anticlockwise of $\Psi_1 = 0$, the BP splits and again generates an isolated backbone curve, S_1^-, however below the two primary backbone curves, S_1^+ and S_2^-, shown in Fig. 3.9*i*.

4. **a softening structure with a hardening attachment (the fourth quadrant)** Crossing from the third to the fourth quadrant leads to the disappearance of the isolated backbone curve, S_1^-, at zero frequency, shown in Figs. 3.9*i* and 3.9*j*. Additionally, the mixed-mode backbone curve, S_2^-, bends rightward, seen in Figs. 3.9*j* and 3.9*k*.

In addition, it can also be found that the hardening systems (the first quadrant) and softening systems (the third quadrant) share the following features:

1) **changes of the contribution of, and the phase relationship between, two modal coordinates**, from being in-phase, to single-mode, and then to anti-phase, or vice versa, when crossing $\Psi_1 = 0$ and $\Psi_2 = 0$;

2) **the emergence and splitting of a BP** on S_2 for a hardening system when crossing $\Psi_2 = 0$, and on S_1 for a softening system when crossing $\Psi_1 = 0$.

Note that the topological evolution of backbone curves, shown in Fig. 3.9, are computed via analytical expressions derived in this section. Even though these expressions are derived based on retaining only the fundamental harmonic of the interacting modes, the boundaries that determine critical topological changes as well as the topology in each region show great agreement with numerical results.

In summary, the backbone curve topology of a single-mode branch with a BP (leading to mixed-mode branches) denotes a critical condition, perturbing from which leads to the *emergence* of isolated backbone curves. Such a condition is defined by relationships (3.30*a*) and (3.30*b*) for hardening and softening systems respectively. In addition to capturing the existence of isolated backbone curves, these critical relationships also serve as boundaries that divide the parameter space into regions, within which backbone curves show topological equivalence for different systems. The following section explores additional boundaries that may exist, which accounts for the *annihilation* of isolated backbone curves.

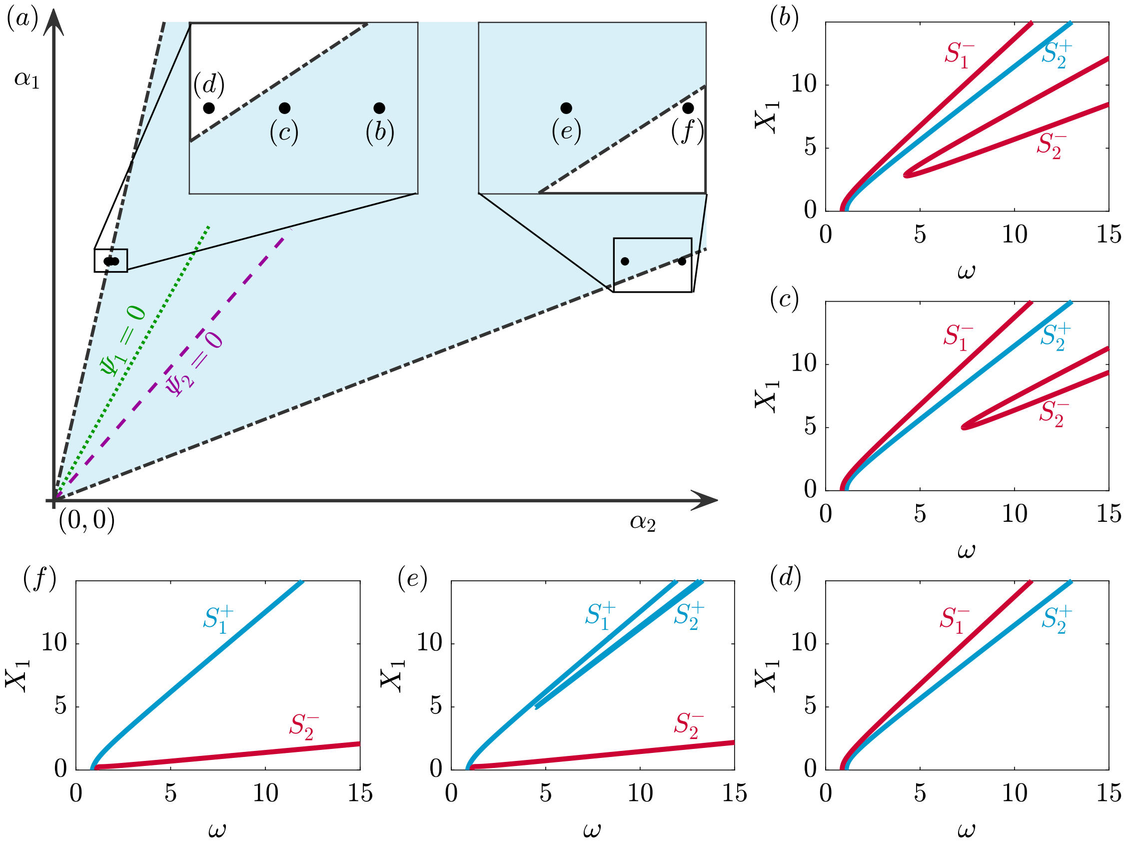

Fig. 3.10 Two additional topological boundaries for the existence of isolated backbone curves. (*a*) The first quadrant of Fig. 3.9, along with two additional boundaries, shown as dash-dotted black lines, differentiating between regions with and without isolated backbone curves. Panels (*b*) → (*f*) are backbone curves of systems denoted by black dots in Panel (*a*).

3.5 Additional topological boundaries

As discussed in §3.4.2, for a hardening system with $\Psi_2 = 0$, it shows the backbone curve topology in Fig. 3.8*b* – S_2 with a BP leading to $S_2^{\pm}$; a perturbation from $\Psi_2 = 0$ splits the BP on S_2 and results in an isolated backbone curve, shown in Figs. 3.9*a* and 3.9*b*.

Here, the further deviation from $\Psi_2 = 0$ is considered, which may cause the isolated backbone curve to move toward a higher response frequency and a larger amplitude, as depicted in Figs. 3.10*b* and 3.10*c* – backbone curves correspond to systems on points labelled (*b*) and (*c*) respectively in Fig. 3.10*a*. Such a transition continues until the isolated backbone curve undergoes topological change from having finite values of frequency and amplitude to infinite values, i.e. being non-existent from a practical perspective. An example capturing this topological change is presented in panels (b), (c) and (d) of Fig. 3.10; one can observe

1) the response frequency, ω, and amplitude, X_1, of the isolated backbone curve first increases at a limited rate, seen from panels (b) and (c) as α_2 changes from 7.5×10^{-4} to 7.0×10^{-4}.
2) the isolated backbone curve then shifts to infinite frequency and amplitude as α_2 approaches *a critical value* of approximately 6.76×10^{-4}, shown in panel (d).

This demonstrates the *annihilation* of the isolated backbone curve – having an infinite response frequency, in comparison to the *emergence* of isolated backbone curve due to bifurcation splitting considered in §3.4.2. As such, the critical parameter values (leading the isolated backbone curve to an infinite frequency) define another topological boundary that distinguishes between backbone curves with and without an isolated backbone curve.

To find the conditions that define such boundaries in nonlinear parameter space, one can track the isolated backbone curve to seek conditions for its existence. It is observed that the isolated backbone curve annihilates when the amplitude of the minimum frequency solution becomes infinite; hence, the conditions that lead to this case are investigated here[6]. Since the solution with the minimum frequency is related to a multiple root of amplitude for the frequency-amplitude relationship (3.33), one can refer to the zero discriminant of the amplitude equation (3.33b) to track the multiple root. The zero discriminant of the quartic equation (3.33b) is a sixth-order polynomial equation with respect to U_1 and it can be written as

$$\mathrm{Disc}_{U_2} = 0: \quad f_6 U_1^6 + f_5 U_1^5 + f_4 U_1^4 + f_3 U_1^3 + f_2 U_1^2 + f_1 U_1 + f_0 = 0\,, \tag{3.34}$$

where f_6 may be seen as a function of nonlinear parameters, α_1 and α_2, written as

$$f_6(\alpha_1,\ \alpha_2) = g_1\alpha_1^6 + g_2\alpha_1^5\alpha_2 + g_3\alpha_1^4\alpha_2^2 + g_4\alpha_1^3\alpha_2^3 + g_5\alpha_1^2\alpha_2^4 + g_6\alpha_1\alpha_2^5 + g_7\alpha_2^6\,, \tag{3.35}$$

and where coefficients $g_1, \ldots, g_7$ are determined by the underlying linear system, some of which are given in Appendix A. Note that $f_0, \ldots, f_5$, g_1, g_2, g_6 and g_7 are not provided as they are not required for the following derivations.

---

[6] There may be other conditions that allow isolated backbone curves to annihilate/emerge; however, this particular case is investigated here as an example of such behaviour, rather than as an exhaustive study.

As the isolated backbone curve reaches the annihilation point, it obtains the infinite amplitude; thus, considering a limit of $U_1 \to \infty$, it gives

$$\mathrm{Disc}_{U_2} \approx f_6 = 0\,. \tag{3.36}$$

After some algebraic manipulation, one can find coefficients g_1 and g_7 have factors $(p-1)^2\,(p+1)^2$, whilst coefficients g_2 and g_6 have factors $(p-1)\,(p+1)$. Recalling that p denotes the phase relationship between modal coordinates and is defined by Eq. (3.31), where $p = \pm 1$. It then follows that $g_1 = g_7 = g_2 = g_6 = 0$, and Eq. (3.36) can be further simplified to give

$$f_6 = \alpha_1^2 \alpha_2^2 \left(g_3 \alpha_1^2 + g_4 \alpha_1 \alpha_2 + g_5 \alpha_2^2 \right) = 0\,, \tag{3.37}$$

where two non-zero solutions for α_2 can be obtained

$$\alpha_2 = \frac{-g_4 \pm \sqrt{g_4^2 - 4 g_5 g_3}}{2 g_5} \alpha_1\,. \tag{3.38}$$

Likewise, if frequency-amplitude relationships (3.33) are rearranged to give a quartic amplitude equation with respect to U_1 rather than U_2, as currently, one can find the same expression as Eq. (3.38) by following the procedure outlined above. This means that U_1 and U_2 approach infinite values simultaneously on the critical conditions described by expression (3.38). The response frequency, ω, is explicitly determined by Eq. (3.33*a*), it also approaches the infinite value when $U_1 \to \infty$ and $U_2 \to \infty$.

As such, the analytical derivations above exactly capture the phenomena observed in the example case in Fig. 3.10 – satisfying parameter conditions (3.38) leads to the annihilation of isolated backbone curves via critically having infinite response frequency and amplitude values. This allows the first quadrant in Fig. 3.9, i.e. the hardening system, to be further divided into additional regions, as shown in Fig. 3.10*a*. The backbone curves for systems within the new divisions anticlockwise of $\Psi_1 = 0$ show:

1) the shaded area anticlockwise of $\Psi_1 = 0$: two primary backbone curves, S_1^- and S_2^+, with one isolated backbone curve, S_2^-, below those two, e.g. panels (*b*) and (*c*).
2) the unshaded area anticlockwise of $\Psi_1 = 0$: two primary backbone curves, S_1^- and S_2^+, without an isolated backbone curve, e.g. panel (*d*).

Whilst the new divisions clockwise of $\Psi_2 = 0$ show:

1) the shaded area clockwise of $\varPsi_2 = 0$: two primary backbone curves, S_1^+ and S_2^-, with one isolated backbone curve, S_2^+, between those two, e.g. panel (*e*);
2) the unshaded area clockwise of $\varPsi_2 = 0$: two primary backbone curves, S_1^+ and S_2^-, without an isolated backbone curve, e.g. panel (*f*).

In summary, expressions (3.30*a*) and (3.30*b*), combined with conditions (3.27), are boundaries for the existence of a BP on the single-mode backbone curve for a hardening and a softening system respectively, perturbing from which the bifurcation splits and an isolated backbone curve *emerges*. For hardening systems, expression (3.38) further describes the other boundaries, at which the isolated backbone curve *annihilates* with infinite frequency and amplitude values. The shaded area in Fig. 3.10*a* highlights the region in which an isolated backbone curve can exist.

In practice, when external forcing is applied, the existence of isolated backbone curves may be related to isolas, which can significantly affect the vibration mitigation performance of a NLTMD, as discussed in §2.3.1 and §3.4. Using the method proposed in this chapter, the existence of isolated backbone curves in the applications of a NLTMD can be analytically determined. To ensure an optimised linear spring coefficient, whilst eliminating isolated backbone curves, the nonlinear spring coefficient can be selected in the unshaded regions of Fig. 3.10*a*. The associated parameter conditions are given by

$$0 < \alpha_2 < \frac{-g_4 - \sqrt{g_4^2 - 4g_5g_3}}{2g_5}\alpha_1\,, \quad \text{or} \quad \alpha_2 > \frac{-g_4 + \sqrt{g_4^2 - 4g_5g_3}}{2g_5}\alpha_1\,. \tag{3.39}$$

When the nonlinear spring coefficient of the NLTMD, α_2, is selected within these intervals, the isolated backbone curves can be eliminated to ensure no correlated isolas may be observed when external forcing is applied.

3.6 Summary

In this chapter, the synchronous NNMs and their correlated isolated backbone curves have been studied with emphasis on conditions for the existence of isolated backbone curves. This was achieved by considering general two-mode interactions due to cubic nonlinearity; two example systems, taking the configurations of a two-mass chain system and a NLTMD-inspired system, were used throughout this chapter to aid interpretations.

First, the backbone curves of a symmetric system was revisted, where one can observe two single-mode backbone curves and mixed-mode backbone curves emerging from a bifurcation point on either of the single-mode branch. As with studies in [139, 141], symmetry breaking splits the bifurcation and leads to the existence of isolated backbone curves. Here, it has been shown that, under certain conditions, the backbone curve topology for a symmetric system can hold for asymmetric cases. This highlights the shared features between symmetric and asymmetric systems, termed *dynamic symmetry* in this thesis.

This concept was then used to explore conditions for the existence of isolated backbone curves. Here, an essentially asymmetric system, in the configuration of a primary system with a NLTMD attached, was considered. The parameter conditions for this system to behave equivalently to a symmetric system, i.e. having dynamic symmetry, were derived analytically. However, in practice, the optimisation of the NLTMD for vibration suppression performance breaks these conditions and leads to the emergence of isolated backbone curves due to bifurcation splitting.

Based on the optimised parameters (a given underlying linear system), the evolutions of backbone curves were investigated with respect to varied nonlinear parameters (to be optimised parameters). It revealed that the nonlinear parameter space can be divided into several regions, within which backbone curves exhibit similar topological features. In addition, the boundaries of these regions define conditions for the *emergence* of the isolated backbone curves. Additional boundaries were then identified to refine these divisions by considering the *annihilation* of isolated backbone curves when they are associated with infinite response frequency and amplitude values. These boundaries, determining the emergence and annihilation of isolated backbone curves, have been derived analytically; together they serve as topological boundaries in the parameter space, distinguishing the parameter regions whether isolated backbone curves exist or not.

In this chapter, the isolated backbone curves were shown to be associated with synchronous NNMs where the phase relationships between modal coordinates are in-phase or anti-phase. The counterpart of synchronous responses, namely the asynchronous responses, have also been briefly discussed and derived, given by Eqs. (3.25); however, this solution branch is related to zero response frequency for the examples considered in this chapter. In Chapter 4, this class of nonlinear responses will be considered to explore its dynamic features. It should also be noted that, even though the non-existence of asynchronous backbone curves is particular to the examples considered in this chapter, asynchronous branches do not exhibit the isolated feature when symmetry is broken. This will be revisted and discussed further for general $m : n$ internal resonances in Chapter 5, where it will be shown that only bifurcations leading to synchronous backbone curves can split due to symmetry breaking.

Chapter 4

Phase-varying backbone curves

In this chapter:

- Geometric features of NNMs are revisited and extended to *general asynchronous* cases by referring to the phase relationships between modal coordinates.
- The existence of general asynchronous NNMs is demonstrated by considering evolutions from the special out-of-unison asynchronous NNMs due to symmetry breaking.
- Analytical models of backbone curves are derived; they are used to determine the evolutions from phase-fixed out-of-unison backbone curves to phase-varying backbone curves due to the mechanism of phase-amplitude coupling.
- The existence of phase-varying behaviours is determined in a cable model with an externally attached support.

Publications related to this work

- D. Hong, E. Nicolaidou, T. L. Hill, S. A. Neild, 2020. Identifying phase-varying periodic behaviour in conservative nonlinear systems, *Proceedings of the Royal Society A: Mathematical, Physical and Engineering Sciences* 476 (2237) 20200028.
- D. Hong, E. Nicolaidou, T. L. Hill, S. A. Neild, 2021. Identifying phase-varying periodic behaviours in a conservative cable model, 2nd *International Nonlinear Dynamics Conference.*

4.1 Introduction

To understand nonlinear phenomena, extending linear modal analysis to the nonlinear context is extensively considered using the concept of NNMs [32, 31, 139, 87]. As demonstrated in §2.2.1, employing a geometric perspective, the NNMs can be categorised as synchronous and asynchronous NNMs [73, 31]. The synchronous NNMs, or in-unison NNMs, refer to cases where all components of the system reach their equilibrium and extrema simultaneously during periodic responses [73]. Such nonlinear responses can be observed in a variety of nonlinear systems, e.g. beam structures [144, 237], rotor systems [238], cable structures [129] and example systems in Chapter 3.

The counterpart of synchronous NNMs, i.e. asynchronous NNMs, represent cases where the system components *do not* reach their displacement extrema and equilibrium simultaneously. One example of asynchronous NNMs is the whirling motion, or out-of-unison motions, observed in cable structures [242, 129], and rotor systems [238]. Such an out-of-unison motion may be seen as a special case of asynchronous NNMs where one coordinate reaches an extremum whilst the other passes through the equilibrium point. This can also be interpreted by referring to the phase relationship between the vibrating coordinates and, for the out-of-unison case, it is characterised by a ±90° phase difference. Besides this special case, the more general case with an arbitrary phase difference (not necessarily ±90° out-of-phase), receives less attention in the literature. The existence of such general asynchronous motions represents a large family of nonlinear oscillations that requires an in-depth study to further understand the mechanism that underpins the dyanamic features. In addition, their existence means that phase relationships between coordinates are important parameters in characterising NNMs of dynamical systems. In terms of applications, due to their special features, the general asynchronous motions may potentially be exploited, as with the exploitation of synchronous motions in the context of vibration suppression and energy harvesting (as introduced in §2.3).

This chapter aims to demonstrate the existence of such general asynchronous NNMs, explore their features, and identify their existence in practical engineering systems. To this end, the rest of this chapter is organised as follows.

In §4.2, the concept NNMs is revisited for a two-mode system with $1:1$ internal resonance. Based on discussions in §3.2, an extension to account for general asynchronous NNMs is demonstrated. Features of such general cases and those previously considered ones are distinguished by referring to the response geometry in the configuration space and the phase relationships between modal coordinates. A numerical method is then used to demonstrate the existence of general asynchronous NNMs for a simple single-mass oscillator. It will be shown that these NNMs may be interpreted as asymmetric evolutions from special out-of-unison NNMs due to symmetry breaking.

Building on this observation, in §4.3, an analytical technique is used to further quantify the characteristics of asynchronous NNMs. Analytical phase relationships of the backbone curves verify the results found in §4.2. They further reveal that, along with the breaking of symmetric configurations, the out-of-unison backbone curve evolves to a family of asynchronous NNMs whose phase relationships are varying along the backbone curve. This class of backbone curve is defined here as a *phase-varying backbone curve*, and represents the locus of general asynchronous NNMs.

In §4.4, using insights obtained from the single-mass model, the existence of phase-varying backbone curves is identified for a cable model (a common mechanical structure that exhibits out-of-unison backbone curves [129]). This is achived by firstly deriving a reduced-order cable model, which is validated using an existing analytical model [232]. Next, the addition of a support near the cable root is then considered – this resembles the engineering practice of installing external devices to suppress cable vibrations [243, 244, 242]. This support breaks the symmetric configuration of the cable and, as with the single-mass model, causes the out-of-unison motions (i.e. whirling motions) to evolve to general asynchronous motions on a phase-varying backbone curve.

Finally, a summary is presented in §4.5.

4.2 Asynchronous NNMs of a two-mode system

In this section, the concept of NNMs [31, 100], is revisited for a two-mode system, but an extension is introduced to that considered in §3.2 by accounting for general asynchronous NNMs.

As discussed in §3.2, NNMs can be categorised as either synchronous or asynchronous motions by considering their geometric features. For illustration, modal interactions are discussed using the configuration space. In this space, synchronous single-mode and mixed-mode NNMs are shown in Figs. 4.1a and 4.1b respectively, where the lines represent the oscillations over time (q_1 and q_2 denote the first and second linear modal coordinates respectively). In this case, regarding the definition of synchronous motions, the extrema of q_1 and q_2 (denoted '$\circ$' and '$\times$' respectively) are achieved simultaneously. Equivalently, such synchronous features can also be captured by the modal state (i.e. q_i

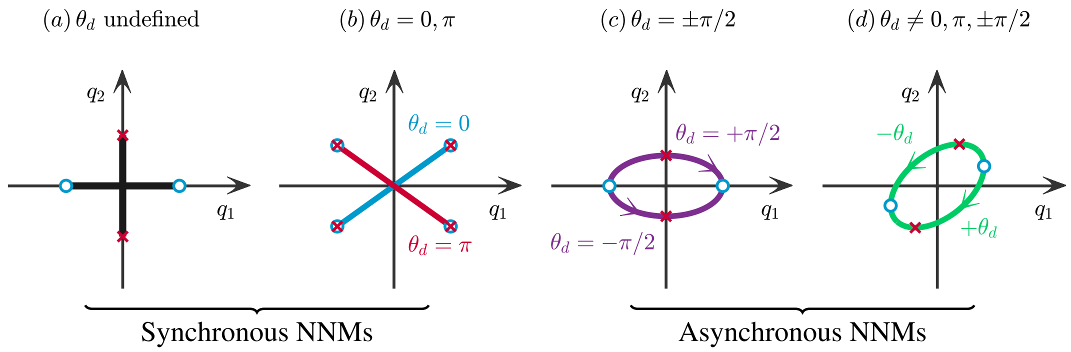

Fig. 4.1 Schematic representations of synchronous and asynchronous NNMs for a two-mode system with $1:1$ internal resonance. The responses are illustrated in the modal configuration space, i.e. the projection of the first and second linear modal coordinates, $q_1(t)$ and $q_2(t)$, parameterised in time. (a) The single-mode NNMs. (b) The in-phase ($\theta_d = 0$) and anti-phase ($\theta_d = \pi$) NNMs. (c) The $\pm\pi/2$ out-of-phase NNMs, where the '+' and '−' signs denote clockwise and anticlockwise motions respectively. (d) The $\pm\theta_d$ out-of-phase NNMs.

and $\dot{q}_i$) at extrema – both modes have non-zero displacements with zero velocities. An alternative method to characterise synchronous NNMs is referring to phase relationships between modal coordinates, where the single-mode NNMs in Fig. 4.1a have undefined phase, whilst the mixed-mode NNMs in Fig. 4.1b are either in-phase or anti-phase. Here, synchronous motions are briefly revisited, for detailed discussions, the reader is directed to §3.2 and Refs. [73, 31].

An example of an asynchronous NNM is shown in Fig. 4.1c where one modal coordinate reaches an extremum when the other passes through the equilibrium point – a loop in the configuration space. In this case, the linear modal coordinates exhibit $\pm\pi/2$ out-of-phase relationships (the '+' and '−' signs here denote the clockwise and anticlockwise motions in the configuration space respectively – see arrows on the loop in Fig. 4.1c). Likewise, such motions can be captured by the modal state at extrema – a non-zero *displacement* for one modal coordinate with a non-zero *velocity* for the other, or vice versa. This class of NNM is termed an out-of-unison NNM in [129], and captures whirling motions of, for example, cables [129] and rotor-shaft systems [238].

Up to this point, the commonly-observed NNM motions can, therefore, be categorised as single-mode (panel (a), where θ_d is undefined), in-phase and anti-phase synchronous (panel (b), $\theta_d = 0, \pi$ respectively) and out-of-unison asynchronous (panel (c), $\theta_d = \pm\pi/2$). Observing that all mixed-mode motions exhibit *specific* phase relationships, i.e. $\theta_d \in \{0,\ \pi,\ \pm\pi/2\}$, between modal components, a logical extension to these particular cases

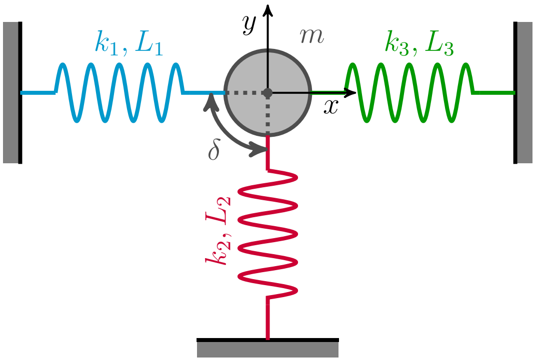

Fig. 4.2 A schematic diagram of a single-mass, two-mode system. A mass, with mass value m, has x and y denoting horizontal and vertical in-plane displacements respectively. This mass is grounded by two horizontal springs with coefficients k_1 and k_3, and unstretched lengths L_1 and L_3. Another spring, with coefficient k_2 and unstretched length L_2, grounds the mass, with δ representing the angle between k_1 and k_2. The system has a symmetric configuration when $\delta = 90°$, $k_1 = k_3$ and $L_1 = L_3$.

results in periodic motions with *arbitrary* phase relationships between components. An example of such NNMs is depicted in Fig. 4.1d – it exhibits geometric similarity to that of out-of-unison motions in panel (c) (i.e. a loop in the configuration space) but with a different phase relationship. Indeed, this class represents a *general* asynchronous NNM where the phase relationship between modal coordinates is θ_d out-of-phase (to differentiate from these previously discussed cases, $\theta_d \notin \{0,\ \pi,\ \pm\pi/2\}$). In contrast to the synchronous and out-of-unison asynchronous NNMs, this NNM represents responses where displacements and velocities can *never* simultaneously be zero.

To explore the existence of this general asynchronous NNM, and understand the mechanism that underpins its features, a two-mode, single-mass system, schematically shown in Fig. 4.2, is firstly considered. This example system consists of one mass, with mass value m, and has displacements x and y, denoting horizontal and vertical in-plane motions respectively. This mass is grounded by three linear springs with coefficients k_1, k_2, and k_3, and with unstretched lengths L_1, L_2, and L_3 respectively. At equilibrium, all the springs are unstretched and springs, k_1 and k_3, are laying in the x-direction; whilst the angle between k_1 and k_2 is denoted δ (when $\delta = 90°$, spring k_2 is orthogonal to springs k_1 and k_3). It can be observed that the model has a symmetric configuration when $\delta = 90°$, $k_1 = k_3$, and $L_1 = L_3$; conversely, it has an asymmetric configuration when these parameter conditions are broken.

In considering the dynamic responses of the system, it can exhibit nonlinear behaviours when vibrating at large amplitudes due to geometric nonlinearity. Using ΔL_i to denote the stretch or compression of springs k_i, the Lagrangian of the one-mass, two-mode system can be written as

$$\begin{aligned}\mathcal{L} &= \mathcal{T} - \mathcal{V}, \\ &= \frac{1}{2}m\dot{x}^2 + \frac{1}{2}m\dot{y}^2 - \left(\frac{1}{2}k_1\left(\Delta L_1\right)^2 + \frac{1}{2}k_2\left(\Delta L_2\right)^2 + \frac{1}{2}\left(\Delta L_3\right)^2\right), \\ &= \frac{1}{2}m\dot{x}^2 + \frac{1}{2}m\dot{y}^2 - \frac{1}{2}k_1\left(\sqrt{\left(L_1+x\right)^2+y^2} - L_1\right)^2 \\ &\quad - \frac{1}{2}k_2\left(\sqrt{\left[L_2\cos\left(\delta\right)+x\right]^2+\left[L_2\sin\left(\delta\right)+y\right]^2} - L_2\right)^2 \\ &\quad - \frac{1}{2}k_3\left(\sqrt{\left(L_3-x\right)^2+y^2} - L_3\right)^2 .\end{aligned} \tag{4.1}$$

The equations of motion, with variables of the physical coordinates, x and y, can then be obtained via the Euler-Lagrange equations, leading to

$$\begin{aligned}&m\ddot{x} + k_1\left(L_1+x\right) - \frac{k_1L_1\left(L_1+x\right)}{\sqrt{\left(L_1+x\right)^2+y^2}} + k_2\left[L_2\cos\left(\delta\right)+x\right] \\ &\quad - \frac{k_2L_2\left[L_2\cos\left(\delta\right)+x\right]}{\sqrt{\left[L_2\cos\left(\delta\right)+x\right]^2+\left[L_2\sin\left(\delta\right)+y\right]^2}} - k_3\left(L_3-x\right) - \frac{k_3L_3\left(x-L_3\right)}{\sqrt{\left(L_3-x\right)^2+y^2}} = 0\,,\end{aligned} \tag{4.2a}$$

$$\begin{aligned}&m\ddot{y} + k_1y - \frac{k_1L_1y}{\sqrt{\left(L_1+x\right)^2+y^2}} + k_2\left[L_2\sin\left(\delta\right)+y\right] \\ &\quad - \frac{k_2L_2\left[L_2\sin\left(\delta\right)+y\right]}{\sqrt{\left[L_2\cos\left(\delta\right)+x\right]^2+\left[L_2\sin\left(\delta\right)+y\right]^2}} + k_3y - \frac{k_3L_3y}{\sqrt{\left(L_3-x\right)^2+y^2}} = 0\,.\end{aligned} \tag{4.2b}$$

Using this two-mode model, the existence of the general asynchronous NNMs, shown in Fig. 4.1*d*, is investigated based on one potential mechanism – the breaking of the symmetric configuration. Note that, as discussed in Chapter 3, symmetry breaking transforms single-mode NNMs into mixed-mode in-phase or anti-phase NNMs (i.e. from Fig. 4.1*a* to Fig. 4.1*b*); hence, it is logical to assume that symmetry breaking can, likewise, lead to evolutions from out-of-unison NNMs to general asynchronous NNMs (i.e. from Fig. 4.1*c* to Fig. 4.1*d*). To investigate this symmetry-breaking mechanism, it is achieved by comparing the NNM responses for the symmetric and asymmetric cases. The NNM branches, or backbone curves, are directly computed via Eqs. (4.2) using the `po`-toolbox

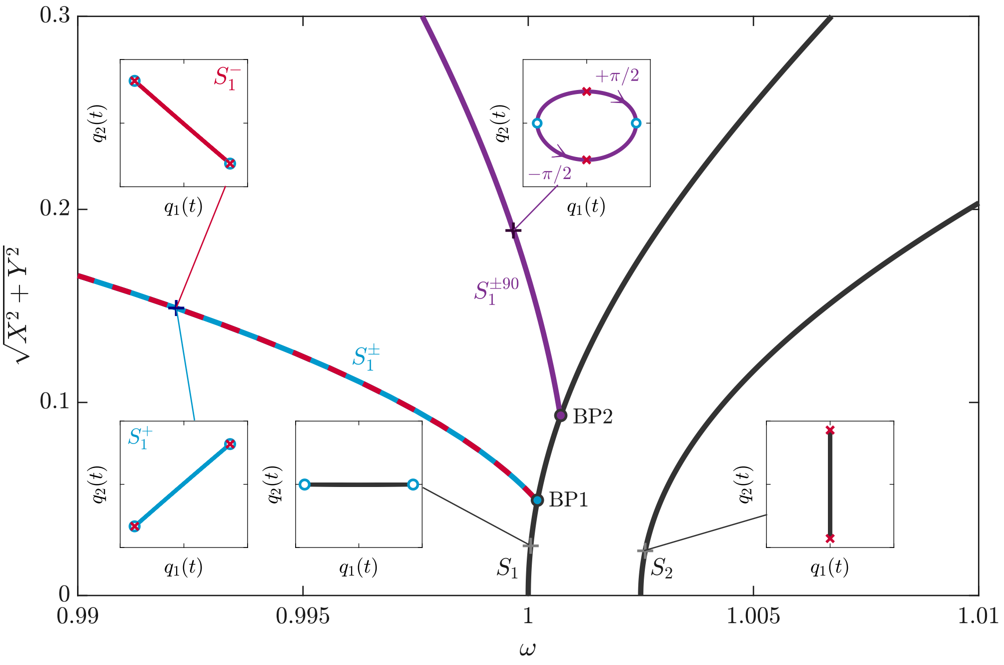

Fig. 4.3 Backbone curves for the single-mass, two-mode system in Fig. 4.2 with a symmetric configuration. The backbone curves are shown in the projection of the response frequency, ω, against the absolute displacement of the mass for a system with $m = 1, k_1 = k_3 = 0.5, k_2 = 1.005, L_1 = L_2 = L_3 = 1$ and $\delta = 90°$. Bifurcation points on backbone curve S_1 are denoted as solid dots, labelled 'BP1' and 'BP2'. Five embedded plots, in the modal configuration space, $(q_1(t),\ q_2(t))$, represent the time-parameterised NNM responses on the corresponding backbone curves; the extrema of modal coordinates $q_1(t)$ and $q_2(t)$ are marked by '∘' and '×' respectively in these embedded plots. Arrows in the embedded plot linked to $S_1^{\pm 90}$ denote clockwise and anticlockwise motions.

of COCO [99], which makes use of the collocation method to find periodic solutions. Note that no analytical approximation is introduced for the results shown in this section.

4.2.1 NNMs of the symmetric system

First the symmetric case is considered via an example system with $m = 1, k_1 = k_3 = 0.5, k_2 = 1.005, L_1 = L_2 = L_3 = 1$, and $\delta = 90°$. The backbone curves of this system are shown in Fig. 4.3 in the projection of the response frequency, ω, against the absolute displacement amplitude of the mass, $\sqrt{X^2 + Y^2}$, where X and Y are the maximum amplitudes of displacements x and y respectively.

In this region, there are two single-mode backbone curves S_1 and S_2;[1] in addition, two mixed-mode backbone curves, S_1^+ and S_1^-, bifurcate from S_1 via bifurcation point BP1 (as previously, the subscripts of S_1^+ and S_1^- indicate the backbone curve from which they bifurcate, in this case from S_1). Note that, due to the symmetry of configuration, S_1^+ and S_1^- are superimposed in this projection. The NNMs on these single-mode and mixed-mode backbone curves are synchronous periodic responses – see the time-parameterised responses of NNMs on these backbone curves in the embedded plots, which are analogous to those shown in Fig. 4.1*a* and 4.1*b* respectively.

In contrast to these synchronous backbone curves, one can also find asynchronous, out-of-unison backbone curves, $S_1^{\pm 90}$, that bifurcate from S_1 through bifurcation point, BP2. The embedded plot, near $S_1^{\pm 90}$ in Fig. 4.3, describes the time-parameterised NNM response on $S_1^{\pm 90}$ – q_1 reaches its extreme displacement when q_2 has a zero value and vice versa; the arrows on the response curve in the configuration space denote the clockwise motion ($\theta_d = +\pi/2$) and anticlockwise motion ($\theta_d = -\pi/2$) respectively. One can also find the similarity between the out-of-unison NNMs, in the embedded plot, and those in Fig. 4.1*c*.

Using numerical continuation, the backbone curves for a symmetric case have been computed and discussed, where special out-of-unison branches are identified. In the following, symmetry breaking is introduced to the system to investigate the asymmetric evolutions of NNMs.

4.2.2 NNMs of the asymmetric system

With δ perturbed away from 90° whilst other parameters remain unchanged, the symmetric configuration of the system is broken. With $\delta = 89.5°$, the symmetry-breaking effect on the backbone curves is shown in Fig. 4.4. For comparison, backbone curves for the symmetric case are also presented using dash-dotted grey lines in the same figure.

Symmetry breaking splits the bifurcation point, BP1, on the single-mode backbone curve, S_1, and generates one primary in-phase backbone curve, S_1^+, and one isolated anti-phase backbone curve S_1^-.[2] Additionally, the broken symmetry gives rise to an

---

[1] Note that responses on the backbone curve S_1 do contain a small component of the second mode, q_2; however, this is dominated by a response at twice the fundamental frequency and there is no component at the fundamental frequency - i.e. the motion is similar to the swaying of a cable, observed at low amplitude [245]. For consistency with later sections, we denote this as a single-mode backbone curve, representing the fact that only one mode (q_1) has a component at the fundamental frequency.

[2] Note that interested reader is directed to Chapter 3 for discussions on conditions for the existence of this isolated backbone curve.

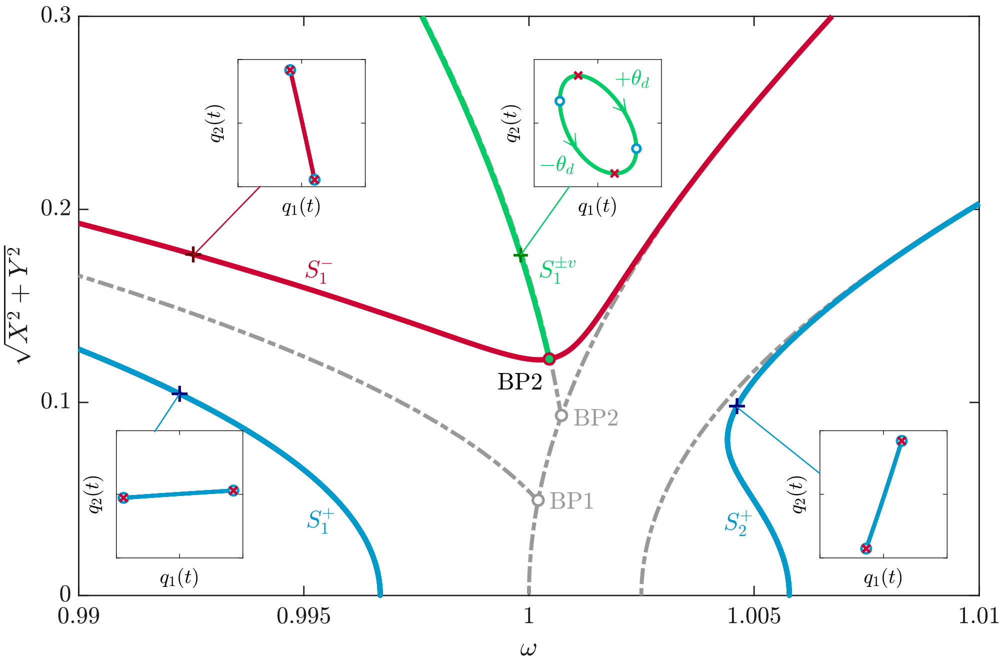

Fig. 4.4 Backbone curves for the single-mass, two-mode system in Fig. 4.2 with an asymmetric configuration. The backbone curves are shown in the projection of the response frequency, ω, against absolute displacement of the mass for a system with $m = 1, k_1 = k_3 = 0.5, k_2 = 1.005, L_1 = L_2 = L_3 = 1$ and $\delta = 89.5°$. Four embedded plots, in the modal configuration space, $(q_1(t),\ q_2(t))$, show the NNM responses on the corresponding backbone curves. In these embedded plots, the extrema of modal coordinates $q_1(t)$ and $q_2(t)$ are marked by '$\circ$' and '$\times$' respectively. Arrows in the embedded plot linked to $S_1^{\pm v}$ denote clockwise and anticlockwise motions. For comparison, the backbone curves for the symmetric case in Fig. 4.3 are shown as dash-dotted curves with bifurcations denoted by hollow dots.

in-phase primary backbone curve S_2^+. These three mixed-mode backbone curves, as with the symmetric case, are composed of synchronous NNMs – seen from the embedded plots in the configuration space, $(q_1(t),\ q_2(t))$, where the time-parameterised responses are lines passing through the origin – analogues to that in Fig. 4.1*b*.

The other bifurcation point, BP2, remains intact for the asymmetric case, and connects the anti-phase backbone curve S_1^- to $S_1^{\pm v}$, which can be viewed as asymmetric evolutions from the out-of-unison backbone curves, $S_1^{\pm 90}$. The NNM responses on $S_1^{\pm v}$ are shown in the embedded plot linked to the $S_1^{\pm v}$ curves, and they exhibit asynchronous features – a loop in the configuration space, similar to that on the out-of-unison backbone curves; however, the phase relationships between modal coordinates, θ_d, are not $\pm\pi/2$, but instead are similar to the ones in Fig. 4.1*d*. This is highlighted by the dots and crosses, i.e. the extrema of q_1 and q_2 respectively in the embedded plot, which illustrate that the extrema and equilibria of modal coordinates are reached at different times.

By comparing results shown in Figs. 4.3 and 4.4, this example demonstrates that NNMs with a general asynchronous motion can exist due to symmetry breaking. As will be shown in the next section, for asymmetric systems, the phase relationships, θ_d, of NNMs on the asynchronous backbone curves exhibit *phase-amplitude coupling*; in other words, phase relationships of NNMs are varying along the backbone curves. As such, they are termed *phase-varying backbone curves*, as denoted with the superscript, $\bullet^{\pm v}$. Additionally, it should also be noted that, in this example case, the bifurcation leading to synchronous backbone curves splits due to symmetry breaking; however, the bifurcation onto the asynchronous backbone curves remains intact under symmetry breaking. The different effects of symmetry breaking on bifurcations splitting/remaining will be analytically investigated in Chapter 5 for more general cases.

In this section, the periodic responses, i.e. the NNMs, of a two-mode system were firstly reviewed, emphasising the less studied asynchronous NNMs. A specific example of such asynchronous NNMs is the out-of-unison NNM, studied in [129], where the modal coordinates have $\pm\pi/2$ phase difference. To explore the existence of a more general asynchronous case, where the NNM exhibits a phase difference $\theta_d \notin \{0,\ \pi,\ \ \pm\pi/2\}$ between linear modal coordinates, a simple two-mode system, depicted in Fig. 4.2, has been considered. It has been found that the *symmetry breaking* can transform the out-of-unison NNMs to the more general asynchronous ones. In the next section, analytical studies are carried out to further study the dynamic characteristics of the asynchronous NNMs.

4.3 Analytical study of the asynchronous backbone curves

In this section, the backbone curves of the single-mass, two-mode system are derived analytically using the harmonic balance technique. The obtained backbone curve expressions are then used to interpret the dynamic behaviours from a symmetry-breaking perspective. With the emphasis on the evolutions of asynchronous motions, studies in this section aim to further the understanding obtained in §4.2.

To simplify the analytical study of the system in Fig. 4.2, the restoring force of the full model, given in Eqs. (4.2), is firstly approximated as a polynomial function of physical coordinates, x and y, via a Taylor series expansion about the equilibrium point ($x = 0,\ y = 0$); it is then truncated by retaining nonlinear terms up to the cubic order. In this way, the obtained equations of motion are given by

$$\mathbf{M}\ddot{\mathbf{x}} + \mathbf{K}\mathbf{x} + \mathbf{N_x} = \mathbf{0}\,, \tag{4.3}$$

where $\mathbf{M}$ and $\mathbf{K}$ are mass and linear stiffness matrices respectively; $\mathbf{N_x}$ is a vector of nonlinear terms; and $\mathbf{x}$ is a vector representing physical displacements, defined respectively as

$$\mathbf{M} = \begin{bmatrix} m & 0 \\ 0 & m \end{bmatrix}, \quad \mathbf{K} = \begin{bmatrix} k_1 + k_2\cos^2(\delta) + k_3 & k_2\sin(\delta)\cos(\delta) \\ k_2\sin(\delta)\cos(\delta) & k_2\sin^2(\delta) \end{bmatrix},$$
$$\mathbf{N_x} = \begin{pmatrix} 3\beta_1 x^2 + 2\beta_2 xy + \beta_3 y^2 + 4\gamma_1 x^3 + 3\gamma_2 x^2 y + 2\gamma_3 xy^2 + \gamma_4 y^3 \\ \beta_2 x^2 + 2\beta_3 xy + 3\beta_4 y^2 + \gamma_2 x^3 + 2\gamma_3 x^2 y + 3\gamma_4 xy^2 + 4\gamma_5 y^3 \end{pmatrix}, \quad \mathbf{x} = \begin{pmatrix} x \\ y \end{pmatrix},$$

and where the coefficients of quadratic and cubic nonlinear terms, β_1, β_2, $\cdots$, β_4, γ_1, γ_2, $\cdots$, γ_5, are defined by Eq. (A.5) (in Appendix A).

To compute backbone curves, the system is then transformed into the modal domain by applying linear modal transform, i.e. $\mathbf{x} = \mathbf{\Phi}\mathbf{q}$, defined by Eq. (3.11), where $\mathbf{\Phi}$ is the modeshape matrix and $\mathbf{q}$ is a vector of linear modal coordinates. After applying the linear modal transform, and some algebraic manipulation, the obtained equations of motion in the modal domain are given by

$$\ddot{\mathbf{q}} + \mathbf{\Lambda}\mathbf{q} + \mathbf{N_q} = \mathbf{0}\,, \tag{4.4}$$

where

$$\mathbf{\Lambda} = \begin{bmatrix} \omega_{n1}^2 & 0 \\ 0 & \omega_{n2}^2 \end{bmatrix}, \ \mathbf{N_q} = \begin{pmatrix} \varXi_3 q_1^2 + 2\varXi_1 q_1 q_2 + \varXi_2 q_2^2 + \varPsi_4 q_1^3 + 3\varPsi_1 q_1^2 q_2 + \varPsi_3 q_1 q_2^2 + \varPsi_2 q_2^3 \\ \varXi_1 q_1^2 + 2\varXi_2 q_1 q_2 + \varXi_4 q_2^2 + \varPsi_1 q_1^3 + \varPsi_3 q_1^2 q_2 + 3\varPsi_2 q_1 q_2^2 + \varPsi_5 q_2^3 \end{pmatrix}, \tag{4.5}$$

and where $\mathbf{\Lambda}$ is a diagonal matrix with leading diagonal elements, ω_{n1}^2 and ω_{n2}^2, denoting the squares of the first and second linear natural frequencies respectively; $\mathbf{N_q}$ is the vector of nonlinear terms with $\varXi_1, \varXi_2, \cdots, \varXi_4$ and $\varPsi_1, \varPsi_2, \cdots, \varPsi_5$ denoting the coefficients of the quadratic and cubic nonlinear terms respectively. These coefficients are defined by Eq. (A.6) in Appendix A.

Equation (4.4) can directly be used to compute backbone curves via numerical continuation; however, to find analytical expressions of backbone curves, the harmonic balance method is used. As with discussions in §3.3, it is assumed that the modal displacements may be approximated by a single harmonic, given by Eq. (3.5), i.e. $q_i \approx u_i = U_i \cos(\omega_{ri} t - \theta_i)$. It is further assumed that the fundamental frequencies of the two modes are equal, i.e. $\omega_{r1} = \omega_{r2} = \omega$, which accounts for $1:1$ internal resonance. This $1:1$ assumption can be justified by numerical results shown in Figs. 4.3 and 4.4, where the periodic motions on mixed-mode backbone curves (that emerge from internal resonance) indeed exhibit $1:1$ frequency commensurate relationships.

Following the procedure outlined in §3.3 – with substitution of the assumed solutions, $q_i \approx u_i = U_i \cos(\omega_{ri} t - \theta_i)$, into equations of motion (4.4), and the non-resonant terms removed, one can obtain the expressions for backbone curves in the same form as Eqs. (3.8), i.e.

$$4\left(\omega_{n1}^2 - \omega^2\right) U_1 + 3\varPsi_4 U_1^3 + \varPsi_3 U_1 U_2^2 \left[1 + 2\cos^2(\theta_d)\right] + 3\left(\varPsi_2 U_2^3 + 3\varPsi_1 U_1^2 U_2\right)\cos(\theta_d) = 0\,, \quad (4.6a)$$

$$4\left(\omega_{n2}^2 - \omega^2\right) U_2 + 3\varPsi_5 U_2^3 + \varPsi_3 U_1^2 U_2 \left[1 + 2\cos^2(\theta_d)\right] + 3\left(\varPsi_1 U_1^3 + 3\varPsi_2 U_1 U_2^2\right)\cos(\theta_d) = 0\,, \quad (4.6b)$$

$$\left[2\varPsi_3 U_1 U_2 \cos(\theta_d) + 3\varPsi_1 U_1^2 + 3\varPsi_2 U_2^2\right]\sin(\theta_d) = 0\,, \quad (4.6c)$$

where $\theta_d = \theta_1 - \theta_2$ denotes the phase difference between two modal coordinates. These equations can then be used to compute the backbone curves of the two-mode system shown in Fig. 4.2. Note that the quadratic terms, presented in Eqs. (4.4), are non-resonant components which do not lead to $1:1$ internal resonance [246], hence their coefficients, $\varXi_i$, do not present in Eqs. (4.6). The influence of the quadratic terms on $1:1$ internally resonant response may be represented as a DC offset from the equilibrium position for the time trajectory.

As the govening equations for backbone curves, Eqs. (4.6), take the same form as that derived in §3.3, the expressions for single-mode and mixed-mode backbone curves for the symmetric case are directly given here for reference; whilst the detailed derivations can be found in §3.3.

For *symmetric* cases, i.e. $\delta = 90^\circ$, $k_1 = k_3$ and $L_1 = L_3$, the system has $\varPsi_1 = \varPsi_2 = 0$, found from expressions (*A*.5) and (*A*.6). The backbone curve expressions for such symmetric cases are given by:

1) Single-mode synchronous backbone curves

$$S_1(\omega,\ U_1): \quad U_2 = 0\,, \quad \omega^2 = \omega_{n1}^2 + \frac{3}{4}\varPsi_4 U_1^2\,, \quad (4.7)$$

$$S_2(\omega,\ U_2):\quad U_1 = 0\,,\quad \omega^2 = \omega_{n2}^2 + \frac{3}{4}\,\Psi_5 U_2^2\,. \tag{4.8}$$

The NNMs on these single-mode branches, as discussed previously, can be schematically illustrated by Fig. 4.1*a*.

2) Mixed-mode synchronous, or in-phase/anti-phase, backbone curves

$$S_{1,2}^{\pm}(\omega,\ U_1,\ U_2):\quad U_1^2 = \frac{4\left(\omega_{n2}^2 - \omega_{n1}^2\right) + 3\,(\Psi_5 - \Psi_3)\,U_2^2}{3\,(\Psi_4 - \Psi_3)}\,, \tag{4.9a}$$

$$\omega^2 = \frac{4\left(\Psi_4\omega_{n2}^2 - \Psi_3\omega_{n1}^2\right) + 3\left(\Psi_4\,\Psi_5 - \Psi_3^2\right)U_2^2}{4\,(\Psi_4 - \Psi_3)}\,. \tag{4.9b}$$

The NNM responses on these synchronous backbone curves can be schematically described by Fig. 4.1*b*.

3) Mixed-mode asynchronous, or out-of-unison, backbone curves

$$S_{1,2}^{\pm 90}(\omega,\ U_1,\ U_2):\quad U_1^2 = \frac{4\left(\omega_{n2}^2 - \omega_{n1}^2\right) + (3\,\Psi_5 - \Psi_3)\,U_2^2}{3\,\Psi_4 - \Psi_3}\,, \tag{4.10a}$$

$$\omega^2 = \frac{4\left(3\,\Psi_4\omega_{n2}^2 - \Psi_3\omega_{n1}^2\right) + \left(9\,\Psi_4\,\Psi_5 - \Psi_3^2\right)U_2^2}{4\,(3\,\Psi_4 - \Psi_3)}\,. \tag{4.10b}$$

NNMs on these backbone curves exhibit $\pm\pi/2$ phase relationships between two modes, where the responses are schematically shown in Fig. 4.1*c*.

For *asymmetric* cases, for example the case considered in §4.2.2 where $\delta \neq 90^\circ$, the single-mode solution is no longer obtainable. Instead, there are mixed-mode solution branches which are related to the phase condition of $\sin(\theta_d) = 0$, or $\theta_d = n\pi$, found from Eq. (4.6*c*). These branches correspond to the in-phase and anti-phase backbone curves, $S_{1,2}^{\pm}$, whose frequency-amplitude relationships are governed by

$$S_{1,2}^{\pm}(\omega, U_1, U_2):$$

$$\omega^2 = \omega_{n1}^2 + \frac{3}{4}\left[\Psi_4 U_1^3 + \Psi_3 U_2^2 U_1 + p\left(\Psi_2 U_2^3 + 3\,\Psi_1 U_1^2 U_2\right)\right]U_1^{-1}\,, \tag{4.11a}$$

$$\begin{aligned} 0 = {} & \left(-3p\,\Psi_2 U_1^{-1}\right)U_2^4 + 3\,(\Psi_5 - \Psi_3)\,U_2^3 + \left[9p\,(\Psi_2 - \Psi_1)\,U_1\right]U_2^2 + {} \\ & \left[4\omega_{n2}^2 - 4\omega_{n1}^2 + 3\,(\Psi_3 - \Psi_4)\,U_1^2\right]U_2 + 3p\,\Psi_1 U_1^3\,, \end{aligned} \tag{4.11b}$$

where $p = \cos(n\pi)$; $p = +1$ for even n and it represents in-phase backbone curves $S_{1,2}^{+}$; whilst $p = -1$ for odd n and it denotes anti-phase backbone curves $S_{1,2}^{-}$. Note that such mixed-mode synchronous backbone curves have been investigated in detail in Chapter 3.

In addition to the synchronous cases, the other phase relationship can be established – a zero value of the terms in the bracket of Eq. (4.6c). This phase relationship can be rearranged as

$$\cos\left(\theta_d\right) = -\frac{3\left(\varPsi_1 U_1^2 + \varPsi_2 U_2^2\right)}{2\,\varPsi_3 U_1 U_2}\,. \tag{4.12}$$

This expression indicates that the phase relationship, θ_d, is a function of the amplitudes (U_1 and U_2), suggesting that θ_d is varying along the backbone curve as amplitude varies. Here, such an asynchronous NNM branch with an amplitude-dependent phase relationship between modal coordinates is termed as a *phase-varying backbone curve*. To find the expressions of this phase-varying backbone curve, the phase relationship (4.12) is substituted into Eqs. (4.6b) and (4.6c); after some rearrangement, the following frequency-amplitude relationship can be found, namely

$$S_{1,2}^{\pm v}(\omega,\ U_1,\ U_2):$$

$$U_1^2 = \frac{4\,\varPsi_3\left(\omega_{n1}^2 - \omega_{n2}^2\right) + \varPsi_3\left(\varPsi_3 - 3\,\varPsi_5\right)U_2^2 + 9\,\varPsi_2\left(\varPsi_2 - \varPsi_1\right)U_2^2}{\varPsi_3\left(\varPsi_3 - 3\,\varPsi_4\right) + 9\,\varPsi_1\left(\varPsi_1 - \varPsi_2\right)}\,, \tag{4.13a}$$

$$\omega^2 = \frac{\begin{array}{r}\Big[\varPsi_3\left(\varPsi_3^2 - 9\,\varPsi_4\,\varPsi_5\right)U_2^2 + 9\left(3\,\varPsi_5\,\varPsi_1^2 + 3\,\varPsi_2^2\,\varPsi_4 - 2\,\varPsi_1\,\varPsi_2\,\varPsi_3\right)U_2^2 + \\ 4\,\varPsi_3\left(\varPsi_3\omega_{n1}^2 - 3\,\varPsi_4\omega_{n2}^2\right) + 36\,\varPsi_1\left(\varPsi_1\omega_{n2}^2 - \varPsi_2\omega_{n1}^2\right)\Big]\end{array}}{4\,\varPsi_3\left(\varPsi_3 - 3\,\varPsi_4\right) + 36\,\varPsi_1\left(\varPsi_1 - \varPsi_2\right)}\,. \tag{4.13b}$$

As previously discussed, a system with a symmetric configuration has modal coefficients $\varPsi_1 = 0$ and $\varPsi_2 = 0$. Substituting these into Eqs. (4.13), the amplitude-frequency expressions of phase-varying backbone curves are reduced to the ones describing out-of-unison backbone curves, given by Eqs. (4.10). In addition, with $\varPsi_1 = 0$ and $\varPsi_2 = 0$, the amplitude-dependent phase relationship, defined by the expression (4.12), is reduced to $\cos\left(\theta_d\right) = 0$; this phase relationship is again identical to that for the out-of-unison backbone curves, which have $\theta_d = \pm\pi/2$. This therefore indicates that *the phase-varying backbone curve is an evolution of the out-of-unison backbone curve due to symmetry breaking, through the mechanism of phase-amplitude coupling*, described by Eq. (4.12).

To illustrate these analytical results, Fig. 4.5a presents the analytically-computed backbone curves (using equations from (4.7) to (4.13)) in the projection of the response frequency, ω, against the absolute displacement of the mass, $\sqrt{X^2 + Y^2}$, for the single-mass system schematically shown in Fig. 4.2. Backbone curves for the symmetric case (i.e. $m = 1, k_1 = k_3 = 0.5, k_2 = 1.1, L_1 = L_2 = L_3 = 1$ and $\theta = 90^\circ$) are presented by

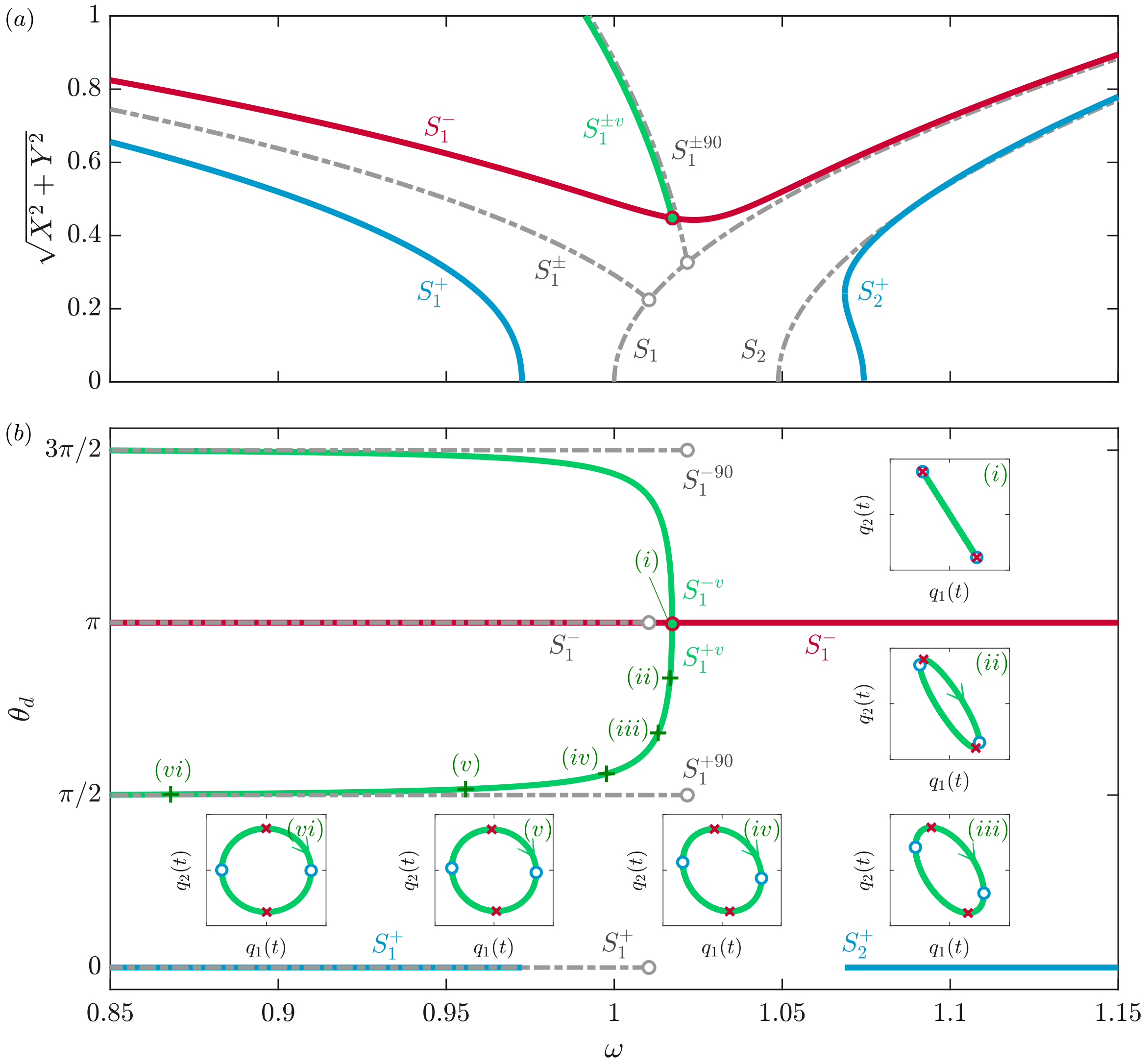

Fig. 4.5 Analytically computed backbone curves of the single-mass, two-mode system in Fig. 4.2 for symmetric and asymmetric cases. The backbone curves for the symmetric case, i.e. $m = 1, k_1 = k_3 = 0.5, k_2 = 1.1, L_1 = L_2 = L_3 = 1$ and $\delta = 90°$, are shown as dash-dotted grey curves; whilst the backbone curves for the asymmetric case, i.e. with δ changed from 90° to 85°, are presented using solid curves. (a) Backbone curves in the projection of the response frequency, ω, against the absolute displacement of the mass. (b) The modal phase relationships on the backbone curves in the projection of the response frequency, ω, against the phase difference, θ_d, between two modal coordinates. Six embedded plots, labelled $(i) \rightarrow (vi)$, show the phase-varying behaviours in the modal configuration space, $(q_1(t), q_2(t))$, of NNM responses on the phase-varying backbone curve, S_1^{+v}. The extrema of $q_1(t)$ and $q_2(t)$, in these embedded plots, are labelled with '○' and '×' respectively to highlight the varied phases.

dash-dotted lines; whilst backbone curves for the asymmetric case, obtained by changing δ from 90° to 85°, are shown as solid lines. It should be noted that these backbone curves are computed without taking into account the effect of quadratic nonlinearity as they show a non-resonant effect which is eliminated during derivation; however, neglecting the quadratic terms does not lead to qualitative differences in backbone curves. In the remaining discussions, the effect of cubic nonlinearity is considered with a focus on how symmetry breaking leads to the existence of general asynchronous NNMs.

Similar to Fig. 4.4, Fig. 4.5*a* shows the effect of symmetry breaking on backbone curves. It causes the bifurcation, BP1, on the single-mode backbone curve, S_1, to split into one primary in-phase backbone curve, S_1^+, and one isolated anti-phase backbone curve S_1^-. Whilst, the bifurcation point, BP2, remains intact and the out-of-unison backbone curves, $S_1^{\pm 90}$, evolve to the phase-varying backbone curves $S_1^{\pm v}$. Note that two phase-varying backbone curves are superimposed in this projection with one showing clockwise motions $(+\theta_d)$ and the other showing anticlockwise motions $(-\theta_d)$.

Figure 4.5*b* shows the phase relationships on these backbone curves in the projection of the response frequency, ω, against the phase difference, θ_d, between fundamental components of the modal coordinates, q_1 and q_2. For the symmetric case, as expected, different NNMs on any backbone curve exhibit the same fixed phase relationship between q_1 and q_2, indicated by the dash-dotted straight lines in this figure. For the asymmetric case, the synchronous backbone curves, S_1^+, S_1^- and S_2^+, exhibit fixed phase relationships; in contrast, the phase relationships of backbone curves, $S_1^{\pm v}$, vary with frequency and amplitude. One branch of these phase-varying backbone curves, S_1^{+v}, has a phase relationship varying from $\theta_d = \pi$ (the bifurcation on S_1^-) to asymptotically $\theta_d = \pi/2$, with the decrement of response frequency (along with the increment of displacement amplitude – see panel (a)). The embedded plots of panel (b), labelled $(i) \rightarrow (vi)$, present the time-parameterised responses of a selection of periodic motions on S_1^{+v}. It can be seen that the NNMs evolve from an anti-phase NNM ($\theta_d = \pi$ on the bifurcation) towards a clockwise out-of-unison NNM ($\theta_d = \pi/2$). Such a phase-varying behaviour can also be observed from the evolutions of displacement extrema of $q_1(t)$ and $q_2(t)$, denoted by '$\circ$' and '$\times$' respectively in the embedded plots. The other phase-varying backbone, S_1^{-v}, shows similar behaviours, except for having NNMs exhibiting anticlockwise motions.

In this section, the harmonic balance technique has been employed to find the analytical expressions of backbone curves for the single-mass system with symmetric and asymmetric configurations. Analytical study showed that the general asynchronous backbone curve, discussed in §4.2, exhibits an amplitude-dependent phase relationship between the linear modal coordinates. This backbone curve is termed as a phase-varying backbone curve, and it can be seen as an asymmetric evolution from the out-of-unison backbone curve through symmetry breaking. Such a backbone curve represents a novel family of nonlinear dynamic behaviours that are distinct from the commonly observed phase-fixed backbone curves. Its existence highlights the importance of determining phase relationships between modal coordinates when computing NNMs, a key implication of which is when applying harmonic balance method numerically to compute NNMs. In the next section, numerical analysis is carried out to investigate the existence of phase-varying backbone curves in a cable model.

4.4 Phase-varying backbone curves of a cable model

In previous discussions, the existence of phase-varying backbone curves has been identified analytically in a simple single-mass, two-mode system. In this section, the phase-varying behaviour is investigated by considering an engineering-relevant system – a nonlinear cable system.

Such a cable system is schematically shown in Fig. 4.6, where the cable profile is represented by a blue line; near one of the fixed ends, an additional elastic support connects the cable to the ground – this is analogous to the common practice of using a grounded device to suppress cable vibration. The dynamics of the cable system are modelled based on a lumped-mass approach, similar to the method in [247]. A brief description is given here for completeness.

The model is formulated by discretising the cable into N identical elastic elements, connected in series between $N+1$ nodes. The two end nodes are fixed, resulting in a total of $3(N-1)$ degrees of freedom in three-dimensional space. The mass of the cable is equally distributed between the elements, and for each element, half of its mass is lumped on either end. The elements are assumed to be undamped and linearly elastic.

Regarding the parameters, the cable has an unstretched length of L_0, uniform density ρ, Young's modulus E, and a constant cross-section of diameter d. Axial stress is assumed to be uniformly distributed over the cross-sectional area, and a static axial pre-tension with a horizontal component T is applied at both cable ends. The forces considered acting on the cable are due to gravity and elasticity, whilst viscous and aerodynamic effects are neglected. An additional undamped, linearly elastic element is attached to the cable at a position z_s along its span. This element lies within the cross-sectional plane,

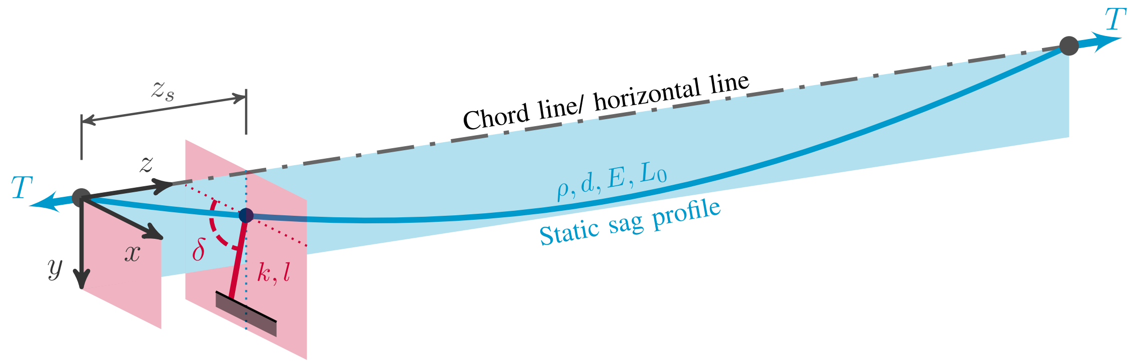

Fig. 4.6 A schematic diagram of a cable with an unstretched length of L_0, uniform density ρ, Young's modulus E, a constant cross-section of diameter d, and a static pre-tension applied at both ends with a horizontal component T. A physical coordinate system is defined at one end of the cable, with the (y, z) plane denoting the cable profile, where the z- and y-axis are in the direction of the chord line and the gravity respectively. An additional elastic support is attached to the cable at a position z_s along the cable span in the (x, y) plane, and it is modelled using a linear stiffness, k, and a support length, l, with δ indicating the angle between the support and the negative x-axis.

(x, y), at an angle δ from the horizontal. It has a length l, stiffness k, and is unstretched when the system is at equilibrium.

A 2-DOF nonlinear reduced-order model (ROM) of the cable system, which captures its salient dynamic behaviour near the first two natural frequencies, is obtained using a force-based indirect reduction method [106]. This involves a projection of the equations of motion of the full model, onto a 2-DOF reduced basis. The reduction/projection basis consists of the first out-of-plane and the first in-plane transverse mass-normalised linear modeshapes of the cable about its equilibrium position. As such, the equations of motion of the ROM can be written as

$$\ddot{q}_1 + \omega_{n1}^2 q_1 + f_1(q_1, q_2) = 0\,, \tag{4.14a}$$

$$\ddot{q}_2 + \omega_{n2}^2 q_2 + f_2(q_1, q_2) = 0\,, \tag{4.14b}$$

where f_1 and f_2 are the nonlinear restoring forces. For linear elastic finite element models with geometric nonlinearities, the forcing functions typically take the form of quadratic and cubic polynomials [106, 105, 112], i.e.

$$f_1(q_1, q_2) = \varXi_3 q_1^2 + 2\varXi_1 q_1 q_2 + \varXi_2 q_2^2 + \varPsi_4 q_1^3 + 3\,\varPsi_1 q_1^2 q_2 + \varPsi_3 q_1 q_2^2 + \varPsi_2 q_2^3\,, \tag{4.15a}$$

$$f_2(q_1, q_2) = \varXi_1 q_1^2 + 2\varXi_2 q_1 q_2 + \varXi_4 q_2^2 + \varPsi_1 q_1^3 + \varPsi_3 q_1^2 q_2 + 3\,\varPsi_2 q_1 q_2^2 + \varPsi_5 q_2^3\,. \tag{4.15b}$$

Note that linear dependencies are imposed on the coefficients in Eqs. (4.15), such that the energy in the system is conserved [112, 108], similar to Eqs. (4.4).

The linear properties in Eqs. (4.14) can be obtained directly through an eigenanalysis of the full system. However, the coefficients of the nonlinear terms, $\varXi_i$ and $\varPsi_i$, in Eqs. (4.15) are computed in a non-intrusive manner, using a set of static solutions of the lumped-mass model[3]. The static solutions are obtained by applying a set of prescribed static loads and computing the corresponding displacements. The selected loading cases consist of scaled linear combinations of the retained modes. For each load case, the computed static displacement of the full system is then projected onto the reduced modal space. Finally, the coefficients of the nonlinear terms in Eqs. (4.15) are estimated through regression analysis in a least-squares manner, using the modal force-modal displacement dataset.

The lumped-mass discretisation approach and subsequent reduction method are first validated by comparing the backbone curves of a ROM, with those obtained using an analytically derived dynamic model of a small-sag cable system, proposed in [232][4]. Here, for validation purposes, a 40-element, 117-DOF cable model with the following physical parameters is considered: $L_0 = 1.5\,\mathrm{m}$, $d = 5\,\mathrm{mm}$, $\rho = 3000\,\mathrm{kg\,m^{-3}}$, $E = 200\,\mathrm{GPa}$, and the cable is subjected to a static pre-tension with a horizontal component $T = 200\,\mathrm{N}$. Note that, in validating the reduced-order model, the additional support near the fixed end is not considered for the applicability of the analytical model. The modal coefficients obtained via the analytical method and order-reduction method are respectively given in Table 4.1. The backbone curves for the ROM, as well as that for the analytical model, are shown in Fig. 4.7 in the projection of response frequency, ω, against abolute modal displacement of the cable. The results show excellent agreement both in quantitative and qualitative, which demonstrates the applicability of the proposed reduced-order model.

Two additional support layouts are then considered to study the effect of symmetry breaking of the configuration – one corresponds to the case where the spring is aligned with the y-axis, i.e. when $\delta = 90°$, and this is denoted as the symmetric case; whilst, the other relates to the case where $\delta = 60°$, and this is denoted as the asymmetric case. Note that the static pre-tension is reduced to $T = 100\,\mathrm{N}$ to highlight the nonlinear significance induced by the sag cable profile; whilst other parameters remain the same

---

[3] Note that, even though the lumped-mass cable model is developed ad hoc, and the full equations of motion are known and accessible, these are not explicitly used to construct the reduced-order model as such. The indirect approach used instead, does not require knowledge of the exact equations of motion, and is applicable to finite element models built using commercial finite element software packages.

[4] The analytical model is applicable to highly stressed cables with a small weight-to-tension ratio, such that axial modal motions can be neglected.

Table 4.1 Comparison between the values of the estimated model parameters, using the analytical cable model in [232], and the 2-DOF reduced-order-model (ROM) via reduction method outlined in §4.4.

	ω_{n1}	ω_{n2}	Ξ_1	Ξ_2	Ξ_3	Ξ_4
cable model in [232]	122.04	123.87	$1.28 \cdot 10^6$	0	0	$3.84 \cdot 10^6$
2-DOF ROM	122.07	123.90	$1.28 \cdot 10^6$	$1 \cdot 10^{-8}$	$3 \cdot 10^{-8}$	$3.84 \cdot 10^6$
	Ψ_1	Ψ_2	Ψ_3	Ψ_4	Ψ_5	
cable model in [232]	0	0	$7.26 \cdot 10^9$	$7.24 \cdot 10^9$	$7.24 \cdot 10^9$	
2-DOF ROM	$3 \cdot 10^{-7}$	$1 \cdot 10^{-7}$	$7.26 \cdot 10^9$	$7.24 \cdot 10^9$	$7.24 \cdot 10^9$	

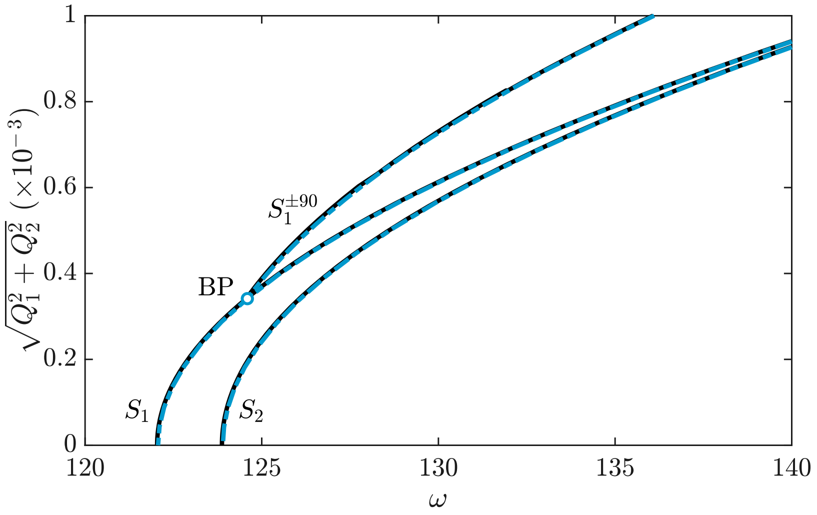

Fig. 4.7 Comparison between the backbone curves of the 2-DOF analytically derived model in [232] (solid black line), and those of the 2-DOF reduced-order model (dash-dotted blue line).

as that considered in validation process. The estimated parameters of either model can be found in Table 4.2. From this table, one can observe that the symmetric case has $\Psi_1 \approx 0$ and $\Psi_1 \approx 0$; whilst symmetry breaking leads to non-zero values, in line with the derivations given in §4.3.

For the symmetric case, the backbone curves of the 2-DOF nonlinear cable ROM are computed via numerical continuation and shown in Fig. 4.8*a* in the projection of response frequency, ω, against absolute physical displacement of the cable. Two single-mode backbone curves can be found, namely S_1 and S_2; via bifurcation point on the single-mode backbone curve, S_1, out-of-unison backbone curves, $S_1^{\pm 90}$, emerge. The phase relationships on these backbone curves are shown in Fig. 4.8*b* – either out-of-unison backbone curve exhibits a fixed phase relationship (represented by a straight line denoting

Table 4.2 Values of the estimated parameters of the reduced-order model for the symmetric and asymmetric cases.

	ω_{n1}	ω_{n2}	Ξ_1	Ξ_2	Ξ_3	Ξ_4
symmetric case	86.31	103.73	$2.72 \cdot 10^6$	$2 \cdot 10^{-6}$	$6 \cdot 10^{-6}$	$8.70 \cdot 10^6$
asymmetric case	87.71	102.76	$2.58 \cdot 10^6$	$6.22 \cdot 10^5$	$18.60 \cdot 10^5$	$8.43 \cdot 10^6$
	Ψ_1	Ψ_2	Ψ_3	Ψ_4	Ψ_5	
symmetric case	$6 \cdot 10^{-4}$	$1 \cdot 10^{-3}$	$8.18 \cdot 10^9$	$7.28 \cdot 10^9$	$9.72 \cdot 10^9$	
asymmetric case	$2.63 \cdot 10^8$	$3.64 \cdot 10^8$	$8.22 \cdot 10^9$	$7.44 \cdot 10^9$	$9.52 \cdot 10^9$	

either $\theta_d = \pm 90°$), the same as the out-of-unison branches for the single-mass system considered in §4.3.

A selection of NNMs (labelled by '+' signs in panels (a) and (b)) on S_1^{-90} are shown in panel (c) in the modal configuration space, $(q_1(t),\ q_2(t))$; and panel (d) in the physical configuration space, $(x_{\text{mid}}(t),\ y_{\text{mid}}(t))$, where $\bullet_{\text{mid}}$ denotes the mid-span position of the cable. The extrema of q_1 and x_{mid} are denoted via '$\circ$', whilst the extrema of q_2 and y_{mid} are denoted via '$\times$' to highlight the phase relationships. Due to the variation of tension in cable during oscillation, a non-resonant q_2 component arises from the nonlinear quadratic terms in expressions (4.15). This leads to a shift of the extrema $q_1(t)$, as well as $x_{\text{mid}}(t)$, along the backbone curve [245]; nonetheless, an anticlockwise out-of-unison (or equivalently $\theta_d = -90°$) phase relationship between q_1 and q_2 can still be observed in both panels (c) and (d) – analogues to the schematic in Fig. 4.1c. Likewise, similar behaviours can be expected for the other out-of-unison branch, S_1^{+90}, except for showing clockwise motions (or equivalently $\theta_d = +90°$).

For the asymmetric case, where the external support is attached to the cable with $\delta \neq 90°$, the backbone curves are shown in Fig. 4.9a. The corresponding phase relationships on these backbone curves are depicted in panel (b). Along with the breaking of symmetry, it leads the single-mode backbone curves, S_1 and S_2, to mixed-mode backbone curves, S_1^+ and S_2^-, respectively. The out-of-unison backbone curves, $S_1^{\pm 90}$, evolve to phase-varying backbone curves, $S_1^{\pm v}$, and remain bifurcating from the in-phase mixed-mode backbone curve S_1^+, similar to the single-mass model considered in §4.3. In this cable system, the phase-varying backbone curves exhibit phase relationship evolvutions from $\theta_d = 0$ (in-phase motions at the bifurcation) to $\theta_d \approx \pm\pi/2$ (nearly out-of-unison motions), as depicted in panel (b). To demonstrate the evolutions of responses, a selection of NNM motions (labelled '+' in panels (a) and (b)) are presented in the $(q_1(t),\ q_2(t))$ space in panel (c). Corresponding physical motions at the mid-span position of the cable are shown in panel (d), which again exhibit phase-varying behaviour. Such phase-varying

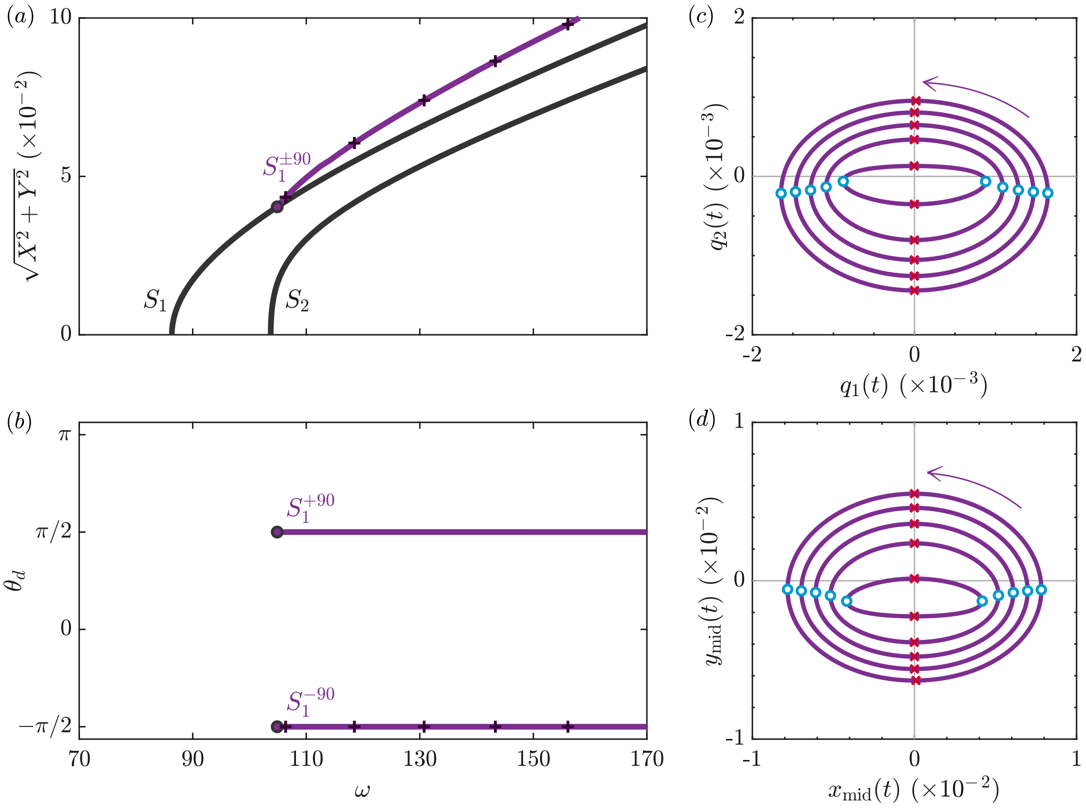

Fig. 4.8 Numerically computed backbone curves and NNM responses for the cable system in Fig. 4.6 with $\delta = 90°$, other modal parameters are listed in Table 4.2. (*a*) Backbone curves in the projection of the response frequency, ω, against the absolute displacement of the cable in the $(x,\, y)$ plane. (*b*) The phase difference between two modal coordinates of NNMs on the backbone curves. (*c*) and (*d*) The NNM responses on the out-of-unison backbone curve, S_1^{-90}, in the modal configuration space, $q_1(t)$ against $q_2(t)$, and physical configuration space, $x_{\mathrm{mid}}(t)$ against $y_{\mathrm{mid}}(t)$, respectively, where $\bullet_{\mathrm{mid}}$ denote the mid-span position. The extrema of $q_1(t)$ and $x_{\mathrm{mid}}(t)$ are labelled with '$\circ$'; whilst that of $q_2(t)$ and $y_{\mathrm{mid}}(t)$ are labelled with '$\times$'. Note that the arrows in panels (*c*) and (*d*) denote the anticlockwise motions. The motions of NNMs on the other out-of-unison backbone curve, S_1^{+90}, have the same trajectories but with clockwise motions.

behaviours can also be observed by tracking the evolutions of coordinate extrema, labelled '$\circ$' and '$\times$' in panels (*c*) and (*d*) – the '$\circ$' and '$\times$' are deviating from being superimposed (synchronous anti-phase motions) to spreading over (nearly out-of-unison motions).

In this section, the phase-varying behaviours have been identified in a nonlinear cable model. As a common practice aiming for vibration mitigation, the additional support near the cable end can break the symmetric configuration if its installation does not align with the vertical direction. The induced symmetry breaking transforms the whirling, or

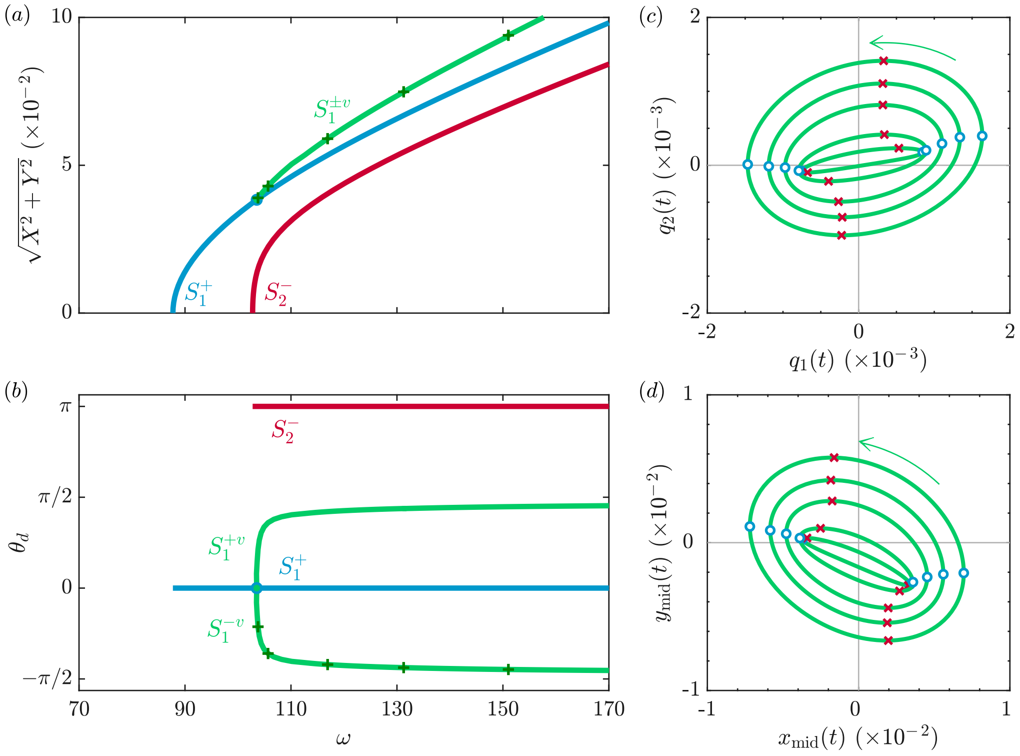

Fig. 4.9 Numerically computed backbone curves and NNM responses for the cable system in Fig. 4.6 with $\delta = 60°$, other modal parameters are listed in Table 4.2. (*a*) Backbone curves in the projection of the response frequency, ω, against the absolute displacement of the cable in (x, y) plane. (*b*) The phase difference between two modal coordinates of NNMs on the backbone curves. (*c*) and (*d*) The NNM responses on the phase-varying backbone curve, S_1^{-v}, in the projection of modal configuration space, $(q_1(t),\ q_2(t))$, and physical configuration space, $(x_{\mathrm{mid}}(t),\ y_{\mathrm{mid}}(t))$, respectively. The extrema of $q_1(t)$ and $x_{\mathrm{mid}}(t)$ are labelled with '$\circ$'; whilst the extrema of $q_2(t)$ and $y_{\mathrm{mid}}(t)$ are labelled with '$\times$'. The arrows in panels (*c*) and (*d*) denote the anticlockwise motions; the NNM responses on the other phase-varying backbone curve, S_1^{+v}, have the same trajectories but clockwise motions.

out-of-unison, motions into phase-varying motions as response amplitude and frequency varies. Similarly, whirling motions have been extensively observed in other mechanical systems, for example, a rotor-shaft system [238]; imperfections, non-uniform density, or degenerations can potentially cause asymmetry in configuration and lead to the existence of phase-varying behaviours. This mechanism highlights the importance of accounting for such dynamic features in engineering practice.

4.5 Summary

In this chapter, asynchronous NNMs, the counterpart of synchronous NNMs considered in Chapter 3, have been studied. The symmetry-breaking mechanism that underpins the existence of general asynchronous NNMs was investigated; a new class of nonlinear phenomenon, namely the phase-varying behaviours, was identified in conservative systems.

In §4.2, by revisiting the geometric features of synchronous and asynchronous NNMs, it was shown that the out-of-unison NNM (where the modal coordinates exhibit a ±90° phase difference) is a special case of a more general asynchronous NNM set where the phase relationships can be arbitrary values. Then, using a simple single-mass, two-mode system, it was demonstrated how the special out-of-unison case evolves to the general cases through symmetry breaking.

Building on these findings, in §4.3, an analytical study was employed to identify the mechanism that underpins the existence of general asynchronous NNMs from a symmetry-breaking perspective. With the breaking of symmetry, it was demonstrated that the out-of-unison backbone curve evolves to a branch with a varying phase relationship between modal components. The derived analytical phase expression revealed the mechanism that governs the varying phase – a phase-amplitude coupling. Such an NNM branch is thus defined as a *phase-varying backbone curve*, distinguishing from the commonly observed phase-fixed backbone curves. Its existence highlights the importance of determining phase relationships when computing NNMs.

In §4.4, the existence of phase-varying backbone curves was then investigated in a cable model, through the attachment of a near-cable-end support. The additional support breaks the symmetric cable configuration and causes the out-of-unison (whirling) NNMs to evolve to general asynchronous NNMs, and the correlated phase-varying behaviours. This demonstrates that these general asynchronous motions can exist in real engineering structures and highlights the significance of accounting for their existence and features in engineering practice.

Accompanying with Chapter 3, these two chapters have investigated synchronous and asynchronous backbone curves, with their correlated isolated and phase-varying backbone curves. Mechanisms underpinning these nonlinear behaviours have been obtained from a symmetry-breaking perspective via numerical and analytical studies. In these two chapters, the focus was on $1:1$ modal interactions where the response frequency between the interacting modes are the same. These special $1:1$ cases reflect important dynamic behaviours in many engineering systems, for example, the vibration suppression performance of a NLTMD, considered in Chapter 3, and the whirling motions of cable systems in this chapter.

However, many engineering systems also exhibit other types of internal resonances [36, 127, 41, 52]; the even more intricate cases lie in scenarios where a system may exhibit multiple types of internal resonances when it is vibrating at large amplitudes. Such intricate examples have been reported and highlighted in many engineering systems, even in simple two-mode systems [31, 104, 52], as discussed in §2.2.2.

In the following chapter, the current framework is further extended to a more general context to account for $m : n$ internal resonance between two modes for an arbitrary response frequency and amplitude range.

Chapter 5

Topological mappings of backbone curves

In this chapter:

- An analytical model is derived to study $m : n$ internal resonance of a symmetric two-mode system with an arbitrary natural frequency ratio for arbitrary response frequency and amplitude ranges.
- The effect of asymmetry on internal resonances is investigated from a symmetry-breaking perspective.
- Topologies of internal resonances are investigated by considering the convergence and divergence of correlated bifurcations; using these topological features, the existence of internal resonances is studied.
- A simulation-free method is proposed for efficient determination of the existence and locations of internal resonances.

Publications related to this work

- D. Hong, T. L. Hill, S. A. Neild, 2022. Existence and location of internal resonance of two-mode nonlinear conservative oscillators, *Proceedings of the Royal Society A: Mathematical, Physical and Engineering Sciences* 478 (2260) 20210659.

5.1 Introduction

As discussed in §2.1, nonlinear systems can exhibit intricate dynamic behaviours that have no counterparts in linear systems, for example, the targeted energy transfer [57, 146, 169], nonlinear sound synthesis [248, 249], isolated response curves (e.g. Chapter 3 and Refs. [203, 198, 141, 202]), and phase-varying behaviours (e.g. Chapter 4). These phenomena are characterised by interactions between modal components, and can be described via equations of motion with nonlinear terms that couple the modal motions.

In engineering practice, the existence of modal interactions, or internal resonance, can pose challenges in analysis and design of nonlinear systems, e.g. detecting isolas and isolated backbone curves [131, 132]; nontheless, their existence also gives rise to beneficial applications, such as energy converters [173, 174, 250], vibration suppression devices [133, 192, 190, 44] and sensitive signal processing filters [231, 24], as discussed in §2.3. Therefore, interpretating and quantifying internal resonances are topics that have attracted long-term attention in both research and engineering practice.

The presence of internal resonances can be related to the commensurate relationships between the *nonlinear response frequencies* of the interacting modes. This results in the established terminology of a $m : n$ internal resonance [33, 34], where $m : n$ denotes the frequency commensurability of modes. In this context, the cases studied in Chapters 3 and 4 are classed as $1 : 1$ internal resonance where the two interacting modes oscillate at the same response frequency. To determine the types of internal resonances for a given system, one can obtain an approximate estimate by referring to the ratio of *natural frequencies*, if the system is vibrating at *small* to *moderate* amplitudes when the frequency detuning due to nonlinearity is small. For example, a system with a natural frequency ratio of approximately $1 : 3$ is expected to exhibit a $1 : 3$ internal resonance. Extensive works, addressing particular types of internal resonances, can be found in a wide range of systems [127, 41, 38, 35, 251, 128].

In practice, fully exploiting the performance of nonlinear systems, or operating under extreme environments, may lead to large-amplitude responses. In this case, the small detuning condition is no longer satisfied and the analysis of internal resonance becomes challenging due to the necessity of access to the nonlinear frequency [111]. In addition, systems vibrating at large amplitudes can exhibit multiple types of internal resonances, even in a simple two-mode system, see Refs. [31, 104, 52]. Consequently, the determination of internal resonance is usually associated with computationally expensive numerical simulations. How to robustly and efficiently determine the existence and locations of internal resonances for an arbitrary system, regardless of the response frequency and amplitude range, needs to be further explored.

In addition to referring to commensurate frequency matches, an alternative method to characterise the internal resonance is employing a geometric perspective via the concept of NNMs. As introduced in §2.2.2 and extensively used in studies in Chapters 3 and 4, the NNM motions can be categorised as either synchronous or asynchronous responses [73, 74, 31]. In these two chapters, the synchronous and asynchronous motions, as well as their correlated isolated and phase-varying backbone curves, have been studied separately for the special $1:1$ resonant case. However, many interesting questions arising from previous studies are not yet addressed – what are the connections between those two geometrically different motions, why do they exhibit different bifurcation features under symmetry breaking, and how can those concepts be further extended to the general $m:n$ case? Answers to these questions are key in engineering practice because they uncover the mechanism that underpins the modal interactions and allows these nonlinear features to be quantitatively interpreted and reliably accounted for in analysis and design.

In this chapter, the existence and locations of internal resonances are investigated for large-amplitude vibrations of nonlinear systems with arbitrary eigenfrequency ratio. This chapter generalises the results obtained in previous chapters and establishes the relationships between synchronous motions (studied in Chapter 3) and asynchronous motions (considered in Chapter 4); in addition, studies in this chapter extend the analysis beyond $1:1$ internal resonances to $m:n$ cases. To achieve this, the rest of this chapter is organised as follows.

In §5.2, the motivating example of a pinned-pinned beam is first considered to demonstrate internal resonance in a common engineering system. The concept of NNMs is again revisited but the $1:1$ internal resonance, considered in previous chapters, is extended to general $m:n$ cases. Inspired by Rosenberg's geometric perspective (synchronous and asynchronous motions), the concept of NNMs is re-generalised by referring to the Fourier components of the interacting modes. This generalisation accounts for the geometric feature in the complex plane and provides a unique classification. In accordance with this generalisation, the terminology of *Fourier-real* and *Fourier-complex* NNMs are proposed. In addition, using this motivating example, the intricate topology of internal resonances is also presented, i.e. satisfying multiple frequency commensurate matches, and having two solution branches with almost identical amplitudes and response frequencies.

In order to interpret the internal resonances, and also to study their topological features, a general two-mode system with an arbitrary eigenfrequency ratio is considered in §5.3.

Firstly, an analytical model of internal resonances, in the neighbourhood of the primary backbone curve, is derived, which is approximately captured by Mathieu equation; the solution sets are associated with the Fourier-real and -complex generalisations, given in §5.2. Additionally, it is shown that these Fourier-real and -complex NNMs exist as pairs; for each pair, the interacting modes exhibit the same frequency commensurability but with different phase relationships. Next, considering the convergence and divergence of such NNM pairs, the topological evolutions of internal resonances are studied. Analytical formulas are derived, which reveal that the existence of internal resonance is governed by two parameter ratios: the eigenfrequency ratio and nonlinear coefficient ratio. This brings about a simulation-free method for efficient determination of the existence and locations of internal resonances.

In §5.4, the effect of symmetry breaking on internal resonance is investigated by accounting for both quasi-static and dynamic coupling mechanisms. The analytical derivation leads to a nonhomogenous extended Mathieu equation, whose solution sets are asymmetric evolutions of internal resonances from that obtained in §5.3. In the limit of an *asymmetric perturbation*, the symmetry-breaking effect is captured by a *nonhomogenous perturbation*, governing the bifurcation splitting/remaining phenomena for the internal resonance. This mechanism also underpins the different effects of symmetry breaking on Fourier-real and -complex NNMs, observed in previous chapters (for synchronous and asynchronous NNMs).

Finally, this chapter is closed with a summary in §5.5.

5.2 Internal resonances in two-mode systems

In this section, the two-mode conservative system with cubic nonlinearity is again considered. However, discussions herein are further extended to account for two interacting modes with an arbitrary natural frequency ratio that exhibit $m : n$ internal resonances. Such a two-mode system represents a generalisation of the special $1 : 1$ internally resonant cases considered in Chapters 3 and 4.

To account for this general case, the Lagrangian is re-written as

$$\mathcal{L} = \frac{1}{2}\dot{q}_r^2 + \frac{1}{2}\dot{q}_s^2 - \frac{1}{2}\omega_{nr}^2 q_r^2 - \frac{1}{2}\omega_{ns}^2 q_s^2 - \frac{1}{4}\Psi_4 q_r^4 - \Psi_1 q_r^3 q_s - \frac{1}{2}\Psi_3 q_r^2 q_s^2 - \Psi_2 q_r q_s^3 - \frac{1}{4}\Psi_5 q_s^4 , \quad (5.1)$$

where q_r and q_s denote linear modal displacements of two interacting modes, whose natural frequencies are ω_{nr} and ω_{ns} respectively, and Ψ_i are coefficients of nonlinear terms. Without loss of generality, the terminology, q_r and q_s, is used to denote internal resonances where q_r is the dominant mode, whilst q_s is the mode with which it resonates. In this context, the natural frequency ratio between q_r and q_s can be an arbitrary positive real value. Consequently, the modal interaction scenario, where q_r interacts with a *lower*-eigenfrequency q_s, is captured by an eigenfrequency ratio $\omega_{nr}/\omega_{ns} > 1$; whilst, the other scenario, where q_r interacts with a *higher*-eigenfrequency q_s, is denoted $\omega_{nr}/\omega_{ns} < 1$. Note that, when $q_r := q_1$ and $q_s := q_2$ and, assuming $1:1$ internal resonance, it reduces to the cases considered in Chapters 3 and 4.

Applying the Euler-Lagrange equation to the Lagrangian (5.1), the equations of motion can be obtained

$$\ddot{q}_r + \omega_{nr}^2 q_r + \varPsi_4 q_r^3 + 3\,\varPsi_1 q_r^2 q_s + \varPsi_3 q_r q_s^2 + \varPsi_2 q_s^3 = 0\,, \tag{5.2a}$$

$$\ddot{q}_s + \omega_{ns}^2 q_s + \varPsi_1 q_r^3 + \varPsi_3 q_r^2 q_s + 3\,\varPsi_2 q_r q_s^2 + \varPsi_5 q_s^3 = 0\,. \tag{5.2b}$$

Note that this two-mode model can also be derived from a continuous system using Galerkin's method with a two-mode truncation [36, 94] or reduce-order modelling techniques [109, 111]. Viewed as representative of many nonlinear systems, such a two-mode model has been extensively used in studies of modal interactions [36, 46, 137, 43, 192]. Here, a motivating example (a two-mode, pinned-pinned beam) is considered to demonstrate the intricate modal interactions between its first two modes, q_r and q_s. The coefficients of equations of motion (5.2), i.e. ω_{nr}, ω_{ns}, $\varPsi_1, \dots, \varPsi_5$, can be obtained by applying Galerkin's method to the governing equation of a von Kármán model, i.e.

$$\rho A \frac{\partial^2 w(x,t)}{\partial t^2} + EI \frac{\partial^4 w(x,t)}{\partial x^4} - T \frac{\partial^2 w(x,t)}{\partial x^2} = 0\,, \tag{5.3}$$

where ρ, A, E, I and T denote the density, cross-sectional area, Young's modulus, second moment of area and axial force of the beam, respectively, and where $w(x,t)$ represents the transverse displacement at axial position x at time t. As this system is used for illustration, rather than provide a detailed study on beam dynamics, derivations of the coefficients are not provided here; however, the interested reader is directed to Refs. [252, 52] or Appendix B for details.

Here, an example system with $\omega_{nr} = \pi^2$, $\omega_{ns} = 4\pi^2$, $\varPsi_1 = \varPsi_2 = 0$, $\varPsi_3 = 2\pi^4$, $\varPsi_4 = \pi^4/2$ and $\varPsi_5 = 8\pi^4$ is considered; a similar dimensionless example has been studied in [233, 52]. Note that, due to the symmetric configuration, such a beam system has $\varPsi_1 = \varPsi_2 = 0$. To study internal resonance, the NNM branches, or backbone curves, for the system are then computed via the `po`-toolbox of COCO [99], shown in Fig. 5.1*a*. The primary backbone

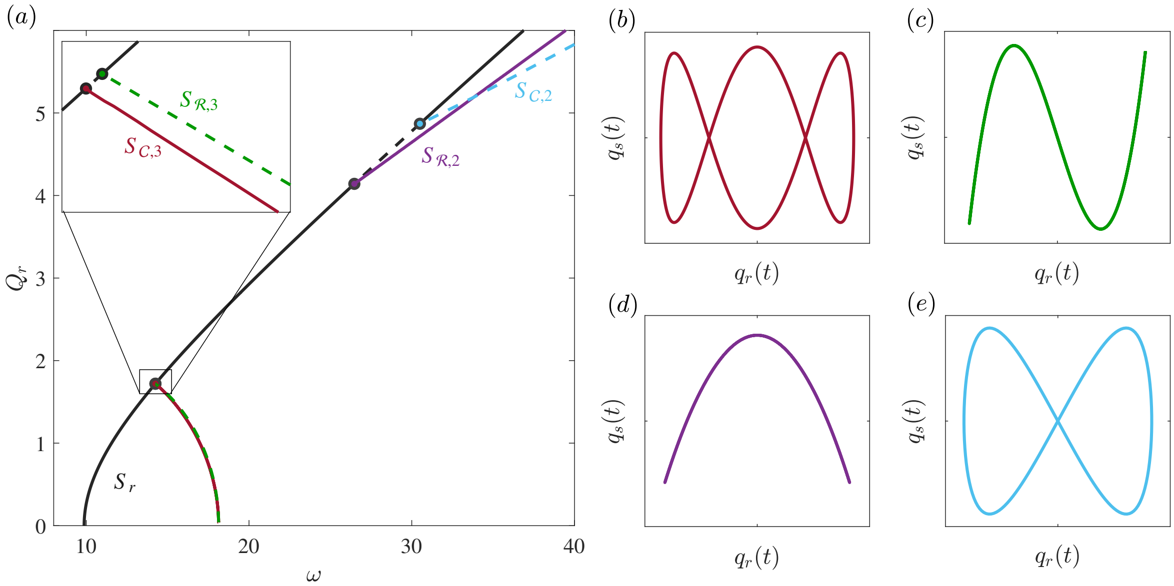

Fig. 5.1 Internal resonances of a two-mode pinned-pinned beam. (a) The backbone curves in the projection of response frequency, ω, against displacement amplitude of the first mode, Q_r. The stable and unstable segments are represented by solid and dashed lines repsectively. $(b) \to (e)$ The schematic time-parameterised responses, i.e. $q_r(t)$ against $q_s(t)$, of NNM solutions on backbone curves in panel (a).

curve, emerging from the first natural frequency, ω_{nr}, is shown as a black line. As this primary backbone curve contains only q_r, it can also be termed a single-mode backbone curve, denoted by S_r. Four other solution branches, containing both modal components, q_r and q_s, bifurcate from the single-mode branch via pitchfork bifurcations [252, 52], along with stability change of the primary backbone curve. These four mixed-mode backbone curves emerge due to modal interactions, or internal resonances, between q_r and q_s.

The periodic responses on these branches are depicted respectively in panels $(b) \to (e)$ in the configuration space, $(q_r(t),\ q_s(t))$. From the modal lines, or loops, in these plots, the commensurate frequency relationships between q_r and q_s can be determined to categorise the associated internal resonances. In this case, the dominant response frequency of the second mode, q_s, is an integer multiple of that of the first mode, q_r; for example, in panel (b), for every period of q_r response, q_s undergoes three periods of oscillation. As such, the observed internal resonance in panel (b) may be classified as a $1:3$ internal resonance; likewise, panel (c) also exhibits a $1:3$ resonance, whilst panels (d) and (e) capture $1:2$ internal resonances.

Table 5.1 Classification of NNMs by referring to Fourier components of q_r and q_s.

NNM type	**Fourier components of q_r and q_s**	**Examples**
Fourier-real NNM	q_r : real Fourier components; q_s : real Fourier components	Figs. 5.1*c* and 5.1*d*
Fourier-complex NNM	q_r : real Fourier components; q_s : complex Fourier components	Figs. 5.1*b* and 5.1*e*

As previously discussed in Chapters 3 and 4, these internal resonances can be alternatively specified by referring to Rosenberg's definition of NNMs, where panel (*c*) represents an in-unison, or synchronous, NNM [73, 74], as both modal coordinates reach their extrema and equilibrium simultaneously. Whilst the other panels, (*b*), (*d*) and (*e*), are asynchronous NNMs [31]. Combining these two terminologies, i.e. considering the commensurate frequency matches and the geometry in the configuration space, panels (*b*) and (*c*) are defined as 1 : 3 asynchronous and 1 : 3 synchronous NNMs respectively; however, panels (*c*) and (*d*) are both classified as 1 : 2 asynchronous NNMs. Having two geometrically different motions defined using the same terminology is certainly less than optimal.

To obtain a *unique* classification for each NNM, and also to capture their geometric features in the complex plane, the classification is reorganised by referring to the Fourier components of q_r and q_s. Here, a periodic response where both q_r and q_s are composed of real Fourier components (equivalently, consisting of only cosine components in the trigonometric sense) is defined as *a Fourier-real* NNM. Any Fourier-real NNM can be characterised by a *line* in the configuration space, e.g. panels (*c*) and (*d*). Whilst a periodic response where q_r is composed of real Fourier components and q_s is composed of complex Fourier components (equivalently consisting of sine components, or both sine and cosine components), is termed as *a Fourier-complex* NNM. In contrast to Fourier-real NNMs, any Fourier-complex NNM is depicted as a *loop* in the configuration space, for instance, panels (*b*) and (*e*). These definitions are summarised in Table 5.1.

Combining the frequency commensurability with the Fourier components of the two modes, these four NNM solutions, in panels (*b*), (*c*), (*d*) and (*e*), can be uniquely termed 1 : 3 Fourier-complex, 1 : 3 Fourier-real, 1 : 2 Fourier-real and 1 : 2 Fourier-complex NNMs, respectively; and their corresponding backbone curves are denoted by $S_{\mathcal{C},3}$, $S_{\mathcal{R},3}$, $S_{\mathcal{R},2}$ and $S_{\mathcal{C},2}$, where the subsripts $\bullet_{\mathcal{R}}$ and $\bullet_{\mathcal{C}}$ denote Fourier-*real* and -*complex* respectively, whilst the other subscript denotes the commensurate relationship between q_s and q_r. Note that, in this context, the NNMs considered in Chapters 3 and 4 can be termed 1 : 1 Fourier-real and -complex NNMs respectively; the backbone curves can be accordingly denoted $S_{\mathcal{R},1}$ and $S_{\mathcal{C},1}$.

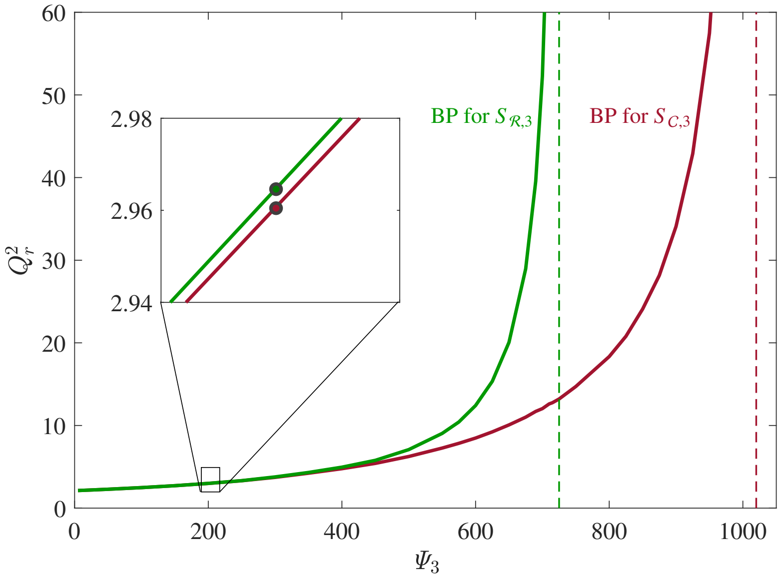

Fig. 5.2 Evolutions of the bifurcation points (BPs) that lead to 1 : 3 Fourier-real and -complex backbone curves, $S_{\mathcal{R},3}$ and $S_{\mathcal{C},3}$. The embedded plot presents the BPs for the beam system shown in Fig. 5.1.

In addition to showing multiple types of internal resonances, the 1 : 3 Fourier-real and -complex backbone curves, $S_{\mathcal{R},3}$ and $S_{\mathcal{C},3}$, in this case, are almost indistinguishable in panel (a), in contrast to the well-separated 1 : 2 branches, $S_{\mathcal{R},2}$ and $S_{\mathcal{C},2}$. To further study this case, evolutions of the bifurcation amplitudes with respect to varied Ψ_3 (with other parameters fixed) are shown in Fig. 5.2. As Ψ_3 increases, the amplitudes of the bifurcations grow, and two corresponding asymptotes can be observed, where the amplitudes of bifurcations grow asymptotically to infinity. Another limit is associated with $\Psi_3 \to +0$, when the amplitudes of two bifurcations converge to an identical finite value. As such, the coexistence of $S_{\mathcal{C},3}$ and $S_{\mathcal{R},3}$ can be expected when Ψ_3 is below the the values of asymptotes. The pinned-pinned beam case, studied above, has $\Psi_3 = 2\pi^4$, and the bifurcations are marked by dots in the embedded plot of Fig. 5.2. Shown in both Figs. 5.1a and 5.2, due to similarity in response frequencies and amplitudes, an extremely small step size is required in numerical continuation to distinguish the two 1 : 3 Fourier-real and -complex bifurcations as well as their associated mixed-mode backbone curves. This can result in expensive numerical computations even in a conceptually simple two-mode system.

In practice, NNMs have proved to be an efficient tool in capturing the fundamental features of internal resonances and offer a rigorous and robust concept for their analysis

[31, 100, 245]. To achieve this, the complete structure of NNMs must be found, otherwise the associated dynamics may go undetected. However, fulfilling such a requirement using numerical techniques requires significant computational effort and knowledge to ensure intricate internal resonances are fully captured, such as distinguishing the two 1 : 3 internal resonances in the example beam system. The following studies aim to efficiently predict internal resonances between two interacting modes with an arbitrary natural frequency ratio. To this end, an analytical framework is first used to derive internal resonances using NNM concepts; next, by investigating the bifurcation scenarios of these internal resonances, a simulation-free method to efficiently determine the types and locations of internal resonances is proposed.

5.3 Existence and interpretation of internal resonances

In this section, the general two-mode cases are considered, whilst the specific pinned-pinned beam system will be revisted to aid interpretation whenever necessary. Here, a symmetry-breaking perspective is employed to understand internal resonances, as previously employed in Chapters 3 amd 4. As such, the symmetric case where $\Psi_1 = \Psi_2 = 0$ is considered in this section; whilst the effect of symmetry breaking, i.e. $\Psi_1 \neq 0$ and $\Psi_2 \neq 0$, will be considered in §5.4.

With symmetry, the equations of motion (5.2) in the modal domain can be reduced to

$$\ddot{q}_r + \omega_{nr}^2 q_r + \Psi_4 q_r^3 + \Psi_3 q_r q_s^2 = 0\,, \tag{5.4a}$$
$$\ddot{q}_s + \omega_{ns}^2 q_s + \Psi_3 q_r^2 q_s + \Psi_5 q_s^3 = 0\,. \tag{5.4b}$$

As discussed in §5.2, without loss of generality, the scenario where internal resonances in the neighbourhood of S_r is considered. In this context, the internal resonance is captured by NNMs in which q_r is the dominant mode and q_s is the mode with which it is resonating. Consequently, it may be assumed that q_s is a smaller term when compared with q_r; this allows q_s^2 and q_s^3 to be considered as higher-order small terms, $\mathcal{O}(q_s^2)$. Using this representation, Eqs. (5.4) may be rearranged as

$$\ddot{q}_r + \omega_{nr}^2 q_r + \Psi_4 q_r^3 + \mathcal{O}(q_s^2) = 0\,, \tag{5.5a}$$
$$\ddot{q}_s + \omega_{ns}^2 q_s + \Psi_3 q_r^2 q_s + \mathcal{O}(q_s^2) = 0\,. \tag{5.5b}$$

For dynamical systems governed by these equations, trivial solutions, associated with $q_r = q_s = 0$, can be found with respect to static equilibrium. Whilst, non-trivial solutions can be found with respect to either $q_r \neq 0$ and $q_s = 0$ or $q_r \neq 0$ and $q_s \neq 0$, which describe the primary single-mode backbone curve and mixed-mode backbone curves respectively. For these non-trivial cases, solutions of q_r can be assumed as a sum of harmonic components, given by

$$q_r = \sum_{m=0}^{\infty} Q_{r,m} \cos(m\omega t), \tag{5.6}$$

where $Q_{r,m}$ and $m\omega$ denote the response amplitude and frequency of the m^{th} harmonic respectively. In evaluating q_r, previous chapters, as well as the literature, show that accounting for the leading-order term, i.e. the fundamental harmonic, can accurately capture the nonlinear behaviours [233, 139, 144, 137]. In this chapter, such a formulation is firstly employed, termed as having a *first-order accuracy* [30]; it captures the enssential nonlinear phenomena but discrepancies from exact solutions can be found when higher-order terms become significant. This limitation is then addressed by accounting for contributions from higher-order harmonics, termed as having a *higher-order accuracy*, which reveals an improved accuracy.

5.3.1 Formulation with a first-order accuracy

Here, a single-harmonic approximation is first considered by assuming that $q_r \approx Q_{r,1}\cos(\omega t)$, i.e. remaining the leading-order term of q_r. Combined with $q_s = 0$, single-mode backbone curves can be solved from Eqs. (5.5), i.e.

$$S_r(\omega, Q_{r,1}): \quad \omega^2 = \omega_{nr}^2 + \frac{3}{4}\Psi_4 Q_{r,1}^2. \tag{5.7}$$

Another non-trivial solution set, i.e. the mixed-mode backbone curves with $q_r \neq 0$ and $q_s \neq 0$, arises from internal resonances. Ignoring the contributions from higher-order small terms, $\mathcal{O}(q_s^2)$, namely, considering internal resonances in the neighbourhood of S_r, expressions for internal resonances can be obtained by substituting solutions of q_r, i.e. $q_r = Q_{r,1}\cos(\omega t)$, into Eq. (5.5b). After some algebraic manipulation, the internal resonances are found to be captured by the Mathieu equation, given by

$$\frac{\partial^2 q_s}{\partial \tau^2} + \left[\delta + \epsilon \cos(\tau)\right] q_s = 0, \tag{5.8}$$

where

$$\tau = 2\omega t, \qquad \delta = \frac{2\omega_{ns}^2 + \Psi_3 Q_{r,1}^2}{8\omega^2}, \qquad \epsilon = \frac{\Psi_3 Q_{r,1}^2}{8\omega^2}. \tag{5.9}$$

The Mathieu equation has been shown to be closely related to many nonlinear dynamic problems [253, 254]. It may be interpreted as the dynamics of a single degree-of-freedom system, q_s, with a parametric forcing (chracterised by coefficients δ and ϵ) acting on it [254]. In the context of internal resonances, when they are formulated with a first-order accuracy in the neighbourhood of the primary backbone curve, the equivalence between the internal resonances and the Mathieu equation is shown here. This offers a novel perspective to understand internal resonances – the dynamics of the internally resonant mode, q_s, with parametric forcing from the dominant mode, q_r. Note that, in §5.3.2, a formulation with a higher-order accuracy will be derived; it will be shown to connect to an extended Mathieu equation.

With an assumed solution for q_r, the dynamics of q_s are entirely determined by the two parameters, δ and ϵ. These parameters are functions of ω and $Q_{r,1}$, and hence will vary for different responses on the single-mode backbone curve, S_r. To solve this equation and find the expressions governing mixed-mode NNMs, the response of q_s is approximated using a sum of harmonics, i.e.

$$\begin{aligned} q_s &= Q_{sa,0} + \sum_{n=1}^{\infty} Q_{sa,n} \cos\left(n\omega t\right) + Q_{sb,n} \sin\left(n\omega t\right) \\ &= Q_{sa,0} + \sum_{n=1}^{\infty} Q_{sa,n} \cos\left(\frac{n}{2}\tau\right) + Q_{sb,n} \sin\left(\frac{n}{2}\tau\right), \end{aligned} \tag{5.10}$$

where $Q_{sa,n}$ and $Q_{sb,n}$ denote the amplitudes of the n^{th} cosine and sine harmonics, or equivalently real and complex Fourier components, respectively. It should be noted, unlike q_r that is assumed with a first-order approximation, q_s can be exactly captured by such a harmonic series. Substituting the assumed solutions (5.10) into Eq. (5.8), the harmonic components can be balanced to give four groups of equations [254]. These equation sets deal with unknown variables, $Q_{sa,n}$ and $Q_{sb,n}$, respectively, with n denoting either even or odd non-negative integers, $\mathbb{Z}^+$, i.e.

$1 : n$ Fourier-real NNMs for even n, $S_{\mathcal{R},n}$:

$$\begin{bmatrix} \delta & \epsilon/2 & 0 & \\ \epsilon & \delta - 1 & \epsilon/2 & \cdots \\ 0 & \epsilon/2 & \delta - 4 & \\ & \vdots & & \end{bmatrix} \begin{pmatrix} Q_{sa,0} \\ Q_{sa,2} \\ Q_{sa,4} \\ \vdots \end{pmatrix} = \mathbf{0}, \tag{5.11a}$$

$1:n$ Fourier-complex NNMs for even n, $S_{\mathcal{C},n}$:

$$\begin{bmatrix} \delta-1 & \epsilon/2 & 0 & \\ \epsilon/2 & \delta-4 & \epsilon/2 & \cdots \\ 0 & \epsilon/2 & \delta-9 & \\ & \vdots & & \end{bmatrix} \begin{pmatrix} Q_{sb,2} \\ Q_{sb,4} \\ Q_{sb,6} \\ \vdots \end{pmatrix} = \mathbf{0}, \tag{5.11b}$$

$1:n$ Fourier-real NNMs for odd n, $S_{\mathcal{R},n}$:

$$\begin{bmatrix} \delta-1/4+\epsilon/2 & \epsilon/2 & 0 & \\ \epsilon/2 & \delta-9/4 & \epsilon/2 & \cdots \\ 0 & \epsilon/2 & \delta-25/4 & \\ & \vdots & & \end{bmatrix} \begin{pmatrix} Q_{sa,1} \\ Q_{sa,3} \\ Q_{sa,5} \\ \vdots \end{pmatrix} = \mathbf{0}, \tag{5.11c}$$

$1:n$ Fourier-complex NNMs for odd n, $S_{\mathcal{C},n}$:

$$\begin{bmatrix} \delta-1/4-\epsilon/2 & \epsilon/2 & 0 & \\ \epsilon/2 & \delta-9/4 & \epsilon/2 & \cdots \\ 0 & \epsilon/2 & \delta-25/4 & \\ & \vdots & & \end{bmatrix} \begin{pmatrix} Q_{sb,1} \\ Q_{sb,3} \\ Q_{sb,5} \\ \vdots \end{pmatrix} = \mathbf{0}. \tag{5.11d}$$

Nontrivial solutions to these four equation sets represent dynamic responses in q_s (the unknown variables), triggered by the response of q_r (the elements in matrices). Considering equation set (5.11a) for example, any q_s solution is composed of a series of cosine components, whose response frequencies are even multiples of that of q_r, as indicated by the unknown vector elements, $Q_{sa,0}$, $Q_{sa,2}$, $\cdots$. Recalling $q_r \approx Q_{r,1}\cos(\omega t)$, both q_r and q_s are composed of cosine components; thus, solutions to equation set (5.11a) are $1:n$ Fourier-real NNMs for even n, e.g. the $1:2$ Fourier-real NNM shown in Fig. 5.1*d*. Likewise, solutions to equation sets (5.11b), (5.11c) and (5.11d) denote $1:n$ Fourier-complex (even n), $1:n$ Fourier-real (odd n), and $1:n$ Fourier-complex (odd n) NNMs, respectively; corresponding examples are shown in Figs. 5.1*e*, 5.1*c* and 5.1*b*.

As discussed in §5.2 for the symmetric system, the existence of internal resonances is captured by solution branches that emerge from the primary backbone curve and lead to stability change of the primary branch. To determine the stability-change bifurcations, and the existence of internal resonances, Hill's method is used [254]. The so-called Hill's method can determine the stability of responses by referring to determinants of the four coefficient matrices in Eqs. (5.11); as such, these determinants are also termed Hill's determinants. Using Hill's method in determining stability yields the equivalent results as those found using Floquet exponents [255]. Once the bifurcation on the primary backbone curve is determined, the unknown internally resonant components in the neighbourhood of that bifurcation can be solved from Eq. (5.11). It should also be noted that zero determinants are conditions to obtain non-trivial solutions.

In Fig. 5.3, the stability boundaries (where the stability changes) are computed via zero determinants and shown as coloured solid lines in the $(\delta,\ \epsilon)$ space, with unstable regions shaded in colour. It should be highlighted that these boundaries are computed with respect to δ and ϵ – parameters that govern the dynamics of the approximated modal interactions, given by Eq. (5.8). Without assuming any specific parameters of the system, these boundaries capture the stability change, and consequently the bifurcations emerging from internal resonance, for *arbitrary* systems. Using interpretations of the four equation sets (5.11), the stability boundaries are denoted with the correlated types of bifurcated NNMs and labelled $\mathcal{B}_{\mathcal{R},n}$ and $\mathcal{B}_{\mathcal{C},n}$. Note that this diagram is equivalent to the Ince-Strutt diagram, or Arnold tongues, which has been widely used to study the stability of dynamical systems [253, 235]. In the context considered here, i.e. internal resonances between two modes, this Ince-Strutt diagram is equivalent to a formulation generated to a first-order of accuracy.

In this space, using expressions (5.9), the primary backbone curve, defined by Eq. (5.7), can be mapped as a linear function with variables δ and ϵ, written as

$$S_r(\omega,\ Q_{r,1}) \mapsto S_r(\delta,\ \epsilon) : \epsilon = \frac{2\,\Psi_3\omega_{nr}^2}{2\,\Psi_3\omega_{nr}^2 - 3\,\Psi_4\omega_{ns}^2}\delta - \frac{\Psi_3\omega_{ns}^2}{2\,(2\,\Psi_3\omega_{nr}^2 - 3\,\Psi_4\omega_{ns}^2)}, \tag{5.12}$$

where

$$\delta \in \left[\frac{\omega_{ns}^2}{4\omega_{nr}^2},\ \frac{\Psi_3}{6\,\Psi_4}\right) \text{ and } \epsilon \in \left[0,\ \frac{\Psi_3}{6\,\Psi_4}\right). \tag{5.13}$$

This means that the primary backbone curve, S_r, is a *straight line* with a finite length – it emerges at coordinate $\left(\omega_{ns}^2/(4\omega_{nr}^2),\ 0\right)$ with a zero amplitude at its natural frequency, ω_{nr}, and asymptotically approaches the coordinate $(\Psi_3/(6\,\Psi_4),\ \ \Psi_3/(6\,\Psi_4))$ as the response amplitude and frequency increase.

By mapping the backbone curve to the $(\delta,\ \epsilon)$ space, the intersections between S_r and the stability boundaries ($\mathcal{B}_{\mathcal{R},n}$ and $\mathcal{B}_{\mathcal{C},n}$) represent pitchfork bifurcations, which lead to

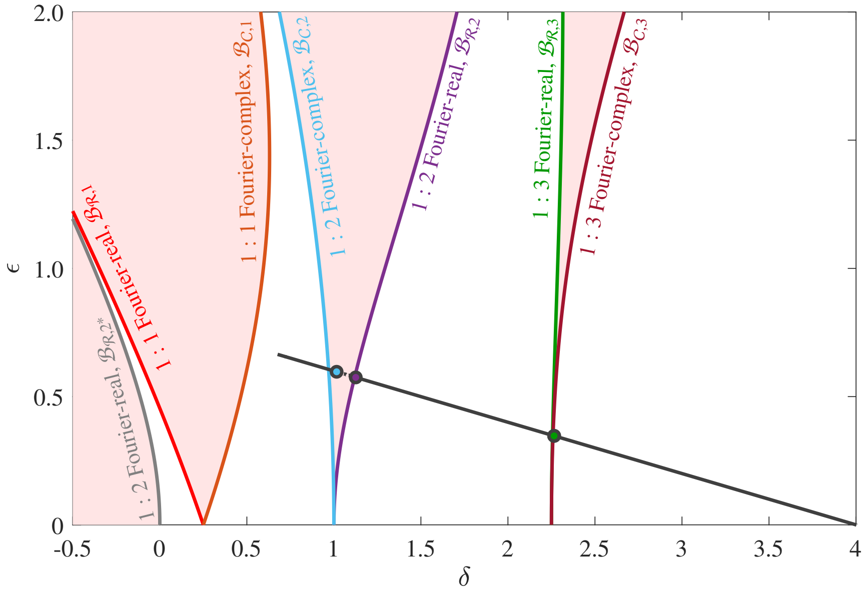

Fig. 5.3 Determining the existence and locations of internal resonances. The stability boundaries, representing the collections of bifurcations on S_r for arbitrary two-mode systems, are labelled with the types of bifurcated mixed-mode backbone curves. The first single-mode backbone curve for the pinned-pinned beam system, studied in §5.2, is computed via numerical continuation and projected as a straight line with a finite length, on which the bifurcations are marked by solid dots.

mixed-mode backbone curves of the labelled types, along with stability changes on S_r. For example, the first single-mode backbone curve of the two-mode beam system, considered in §5.2, is computed via numerical continuation and mapped as a straight line in Fig. 5.3. The bifurcations are marked by dots, which approximately lie on the stability boundaries, capturing the existence of internal resonances that are observed in the system – see Fig. 5.1. There are some small discrepancies between the numerically solved bifurcations and the analytically defined stability boundaries, especially at higher amplitudes. This is because the stability boundaires, presented here, are computed with a first-order approximation, which only accounts for contributions from the fundamental component in q_r; whilst, as amplitude increases, the contributions from harmonics become more significant. To improve the accuracy, a formulation with a higher-order approximation is required by accounting for the harmonic contributions, derived in the following.

5.3.2 Formulation with a higher-order accuracy

To account for harmonic contributions in modal interactions between q_r and q_s, a formulation considering two harmonics in q_r is derived (termed as having a second-order-accuracy [30]). The accuracy of this formulation is then compared with the first-order formulation, derived in the previous section.

Unlike the formulation given in §5.3.1, where q_r is approximated by its fundamental component, here, q_r is assumed as a sum of two harmonics, e.g. the first and third harmonics[1],

$$q_r = Q_{r,1}\cos(\omega t) + Q_{r,3}\cos(3\omega t), \tag{5.14}$$

where $Q_{r,3}$ denotes the amplitude of the third harmonic, which may be assumed small when compared with the fundamental component, $Q_{r,1}$; as such, $Q_{r,3}^2$ and $Q_{r,3}^3$ may be considered as higher-order small terms, $\mathcal{O}(Q_{r,3}^2)$.

To find the expressions of mixed-mode NNMs that emerge from internal resonance, the assumed solution (5.14) is substituted into Eq. (5.5b). Next, the contributions from higher-order small terms, $\mathcal{O}(q_2^2)$ and $\mathcal{O}(Q_{r,3}^2)$ is neglected, namely considering internal resonance in the neighbourhood of the primary backbone curve, S_r. Consequently, after some algebraic manipulation, the mixed-mode responses are written as

$$\frac{\partial^2 q_s}{\partial \tau^2} + \left[\tilde{\delta} + \tilde{\epsilon}_1\cos(\tau) + \tilde{\epsilon}_2\cos(2\tau)\right] q_s = 0, \tag{5.15}$$

where

$$\tau = 2\omega t,\ \tilde{\delta} = \frac{2\omega_{ns}^2 + \Psi_3 Q_{r,1}^2}{8\omega^2},\ \tilde{\epsilon}_1 = \frac{\Psi_3\left(Q_{r,1}^2 + 2Q_{r,1}Q_{r,3}\right)}{8\omega^2}\ \text{and}\ \tilde{\epsilon}_2 = \frac{\Psi_3 Q_{r,1}Q_{r,3}}{4\omega^2}, \tag{5.16}$$

Compared to Eq. (5.8) (with a first-order approximation), expression (5.15) represents an extended Mathieu equation with an additional term characterised by coefficient $\tilde{\epsilon}_2$. To find the mixed-mode solutions for Eq. (5.15), harmonic balance technique is again used. Assuming q_s as a sum of harmonic components, i.e. expression (5.10), and stubstituting the assumed solution into Eq. (5.15), the harmonic components can be balanced to give four solution sets (similar to the formulation with a first-order accuracy), namely

1 : n Fourier-real NNMs for even n, $S_{\mathcal{R},n}$:

---

[1] Note that this assumed solution is considered here as an example, similar formulations can be obtained if other harmonics are accounted for.

$$\begin{bmatrix} \tilde{\delta} & \tilde{\epsilon}_1/2 & \tilde{\epsilon}_2/2 & 0 & \\ \tilde{\epsilon}_1 & \tilde{\delta}-1+\tilde{\epsilon}_2/2 & \tilde{\epsilon}_1/2 & \tilde{\epsilon}_2/2 & \cdots \\ \tilde{\epsilon}_2 & \tilde{\epsilon}_1/2 & \tilde{\delta}-4 & \tilde{\epsilon}_1/2 & \\ 0 & \tilde{\epsilon}_2/2 & \tilde{\epsilon}_1/2 & \tilde{\delta}-9 & \\ & & \vdots & & \end{bmatrix} \begin{pmatrix} Q_{sa,0} \\ Q_{sa,2} \\ Q_{sa,4} \\ Q_{sa,6} \\ \vdots \end{pmatrix} = \mathbf{0}, \tag{5.17a}$$

$1:n$ Fourier-complex NNMs for even n, $S_{\mathcal{C},n}$:

$$\begin{bmatrix} \tilde{\delta}-1-\tilde{\epsilon}_2/2 & \tilde{\epsilon}_1/2 & \tilde{\epsilon}_2/2 & 0 & \\ \tilde{\epsilon}_1/2 & \tilde{\delta}-4 & \tilde{\epsilon}_1/2 & \tilde{\epsilon}_2/2 & \cdots \\ \tilde{\epsilon}_2/2 & \tilde{\epsilon}_1/2 & \tilde{\delta}-9 & \tilde{\epsilon}_1/2 & \\ 0 & \tilde{\epsilon}_2/2 & \tilde{\epsilon}_1/2 & \tilde{\delta}-16 & \\ & & \vdots & & \end{bmatrix} \begin{pmatrix} Q_{sb,2} \\ Q_{sb,4} \\ Q_{sb,6} \\ Q_{sb,8} \\ \vdots \end{pmatrix} = \mathbf{0}, \tag{5.17b}$$

$1:n$ Fourier-real NNMs for odd n, $S_{\mathcal{R},n}$:

$$\begin{bmatrix} \tilde{\delta}-1/4+\tilde{\epsilon}_1/2 & \left(\tilde{\epsilon}_1+\tilde{\epsilon}_2\right)/2 & \tilde{\epsilon}_2/2 & 0 & \\ \left(\tilde{\epsilon}_1+\tilde{\epsilon}_2\right)/2 & \tilde{\delta}-9/4 & \tilde{\epsilon}_1/2 & \tilde{\epsilon}_2/2 & \cdots \\ \tilde{\epsilon}_2/2 & \tilde{\epsilon}_1/2 & \tilde{\delta}-25/4 & \tilde{\epsilon}_1/2 & \\ 0 & \tilde{\epsilon}_2/2 & \tilde{\epsilon}_1/2 & \tilde{\delta}-49/4 & \\ & & \vdots & & \end{bmatrix} \begin{pmatrix} Q_{sa,1} \\ Q_{sa,3} \\ Q_{sa,5} \\ Q_{sa,7} \\ \vdots \end{pmatrix} = \mathbf{0}, \tag{5.17c}$$

$1:n$ Fourier-complex NNMs for odd n, $S_{\mathcal{C},n}$:

$$\begin{bmatrix} \tilde{\delta}-1/4-\tilde{\epsilon}_1/2 & \left(\tilde{\epsilon}_1-\tilde{\epsilon}_2\right)/2 & \tilde{\epsilon}_2/2 & 0 & \\ \left(\tilde{\epsilon}_1-\tilde{\epsilon}_2\right)/2 & \tilde{\delta}-9/4 & \tilde{\epsilon}_1/2 & \tilde{\epsilon}_2/2 & \cdots \\ \tilde{\epsilon}_2/2 & \tilde{\epsilon}_1/2 & \tilde{\delta}-25/4 & \tilde{\epsilon}_1/2 & \\ 0 & \tilde{\epsilon}_2/2 & \tilde{\epsilon}_1/2 & \tilde{\delta}-49/4 & \\ & & \vdots & & \end{bmatrix} \begin{pmatrix} Q_{sb,1} \\ Q_{sb,3} \\ Q_{sb,5} \\ Q_{sb,7} \\ \vdots \end{pmatrix} = \mathbf{0}. \tag{5.17d}$$

With these equation sets, the stability boundaries, capturing bifurcations to mixed-mode solutions, can be found via Hill's diterminants, similar to discussions in §5.3.1. However, with the formulation of a higher-order accuracy, these boundaries are functions of $\tilde{\delta}$, $\tilde{\epsilon}_1$ and $\tilde{\epsilon}_2$ – see matrices of Eqs. (5.17). As such, any primary backbone curve is a three dimensional line with a finite length in the $(\tilde{\delta},\ \tilde{\epsilon}_1,\ \tilde{\epsilon}_2)$ space; its intersections with the stability boundaries denote pitchfork bifurcations that lead to correlated mixed-mode backbone curves.

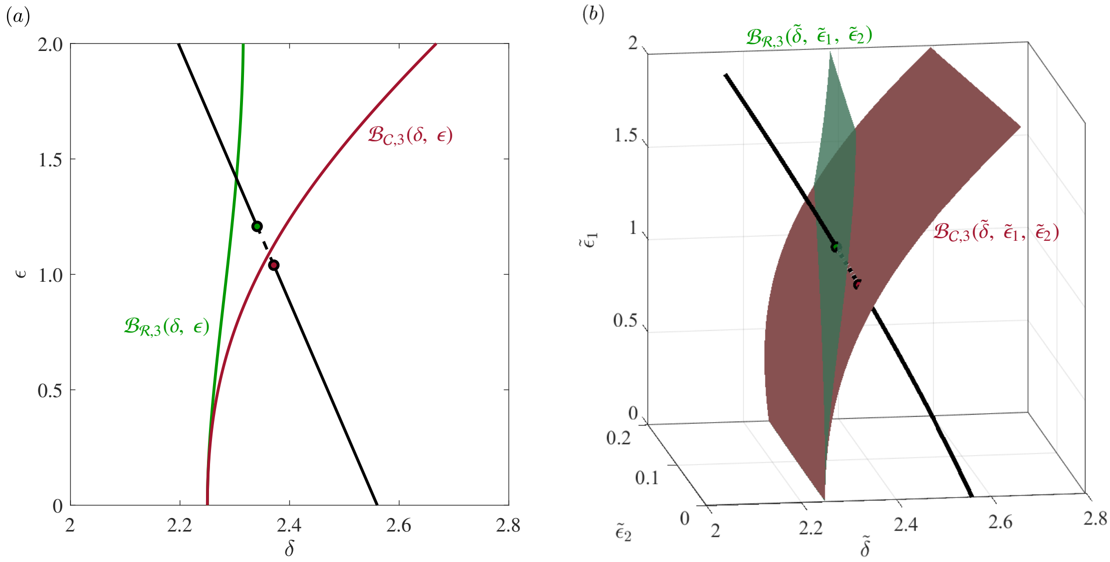

Fig. 5.4 Comparing the predicted results using formulations of a first-order accuracy (panel (*a*)) and a second-order accuracy (panel (*b*)) for a system with $\omega_{nr} = 1$, $\omega_{ns} = 3.2$, $\varPsi_3 = 13$ and $\varPsi_4 = 1$.

Here, an example system with $\omega_{nr} = 1$, $\omega_{ns} = 3.2$, $\varPsi_3 = 13$ and $\varPsi_4 = 1$ is considered. The primary backbone curve, S_r, is computed via numerical continuation and mapped to the $(\delta,\ \epsilon)$ space via Eq. (5.12), shown in Fig. 5.4*a*. It can be observed that the existence of bifurcations is captured, whilst, with discrepancies between numerically solved bifurcations and analytically approximated stability boundaries. Such discrepancies arise due to neglecting harmonic contributions in q_r in derivations with a first-order approximation. For comparison, the numerically computed S_r is also mapped to the $(\tilde{\delta},\ \tilde{\epsilon}_1,\ \tilde{\epsilon}_2)$ space via Eq. (5.16), shown in Fig. 5.4*b*. It clearly shows an improved accuracy, where a great agreement can be observed between the bifurcations and the stability boundaries (the bifurcations are accurately on the boundaries surfaces).

In summary, compared to the formulation with a first-order accuracy, accounting for the harmonic contributions of q_r revealed improved accuracy. In the higher-order-accuracy case, the internal resonances in the neighbourhood of the primary backbone curve are captured by an *extended Mathieu equation*. Derivations in this section also showed that the inclusion of one additional harmonic leads to an extra term in the extended Mathieu equation and an extra parameter in describing stability boundaries. Consequently, the formulation with a second-order approximation results in a three-dimensional parameter space, shown in Fig. 5.4*b*. In addition, in this three-dimensional space, the primary

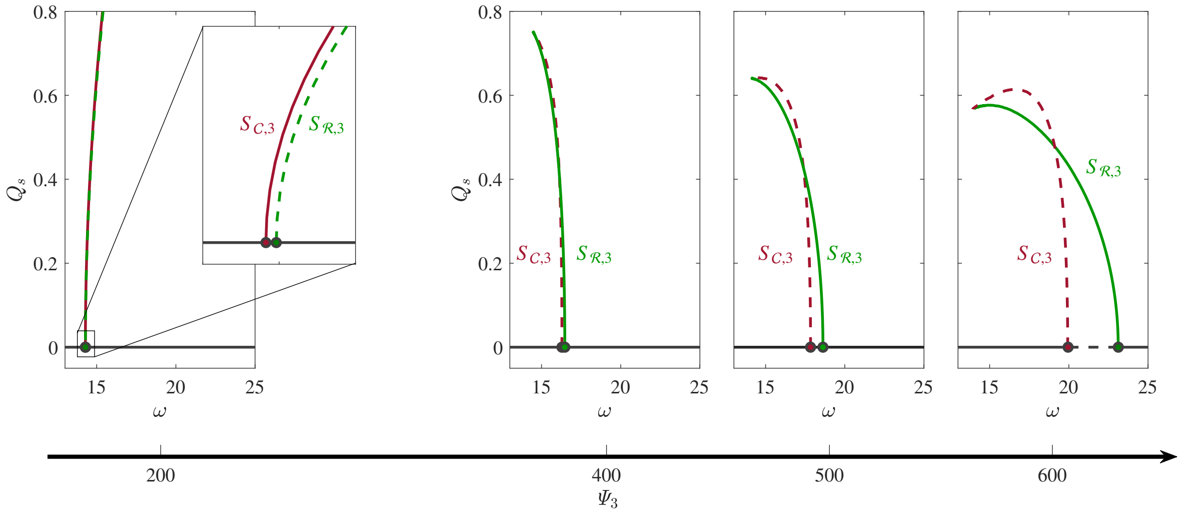

Fig. 5.5 Convergence of bifurcations and backbone curves ememging from internal resonances. The embedded plots show evolutions of $S_{\mathcal{R},3}$ and $S_{\mathcal{C},3}$ for a two-mode system with $\omega_{ns}/\omega_{nr} = 4$, $\Psi_4 = \pi^4/2$ and a varied Ψ_3, in the projection of response frequency, ω, against amplitude of q_s.

backbone curve is a three-dimensional line with curvature, rather than the straight line in the two-dimensional space, $(\delta,\ \epsilon)$, for the first-order-accuracy formulation.

Even though there are small discrepancies using the first-order-accuracy formulation, the essential topologies of internal resonances are captured, and it provides an efficient method for determining internal resonance due to the simple geometry of the primary backbone curve (a straight line with a finite length) in the $(\delta,\ \epsilon)$ space. As such, in the following discussions, the formulation of a first-order accuracy will be employed for simplicity. Using this method, the existence of internal resonances will be further investigated to understand their topological features.

5.3.3 Topologies of internal resonances: the converging behaviour

As discussed in §5.3.1, the formulation of a first-order accuracy yields stability boundaries in the $(\delta,\ \epsilon)$ space, i.e. Fig. 5.3. In this figure, the $1 : n$ Fourier-real and -complex boundaires, $\mathcal{B}_{\mathcal{R},n}$ and $\mathcal{B}_{\mathcal{C},n}$, exist as a pair, and those two boundaries share an identical solution in the limit of $\epsilon \to 0$, i.e. the horizontal axis. Recalling that any stability boundary represents a collection of bifurcations, the coalescence of a boundary pair indicates the convergence of two bifurcations, as already observed with the limit of $\Psi_3 \to 0$ for the two-mode beam system in Fig. 5.2.

Here, taking the $1:3$ internal resonance as an example, the converging behaviour is further investigated. Shown in Fig. 5.5, the evolutions of bifurcations and backbone curves, $S_{\mathcal{R},3}$ and $S_{\mathcal{C},3}$, are presented with respect to a varied Ψ_3 for a system with $\omega_{ns}/\omega_{nr} = 4$, $\Psi_4 = \pi^4/2$. Four example cases are shown in the embedded plots where the backbone curves are in the projection of response frequency, ω, against the displacement amplitude of q_s. It can be observed that the bifurcations converge as Ψ_3 decreases; likewise, the two correlated mixed-mode backbone curves, $S_{\mathcal{R},3}$ and $S_{\mathcal{C},3}$, also converge.

Considering the limit of $\Psi_3 \to 0$, $S_{\mathcal{R},3}$ and $S_{\mathcal{C},3}$ share *identical amplitudes and response frequencies* – this can also be analytically derived from Eqs. (5.11c) and (5.11d), where the coefficient matrices are identical as $\Psi_3 \to 0$. In contrast, as indicated by the subscripts of the unknown variables for Eqs. (5.11c) and (5.11d), these two mixed-mode solutions contain different types of Fourier components in q_s, namely real and complex Fourier components respectively. One can recall that having different types of Fourier components in q_s indicates different phase relationships between q_r and q_s. Having identical coefficient matrices but different unknown variables, the solution (a mixed-mode NNM) to Eqs. (5.11c) and (5.11d) exhibits the same determined response amplitude and frequency but *undetermined phase relationships* between interacting modes – either Fourier-real or -complex. Consequently, in this limit case, the $1:3$ internal resonances are captured by NNMs with *unlocked* phase relationships, representing resonances that are rarely observed in the presence of damping and external forcing, as a significant amount of energy is required to perturb the NNMs to forced responses [143, 140].

This feature can be alternatively observed from equations of motion (5.4), which reduce to two *uncoupled* Duffing's oscillators when $\Psi_3 \to 0$ (as Ψ_3 is the only coupling parameter for the symmetric case). For these two uncoupled oscillators, the converged solutions represent motions where q_r and q_s are vibrating with the same amplitude and a constant response frequency ratio, yet independently rather than interactionally as they are not constrained by a specific phase relationship. Similar converging behaviours and phase-unlocking NNMs can also be observed for other $1:n$ internal resonances.

5.3.4 Topologies of internal resonances: topological divisions

In previous discussions, it is shown that the intricate internal resonances for the pinned-pinned beam example, see Fig. 5.1, are well captured by the proposed method, as shown in Fig. 5.3. This reduces the identification of internal resonances from computationally expensive simulations to an efficient graphical check. Note that such an intricate topology of internal resonances is not unique to this special example but has been reported in many other systems [31, 104, 52]. In addition to determining the existence of internal resonances, quantifying the resonant features (such as the response amplitude and frequency) are also of importance in understanding and optimising the system dynamics, allowing for example the exploitation or elimination of internal resonances. In the following, by considering the evolutions of internal resonances, it will be shown how the proposed method can be used to meet these needs.

First, it can be found that the axes of the $(\delta,\ \epsilon)$ space, defined by Eqs. (5.9), are functions of the system states and coefficients; as such, stability boundaries in this space cannot provide direct physical interpretations of the internal resonances, for example, locations of the correlated bifurcations. To address this, the stability boundaries, shown in Fig. 5.3, are remapped from the $(\delta,\ \epsilon)$ space to the $\left(\Psi_3/\Psi_4,\ Q_{r,1}^2\right)$ space, where Ψ_3/Ψ_4 denotes the system parameters, whilst $Q_{r,1}^2$ captures the response amplitude of q_r. Using expressions (5.7) and (5.9), the projection is defined as

$$\begin{gathered}\mathcal{B}_{\mathcal{R},n}(\delta,\ \epsilon) \mapsto \mathcal{B}_{\mathcal{R},n}(\Psi_3/\Psi_4,\ Q_{r,1}^2) \quad \text{or} \quad \mathcal{B}_{\mathcal{C},n}(\delta,\ \epsilon) \mapsto \mathcal{B}_{\mathcal{C},n}(\Psi_3/\Psi_4,\ Q_{r,1}^2): \\ \frac{\Psi_3}{\Psi_4} = \frac{6\epsilon\omega_{ns}^2}{\omega_{ns}^2 - 4\omega_{nr}^2\left(\delta-\epsilon\right)},\ Q_{r,1}^2 = \frac{4\left(\epsilon-\delta\right)\omega_{nr}^2 + \omega_{ns}^2}{3\,\Psi_4\left(\delta-\epsilon\right)}.\end{gathered} \tag{5.18}$$

Note that, using this projection, the physical interpretations of mixed-mode backbone curves, emerging from internal resonances, can be directly captured via axes of the space they mapped to.

The case where $\omega_{nr} < \omega_{ns}$

First, the case where $\omega_{nr} < \omega_{ns}$ is considered to study internal resonances that the dominant mode, q_r, is interacting with a *higher*-eigenfrequency mode, q_s. With $\omega_{ns}/\omega_{nr} = 4$ and $\Psi_4 = \pi^4/2$, using Eq. (5.18) gives the remappings of the stability boundaries, $\mathcal{B}_{\mathcal{R},n}$ and $\mathcal{B}_{\mathcal{C},n}$, from Fig. 5.3 to Fig. 5.6*a*. For any system with a given Ψ_3/Ψ_4, the primary backbone curve emerging from natural frequency, ω_{nr}, is a vertical line in this space; and as previously discussed, the intersections between the backbone curve and the stability boundaries indicate bifurcations that lead to mixed-mode backbone curves of the labelled types. Example NNM responses on the bifurcated backbone curves are shown in the configuration space in panel (c), where the frequency commensurate relationships can also be checked – q_s (the mode with a *higher* natural frequency), is resonating at frequencies that are integer multiples of that of q_r (the mode with a *lower* natural frequency). Note that, the schematic NNM responses in the configuration space (panel (c)) are obtained via numerical computations rather than using the derived method in this chapter. By

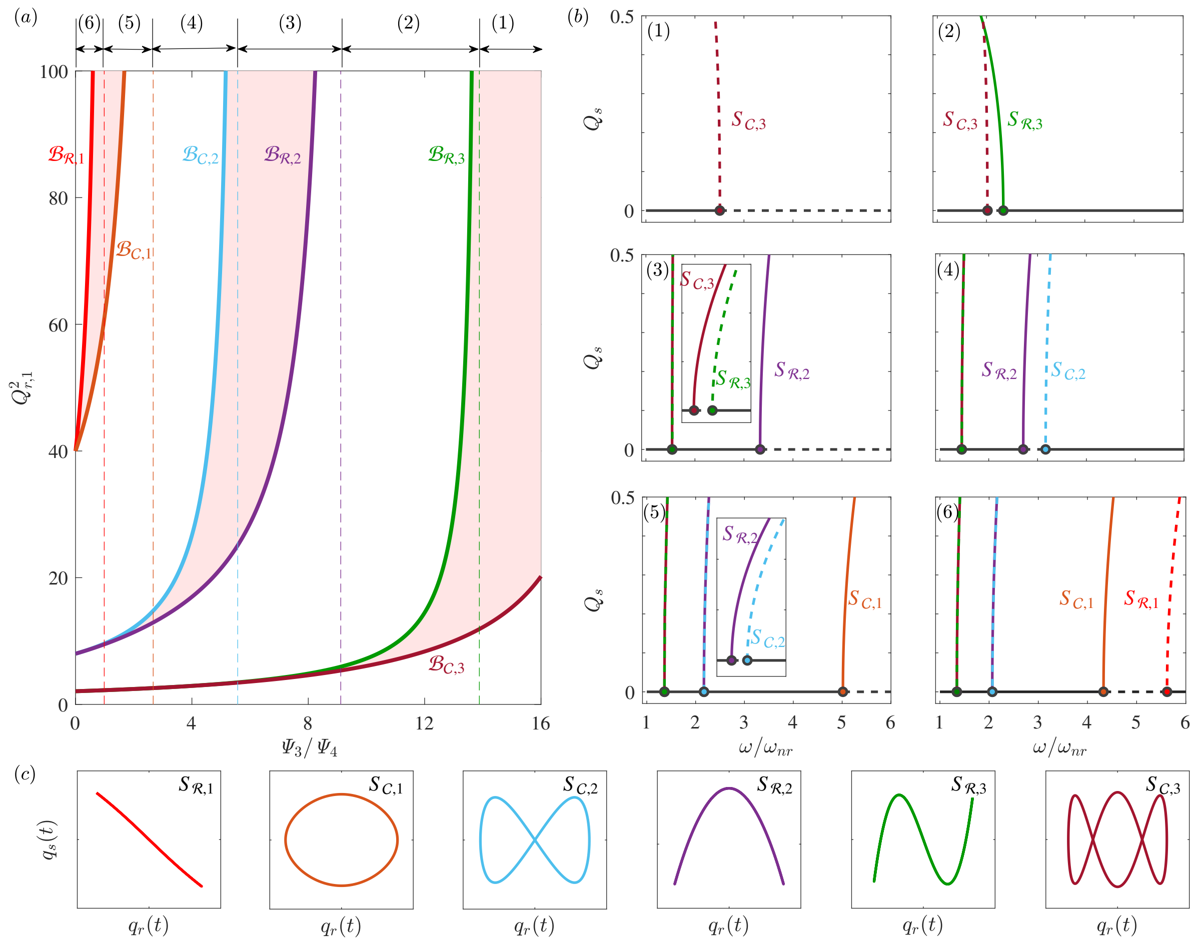

Fig. 5.6 Topological evolutions of internal resonances that bifurcate from the first single-mode backbone curve for a two-mode system with $\omega_{ns}/\omega_{nr} = 4$ and $\Psi_4 = \pi^4/2$. (a) The evolutions of BP amplitude with respect to a varied coefficient Ψ_3/Ψ_4. This plot is divided by the asymptotes of the loci into six regions, capturing the topological changes in internal resonances. (b) The corresponding topologies of internal resonances for regions (1) → (6) in panel (a). (c) The schematic time-parameterised NNM responses on the Fourier-real and -complex backbone curves.

comparing the predicting results in panel (a) with numerical results in panel (c), it verifies the internal resonance predicting method proposed in this chapter – it shows consistency with the numerical results. Alternatively, one can substitute the parameters at the intersections into Eq. (5.11), and it can be used to compute the internally resonant components.

In this new projection, Fig. 5.6a, the amplitude of bifurcations for $1:n$ Fourier-real and -complex NNMs converge to an identical finite value with the decrement of Ψ_3; whilst they diverge to an infinite value with the increament of Ψ_3, similar to the numerically obtained boundaries for the beam system in Fig. 5.2. Correlated asymptotes, where the amplitude of bifurcation critically grows to infinity (i.e. being non-existent), are represented by dashed lines in Fig. 5.6*a*. Therefore, the asymptote-related system parameter, Ψ_3/Ψ_4, denotes the *critical condition for the annihilation of specific internal resonance*. Combining all asymptotes of the stability boundaries, they together serve as divisions capturing the topological changes of bifurcations and their correlated internal resonances. For instance, using the asymptotes, Fig. 5.6*a* can be divided into six regions[2], the corresponding topology of backbone curves in each region is shown in panel (*b*) in the projection of response frequency, ω, against amplitude of q_s.

In region (1), S_r only intersects with $\mathcal{B}_{\mathcal{C},3}$, i.e. the stability boundary related to $1:3$ Fourier-complex NNMs; as such, the backbone curve topology (1) in panel (*b*) can be observed – a single mode backbone curve with a bifurcation leading to $S_{\mathcal{C},3}$. Note that, for this case, $S_{\mathcal{C},3}$ is unstable due to the subcritical bifurcation. As Ψ_3/Ψ_4 decreases, it moves from region (1) to region (2). In addition to an intersection with $\mathcal{B}_{\mathcal{C},3}$, S_r has an additional intersection with $\mathcal{B}_{\mathcal{R},3}$; this indicates the bifurcation, leading to $S_{\mathcal{R},3}$, merges from an infinite amplitude, and evolves to a smaller amplitude as Ψ_3/Ψ_4 decreases. The topology of backbone curves, for systems in region (2), are shown in plot (2) of panel (*b*) – a single mode backbone curve with $1:3$ Fourier-real and -complex backbone curves, $S_{\mathcal{R},3}$ and $S_{\mathcal{C},3}$. Decreasing Ψ_3/Ψ_4 leads to region (3), where $S_{\mathcal{R},2}$ merges, and where the two bifurcations of $1:3$ internal resonances further converge to similar amplitudes. Likewise, further decreasing Ψ_3/Ψ_4 leads to the emergence of $S_{\mathcal{C},2}$, $S_{\mathcal{C},1}$ and $S_{\mathcal{R},1}$ in turn respectively. The topological evolutions of backbone curves are shown in plots (4) → (6) of panel (*b*). For small values of Ψ_3/Ψ_4, e.g. in region (6), the NNMs emerging from $1:2$ internal resonances, as well as $1:3$ resonances, exhibit almost identical amplitudes and response frequencies, see plot (6) in panel (*b*). A small step size in numerical continuation would be required to distinguish between them. Note that the beam system, considered in §5.2, has $\Psi_3/\Psi_4 = 4$. Its first primary backbone curve lies in region (4), as such, $1:3$ and $1:2$ internal resonances are expected, topologically shown in Fig. 5.6*b*(4), in line with numerical results shown in Fig. 5.1*a*.

---

[2] Unlike Fig. 5.3, where the $(\delta,\ \epsilon)$ projection is universal to arbitrary single-mode backbone curve, the asymptotic features in Fig. 5.6*a* are dependent on the parameters considered here, i.e. $\omega_{ns}/\omega_{nr} = 4$ and $\Psi_4 = \pi^4/2$. Therefore, a system with different parameters, for example different natural frequency ratios, may give rise to different asymptotic features.

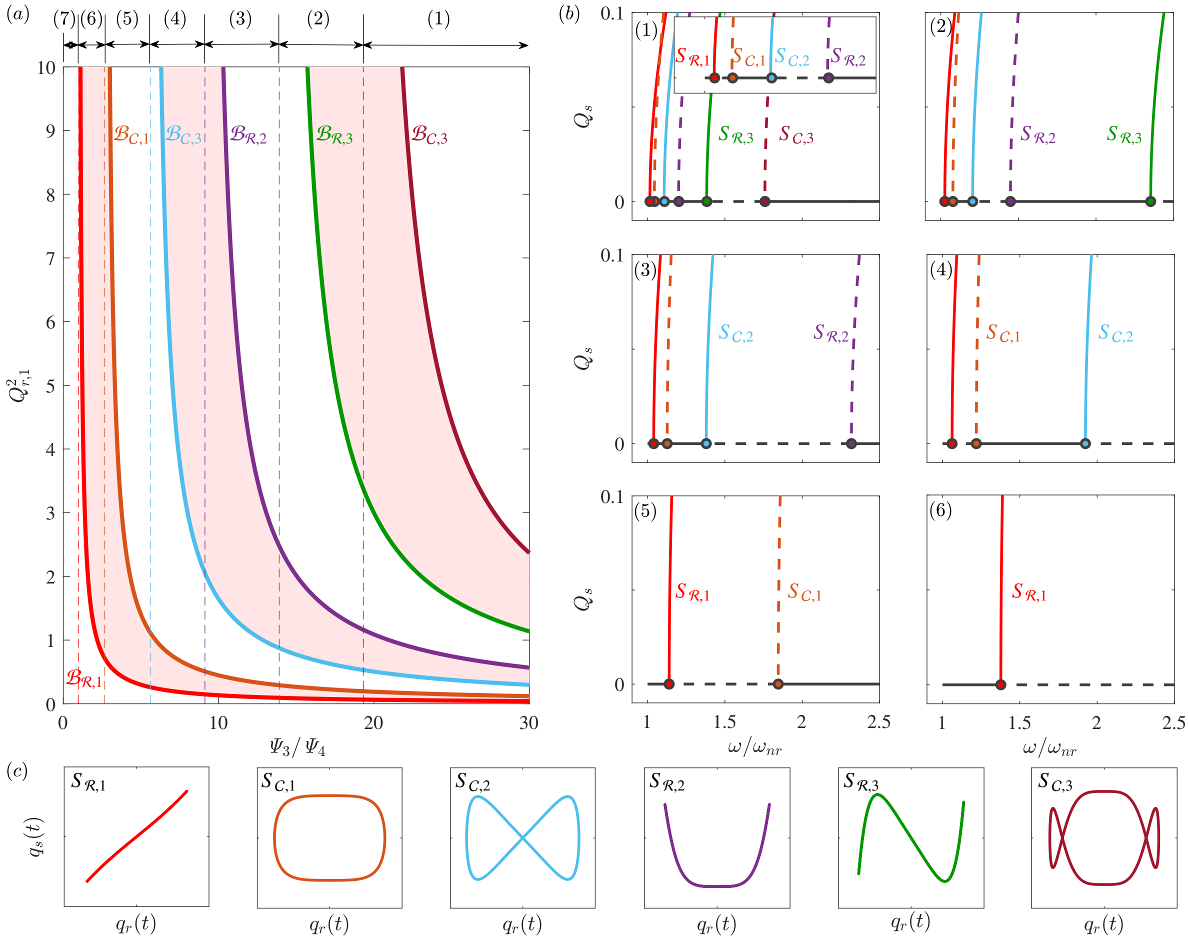

Fig. 5.7 Topological evolutions of internal resonances that bifurcate from the *second* single-mode backbone curve for a two-mode system with $\omega_{ns}/\omega_{nr} = 0.3$ and $\Psi_4 = 1$. (*a*) The amplitude evolutions of the bifurcations with respect to a varied coefficient Ψ_3/Ψ_4. This plot is divided by the asymptotes of the loci into seven regions, capturing the topological changes of internal resonances. (*b*) The corresponding topologies of internal resonances for regions (1) → (6) in panel (*a*). (*c*) The schematic time-parameterised NNM responses on the Fourier-real and -complex backbone curves.

The case where $\omega_{nr} > \omega_{ns}$

Up to this point, the existence and interpretations of internal resonances, where the dominant mode, q_r, is interacting with a *higher*-eigenfrequency mode, q_s, have been studied. It is also of interest to consider the other scenario – cases where $\omega_{nr} > \omega_{ns}$, i.e. q_r is interacting with a *lower*-eigenfrequency mode, q_s. Figure 5.7 shows the topological evolutions of internal resonances for a system with $\omega_{ns}/\omega_{nr} = 0.3$, $\Psi_4 = 1$ and a varied Ψ_3. Like the case in Fig. 5.6*a*, there is an asymptote (denoted by dashed lines) for each stability boundary, differentiating the topologies of backbone curves, correspondingly

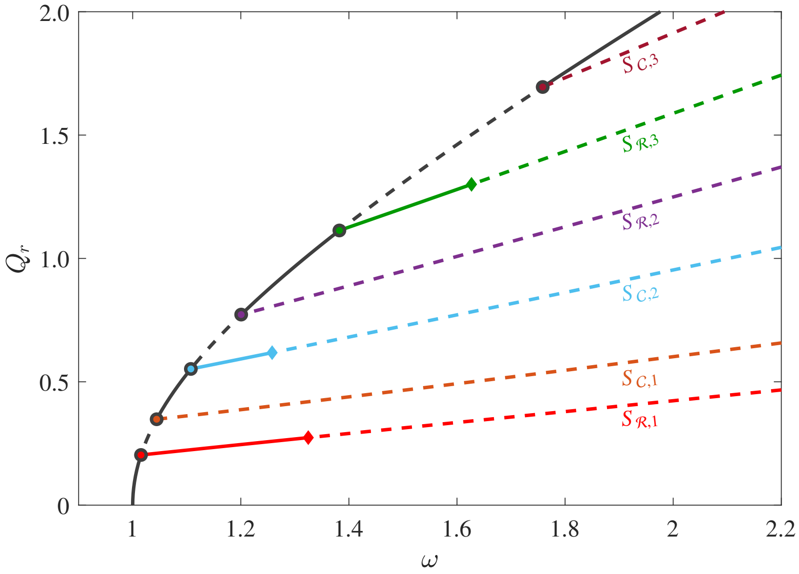

Fig. 5.8 Backbone curves for a system with $\omega_{nr} = 1$, $\omega_{ns} = 0.3$, $\Psi_3 = 30$ and $\Psi_4 = 1$. The stable and unstable segments are denoted by solid and dashed lines respectively. The pitchfork bifurcations leading to mixed-mode backbone curves are marked by solid dots; whilst secondary bifurcations on these mixed-mode backbone curves are marked by diamonds.

shown in panel (b) in the projection of response frequency against the amplitude of q_s. Whilst plots in panel (c) show the schematic time-parameterised responses of the NNMs, obtained via numerical computations to verify the results given in panel (a). Note that, compared to the example responses in Fig. 5.6c, some distortions can be observed in the responses in Fig. 5.7c due to the increment of harmonic components at different response frequencies.

In the case considered herein, where $\omega_{nr} > \omega_{ns}$, q_s is resonating at frequencies that are integer multiples of that of q_r, as with the cases considered in Fig. 5.6. In contrast to Fig. 5.6a where the stability boundaries converge as the *decrement* of Ψ_3, they converge as the *increment* of Ψ_3 in Fig. 5.7a. As such, with the increament of response amplitude and along the single-mode backbone curve, S_r, the very first mixed-mode backbone curve to be observed is the 1 : 1 Fourier-real type. This asymptotic feature also results in a region where no internal resonance can be observed that bifurcates from S_r, see region (7) in panel (a) for systems with small Ψ_3/Ψ_4 values.

The backbone curves for an example system with $\Psi_3/\Psi_4 = 30$, i.e. in region (1) of Fig. 5.7a, are shown in Fig. 5.8. The stable and unstable segments are denoted by solid and dashed lines respectively. The pitchfork bifurcations, emerging from internal resonances and leading to mixed-mode backbone curves, are marked by solid dots. As predicted from Fig. 5.7*a*, a series of mixed-mode backbone curves, $S_{\mathcal{R},1}$, $S_{\mathcal{C},1}$, $S_{\mathcal{C},2}$, $S_{\mathcal{R},2}$, $S_{\mathcal{R},3}$ and $S_{\mathcal{C},3}$ can be observed, and they are all detected via numerical continuation. Note that, some secondary bifurcations on the mixed-mode backbone curves are also detected, which are marked by diamonds. As these bifurcations are beyond the scope of the study, the bifurcated branches are not shown here.

In this section, the existence and locations of internal resonances have been considered and the asymptotic features of bifurcations and their correlated backbone curves have been demonstrated. It allows quantitative determination of the existence and locations of internal resonances for any given system by checking the intersections between primary backbone curves and stability boundaries. In the following section, an analytical study is given to further extend the technique to a *simulation-free method for arbitrary systems*.

5.3.5 Topologies of internal resonances: an arbitrary system

In §5.3.3 and §5.3.4, the convergence and divergence of bifurcations (arising from internal resonances) have been demonstrated respectively via examples in Figs. 5.5, 5.6 and 5.7. In this section, these insights are used for analytical investigations on two-mode interactions for a symmetric system with arbitrary parameters, i.e. arbitrary eigenfrequencies, ω_{nr} and ω_{ns}, and coefficients of nonlinear terms, Ψ_i.

As discussed in §5.3.4, in the $(\Psi_3/\Psi_4,\ Q_{r,1}^2)$ space, each stability boundary has a critical Ψ_3/Ψ_4 value, where the bifurcation amplitude, $Q_{r,1}^2$, diverges to an infinite value (i.e. the annihilation of internal resonances). This limiting case can be generalised as

Annihilation of $1:n$ Fourier-real NNMs, $S_{\mathcal{R},n}$:

$$\lim_{\Psi_3/\Psi_4 \to \mathcal{A}_{\mathcal{R},n}} Q_{r,1}^2 = \infty, \quad \text{for any } \mathcal{B}_{\mathcal{R},n} \text{ with } n \in \mathbb{Z}^+ \,, \tag{5.19a}$$

Annihilation of $1:n$ Fourier-complex NNMs, $S_{\mathcal{C},n}$:

$$\lim_{\Psi_3/\Psi_4 \to \mathcal{A}_{\mathcal{C},n}} Q_{r,1}^2 = \infty, \quad \text{for any } \mathcal{B}_{\mathcal{C},n} \text{ with } n \in \mathbb{Z}^+ \,, \tag{5.19b}$$

where $\mathcal{A}_{\mathcal{R},n}$ and $\mathcal{A}_{\mathcal{C},n}$ denote critical Ψ_3/Ψ_4 values for $\mathcal{B}_{\mathcal{R},n}$ and $\mathcal{B}_{\mathcal{C},n}$ respectively. Substituting expressions of Ψ_3/Ψ_4 and $Q_{r,1}^2$, given by Eq. (5.18), into Eqs. (5.19), the limits can be analytically translated into

Annihilation of $1:n$ Fourier-real NNMs, $S_{\mathcal{R},n}$:

$$\lim_{\Psi_3/\Psi_4 \to \mathcal{A}_{\mathcal{R},n}} Q_{r,1}^2 = \infty \quad \Longleftrightarrow \quad (\delta - \epsilon) = 0 \ \text{ and } \ \mathcal{A}_{\mathcal{R},n} = 6\epsilon \text{ for any } \mathcal{B}_{\mathcal{R},n}\,, \tag{5.20a}$$

Annihilation of 1 : n Fourier-complex NNMs, $S_{\mathcal{C},n}$:

$$\lim_{\Psi_3/\Psi_4 \to \mathcal{A}_{\mathcal{C},n}} Q_{r,1}^2 = \infty \quad \Longleftrightarrow \quad (\delta - \epsilon) = 0 \ \text{ and } \ \mathcal{A}_{\mathcal{C},n} = 6\epsilon \text{ for any } \mathcal{B}_{\mathcal{C},n}\,. \tag{5.20b}$$

It is shown that the limits are associated with functional relationships between δ and ϵ for each stability boundary, $\mathcal{B}_{\mathcal{R},n}$ and $\mathcal{B}_{\mathcal{C},n}$. In addition, recalling the definitions of the stability boundaries, they are given by Hill's determinants, i.e. the zero determinants of coefficient matrices in Eqs. (5.11), which are also funcations of δ and ϵ. This means that the critical Ψ_3/Ψ_4 values can be computed via Eqs. (5.20), provided the expressions of $\mathcal{B}_{\mathcal{R},n}$ and $\mathcal{B}_{\mathcal{C},n}$ are found.

To find the expressions of stability boundaries, a method is given in [256]; they are derived based on a physical model – a rigid planar pendulum with a pivot, whose dynamics is described by the generalised Mathieu equation. The stability boundaries are given by

$$\mathcal{B}_{\mathcal{R},1}(\delta,\ \epsilon): \quad \epsilon = \frac{1}{4}\left(\sqrt{(9-4\delta)(13-20\delta)} - (9-4\delta)\right), \quad (\delta < 1/4)\ , \tag{5.21a}$$

$$\mathcal{B}_{\mathcal{C},1}(\delta,\ \epsilon): \quad \epsilon = \frac{1}{4}\left((9-4\delta) \mp \sqrt{(9-4\delta)(13-20\delta)}\right), \quad (1/4 < \delta < 13/20)\ , \tag{5.21b}$$

$$\mathcal{B}_{\mathcal{C},2}(\delta,\ \epsilon): \quad \epsilon = \sqrt{\frac{2(\delta-1)(\delta-4)(\delta-9)}{\delta-5}}, \quad (13/20 < \delta < 1)\ , \tag{5.21c}$$

$$\mathcal{B}_{\mathcal{R},2}(\delta,\ \epsilon): \quad \epsilon = 2\sqrt{\frac{\delta(\delta-1)(\delta-4)}{3\delta-8}}, \quad (\delta > 1)\ . \tag{5.21d}$$

In addition to the rigorous physical interpretation of the dynamical system, expressions (5.21) also provide a simple finite-form formulas to describe stability boundaries. Nonetheless, as only a limited number of boundaries were derived in [256], to account for the general case of multiple internal resonances, additional formulas are required. An alternative method to derive stability boundaires can be found in [235, 254], where a power series is employed to approximate the boundary. Here, such a power series approximation is used to find the analytical expressions for stability boundaries of the 1 : 3 internal resonance; they are given by

$$\mathcal{B}_{\mathcal{R},3}(\delta,\ \epsilon): \quad \delta = \frac{9}{4} + \frac{\epsilon^2}{16} - \frac{\epsilon^3}{32} + \frac{13\epsilon^4}{5120} + \frac{5\epsilon^5}{2048} - \frac{1961\epsilon^6}{1474560} + \cdots\ , \tag{5.22a}$$

$$\mathcal{B}_{\mathcal{C},3}(\delta,\ \epsilon): \quad \delta = \frac{9}{4} + \frac{\epsilon^2}{16} + \frac{\epsilon^3}{32} + \frac{13\epsilon^4}{5120} - \frac{5\epsilon^5}{2048} - \frac{1961\epsilon^6}{1474560} + \cdots\ , \tag{5.22b}$$

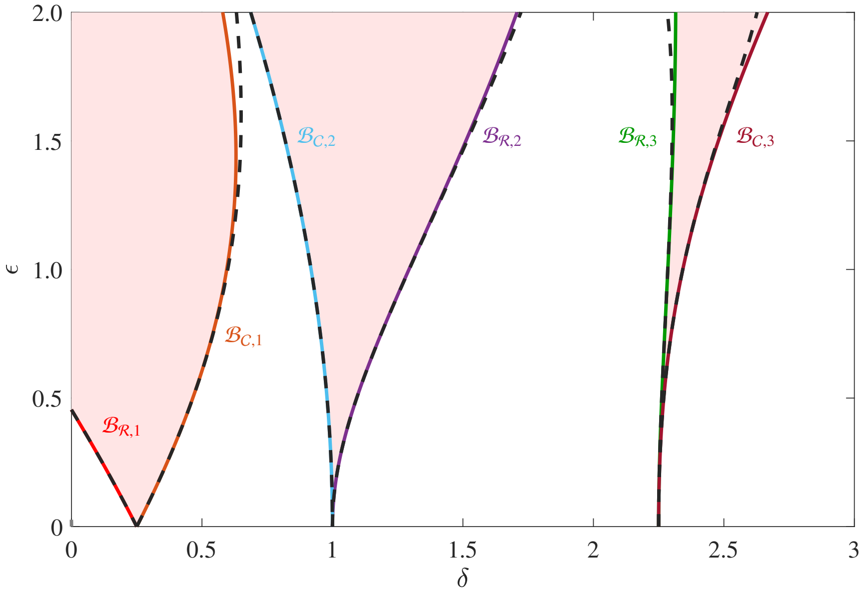

Fig. 5.9 Comparison between analytically and numerically solved stability boundaries. The solid lines represent numerically solved stability boundaires via Eq. (5.11). The dashed lines represent analyticalled solved stability boundaires, computed via Eqs. (5.21) and (5.22).

which, in contrast to that in Eqs. (5.21), are infinite-form formulas but can be truncated to arbitrary order. Note that here only 1 : 1, 1 : 2 and 1 : 3 internal resonances are considered, as such motions represent the most widely observed cases in engineering practice; whilst, a further extension to account for other cases could be achieved via the procedure outlined in this section. It should also be noted that, even though a power series approximation is used, it does not alter the essential feature of the stability boundaries as functions of δ and ϵ.

Figure 5.9 presents the analytically defined stability boundaries (dashed lines), given by Eqs. (5.21) and (5.22), and numerically computed ones (solid lines) via Eqs. (5.11). It can be observed that those analytical expressions show great agreement with that numerically computed ones; only small discrepancies can be found with lage values of ϵ.

To find how those stability boundaries connect to asymptotic features and topological divisions of internal resonances, Eqs. (5.21) and (5.22) are substituted into expressions (5.20), the critical values, $\mathcal{A}_{\mathcal{R},n}$ and $\mathcal{A}_{\mathcal{C},n}$, can be found, approximately given by

$$\mathcal{A}_{\mathcal{R},1} \approx 0.9864, \quad \mathcal{A}_{\mathcal{C},1} \approx 2.6969\,, \tag{5.23a}$$

$$\mathcal{A}_{\mathcal{C},2} \approx 5.5637, \quad \mathcal{A}_{\mathcal{R},2} \approx 9.1672\,, \tag{5.23b}$$

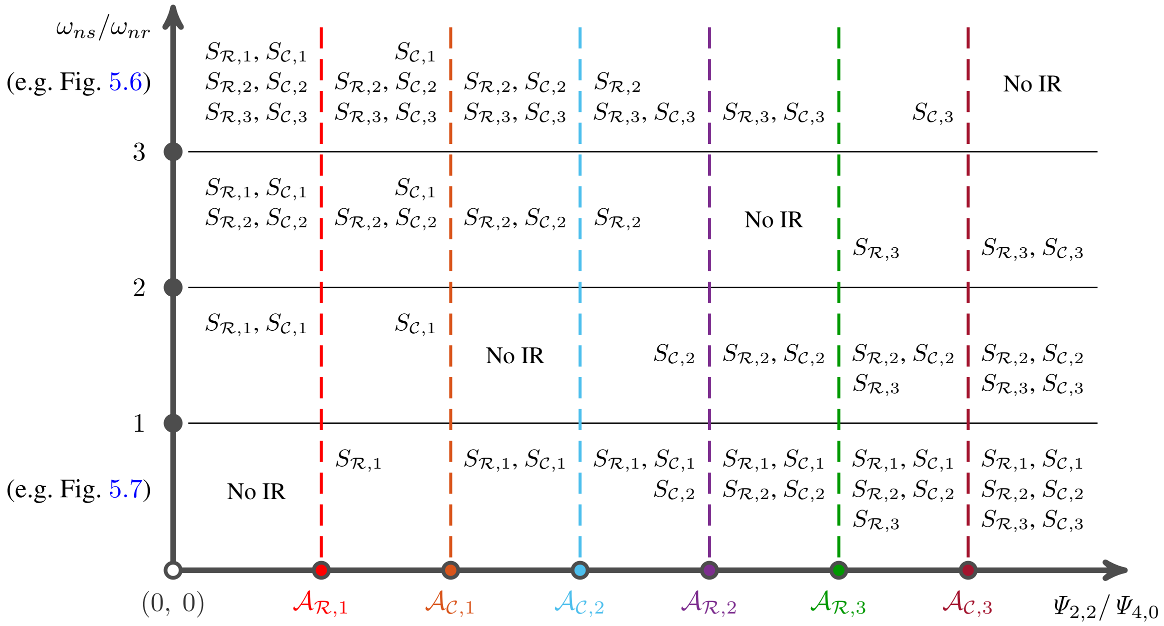

Fig. 5.10 Topologies of Internal Resonances (IRs) for two-mode symmetric systems. Note that, in this table, $1:n$ IRs are considered for $n=1,2,3$.

$$\mathcal{A}_{\mathcal{R},3} \approx 13.6419, \quad \mathcal{A}_{\mathcal{C},3} \approx 20.6495\,. \tag{5.23c}$$

The constant values of $\mathcal{A}_{\mathcal{R},n}$ and $\mathcal{A}_{\mathcal{C},n}$ reveal the independence between system parameters and these critical conditions, at which the stability boundaries, $\mathcal{B}_{\mathcal{R},n}$ and $\mathcal{B}_{\mathcal{C},n}$, asymptotically approach infinite amplitude. This further indicates that, *for arbitrary systems, the same constant critical parameter, Ψ_3/Ψ_4, exists at which the bifurcation, emerging from a specific internal resonance, annihilates with amplitude of an infinite value.*

One could recall previous examples in this chapter, shown in Figs. 5.6 and 5.7, where the critical Ψ_3/Ψ_4 values are indeed the same for these two different systems. Another example can be found in discussions on 1 : 1 internal resonance in Chapter 3; the bifurcation on the first primary backbone curve is defined by Eq. (3.26) with conditions for its existence given by expression (3.27). It can be derived that the bifurcation annihilates with infinite-valued amplitude when $\Psi_3/\Psi_4 = 1$, a first-order approximation of $\mathcal{A}_{\mathcal{R},1}$, computed by keeping leading-order terms of Eq. (5.21a). The third example can be found in Chapter 4, where whirling (out-of-unison) motions were studied. The bifurcation, leading to 1 : 1 whirling motions, annihilates when $\Psi_3/\Psi_4 = 3$; likewise, it is a first-order approximation of $\mathcal{A}_{\mathcal{C},1}$ and can be computed by keeping leading-order terms of Eq. (5.21b).

Having constant asymptotic conditions for bifurcations of arbitrary systems, the topologies of internal resonances can then be investigated for arbitrary eigenfrequencies, ω_{nr} and ω_{ns}, and coefficients of nonlinear terms, Ψ_3/Ψ_4. Here, the results are summarised in Fig. 5.10, where the horizontal axis denotes the values of parameter Ψ_3/Ψ_4; whilst the vertical axis denotes the eigenfrequency ratio between the two interacting modes; the solid dots, labelled $\mathcal{A}_{\mathcal{R},n}$ and $\mathcal{A}_{\mathcal{C},n}$, are critical values given by Eq. (5.23); the dashed lines denote the asymptotic boundaries where the bifurcations, leading to specific mixed-mode backbone curves, annihialate; and where $S_{\mathcal{R},n}$ and $S_{\mathcal{C},n}$, in each cell, denote the existing internal resonances for the given system. Note that the colour schema of dots and dashed lines are in accordance with that in Figs. 5.6 and 5.7.

This figure provides an efficient tool to directly determine the existence of internal resonances by simply checking the parameters of the equations of motion without any simulation. It also provides a reference for the practical design of mechanical systems when a specific type of internal resonance is to be exploited or eliminated. Nonetheless, a closer look at the specific system can reveal additional useful information. For example, considering the $(\Psi_3/\Psi_4,\ Q_{r,1}^2)$ projection can reveal the locations of internal resonances. Besides, as discussed in §5.3.3, the convergence of bifurcations can lead to phase-unlocked NNMs, which can rarely be observed in the presence of damping and external forcing [143]. Determining whether two backbone curves are phase-unlocked or not, a further check about the converging behaviours of bifurcations is required. In addition, to account for the relevance of NNMs to forced responses, the energy balancing method can be employed – this will be detailed in Chapter 6.

In summary, this section considered the existence and locations of $m : n$ internal resonance for a symmetric system. It has been shown that any internal resonance is captured by a pair of mixed-mode backbone curves with one Fourier-real and one Fourier-complex branch. These concepts can be viewed as generalisations of the special cases studied in Chapters 3 and 4, where $1 : 1$ Fourier-real and -complex cases[3] were studied respectively. By studying the topological evolutions of these internally resonant pairs, it has been shown that their converging behaviours lead to uncoupled oscillators with phase-unlocking resonances – exact cases of that studied in [143]; whilst their diverging behaviours lead to the annihilation of internal resonances, and thus serving as their topological divisions. Based on these topological features, a simulation-free method has been proposed to determine the existence and locations of internal resonance for arbitrary two-mode system.

---

[3] The terminologies, $1 : 1$ synchronous and asynchronous motions, used respectively in Chapters 3 and 4, are equivalent to $1 : 1$ Fourier-real and -complex motions defined in this chapter.

5.4 The effect of symmetry breaking on internal resonances

Previous discussions in this chapter have centred around symmetric systems with $\Psi_1 = \Psi_2 = 0$. In this section, the effect of symmetry breaking, i.e. $\Psi_1 \neq 0$ and $\Psi_2 \neq 0$, on internal resonances is studied. It will be shown how the proposed technique can be further extended to asymmetric cases and how this technique can be used in understanding the fundamental mechanism underpinning internal resonances in asymmetric systems. Note that some unaddressed nonlinear features, observed in Chapters 3 and 4, will also be discussed and explained; for example, why the bifurcations leading to synchronous motions (i.e. 1 : 1 Fourier-real motions) split for asymmetry, as observed in Chapter 3; whilst that for asynchronous motions (i.e. 1 : 1 Fourier-complex motions) remain intact for asymmetry for the cable model in Chapter 4.

When taking asymmetry into account, periodic solutions with $q_s = 0$, or the single-mode backbone curve S_r, are no longer obtainable from equations of motion (3.2) due to modal coupling arising from nonlinear terms. Instead, only mixed-mode solutions with $q_r \neq 0$ and $q_s \neq 0$ can be found. In this case, the modal coupling is underpinned by two mechanisms – one is the *dynamic coupling* considered in previous sections, where the interactions between q_r and q_s lead to internal resonances; the other one corresponds to *quasi-static coupling*, where the behaviour of a mode is dictated by the other [107, 109]. Here, to account for both quasi-static and dynamic coupling, q_s is defined as a combination of a quasi-static component, g (dictated by q_r), and a dynamic component, h, written as

$$q_s = g(q_r) + h\,. \tag{5.24}$$

As defined in [109], the quasi-static function, g, represents a solution of

$$\omega_{ns}^2 g + \Psi_1 q_r^3 + \Psi_3 q_r^2 g + 3\,\Psi_2 q_r g^2 + \Psi_5 g^3 = 0\,, \tag{5.25}$$

equivalent to a static solution of q_s to Eq. (3.2b). In this representation, any internal resonance is captured by dynamic interactions between q_r and h, or solutions with these two components.

The Lagrangian of the system is still defined by Eq. (5.1). Replacing $q_s = g(q_r) + h$, and applying the Euler-Lagrange equation, the equations of motion can be obtained with respect to interacting components q_r and h, given by

$$\left[\left(\frac{\partial g}{\partial q_r}\right)^2+1\right]\ddot{q}_r+\frac{\partial g}{\partial q_r}\frac{\partial^2 g}{\partial q_r^2}\dot{q}_r^2+\frac{\partial g}{\partial q_r}\ddot{h}+f_r+\frac{\partial g}{\partial q_r}f_s=0\,, \tag{5.26a}$$

$$\ddot{h}+\frac{\partial^2 g}{\partial q_r^2}\dot{q}_r^2+\frac{\partial g}{\partial q_r}\ddot{q}_r+f_s=0\,, \tag{5.26b}$$

where

$$\begin{aligned} f_r &= \omega_{nr}^2 q_r + \varPsi_4 q_r^3 + 3\,\varPsi_1 q_r^2\,(g+h) + \varPsi_3 q_r\,(g+h)^2 + \varPsi_2\,(g+h)^3\ , \\ f_s &= \omega_{ns}^2\,(g+h) + \varPsi_1 q_r^3 + \varPsi_3 q_r^2\,(g+h) + 3\,\varPsi_2 q_r\,(g+h)^2 + \varPsi_5\,(g+h)^3\ . \end{aligned}$$

By comparing Eqs. (5.2) and (5.26), the additional terms denotes the influence of quasi-static coupling on modal interactions. Therefore, with the limit of $g = 0$, i.e. neglecting quasi-static coupling effect, Eq. (5.26) is reduced to that defined by Eq. (5.2). This model (5.26) was proposed in [117] to detect internal resonances, between q_r and h during reduced-order modelling. It is used here to account for internal resonances in an asymmetric system with the presence of quasi-static coupling.

As discussed in §5.3, in compared to the dominant component, q_r, the internally resonant component, h, is assumed to be small. This can be justified by the weakly asymmetric case considered here, which aims to study the effect of symmetry breaking, rather than provides a complete investigation of asymmetric case. Ignoring the higher-order small terms, $\mathcal{O}(h^2)$, the quasi-static coupling between q_r and q_s can be captured by Eq. (5.26a), and it is interpreted as a primary backbone curve with component q_r and quasi-static component $g(q_r)$. Whilst the dynamic coupling, or internal resonance, between q_r and h, is captured by Eq. (5.26b). Note that, for details of the derivation, the interested reader can be directed to [117]. In this context, it is equivalent to considering internal resonances in the neighbourhood of the primary backbone curve, as with that for the symmetric case considered in §5.3. Next, it will be shown how this similar formulation captures the effect of symmetry breaking on internal resonances.

First, the quasi-static coupling function is solved via Eq. (5.25), where $g(q_r)$ is approximated by a Taylor series up to a cubic order[4], i.e.

$$g(q_r)\approx-\frac{\varPsi_1 q_r^3}{\omega_{ns}^2}. \tag{5.27}$$

---

[4] Similar conclusions can be obtained when considering additional higher-order terms in the Taylor series, as such, a cubic approximation is considered for simplicity.

Expression (5.27) shows how asymmetry, $\Psi_1 \neq 0$, leads to quasi-static coupling. Combining expressions (5.25), (5.26b) and (5.27), and neglecting the contributions from higher-order small terms, the internal resonances between q_r and h are captured by

$$\ddot{h} + \left(\omega_{ns}^2 + \Psi_3 q_r^2 - \frac{6\,\Psi_2\,\Psi_1}{\omega_{ns}^2} q_r^4 + \frac{3\,\Psi_5\,\Psi_1^2}{\omega_{ns}^4} q_r^6\right) h = \frac{6\,\Psi_1}{\omega_{ns}^2} q_r \dot{q}_r^2 + \frac{3\,\Psi_1}{\omega_{ns}^2} q_r^2 \ddot{q}_r. \tag{5.28}$$

The solution for q_r is, as previously discussed, approximated using the fundamental component, $q_r \approx Q_{r,1}\cos(\omega t)$, i.e. having a first-order of accuracy. Substituting q_r back to Eq. (5.28), it can be rearranged as

$$\tfrac{\partial^2 h}{\partial \tau^2} + \left[\delta_0 + \epsilon_1 \cos(\tau) + \epsilon_2 \cos(2\tau) + \epsilon_3 \cos(3\tau)\right] h = P_1 \left[\cos\left(\tfrac{1}{2}\tau\right) + 3\cos\left(\tfrac{3}{2}\tau\right)\right], \tag{5.29}$$

where

$$\begin{aligned}
\delta_0 &= \frac{\omega_{ns}^2}{4\omega^2} + \frac{\Psi_3}{8\omega^2} Q_{r,1}^2 - \frac{9\,\Psi_2\,\Psi_1}{16\omega^2\omega_{ns}^2} Q_{r,1}^4 + \frac{15\,\Psi_1^2\,\Psi_5}{64\omega^2\omega_{ns}^4} Q_{r,1}^6,\\
\epsilon_1 &= \frac{\Psi_3}{8\omega^2} Q_{r,1}^2 - \frac{3\,\Psi_2\,\Psi_1}{4\omega^2\omega_{ns}^2} Q_{r,1}^4 + \frac{45\,\Psi_1^2\,\Psi_5}{128\omega^2\omega_{ns}^4} Q_{r,1}^6,\\
\epsilon_2 &= -\frac{3\,\Psi_2\,\Psi_1}{16\omega^2\omega_{ns}^2} Q_{r,1}^4 + \frac{9\,\Psi_1^2\,\Psi_5}{64\omega^2\omega_{ns}^4} Q_{r,1}^6,\\
\epsilon_3 &= \frac{3\,\Psi_1^2\,\Psi_5}{128\omega^2\omega_{ns}^4} Q_{r,1}^6,\\
P_1 &= -\frac{3\,\Psi_1 Q_{r,1}^3}{16\omega_{ns}^2}.
\end{aligned}$$

This represents an asymmetric evolution to Eq. (5.8) – a *nonhomogeneous extended Mathieu equation*. In comparison to the symmetric case, two additional terms within the bracket, characterised by coefficients, ϵ_2 and ϵ_3, act as additional parametric forcing from q_s on h due to asymmetry; in addition, a nonhomogenous term, characterised by coefficient P_1 on the right-hand side of the equation, also arises from asymmetry.

Here, the responses of the internally resonant mode, h, is approximated via a sum of harmonics (as with the symmetric case in §5.3), i.e.

$$h = H_{a,0} + \sum_{n=1}^{\infty} H_{a,n} \cos\left(\frac{n}{2}\tau\right) + H_{b,n} \sin\left(\frac{n}{2}\tau\right). \tag{5.30}$$

Applying harmonic balancing, the mixed-mode NNMs, emerging from internal resonances, in the neighbourhood of the primary backbone curve, can be obtained, given by the following four equation sets

1 : n Fourier-real NNMs for even n, $S_{\mathcal{R},n}$:

$$\begin{bmatrix} \delta_0 & \epsilon_1/2 & \epsilon_2/2 & \\ \epsilon_1 & \delta_0 - 1 + \epsilon_2/2 & (\epsilon_1+\epsilon_3)/2 & \cdots \\ \epsilon_2 & (\epsilon_1+\epsilon_3)/2 & \delta_0 - 4 & \\ & \vdots & & \end{bmatrix} \begin{pmatrix} H_{a,0} \\ H_{a,2} \\ H_{a,4} \\ \vdots \end{pmatrix} = \mathbf{0}, \tag{5.31a}$$

1 : n Fourier-complex NNMs for even n, $S_{\mathcal{C},n}$:

$$\begin{bmatrix} \delta_0 - 1 - \epsilon_2/2 & (\epsilon_1-\epsilon_3)/2 & \epsilon_2/2 & \\ (\epsilon_1-\epsilon_3)/2 & \delta_0 - 4 & \epsilon_1/2 & \cdots \\ \epsilon_2/2 & \epsilon_1/2 & \delta_0 - 9 & \\ & \vdots & & \end{bmatrix} \begin{pmatrix} H_{b,2} \\ H_{b,4} \\ H_{b,6} \\ \vdots \end{pmatrix} = \mathbf{0}, \tag{5.31b}$$

1 : n Fourier-real NNMs for odd n, $S_{\mathcal{R},n}$:

$$\begin{bmatrix} \delta_0 - 1/4 + \epsilon_1/2 & (\epsilon_1+\epsilon_2)/2 & (\epsilon_2+\epsilon_3)/2 & \\ (\epsilon_1+\epsilon_2)/2 & \delta_0 - 9/4 + \epsilon_3/2 & \epsilon_1/2 & \cdots \\ (\epsilon_2+\epsilon_3)/2 & \epsilon_1/2 & \delta_0 - 25/4 & \\ & \vdots & & \end{bmatrix} \begin{pmatrix} H_{a,1} \\ H_{a,3} \\ H_{a,5} \\ \vdots \end{pmatrix} = \begin{pmatrix} P_1 \\ 3P_1 \\ 0 \\ \vdots \end{pmatrix}, \tag{5.31c}$$

1 : n Fourier-complex NNMs for odd n, $S_{\mathcal{C},n}$:

$$\begin{bmatrix} \delta_0 - 1/4 - \epsilon_1/2 & (\epsilon_1-\epsilon_2)/2 & (\epsilon_2-\epsilon_3)/2 & \\ (\epsilon_1-\epsilon_2)/2 & \delta_0 - 9/4 - \epsilon_3/2 & \epsilon_1/2 & \cdots \\ (\epsilon_2-\epsilon_3)/2 & \epsilon_1/2 & \delta_0 - 25/4 & \\ & \vdots & & \end{bmatrix} \begin{pmatrix} H_{b,1} \\ H_{b,3} \\ H_{b,5} \\ \vdots \end{pmatrix} = \mathbf{0}. \tag{5.31d}$$

Solutions of these four equation sets represent asymmetric evolutions to that described by expressions (5.11). Except for equation set (5.31c), others remain as homogeneous equation sets. As such, semi-trivial solutions can be obtained for $S_{\mathcal{R},n}$ and $S_{\mathcal{C},n}$ for even n, and $S_{\mathcal{C},n}$ for odd n, determined by Eqs. (5.31a), (5.31b) and (5.31d) respectively. This indicates these three types of backbone curves remain as solution branches from the primary backbone curve via bifurcations. As for equation set (5.31c), only non-trivial solutions can be obtained due to nonhomogeneous terms on the right-hand side, indicating backbone curves related to unfolded, or imperfect, bifurcations.

This demonstrates the effect of symmetry breaking, arising from a cubic nonlinearity, on the internal resonances – it splits the bifurcations that lead to $S_{\mathcal{R},n}$ for *odd* n. Likewise, if the asymmetry is induced by nonlinear terms that have q_r with an even valued exponent, e.g. a quadratic nonlinearity, the bifurcations of $S_{\mathcal{R},n}$ for *even* n are unfolded; whilst the other three types remain bifurcating from the primary backbone curve.

It also explains the observed phenomena in previous chapters – the symmetry breaking induced bifurcation splitting leads to isolated in-unison, or Fourier-real, backbone curves in the two-mass oscillators (Chapter 3). However, bifurcations to whirling, or Fourier-complex, motions remain intact for asymmetry of the single-mass ocillator and cable system (Chapter 4).

Equation sets (5.31) can then be used to determine the existence of internal resonance by exploiting its relationship with the stability-change bifurcations. As discussed for the symmetric case in §5.3, the stability boundaries, for asymmetric cases, can also be determined via Hill's determinants, i.e. zero determinants of coefficient matrices in Eqs. (5.31). The first-order approximation derived above results a four-dimensional parameter space, $(\delta_0, \epsilon_1, \epsilon_2, \epsilon_3)$, where the stability boundaries differentiate the stable and unstable regions. Likewise, the primary backbone curve (with contributions from q_r and quasi-static component g) can be mapped to this parameter space, where the intersections between the backbone curve and the stability boundaries denote bifurcations leading to mixed-mode backbone curves.

As an example, symmetry breaking is introduced to the system, shown in Fig. 5.8, by considering $\Psi_1 = 1.5$. The asymmetric evolutions of the backbone curves are computed via numerical continuation and shown in Fig. 5.11, where the backbone curves for the symmetric case are denoted via thin grey lines for comparison. It can be observed in breaking the symmetry two of the bifurcations, those leading to $S_{\mathcal{R},1}$ and $S_{\mathcal{R},3}$ have become imperfect bifurcations; whereas all the other bifurcations remain perfect, as also indicated by Eqs. (5.31) and discussions above.

Another particular case of interest is when the system is seen as a small perturbation from the symmetric case. For this case, the symmetry-breaking parameters, Ψ_1 and Ψ_3, may be assumed to be small. As such, ignoring the higher-order small terms in

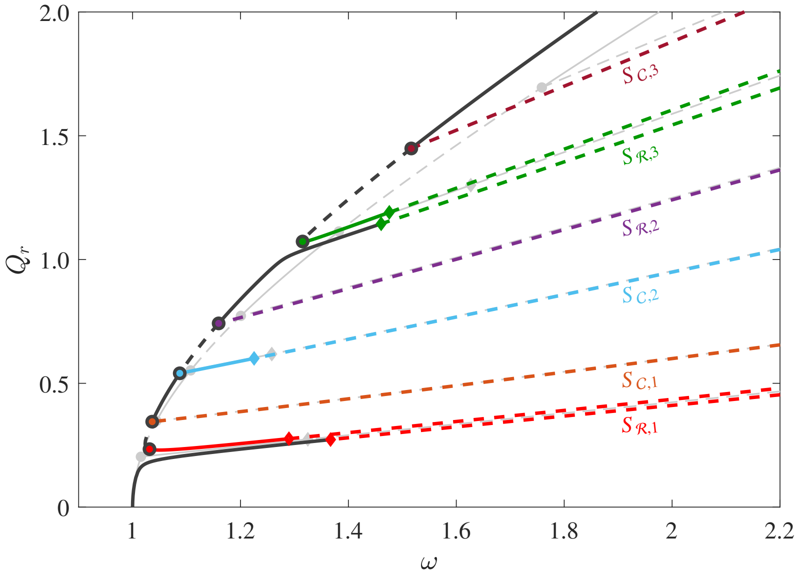

Fig. 5.11 Effect of symmetry breaking on internal resonances. This plot presents backbone curves for an asymmetric example system with $\omega_{nr} = 1$, $\omega_{ns} = 0.3$, $\Psi_1 = 1.5$, $\Psi_3 = 30$ and $\Psi_4 = 1$. Backbone curves for the symmetric case, where $\Psi_1 = 0$, are shown as thin grey lines for comparison.

expression (5.29), it can be further simplified to

$$\frac{\partial^2 h}{\partial \tau^2} + [\delta + \epsilon \cos(\tau)]\, h = P_1 \left[\cos\left(\frac{1}{2}\tau\right) + 3\cos\left(\frac{3}{2}\tau\right)\right], \tag{5.32}$$

which represents a nonhomogeneous Mathieu equation, with left-hand side terms the same as that for the symmetric case, considered in §5.3, whilst with an additional nonhomogenous term on the right-hand side. The formation of expression (5.32) indicates that an asymmetric perturbation is equivalent to a nonhomogeneous perturbation to the internal resonances for a symmetric case; and it leads to bifurcation splitting, the same as elaborations of Eqs. (5.31). In addition, as the frequencies of the nonhomogeneous terms are half integers to that on the left-hand side, there is no difference in the stability boundaries between the homogeneous and nonhomogeneous Mathieu equation [257]. This means the stability boundaries, shown in Fig. 5.3 for symmetric case, can be used to evaluate near-symmetric cases.

In Fig. 5.12a, the primary backbone curve in Fig. 5.8 (for a symmetric system) is projected to the $(\delta,\ \epsilon)$ space via expression (5.12) as a straight line. The bifurcations, leading to mixed-mode backbone curves, are marked by solid dots, which approximately lie

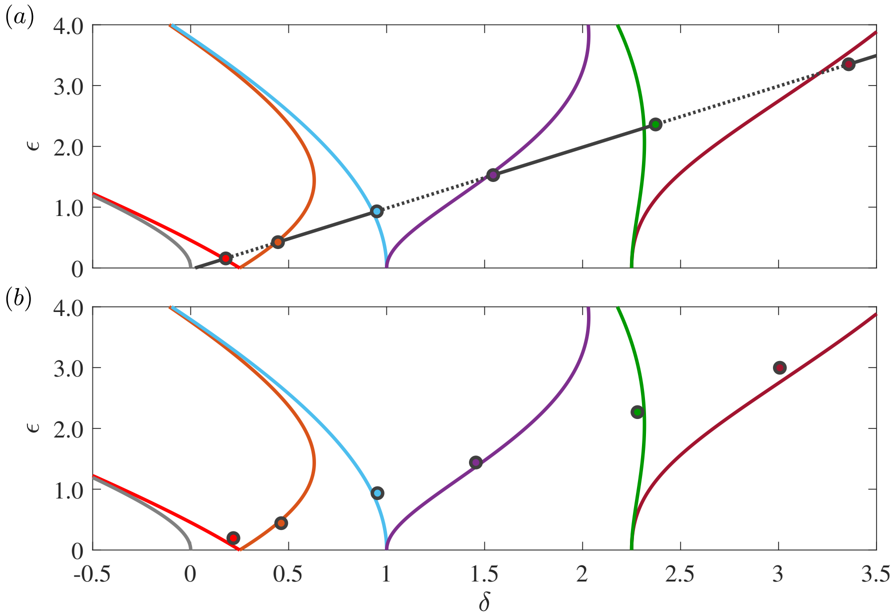

Fig. 5.12 Existence and locations of internal resonances for an asymmetric system. (*a*) The primary backbone curve in Fig. 5.8 (symmetric case), projected as a straight line with bifurcations marked by solid dots. (*b*) The asymmetric evolutions of the bifurcations in panel (*a*) with $\varPsi_1 = 1.5$.

on the stability boundaries. The asymmetric evolutions of these bifurcations are also projected to this space in panel (*b*) for the system whose backbone curves are shown in Fig. 5.11. It can be observed that the stability boundaries well capture the existence of internal resonances for both cases. There are some discrepancies between the numerically obtained bifurcations and the analytically obtained stability boundaries, arising because the formula is of a first-order accuracy. This can be addressed by referring to the formula of a higher-level accuracy, e.g. that derived in §5.3.2.

5.5 Summary

Modal interactions, arising from nonlinear coupling, can be extensively observed in nonlinear systems. When vibrating at large amplitudes, the intricate mechanism underpinning internal resonances can bring about challenges in analysing and designing nonlinear systems. This chapter has considered the existence and locations of internal resonances for a two-mode system with an arbitrary eigenfrequency ratio for an arbitrary response frequency and amplitude range.

The study began with a motivating example of a nonlinear two-mode pinned-pinned beam model in §5.2. Using this example, the concepts of $1:1$ synchronous and asynchronous NNMs, studied in Chapter 3 and 4, have been extended to general $m:n$ internally resonant cases. This was achieved by accounting for the geometric features of NNMs in the complex plane with the proposed terminology – Fourier-real and Fourier-complex NNMs. In addition, it was shown that the example system exhibits an intricate topology of internal resonances, i.e. two Fourier-real and two Fourier-complex backbone curves, among which the $1:3$ Fourier-real and -complex branches exhibit similar response frequencies and amplitudes. With this example, the challenges in quantifying internal resonances was demonstrated – they highlighted the requirement for a rigourous study to uncover the mechanism that underpins the features of internal resonance, as well as an efficient method to ease the computational burden in determining the existence and locations of internal resonances.

In §5.3, a general two-mode symmetric system with cubic nonlinearity has been considered. The analytical derivations have shown that internal resonances in the neighbourhood of the primary backbone curve can be approximately captured by the Mathieu equation. The associated solution sets come in pairs with one Fourier-real and one Fourier-complex NNMs that exhibit the same frequency commensurate relationship but different phase relationships. The topological evolutions, i.e. convergence and divergence, of these internally resonant pairs were then investigated – the convergence of a pair leads to uncoupled oscillators with phase-unlocking internal resonances; whereas their divergence leads to the annihilation of internal resonances. Using these insights, critical boundaries, where the topologies of backbone curves undertake changes, were determined. Based on such topological features, a simulation-free method has been proposed for efficient determination of the existence and locations of internal resonances for any two-mode system with an arbitrary natural frequency ratio.

Discussions in §5.4 extended the symmetric scope to asymmetry. The analytical model of internal resonances for an asymmetric system has been derived, which is captured by a non-homogeneous extended Mathieu equation. The solution sets of the model are asymmetric evolutions to that obtained in §5.3. In breaking the symmetry, the mechanism underpinning the bifurcation splitting/remaining of internal resonances was shown to be governed by the non-homogeneous terms. This mechanism also explains some unaddressed nonlinear behaviours observed in previous chapters, for example, it explains why symmetry breaking leads to bifurcation splitting and generates isolated backbone curves for systems with synchronous/Fourier-real NNMs in Chapter 3; it also explains why bifurcations to whirling motions remain intact for symmetry breaking, as observed in the cable system in Chapter 4.

Up to this point, discussions in Chapters 3, 4, and 5 have centred around the concept of NNMs, i.e. undamped and unforced periodic responses. However, in practice, engineering systems are usually operating under, or subjected, to forced conditions, where the forced response curves (FRCs) are extensively considered for analysis and design of nonlinear systems [31, 30]. In the next chapter, it will be shown how the concept of backbone curves can be used to understand forced periodic motions.

Chapter 6

Multi-harmonic energy balancing analysis using backbone curves

In this chapter:

- The mechanism of energy balancing of nonlinear systems during periodic responses is considered at the system, mode, and harmonic levels. From such an energy-based perspective, the relationships between NNMs and forced responses are established.
- A multi-harmonic energy balancing technique is proposed to interpret forced responses via NNM solutions. This method is constructed based on a semi-analytical framework by combining energy balancing principles, force reductions, and phase constraints.
- The applications of the multi-harmonic energy balancing analysis are demonstrated using a nonlinear cantilever beam under different forcing scenarios.
- The proposed method is applied in the accurate detection of an isolated forced response curve, where multiple harmonics play a significant part.

Publications related to this work:

- D. Hong, T. L. Hill, S. A. Neild, 2022. Efficient Energy Balancing Across Multiple Harmonics of Nonlinear Normal Modes, *Nonlinear Dynamics*.

6.1 Introduction

The concept of backbone curves, or NNM branches, defined as unforced undamped periodic responses [31], has been extensively employed in modal analysis of nonlinear dynamical systems. For example, modal interactions, bifurcations and instability have been investigated in a wide range of engineering systems [130, 246, 198, 143]; the interested reader is directed to §2.2.2 and [31, 100] for an overview.

In previous chapters of this thesis, an NNM-based modal analysis has been employed in the interpretation and quantification of nonlinear dynamic behaviours. A number of practice-relevant applications have been presented – in quantifying the isolated backbone curves in the NLTMD system (Chapter 3); in identifying the phase-varying backbone curves in a cable system (Chapter 4); in interpreting the intricate internal resonances in a pinned-pinned beam system (Chapter 5). These applications have demonstrated the capability of NNMs in capturing the essential nonlinear features, and yet simplifying the intricate nonlinear problems.

Nonetheless, in practice, engineering systems typically operate under forced scenarios, in which case the forced response curves (FRCs) are often used in analysis and design [31, 30]. For example, in studies of the NLTMD system for vibration suppression, the existence of isolated FRCs [131, 43, 133], an analogue of the isolated backbone curves in the forced context, has been reported. The existence of isolated FRCs can significantly affect the performance of a NLTMD as they are challenging to identify and can be related to large-amplitude responses [131, 198]. Another example, seen in studies of cable and rotor systems, the whirling motions, the analogue of out-of-unison/Fourier-complex backbone curves, are important features to quantify [242, 258, 259]. Seen from these examples, a question arises naturally – how are the FRCs related to their unforced and undamped analogues, i.e. the backbone curves?

An approach to establish the relationships between backbone curves and forced periodic responses is the energy balancing analysis, proposed in [139]. This technique considers the energy principle during periodic responses, namely the net energy transfer in and out of any mode must be zero, in combination with the assumption that the near-resonant response is a phase-shift (a perturbation in phase) of an NNM. The energy balancing method has shown its versatility in both theoretical and experimental studies, for example, it has been used to predict the existence of isolated FRCs [139, 198, 141, 142]; to quantify the relative significance of NNMs [143, 260]; and to identify the appropriate number of exitation forces and their distribution in conducting force appropriation [144]. In the motivating example presented in §2.5, the energy balancing method has also been shown to accurately capture the resonances via backbone curves. Later, this energy balancing analysis has been extended to account for the non-conservative nonlinearity with applications in full-scale structures [145, 261]. An alternative approach to build the connections between forced responses and backbone curves is using the Melnikov analysis, presented in [140], where the Melnikov function is revealed to be the leading-order term of periodic energy balancing.

In addition to its versatility, one advantage of the energy balancing method lies in its analytical framework, achieved by the assumption that a single harmonic is representative of the modal response. This assumption allows for efficient computations, but, in turn, can bring inaccuracy in complex scenarios where multiple harmonics are significant. Such a limitation was demonstrated in [142], where inaccurate predictions can be found during the merging of an isolated curve to the primary curve. However, the analytical framework does not allow for a direct extension to account for multiple harmonics, instead, the computationally expensive numerical scheme is required.

This chapter extends the energy balancing analysis to account for multiple harmonics to improve its accuracy and robustness in complex application scenarios. This extension preserves the computational efficiency by employing a semi-analytical framework. To this end, the rest of this chapter is organised as follows.

In §6.2, an overview of the energy balancing principle for forced periodic responses is given, highlighting the relationships between forced responses and NNM solutions. The application of the energy balancing analysis, proposed in [139], is presented using a nonlinear beam system. Its capability of interpretating forced responses using backbone curves, as well as its limitation in complex scenarios, are discussed. The limitation is then explained by considering energy-transfer balancing between harmonics – this also motivates the study to extend the single-harmonic framework in [139] to multi-harmonic framework.

In §6.3, the basic assumption of the proposed energy balancing analysis is firstly introduced – the forced resonant responses are viewed as perturbations from NNMs due to small phase-shifts. With known inputs of NNM solutions, the energy balancing principle (across all harmonics of all modes in an NNM) is combined with the force reductions and phase constraints. This gives rise to a closed-form solution that can be exploited for efficient computations/interpretation of forced responses using backbone curves. An example case, where independent forces are applied in quadrature with harmonic displacements, is given to demonstrate the application of the proposed method; the results are verified by comparing to numerical results via force appropriation [89, 90].

In §6.4, the forcing scenario considered in §6.3 is further extended to account for more practically relevant cases where the applied forcing is in quadrature with the physical displacement at the excitation point. Example cases are presented to show the construction of the energy balancing analysis and demonstrate its application in detecting the existence of an isola with multiple significant harmonics.

Finally, this chapter is closed with a summary in §6.5.

6.2 Energy balancing in nonlinear systems: from system to harmonic levels

In §2.5, the motivating example presented the application of the energy balancing analysis, proposed in [139], in interpreting forced responses via backbone curves. However, for illustration, it was achieved by demonstrating the results without detailed discussions on its mechanism. This section first reviews the mechanism of energy balancing of nonlinear systems duing periodic responses at the level of the system and of the mode, and then to that of the harmonic. From such an energy-based perspective, the relationships between NNMs and forced responses are highlighted. Discussions in this section provide a basic concept, based on which an efficient technique is built for applying energy balancing analysis across multiple harmonics – as introduced in §6.3 and §6.4.

6.2.1 Energy balancing principle at the system level

For a nonlinear system, its dynamics can be expressed, using its linear modal components, in the form

$$\ddot{\mathbf{q}} + \mathbf{D}\dot{\mathbf{q}} + \mathbf{\Lambda}\mathbf{q} + \mathbf{N}_q(\mathbf{q}) = \mathbf{p}(t)\,, \tag{6.1}$$

where $\ddot{\mathbf{q}}$, $\dot{\mathbf{q}}$ and $\mathbf{q}$ are vectors of modal accelerations, velocities and displacements respectively. The diagonal matrix $\mathbf{D}$ contains the linear damping coefficients. This is reflective of a significant number of engineering systems that experience geometric nonlinearity when vibrating at large amplitudes, in which case the damping may be assumed small when compared to external forcing and nonlinear stiffness. As such, the simple case of linear modal damping is often considered [234, 30, 31, 144, 117], which have been verified and validated via experimental tests, to name a few, see Refs. [90, 163, 142]. $\mathbf{\Lambda}$ is a diagonal matrix containing the squares of the linear natural frequencies. Vector $\mathbf{N}_q(\mathbf{q})$ contains the nonlinear stiffness terms (assumed to be conservative, and a function of the displacements, $\mathbf{q}$). The external periodic forcing is captured by the vector $\mathbf{p}$. When considering a two-mode nonlinear system, e.g. discussions in previous chapters, the vector of modal coordinate is $\mathbf{q} = (q_1 \; q_2)^\top$, and the system is reduced to two nonlinearly coupled equations.

At the system level, energy-transfer balancing considers the net energy transfer in and out of a system over one period of motion. As the nonlinear terms considered here are conservative, this energy transfer can only be achieved via the damping and external forcing terms. Over one period, the total energy loss by the system due to these nonconservative terms must sum to zero (as the response cannot remain periodic if the net energy transfer is non-zero), such that

$$E_D + E_P = 0\,, \tag{6.2}$$

where E_D and E_P denote the one-period energy-transfer terms due to damping and forcing respectively.

In the modal domain, the nonlinear system, described by Eq. (6.1), can be seen as a collection of modes, where the equation of motion of the i^{th} mode is written

$$\ddot{q}_i + d_i\dot{q}_i + \omega_{ni}^2 q_i + N_{qi}(\mathbf{q}) = p_i(t)\,, \tag{6.3}$$

and where d_i, ω_{ni} and p_i are the i^{th} modal damping coefficient, linear natural frequency and external modal forcing respectively. As such, the energy-transfer terms in Eq. (6.2) can be translated, using modal components, into summation form

$$\sum_{i=1}^{N} (E_{Di} + E_{Pi}) = 0\,, \tag{6.4}$$

where E_{Di} and E_{Pi} denote energy transfer to the i^{th} mode due to modal damping and forcing respectively, and N is the total number of modes in the system. Note that, the nonlinearities, described by $N_{qi}(\mathbf{q})$, may lead to coupling and energy transfer between modes[1]. Here, the nonlinearity caused net energy transfer to the i^{th} mode from other modes in an NNM over a period of time is termed nonlinear energy transfer and denoted

---

[1] One mechanism that can lead to energy exchange between mode is internal resonance, as discussed in Chapters 3, 4 and 5.

E_{Ni}. The effect of E_{Ni} can be seen as an *internal energy rearrangement* among modes at the system level; hence, it exhibits a conservative effect and has a zero contribution to the energy balancing in Eqs. (6.2) and (6.4).

6.2.2 Energy balancing principle at the mode level

The concept of energy balancing analysis can be extended from the system level to the mode level by considering the energy balancing for each modal component. At this level, in addition to damping and forcing energy-transfer terms, the nonlinear energy transfer, E_{Ni}, is seen as an external energy contribution to the i^{th} mode, which must be accounted for. To find these energy-transfer terms, the i^{th} modal equation of motion (6.3) is firstly multiplied by the velocity of the i^{th} mode, $\dot{q}_i$, and then its time integral over one period is considered, which gives

$$E_{Di} + E_{Pi} + E_{Ni} = 0\,, \tag{6.5}$$

where the terms related to acceleration and linear stiffness are zero due to orthogonality; and where the energy-transfer terms arising from damping, external forcing, and nonlinearity are defined respectively as

$$E_{Di} = \int_0^T \left[d_i \dot{q}_i\right] \dot{q}_i \mathrm{d}t\,, \tag{6.6a}$$

$$E_{Pi} = -\int_0^T \left[p_i(t)\right] \dot{q}_i \mathrm{d}t\,, \tag{6.6b}$$

$$E_{Ni} = \int_0^T \left[N_{qi}(\mathbf{q})\right] \dot{q}_i \mathrm{d}t\,. \tag{6.6c}$$

Eq. (6.5) describes the energy balancing at the mode level, an analogue to that at the system level, Eq. (6.2); it demonstrates that, for a periodic response, the net energy transfer in and out of any mode over one period must be zero.

At the mode level, for an NNM (i.e. undamped and unforced periodic response), the net energy transfer between modes must be zero, i.e. $E_{Ni} = 0$, as no mode may lose or gain energy over one period and still remain periodic. Therefore, if an NNM solution is precisely equal to a forced response, Eq. (6.5) implies that the forcing energy gain must be precisely equal to the damping energy loss for each mode, i.e.

$$E_{Pi} = -E_{Di}\,. \tag{6.7}$$

A schematic of this energy transfer is shown in Fig. 6.1*a*, for a two-mode system.

(*a*) – On an NNM

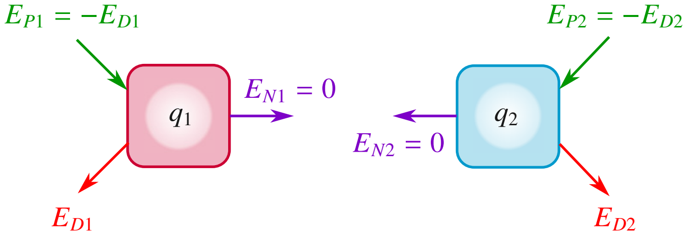

(*b*) – Not on an NNM

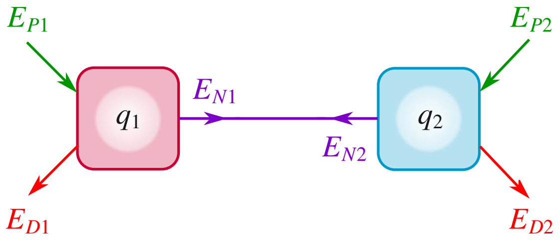

Fig. 6.1 A schematic of the energy transfer at the mode level, for a two-mode system. (*a*) The case where the forcing and damping match precisely, so that the response may equal an NNM. (*b*) The forcing and damping do not match and the response is not precisely on the NNM.

In most applications, however, the applied forcing cannot precisely satisfy Eq. (6.7), i.e. the forcing energy gain for each mode does not equal the damping energy loss (for example, a mode may be damped but unforced). Such a forcing case is referred to here as an *imperfect* forcing. Therefore, Eq. (6.5) reveals that, for an imperfect forcing, $E_{Ni} \neq 0$, which violates a condition of an NNM (i.e. that $E_{Ni} = 0$). A schematic of this energy transfer is shown in Fig. 6.1*b*. This implies that an NNM can never be precisely reached by a system with imperfect forcing. The effect of imperfect forcing, namely the deviations in the energy-transfer schema from Fig. 6.1*a* to Fig. 6.1*b*, can be quantified by considering their differences – the non-zero nonlinear energy-transfer terms, E_{Ni}.

When considering forced responses, particular cases of interest are the resonant responses (where the external force and displacement exhibit quadrature), as they usually represent the most significant responses in a system. In the neighbourhood of resonances, where $E_{Ni} \neq 0$, the forced responses may be viewed as a perturbation from an NNM solution [139, 140]. In this case, the perturbations, leading to an internal energy transfer, E_{Ni}, for periodic responses, can only be achieved via changes in the response frequency, phase, and amplitude. For a given external forcing, the response frequency must be fixed to remain periodic; the change of phase can directly lead to an energy exchange between modes; whilst the amplitude change cannot associate with energy exchange unless accompanied

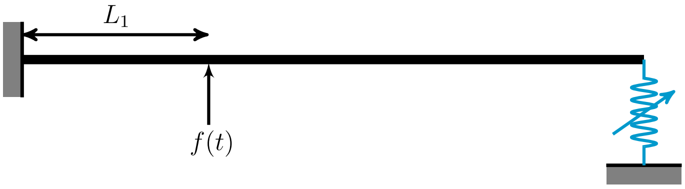

Fig. 6.2 A schematic of a cantilever beam with a nonlinear spring at the free end.

by a phase change. As such, the effect of amplitude change may be seen as of a second order when compared to the phase change.

In this study, the perturbation in the phase, termed a *phase-shift*, of the modal component is considered – it accommodates the internal energy transfer, E_{Ni}, when viewing the forced response as a perturbation from an NNM. If this phase-shift is sufficiently small, it may be assumed that the forced response is close to that of an NNM; conversely, a large phase-shift corresponds to a large change in the response, indicating that the forced response is significantly different to the NNM. Note that, in [139], the proposed technique uses a single harmonic to interpret the energy balancing of a mode via Eqs. (6.5) and (6.7) based on a smallness assumption of phase-shifts; hence it is termed the Mode-level Energy-Transfer Analysis (META).

In §2.5, the META has already shown its capability in accurately capturing the resonances using backbone curves for a simple model, see Fig. 2.5. Here, to demonstrate the application of META, an engineering example is considered, shown in Fig. 6.2 – a cantilever beam with a cubic nonlinear spring at the free end, and excited at a point on the part-span position, L_1, by a single-harmonic force

$$f(t) = F_1 \cos(\Omega t) \,. \tag{6.8}$$

The deflection of this beam is modelled using the first two modes, and the modal equations of motion are given by

$$\ddot{q}_1 + d_1\dot{q}_1 + \omega_{n1}^2 q_1 + N_{q1}(q_1, q_2) = \phi_1 f(t) \,, \tag{6.9a}$$

$$\ddot{q}_2 + d_2\dot{q}_2 + \omega_{n2}^2 q_2 + N_{q2}(q_1, q_2) = \phi_2 f(t) \,, \tag{6.9b}$$

where ϕ_i is the modeshape of the i^{th} mode at the excitation point, and where $d_i = 2\omega_{ni}\zeta$ where ζ is the modal damping. The nonlinear terms are given by

$$N_{q1} = \Psi_4 q_1^3 + 3\Psi_1 q_1^2 q_2 + \Psi_3 q_1 q_2^2 + \Psi_2 q_2^3 \,, \tag{6.10a}$$

Table 6.1 The parameters of the two-mode beam, described by Eqs. (6.9) and (6.10).

Parameter	ω_{n1}	ω_{n2}	d_1	d_2	$\mathit{\Psi}_1$	$\mathit{\Psi}_2$	$\mathit{\Psi}_3$ $\left(\times 10^7\right)$	$\mathit{\Psi}_4$	$\mathit{\Psi}_5$
Value	43.35	134.1	0.434	1.341	-4.005	-6.017	14.73	3.267	7.376

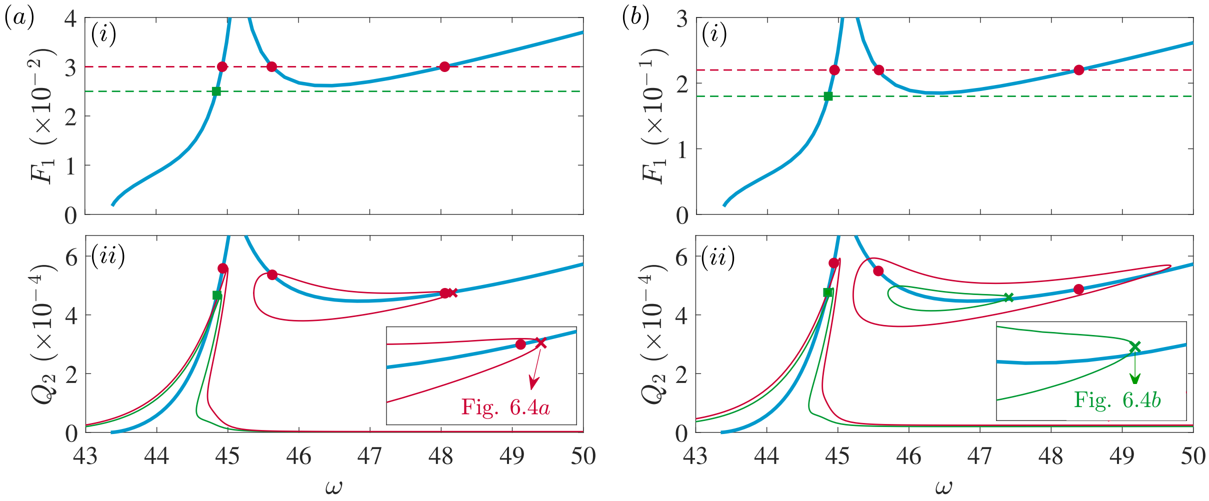

Fig. 6.3 Energy balancing analysis via the Mode-level Energy Transfer Analysis (META). (a) Predicting resonances when the excitation is applied at $L_1 = 0.7L$. Panel (i) shows the forcing amplitude, F_1, required to share solutions with the first NNM branch at frequency ω. Panel (ii) shows the first backbone curve and the forced responses for the two-mode beam in the projection of the response frequency, ω, against the maximum displacement amplitude of the second linear mode, Q_2. The relationships between the backbone curve and forced responses are identified for two forcing cases, labelled by squares and dots in both panels. (b) Predicting results when the excitation is applied at $L_1 = 0.2L$. The energy balancing between harmonics on the forced responses, labelled '×' in the embedded plots, are shown in Fig. 6.4.

$$N_{q2} = \mathit{\Psi}_1 q_1^3 + \mathit{\Psi}_3 q_1^2 q_2 + 3\,\mathit{\Psi}_2 q_1 q_2^2 + \mathit{\Psi}_5 q_2^3\,, \tag{6.10b}$$

where $\mathit{\Psi}_i$ denote coefficients of nonlinear terms. The derivation of the beam model can be found in Refs. [30, 262, 263] or following the procedure outlined in Appendix B. Here, an example system with parameters given in Table 6.1 is considered, where the linear stiffness of the spring is tuned such that the two modes exhibit a 1 : 3 internal resonance, i.e. the fundamental (largest) harmonic of the second mode responds at three times the frequency of the fundamental harmonic of the first mode.

With equations of motion (6.9) and parameters given in Table 6.1, the first backbone curve (i.e. the locus of NNMs emerging from the first linear natural frequency) of the beam is found using the `po`-toolbox of the numerical continuation software COCO [99]. It is shown as a blue line in the bottom panel of Fig. 6.3*a* in the projection of the response frequency, ω, against the maximum response amplitude of the second mode, Q_2. Note that, in this case, the backbone curve is a family of 1 : 3 Fourier-real, or synchronous, NNMs whose response in the modal configuration space is schematically shown in Fig. 5.1*c*.

To account for forced responses, a periodic force, $f(t)$, is applied at a part-span position, $L_1 = 0.7L$. The relationship between the backbone curve and the forced responses is identified via the META using Eq. (6.7). The results are shown in the upper panel of Fig. 6.3*a* – the forcing amplitude, F_1, required for the forced resonant responses to share solutions with the backbone curve at response frequency, ω. Here, two forcing cases (denoted by dashed lines) are considered, where the identified intersections are labelled a square and three dots respectively. These intersections mean the resonant crossing points between FRCs and backbone curves when the corresponding forcing is applied. To verify these predictions, the FRCs are found using numerical continuation and shown as green and red lines in panel (*ii*), with respect to the lower- and higher-amplitude forcing cases in panel (*i*). Excellent agreements are achieved for both forcing cases – the META captures the development of resonances on the primary FRC and the existence of the isola.

The excitation location is then moved from $L_1 = 0.7L$ to $L_1 = 0.2L$, and the energy balancing relationship is again computed via the META, shown in the upper panel of Fig. 6.3*b*. As with the previous example, two forcing cases are considered – the META predicts one intersection for the lower-amplitude forcing, and three crossing points for the larger-amplitude forcing. Considering the similar predictions between two different excitation points, shown in panels (*i*) of Figs. 6.3*a* and 6.3*b*, one would also expect similar results when verifying these predictions. The FRCs for the two forcing cases at $L_1 = 0.2L$ are computed via numcrical continuation and shown in the bottom panel of Fig. 6.3*b*. It can be observed that the numerically computed resonances on the primary FRCs are in strong agreement with the META-identified results. However, unlike the case in Fig. 6.3*a*, the META is unable to capture the existence of the isola for the lower-amplitude forcing. Indeed, one can predict the existence of an isola if the forcing amplitude at the green dashed line is increased; nonetheless, for cases where the existence of isola is predicted, it can show significant errors in the results. One example is the larger-amplitude forcing case (the red dashed line), where the resonances on the isola are not well predicted – see the discrepancies between predictions (solid dots) and resonances on the isola.

In practice, the robust identification of the existence of isolas is highly important, as they can be associated with significant high-amplitude responses in engineering applications, e.g. the NLTMD systems studied in §3.4. However, for the example presented in Fig. 6.3, a robust prediction cannot be guaranteed, and hence, seeking an improved method is needed.

Before introducing the proposed method, the underlying mechanism that governs the applicability and accuracy of the META should firstly be understood in order to overcome its limitations. As the META is an energy-based method, this framework is retained but the energy balancing at the mode level, at which the META is established, is further extended to account for the periodic energy transfer between harmonics. In this way, explanations are given for the different META predictions – it is able to yield accurate predictions when forcing at $L_1 = 0.7L$, but unable to provide accurate results when the forcing is moved to $L_1 = 0.2L$. In the meantime, potential methods to improve the accuracy and robustness are sought.

To account for the energy balancing between harmonics, a mode is viewed as a collection of harmonics, as with the interpretation that a system may be seen as a collection of modes. This allows the modal coordinates to be expressed as a sum of harmonics

$$q_i = \sum_{j \in \mathcal{H}_i} u_{i,j} \,, \tag{6.11}$$

where $u_{i,j}$ is the j^{th} harmonic of the i^{th} mode, and $\mathcal{H}_i$ is a set denoting the harmonics in the i^{th} mode. Considering Eq. (6.11), the energy-transfer balancing at the mode level, Eq. (6.5), can be expressed in summation form

$$\sum_{j \in \mathcal{H}_i} \left(E_{Di,j} + E_{Pi,j} + E_{Ni,j} \right) = 0 \,, \tag{6.12}$$

where the terms within the summation represent the net energy transfer to the j^{th} harmonic of the i^{th} mode due to the damping, forcing and nonlinear terms, respectively.

Here, the periodic energy transfer for resonant responses on the isolas are considered, with respect to the labelled '×' in the embedded plots of Figs. 6.3*a* and 6.3*b*. Note that these two resonances corresponds to cases where META succeeds and fails in predictions respectively. Combining Eqs. (6.6), (6.11) and (6.12), the periodic energy-transfer terms may be computed for each harmonic, and they are shown in Fig. 6.4. Note that, in the considered case, the cantilever beam exhibits 1 : 3 internal resonance, and only

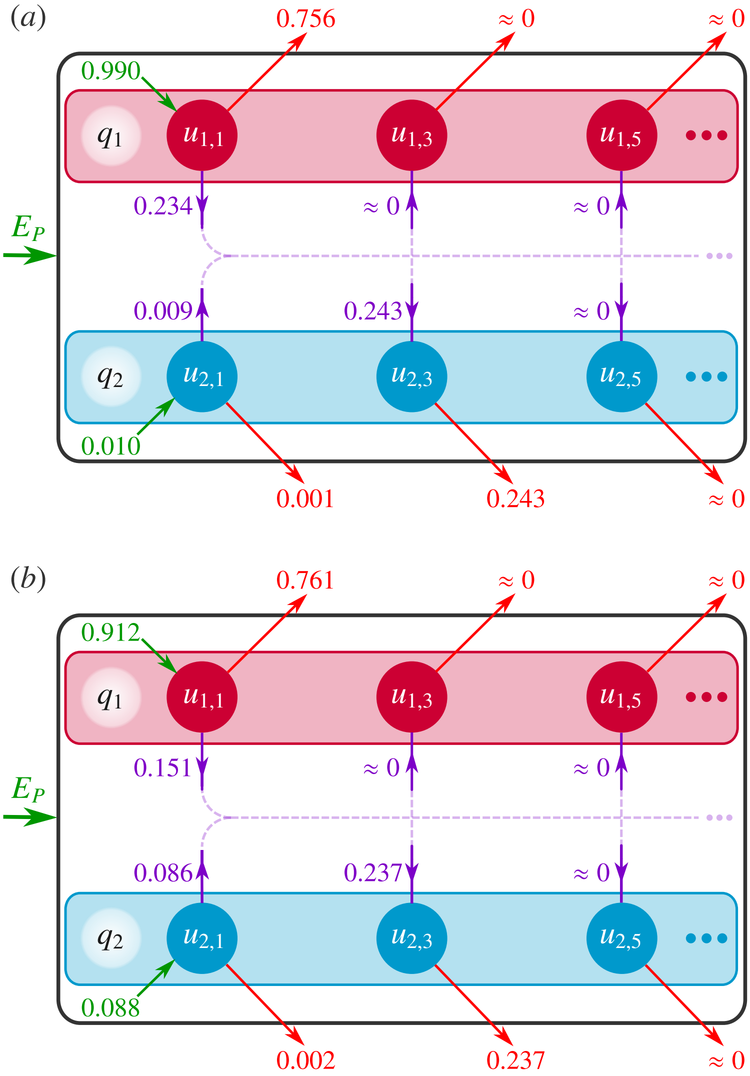

Fig. 6.4 Energy balancing between harmonics of the two-mode cantilever beam. The thin red, green and purple arrows represent the net periodic energy transfer in and out the harmonics, $E_{Di,j}$, $E_{Pi,j}$ and $E_{Ni,j}$ respectively, where the values show the ratio of energy transfer terms over total energy input E_p. (a) Energy balancing for the forced response, labelled '×', on the isolated forced responses in Fig. 6.3a when $L_1 = 0.7L$ and $F_1 = 0.03$. (b) Energy balancing for the forced response, labelled '×', on the isolated forced responses in Fig. 6.3b when $L_1 = 0.2L$ and $F_1 = 0.18$.

odd-numbered harmonics are present in the resonances; as such, the energy transfers to even-numbered harmonics are not shown in Fig. 6.4.

Applying an excitation with forcing frequency, Ω, near the first natural frequency, it inputs energy to the fundamental component of the first mode, $u_{1,1}$, and the first harmonic of the second mode, $u_{2,1}$. When the forcing is at $L_1 = 0.7L$, Fig. 6.4a shows that the major energy input is directed to $u_{1,1}$, with only one percent of energy imparted to $u_{2,1}$. Whilst the major internal energy transfer, caused by nonlinear coupling terms, occurs between fundamental components[2] of the two modes, $u_{1,1}$ and $u_{2,3}$, where the transferred energy is lost via damping. As such, neglecting the small contributions from harmonics (about one percent of the total energy), the energy balancing, Eq. (6.12), can still be accurately captured by the fundamental components. The negligible harmonic contributions underpin the accurate predictions via the META – see Fig. 6.3*a*.

Whilst, for the case in Fig. 6.4*b* where the excitation is at $L_1 = 0.2L$, the major energy input from external forcing is still imparted to $u_{1,1}$, as with the case in Fig. 6.4*a*; however, with an increased amount given to $u_{2,1}$ (about nine percent of the total energy input). As for the internal energy transfer between harmonics, $E_{Ni,j}$, in addition to the fundamental components, a significant involvement of $u_{2,1}$ can also be observed. As such, without accounting for the energy-transfer contributions from harmonics ($u_{2,1}$ in this case), a significant error in energy balancing analysis via the META is shown in Fig. 6.3*b* – it is unable to capture the resonances on the isolated forced responses.

By comparing cases in Fig. 6.3, the limitations of META can be explained by considering the energy transfer between harmonics, shown in Fig. 6.4. It also highlights the importance of considering multiple harmonics in energy transfer analysis – the topic of this chapter. To establish the energy balancing analysis considering multiple harmonics, the mode-level energy balancing, i.e. Eqs. (6.5) and (6.12), is now extended to the harmonic level.

6.2.3 Energy balancing principle at the harmonic level

As with the extension of energy balancing analysis from the system level to the mode level, it can be further extended to the harmonic level. This can be achieved by multiplying the i^{th} modal equation of motion (6.3) with the velocity of the j^{th} harmonic of the i^{th} mode, $\dot{u}_{i,j}$, and integrating over a period of time, which gives

$$E_{Di,j} + E_{Pi,j} + E_{Ni,j} = 0\,. \tag{6.13}$$

where the integrals with respect to acceleration and linear stiffness reveal to be zero, and where the energy-transfer terms due to damping, external forcing and nonlinearity are

---

[2] Note that the forced response exhibits a $1:3$ response so $u_{2,3}$ is the fundamental component of the 2^{nd} mode response.

defined respectively as

$$E_{Di,j} = \int_0^T [d_i \dot{q}_i]\, \dot{u}_{i,j} \mathrm{d}t\,, \tag{6.14a}$$

$$E_{Pi,j} = -\int_0^T [p_i(t)]\, \dot{u}_{i,j} \mathrm{d}t\,, \tag{6.14b}$$

$$E_{Ni,j} = \int_0^T \left[N_{qi}(\mathbf{q})\right] \dot{u}_{i,j} \mathrm{d}t\,. \tag{6.14c}$$

Eq. (6.13) shows the mechanism of energy balancing at the harmonic level – for a periodic response, the net energy transfer in and out of any harmonic must be zero, an analogue to that at the system level, Eq. (6.2), and that at the mode level, Eq. (6.5). This may be seen as the fundamental level as it is established using the fundamental elements – harmonics, and describes the fundamental mechanism of energy transfer of nonlinear systems during periodic responses.

At the harmonic level, for an NNM, the net energy transfer between harmonics must be zero, i.e. $E_{Ni,j} = 0$. Therefore, the relationship between NNMs and forced responses can be obtained from Eq. (6.13), which reads

$$E_{Pi,j} = -E_{Di,j}\,. \tag{6.15}$$

This indicates that the forcing energy gain is balanced by the damping energy loss for each harmonic – an extension of Eq. (6.7) to the harmonic level.

Using relationship (6.15), the force appropriation technique, has been proposed to identify NNM branches experimentally via forced-damped responses [90]. In order to satisfy Eq. (6.15), a quadrature criterion, where the excitation has to compensate for the damping effect, is achieved by applying 90° phase-lagged (with respect to the displacements) forces that contain *all* harmonic components of *all* modes in an NNM.

However, in practice, such a perfect forcing set can never be precisely achieved, which breaks condition (6.15) and causes the response to deviate from the NNM – a non-zero energy transfer between harmonics, i.e. $E_{Ni,j} \neq 0$. Such a non-zero $E_{Ni,j}$ may couple all harmonics of all modes within an NNM – this will be derived analytically in the following discussions. A general energy-transfer schematic for a two-mode multi-harmonic system is shown in Fig. 6.5, which represents an extension of that shown in Fig. 6.1*b* at the mode level; as well as a generalisation of that used for the examples in Fig. 6.4. This illustrates a more complex energy-transfer network among all harmonics at the harmonic level, when compared to taking a higher-level view at the mode level.

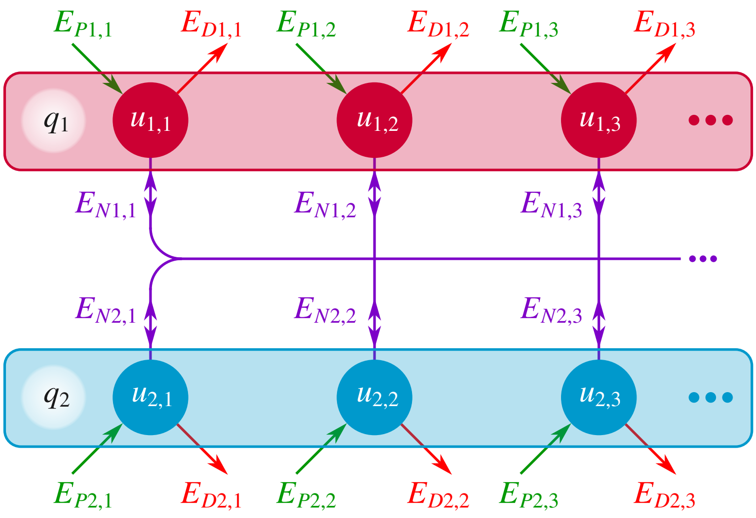

Fig. 6.5 A schematic of the energy transfer between the harmonics of a two-mode system.

Similar to that at the mode level, to evaluate the deviation between a near-resonant response ($E_{Ni,j} \neq 0$) and an NNM solution ($E_{Ni,j} = 0$), the effect of non-zero $E_{Ni,j}$ may be considered. As with the assumption of the META, where a modal phase-shift is used to evaluate the non-zero E_{Ni}, the non-zero nonlinear harmonic energy transfer, $E_{Ni,j}$, may be evaluated by considering the corresponding harmonic phase-shifts. This allows the Harmonic-level Energy-Transfer Analysis (HETA) to be analytically formulated, detailed in the following.

6.3 Harmonic-level Energy-Transfer Analysis

This section considers the extension of the META, proposed in Ref. [139], to account for energy transfer across multiple harmonics. Based on the energy balancing principle, the relationships between forced response and NNMs are established to predict the resonances of FRCs. Before the detailed derivations, a brief overview of the methodology is given here:

- The forced-damped periodic response is interpreted as a perturbation from an NNM solution due to harmonic phase-shifts. This also represents the main assumption of the methodology in this chapter.
- The energy transfer analysis over all harmonics of all modes is then formulated using Eq. (6.13), which leads to an underdetermined problem, i.e. the unknowns (forcing amplitude and phase shift) outnumber the equations.

- The force reduction, along with extra phase constraints imposed by the quadrature conditions, are introduced to formulate a determined, or solvable, equation set.
- The solution to the equation set denotes the required forcing amplitude and harmonic phase shifts in order for the NNM to evolve to the forced periodic response.

To demonstrate the application of the methodology, a nonlinear beam example will be considered where independent modal forces are applied in quadrature with each mode.

6.3.1 Harmonic phase-shifts of NNMs under quadrature forcing

To account for multiple harmonics, the displacement of the i^{th} mode, for an NNM response, is approximated as a sum of a finite number of harmonics, such that

$$\bar{q}_i \approx \sum_{j \in \mathcal{H}_i} \bar{u}_{i,j} = \sum_{j \in \mathcal{H}_i} \bar{U}_{i,j} \cos\left(j\omega t + \bar{\theta}_{i,j}\right), \tag{6.16}$$

where the overbar, $\bar{\bullet}$, indicates that this is an NNM response[3], and where $\bar{u}_{i,j}$ is the j^{th} harmonic of the i^{th} modal displacement, $\bar{q}_i$; and $\mathcal{H}_i$ is the set of harmonics used to approximate $\bar{q}_i$. The amplitude and phase of $\bar{u}_{i,j}$ are represented by $\bar{U}_{i,j}$ and $\bar{\theta}_{i,j}$ respectively, and the frequency ω is defined as $\omega = 2\pi T^{-1}$, where T is the period of the response of the system (i.e. considering all modes).

As with the modal displacements, the external forcing applied to the i^{th} mode may be separated into harmonic components, written

$$p_i = \sum_{j \in \mathcal{H}_i} p_{i,j} = \sum_{j \in \mathcal{H}_i} -P_{i,j} \sin\left(j\omega t + \bar{\theta}_{i,j}\right). \tag{6.17}$$

Note that this assumes that the harmonics of the excitation force are all in quadrature (i.e. at $\pi/2$ out-of-phase, or $\pi/2$ phase-lagged) with the corresponding modal harmonic displacement. This also assumes that all harmonics are forced; however, the unforced harmonics may be specified as those where the excitation amplitude, $P_{i,j}$, is zero – this is revisited later in §6.3.3.

Following the approach used in [139], as described in §6.2, the forced-damped near-resonant response may be seen as a perturbation from an NNM solution with a shift in the phase of the response. Note that this relationship can also be justified using the

---

[3] Note that the introduced notations of an NNM solution, $\bar{q}_i$ and $\bar{u}_{i,j}$, are to differentiate from that of a forced response, q_i and $u_{i,j}$.

Melnikov analysis in [140], where the forced responses are proven to be perturbations from NNMs when external forcing and damping are small in compared to conservative terms. Here, this phase-shift is applied to all harmonics of the response, rather than just the fundamental component (as considered in [139]). The phase-shift of the j^{th} harmonic of the i^{th} mode is written $\hat{\theta}_{i,j}$ and it is assumed small in viewing forced responses as perturbations from NNMs. Introducing these phase-shifts to Eq. (6.16), the forced response of the i^{th} mode is written

$$q_i = \sum_{j \in \mathcal{H}_i} u_{i,j} = \sum_{j \in \mathcal{H}_i} U_{i,j} \cos\left(j\omega t + \bar{\theta}_{i,j} + \hat{\theta}_{i,j}\right) . \tag{6.18}$$

Note that, as discussed in §6.2.2, when considering perturbations from an NNM to a forced response, the change of amplitude may be seen as a second-order effect when compared to the change of phase. Therefore, it is assumed that all amplitudes in the forced response are equal to those in the NNM ($U_{i,j} = \bar{U}_{i,j}$), i.e. the amplitudes are unaffected by the application of forcing and damping, as in Ref. [139].

Based on this smallness assumption of phase-shift, the energy transfer analysis at the harmonic level is now formulated via Eq. (6.13). It will be shown that the energy-transfer terms, $E_{Di,j}$, $E_{Pi,j}$ and $E_{Ni,j}$, may be approximated as linear functions of the excitation amplitude, $P_{i,j}$, and the phase-shifts, $\hat{\theta}_{i,j}$ via known inputs of NNM solutions.

6.3.2 Problem formulation: energy-transfer balancing

Energy balancing principle at the harmonic level, i.e. Eq. (6.13), describes the balancing of damping, forcing and nonlinear energy-transfer terms for the j^{th} harmonic of the i^{th} mode, where these terms may be computed respectively using Eq. (6.14). In addition, in Appendix C, it is derived that these terms may be written as

$$E_{Di,j} = E^{\dagger}_{Di,j} \, , \tag{6.19a}$$

$$E_{Pi,j} \approx E^{\dagger}_{Pi,j} P_{i,j} \, , \tag{6.19b}$$

$$E_{Ni,j} \approx \sum_{n=1}^{N} \sum_{k \in \mathcal{H}_n} E^{\dagger(n,k)}_{Ni,j} \hat{\theta}_{n,k} \, , \tag{6.19c}$$

where the dagger, $\bullet^{\dagger}$, denotes a *known term* – i.e. a term that may be computed using the NNM solution (which is assumed to be known). Whilst the forcing amplitudes, $P_{i,j}$, and phase-shifts, $\hat{\theta}_{n,k}$, are assumed to be unknown and will be computed via the energy balancing analysis. It can be observed that these energy-transfer terms can be approximated as linear functions of the unknowns, i.e. $P_{i,j}$ and $\hat{\theta}_{n,k}$. The known terms are found using

$$E^{\dagger}_{Di,j} = \pi j^2 \omega d_i U^2_{i,j} \,, \tag{6.20a}$$

$$E^{\dagger}_{Pi,j} = -\pi j U_{i,j} \,, \tag{6.20b}$$

$$E^{\dagger(n,k)}_{Ni,j} = \begin{cases} \dfrac{1}{k\omega}\displaystyle\int_0^T \frac{\partial N_{qi}}{\partial q_n}\dot{\bar{u}}_{i,j}\dot{\bar{u}}_{n,k}\mathrm{d}t \,, \\ \qquad\qquad\qquad \text{when: } \{i,j\} \neq \{n,k\} \,, \\ \dfrac{1}{j\omega}\displaystyle\int_0^T \frac{\partial N_{qi}}{\partial q_i}\dot{\bar{u}}^2_{i,j}\mathrm{d}t \\ \qquad + \dfrac{1}{j\omega}\displaystyle\int_0^T N_{qi}\ddot{\bar{u}}_{i,j}\mathrm{d}t \,, \\ \qquad\qquad\qquad \text{when: } \{i,j\} = \{n,k\} \,. \end{cases} \tag{6.20c}$$

Equation (6.19b) shows that the energy transferred to the j^{th} harmonic of the i^{th} mode from external forcing is only due to the force directly applied to that harmonic (i.e. it is only a function of $P_{i,j}$), of which examples are shown in Fig. 6.4. The nonlinear counterpart, Eq. (6.19c), represents the nonlinear energy transfer from all harmonics of all modes in an NNM to the j^{th} harmonic of the i^{th} mode; and it reveals that a phase-shift in any harmonic of any mode, i.e. the k^{th} harmonic of the n^{th} mode, may lead to an energy transfer to the j^{th} harmonic of the i^{th} mode. This demonstrates that *any nonlinear energy-transfer term may couple all harmonics of all modes in an NNM*, as shown in Fig. 6.5.

Substituting the expressions of these energy-transfer terms, Eqs. (6.19), into the energy balancing expression, Eq. (6.13), gives

$$E^{\dagger}_{Di,j} + E^{\dagger}_{Pi,j}P_{i,j} + \sum_{n=1}^{N}\sum_{k\in\mathcal{H}_n} E^{\dagger(n,k)}_{Ni,j}\hat{\theta}_{n,k} = 0 \,. \tag{6.21}$$

By collecting the energy-transfer terms due to damping, forcing and nonlinearity, the energy balancing can be formulated from the j^{th} harmonic, to all harmonics of the i^{th} mode, and to all modes of the system, summarised in Table 6.2, where the total number of harmonics used to represents all N modes of the system is given by

$$R_{\mathcal{H}} = \sum_{i=1}^{N} |\mathcal{H}_i| \,, \tag{6.22}$$

Table 6.2 Harmonic-level energy balancing.

Energy balancing for $u_{i,j}$	Expressions for coefficients
$E^{\dagger}_{Di,j}+E^{\dagger}_{Pi,j}P_{i,j}+\mathbf{E}^{\dagger}_{Ni,j}\hat{\boldsymbol{\theta}}=0$ (6.23)	$\mathbf{E}^{\dagger(n)}_{Ni,j}=\left[E^{\dagger(n,1)}_{Ni,j}\ E^{\dagger(n,2)}_{Ni,j}\ \ldots\ E^{\dagger(n,k)}_{Ni,j}\ \ldots\ E^{\dagger(n,K)}_{Ni,j}\right]$ (6.24a) $\hat{\boldsymbol{\theta}}_n=\left(\hat{\boldsymbol{\theta}}_{n,1}\ \hat{\boldsymbol{\theta}}_{n,2}\ \ldots\ \hat{\boldsymbol{\theta}}_{n,k}\ \ldots\ \hat{\boldsymbol{\theta}}_{n,K}\right)^{\mathsf{T}}$ (6.24b) $\mathbf{E}^{\dagger}_{Ni,j}=\left[\mathbf{E}^{\dagger(1)}_{Ni,j}\ \mathbf{E}^{\dagger(2)}_{Ni,j}\ \ldots\ \mathbf{E}^{\dagger(n)}_{Ni,j}\ \ldots\ \mathbf{E}^{\dagger(N)}_{Ni,j}\right]$ (6.24c) $\hat{\boldsymbol{\theta}}=\left(\hat{\boldsymbol{\theta}}^{\mathsf{T}}_1\ \hat{\boldsymbol{\theta}}^{\mathsf{T}}_2\ \ldots\ \hat{\boldsymbol{\theta}}^{\mathsf{T}}_n\ \ldots\ \hat{\boldsymbol{\theta}}^{\mathsf{T}}_N\right)^{\mathsf{T}}$ (6.24d)
Energy balancing for q_i	Expressions for coefficients
$\mathbf{E}^{\dagger}_{Di}+\mathbf{E}^{\dagger}_{Pi}\mathbf{P}_i+\mathbf{E}^{\dagger}_{Ni}\hat{\boldsymbol{\theta}}=\mathbf{0}$ (6.25)	$\mathbf{E}^{\dagger}_{Di}=\left(E^{\dagger}_{Di,1}\ E^{\dagger}_{Di,2}\ \cdots\ E^{\dagger}_{Di,j}\ \cdots\ E^{\dagger}_{Di,J}\right)^{\mathsf{T}}$ (6.26a) $\mathbf{E}^{\dagger}_{Pi}=\operatorname{diag}\left[E^{\dagger}_{Pi,1}\ E^{\dagger}_{Pi,2}\ \cdots\ E^{\dagger}_{Pi,j}\ \cdots\ E^{\dagger}_{Pi,J}\right]$ (6.26b) $\mathbf{P}_i=\left(P_{i,1}\ P_{i,2}\ \cdots\ P_{i,j}\ \cdots\ P_{i,J}\right)^{\mathsf{T}}$ (6.26c) $\mathbf{E}^{\dagger}_{Ni}=\left[\mathbf{E}^{\dagger}_{Ni,1}{}^{\mathsf{T}}\ \mathbf{E}^{\dagger}_{Ni,2}{}^{\mathsf{T}}\ \cdots\ \mathbf{E}^{\dagger}_{Ni,j}{}^{\mathsf{T}}\ \cdots\ \mathbf{E}^{\dagger}_{Ni,J}{}^{\mathsf{T}}\right]^{\mathsf{T}}$ (6.26d)
Energy balancing for the system	Expressions for coefficients
$\mathbf{E}^{\dagger}_{D}+\mathbf{E}^{\dagger}_{P}\mathbf{P}+\mathbf{E}^{\dagger}_{N}\hat{\boldsymbol{\theta}}=\mathbf{0}$ (6.27)	$\mathbf{E}^{\dagger}_{D}=\left(\mathbf{E}^{\dagger}_{D1}{}^{\mathsf{T}}\ \mathbf{E}^{\dagger}_{D2}{}^{\mathsf{T}}\ \ldots\ \mathbf{E}^{\dagger}_{Di}{}^{\mathsf{T}}\ \ldots\ \mathbf{E}^{\dagger}_{DN}{}^{\mathsf{T}}\right)^{\mathsf{T}}$ (6.28a) $\mathbf{E}^{\dagger}_{P}=\operatorname{diag}\left[\mathbf{E}^{\dagger}_{P1}\ \mathbf{E}^{\dagger}_{P2}\ \cdots\ \mathbf{E}^{\dagger}_{Pi}\ \cdots\ \mathbf{E}^{\dagger}_{PN}\right]$ (6.28b) $\mathbf{P}=\left(\mathbf{P}^{\mathsf{T}}_1\ \mathbf{P}^{\mathsf{T}}_2\ \ldots\ \mathbf{P}^{\mathsf{T}}_i\ \ldots\ \mathbf{P}^{\mathsf{T}}_N\right)^{\mathsf{T}}$ (6.28c) $\mathbf{E}^{\dagger}_{N}=\left[\mathbf{E}^{\dagger}_{N1}{}^{\mathsf{T}}\ \mathbf{E}^{\dagger}_{N2}{}^{\mathsf{T}}\ \cdots\ \mathbf{E}^{\dagger}_{Ni}{}^{\mathsf{T}}\ \cdots\ \mathbf{E}^{\dagger}_{NN}{}^{\mathsf{T}}\right]^{\mathsf{T}}$ (6.28d)

and where the damping energy vector, $\mathbf{E}^{\dagger}_{D}$, the forcing amplitude vector, $\mathbf{P}$, and the harmonic phase-shifts vector, $\hat{\boldsymbol{\theta}}$, all measure $\{R_{\mathcal{H}}\times 1\}$; the forcing energy coefficient matrix, $\mathbf{E}^{\dagger}_{P}$, is a square, diagonal matrix measuring $\{R_{\mathcal{H}}\times R_{\mathcal{H}}\}$; and the nonlinear energy-transfer coefficient matrix, $\mathbf{E}^{\dagger}_{N}$, is a $\{R_{\mathcal{H}}\times R_{\mathcal{H}}\}$ matrix, populated with $E^{\dagger(n,k)}_{Ni,j}$.

Up to this point, the energy transfer analysis is formulated as a set of $R_{\mathcal{H}}$ equations, given by Eq. (6.27), with $2R_{\mathcal{H}}$ unkonwns, consisting of $R_{\mathcal{H}}$ phase-shifts, $\hat{\theta}_{i,j}$, and $R_{\mathcal{H}}$ forcing amplitudes, $P_{i,j}$ – the unknowns outnumber the equations. To solve this underdetermined equation set, in the following section, it will be demonstrated how quadrature conditions can reduce the number of variables and introduce extra constraints, leading to a solvable equation set.

6.3.3 Problem solving: quadrature harmonic forcing

As previously discussed, the current formulation allows all harmonics of all modes to be forced. However, in practical applications, the forcing can only be applied to a limited number of harmonics. Here, the special case is considered where a limited number of independent harmonic forces are applied in quadrature with the corresponding harmonic displacements, as defined in Eq. (6.17), termed *quadrature harmonic forces*. Whilst the more complex, yet more practical, case, where *quadrature physical forces*[4] are applied, will be discussed later in §6.4.

To specify this here the harmonics of the non-zero forcing (applied to the i^{th} mode) are defined as belonging to the set $\tilde{\mathbf{P}}_i$, i.e. the non-zero subset of $\mathbf{P}_i$. As such, the total number of non-zero forcing applied to the system is given by

$$R_{\mathcal{F}} = \sum_{i=1}^{N} |\tilde{\mathbf{P}}_i| \,. \tag{6.29}$$

With this, $\mathbf{P}$ may be simplified by discarding the zero-valued elements to reduce the number of unknowns that need to be estimated. This reduction is achieved by relating the vector of non-zero forcing amplitudes $\tilde{\mathbf{P}}$ (measuring $\{R_{\mathcal{F}} \times 1\}$) to $\mathbf{P}$ via the *force reduction matrix*, $\mathbf{C}_P$, where

$$\mathbf{P} = \mathbf{C}_P \tilde{\mathbf{P}} \,. \tag{6.30}$$

The force reduction matrix may be constructed using a $\{R_{\mathcal{H}} \times R_{\mathcal{H}}\}$ identity matrix and removing the columns associated with unforced harmonics. Hence, $\mathbf{C}_P$ is of size $\{R_{\mathcal{H}} \times R_{\mathcal{F}}\}$. Substituting Eq. (6.30) into Eq. (6.27) leads to

$$\mathbf{E}_D^{\dagger} + \tilde{\mathbf{E}}_P^{\dagger} \tilde{\mathbf{P}} + \mathbf{E}_N^{\dagger} \hat{\boldsymbol{\theta}} = \mathbf{0} \,, \tag{6.31}$$

where $\tilde{\mathbf{E}}_P^{\dagger} = \mathbf{E}_P^{\dagger} \mathbf{C}_P$ is also used, and hence $\tilde{\mathbf{E}}_P^{\dagger}$ measures $\{R_{\mathcal{H}} \times R_{\mathcal{F}}\}$. Through force reduction, the total number of unknowns is now reduced to $(R_{\mathcal{H}} + R_{\mathcal{F}})$, i.e. $R_{\mathcal{H}}$ phase-shifts and $R_{\mathcal{F}}$ forcing amplitudes. However, it is still underdetermined and additional $R_{\mathcal{F}}$ constraints are required to solve the equations.

---

[4] In contrast to a quadrature harmonic forcing, a quadrature physical forcing denotes the case where the applied force is in quadrature with a displacement at a physical location.

As it is assumed that all forces are in quadrature with the harmonic they are forcing, this condition may be enforced using a *phase constraint matrix*, $\mathbf{C}_\theta$, where

$$\mathbf{C}_\theta \hat{\boldsymbol{\theta}} = \mathbf{0}\,. \tag{6.32}$$

This indicates that the forced harmonics do not exhibit a phase-shift – if the forced harmonics did exhibit a phase-shift, they would no longer be in quadrature. Here, $\mathbf{C}_\theta$ is a $\{R_\mathcal{F} \times R_\mathcal{H}\}$ matrix that constrains the phase-shifts of all forced harmonics to be zero. In the case where all harmonic forces are independent, the phase constraint matrix is the transpose of the force reduction matrix, i.e. $\mathbf{C}_\theta = \mathbf{C}_P^\intercal$; hence $\mathbf{C}_\theta$ may be constructed by removing the rows associated with unforced harmonic of a $\{R_\mathcal{H} \times R_\mathcal{H}\}$ identity matrix. The phase constraints introduce $R_\mathcal{F}$ equations, and hence combining Eq. (6.32) with the energy balancing expressions, defined by Eq. (6.31), leads the harmonic-level energy-transfer analysis to a determined, or solvable, equation set.

Equations (6.31) and (6.32) are now combined and written into matrix form as

$$\mathbf{A}\mathbf{v} = \mathbf{B}\,, \tag{6.33}$$

where

$$\mathbf{v} = \begin{pmatrix} \hat{\boldsymbol{\theta}} \\ \tilde{\mathbf{P}} \end{pmatrix}, \quad \mathbf{A} = \begin{bmatrix} \mathbf{E}_N^\dagger & \tilde{\mathbf{E}}_P^\dagger \\ \mathbf{C}_\theta & \mathbf{0} \end{bmatrix}, \quad \mathbf{B} = \begin{pmatrix} -\mathbf{E}_D^\dagger \\ \mathbf{0} \end{pmatrix}, \tag{6.34}$$

and where the unknowns, i.e. $\hat{\boldsymbol{\theta}}$ and $\tilde{\mathbf{P}}$, are collected in the vector $\mathbf{v}$, and the known coefficients are collected in matrices $\mathbf{A}$ and $\mathbf{B}$. As the number of constraints now matches the number of unknowns, the unknown terms are found using

$$\mathbf{v} = \mathbf{A}^{-1}\mathbf{B}\,. \tag{6.35}$$

This allows the phase-shifts of any unforced harmonics and the amplitudes of any forces, which are represented in $\mathbf{v}$, to be computed.

In summary, based on the smallness assumption of phase-shifts, the proposed HETA can be formulated by combining the energy balancing principle (6.27) with force reduction (6.30) and phase constraints (6.32). Closed-form solutions of unknowns, namely the forcing amplitudes and harmonic phase-shifts, can be obtained via Eq. (6.35) with known inputs of NNM solutions; nonetheless, it often results in large-size matrices that, whilst they are all defined analytically, it is more practical to compute digitally.

For the case where the forces applied to the harmonics are independent, the use of the forcing reduction matrix, $\mathbf{C}_P$, and the phase constraint matrix, $\mathbf{C}_\theta$, could be viewed as unnecessary: $\tilde{\mathbf{E}}_P^\dagger$ may be constructed directly by removing the columns of $\mathbf{E}_P^\dagger$ that correspond to the unforced harmonics; likewise, the forced phase-shifts and their corresponding columns in $\mathbf{E}_N^\dagger$ may be removed (as the forced harmonic exhibits a zero phase-shift). In this way, a determined lower-dimension problem can be formulated. However, this approach allows additional constraints to be introduced, as shown later in §6.4. The implementation of this method is now demonstrated using a simple example system.

6.3.4 Example 1: a quadrature harmonic forcing case

To demonstrate the HETA, the cantilever beam, schematically shown in Fig. 6.2, is again considered. To simplify this case, a single-harmonic force is applied to each mode independently, such that the equations of motion are written

$$\ddot{q}_1 + d_1\dot{q}_1 + \omega_{n1}^2 q_1 + N_{q1}\left(q_1, q_2\right) = F_1 \cos\left(\varOmega t\right), \tag{6.36a}$$

$$\ddot{q}_2 + d_2\dot{q}_2 + \omega_{n2}^2 q_2 + N_{q2}\left(q_1, q_2\right) = F_2 \cos\left(3\varOmega t\right), \tag{6.36b}$$

where the nonlinear forces are given by Eq. (6.10). Note that the case where forcing is applied to the part-span will be revisited later in §6.4.

The parameters of the system are the same as considered in §6.2.3, given in Table 6.1. It should be noted that the forcing amplitudes, F_1 and F_2, are assumed to be unknown (and to be found using the HETA). Also note that the linear natural frequencies have a ratio of approximately $1:3$, i.e. $\omega_{n2}/\omega_{n1} \approx 3$. This leads to a $1:3$ modal interaction, as discussed in detail in [262].

Before applying the HETA, the backbone curves of the system need to be obtained to provide known parameters to compute the coefficients in Eq. (6.35). The first backbone curve is presented in Fig. 6.6 by a solid-blue line. The top and bottom panels of Fig. 6.6 show the maximum displacement amplitudes of the first and second modes respectively. In both of these panels, a distinctive *loop* region is seen, indicating a strong internal resonance between the two linear modes. Further discussion of this NNM branch can be found in [262]. For comparison, the forced responses, obtained via force appropriation [90], are also presented by thin red lines, with dots. For the system described by Eq. (6.36), quadrature is achieved when the force applied to the first mode is at 90° to the displacement of the first harmonic, $u_{1,1}$, and when the second modal forcing is at 90° to the displacement of the third harmonic, $u_{2,3}$ – see [90, 144] for further details. As the

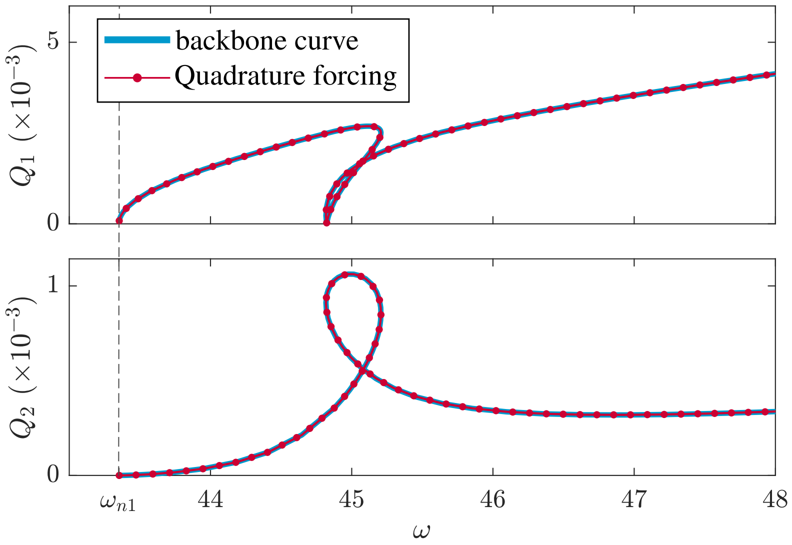

Fig. 6.6 The first backbone curve (blue line) and quadrature branch (red line with dots) for the two-mode beam. The top panel is in the projection of the response frequency, ω, against the maximum displacement amplitude of the first linear mode, Q_1. The bottom panel is in the projection of ω against the maximum displacement amplitude of the second mode, Q_2. The dotted-black line denotes the first linear natural frequency.

NNMs and the forced responses appear to be close, it is expected that the phase-shifts will be small.

To apply HETA, a finite number of harmonics must be used to approximate the modal displacements, as previously discussed in Eq. (6.16). For this example, it is assumed that the first and third harmonics of each mode are sufficient[5], i.e.

$$\mathcal{H}_1 = \{1,\, 3\}\,, \qquad \mathcal{H}_2 = \{1,\, 3\}\,, \tag{6.37}$$

such that

$$q_1 \approx u_{1,1} + u_{1,3}\,, \qquad q_2 \approx u_{2,1} + u_{2,3}\,. \tag{6.38}$$

Whilst additional harmonics would provide greater accuracy, just two harmonics are considered here for simplicity.

To construct the energy balancing equations using Eq. (6.31), the coefficients and unknowns are first assembled into vector/matrix form. The damping energy vector is

---

[5] Note that this system exhibits 1 : 3 internal resonances; as such, only odd-numbered harmonics will be present in the resonant response.

defined, using Eqs. (6.20a), (6.26a) and (6.28a), as

$$\mathbf{E}_D^\dagger = \begin{pmatrix} E_{D1,1}^\dagger \\ E_{D1,3}^\dagger \\ E_{D2,1}^\dagger \\ E_{D2,3}^\dagger \end{pmatrix} = \begin{pmatrix} \pi\omega d_1 U_{1,1}^2 \\ 9\pi\omega d_1 U_{1,3}^2 \\ \pi\omega d_2 U_{2,1}^2 \\ 9\pi\omega d_2 U_{2,3}^2 \end{pmatrix}. \tag{6.39}$$

Then, using Eqs. (6.26b), (6.26c), (6.28b) and (7.15), the matrix of forcing energy coefficients, and vector of unknown forcing amplitudes, are written as

$$\mathbf{E}_P^\dagger = \begin{bmatrix} E_{P1,1}^\dagger & 0 & 0 & 0 \\ 0 & E_{P1,3}^\dagger & 0 & 0 \\ 0 & 0 & E_{P2,1}^\dagger & 0 \\ 0 & 0 & 0 & E_{P2,3}^\dagger \end{bmatrix}, \quad \mathbf{P} = \begin{pmatrix} P_{1,1} \\ P_{1,3} \\ P_{2,1} \\ P_{2,3} \end{pmatrix}. \tag{6.40}$$

As the third harmonic of the first mode, $u_{1,3}$, and the first harmonic of the second mode, $u_{2,1}$, are unforced, the force reduction matrix and reduced vector of forcing amplitudes may be written

$$\mathbf{C}_P = \begin{bmatrix} 1 & 0 \\ 0 & 0 \\ 0 & 0 \\ 0 & 1 \end{bmatrix}, \qquad \tilde{\mathbf{P}} = \begin{pmatrix} P_{1,1} \\ P_{2,3} \end{pmatrix} = \begin{pmatrix} F_1 \\ F_2 \end{pmatrix}, \tag{6.41}$$

where the forcing amplitudes $P_{1,1} = F_1$ and $P_{2,3} = F_2$, from the equations of motion, i.e. Eq. (6.36), have been substituted. Using the force reduction matrix, the reduced matrix of forcing energy coefficient is given by

$$\tilde{\mathbf{E}}_P^\dagger = \mathbf{E}_P^\dagger \mathbf{C}_P = \begin{bmatrix} E_{P1,1}^\dagger & 0 \\ 0 & 0 \\ 0 & 0 \\ 0 & E_{P2,3}^\dagger \end{bmatrix} = \begin{bmatrix} -\pi U_{1,1} & 0 \\ 0 & 0 \\ 0 & 0 \\ 0 & -3\pi U_{1,3} \end{bmatrix}, \tag{6.42}$$

where Eq. (6.20b) has been used to define the forcing energy coefficients.

Next, as defined by Eqs. (6.24a), (6.24c), (6.26d) and (6.28d), the matrix of nonlinear coefficients is written

$$\mathbf{E}_N^\dagger = \begin{bmatrix} E_{N1,1}^{\dagger(1,1)} & E_{N1,1}^{\dagger(1,3)} & E_{N1,1}^{\dagger(2,1)} & E_{N1,1}^{\dagger(2,3)} \\ E_{N1,3}^{\dagger(1,1)} & E_{N1,3}^{\dagger(1,3)} & E_{N1,3}^{\dagger(2,1)} & E_{N1,3}^{\dagger(2,3)} \\ E_{N2,1}^{\dagger(1,1)} & E_{N2,1}^{\dagger(1,3)} & E_{N2,1}^{\dagger(2,1)} & E_{N2,1}^{\dagger(2,3)} \\ E_{N2,3}^{\dagger(1,1)} & E_{N2,3}^{\dagger(1,3)} & E_{N2,3}^{\dagger(2,1)} & E_{N2,3}^{\dagger(2,3)} \end{bmatrix}, \tag{6.43}$$

where the elements of this matrix are computed using Eq. (6.20c).

Finally, the phase constraint matrix and vector of phase-shifts are written

$$\mathbf{C}_\theta = \mathbf{C}_P^\intercal = \begin{bmatrix} 1 & 0 & 0 & 0 \\ 0 & 0 & 0 & 1 \end{bmatrix}, \qquad \hat{\boldsymbol{\theta}} = \begin{pmatrix} \hat{\theta}_{1,1} & \hat{\theta}_{1,3} & \hat{\theta}_{2,1} & \hat{\theta}_{2,3} \end{pmatrix}^\intercal. \tag{6.44}$$

Using the expressions from (6.39) to (6.44), the components to apply harmonic-level energy-transfer analysis, i.e. Eq. (6.35), may be collected as

$$\mathbf{v} = \begin{pmatrix} \hat{\theta}_{1,1} & \hat{\theta}_{1,3} & \hat{\theta}_{2,1} & \hat{\theta}_{2,3} & F_1 & F_2 \end{pmatrix}^\intercal, \tag{6.45a}$$

$$\mathbf{B} = \begin{pmatrix} -E_{D1,1}^\dagger & -E_{D1,3}^\dagger & -E_{D2,1}^\dagger & -E_{D2,3}^\dagger & 0 & 0 \end{pmatrix}^\intercal, \tag{6.45b}$$

$$\mathbf{A} = \begin{bmatrix} E_{N1,1}^{\dagger(1,1)} & E_{N1,1}^{\dagger(1,3)} & E_{N1,1}^{\dagger(2,1)} & E_{N1,1}^{\dagger(2,3)} & E_{P1,1}^\dagger & 0 \\ E_{N1,3}^{\dagger(1,1)} & E_{N1,3}^{\dagger(1,3)} & E_{N1,3}^{\dagger(2,1)} & E_{N1,3}^{\dagger(2,3)} & 0 & 0 \\ E_{N2,1}^{\dagger(1,1)} & E_{N2,1}^{\dagger(1,3)} & E_{N2,1}^{\dagger(2,1)} & E_{N2,1}^{\dagger(2,3)} & 0 & 0 \\ E_{N2,3}^{\dagger(1,1)} & E_{N2,3}^{\dagger(1,3)} & E_{N2,3}^{\dagger(2,1)} & E_{N2,3}^{\dagger(2,3)} & 0 & E_{P2,3}^\dagger \\ 1 & 0 & 0 & 0 & 0 & 0 \\ 0 & 0 & 0 & 1 & 0 & 0 \end{bmatrix}. \tag{6.45c}$$

Noting that all components in **A** and **B** may be computed using an NNM solution. The vector of unknown phase-shifts and forcing amplitudes may now be computed using Eq. (6.35), i.e. $\mathbf{v} = \mathbf{A}^{-1}\mathbf{B}$.

Figure 6.7 shows the forcing amplitudes, $|F_1|$ and $|F_2|$, and the phase-shifts, $\hat{\theta}_{1,3}$ and $\hat{\theta}_{2,1}$, computed via the HETA outlined above and force appropriation. In all panels of Fig. 6.7, the computationally-cheap analytically-predicted values, obtained via the HETA, are represented by blue lines, whilst the computationally-expensive numerically-simulated values, obtained via force appropriation, are shown by red lines with dots. The difference between the analytically-predicted and numerically-simulated forcing amplitudes, $|F_1|$ and $|F_2|$, is indistinguishable, showing that these have been predicted with a very high

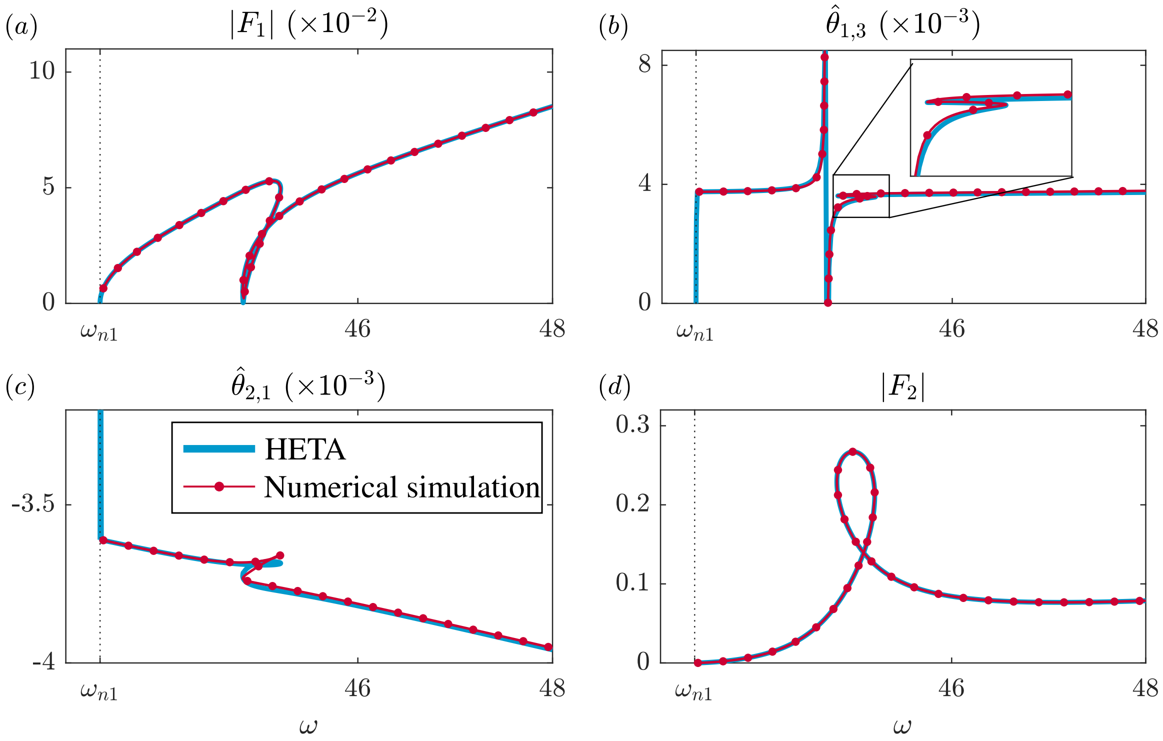

Fig. 6.7 Comparison between the predictions of HETA (using a two-harmonic approximation for each mode) and the numerically-simulated forced responses. (*a*) and (*d*) The response frequency, ω, against the forcing amplitudes $|F_1|$ and $|F_2|$ respectively. (*b*) and (*c*) The response frequency, ω, against the phase-shift parameters, $\hat{\theta}_{1,3}$ and $\hat{\theta}_{2,1}$ respectively. In all panels, the blue lines represent analytically-predicted values (using the NNM data), the red lines (with dots) represent the numerical results and the dotted-black line denotes the first linear natural frequency.

level of accuracy. Although there is some discrepancy, the phase-shift values, $\hat{\theta}_{1,3}$ and $\hat{\theta}_{2,1}$, also show a very good agreement, despite the low number of harmonics used to approximate these responses. The greatest inaccuracy can be seen in phase-shifts, $\hat{\theta}_{1,3}$ and $\hat{\theta}_{2,1}$, near the linear natural frequency, ω_{n1}, (where NNMs are close to the linear response). This is likely due to numerical error in both the simulated and estimated values, as the harmonics are very small for low-amplitude NNMs. Additionally, as the NNM approaches the linear case, the mixed-mode NNM response approaches a linear single-mode response whose phase is no longer defined.

In addition to the strong agreement between results obtained from these two techniques, the results computed via HETA also provide useful information in interpreting nonlinear behaviours. Recalling that harmonic phase-shifts account for the perturbations from NNMs to forced responses, it follows that, by monitoring the evolutions of phase-shifts, the applicability and accuracy of interpreting forced responses via NNMs can be estimated. In this example, the smallness of phase-shifts along the backbone curve, shown in panels (b) and (c), justifies the applicability of the proposed method.

To summarise, the results of HETA, shown in blue in Fig. 6.7, have been estimated via the procedure outlined in this section using only the NNM responses. For the sake of simplicity, this approach has assumed that the response consists of just two harmonics, which limits the accuracy of the predictions. However, owing to the semi-analytical framework, it is convenient to increase the number of harmonics without adding much computational effort. As such, this provides a more efficient technique, whilst preserving the necessary high resolution, for resonance predictions when compared with computationally expensive numerical analysis. The following section will consider additional, more complex, examples and demonstrate the application of this approach to cases with a greater number of parameters.

6.4 Accounting for quadrature physical forcing

The formulation of HETA presented in §6.3 is restricted to cases where independent harmonic forces are applied to each mode of the system; however, in many practical applications, a force may be applied to multiple modes simultaneously. For example, a force applied to the mid-span of a beam is able to excite all modes of the system simultaneously (aside from those that have a node at the forcing location). If one excitation force is applied to multiple modes, the forcing cannot be in quadrature with all forced modal responses, and hence the phase constraints used in §6.3 (i.e. the forced harmonics exhibit zero phase-shifts) become invalid; instead, the modes *must* be free to exhibit different phase-shifts. In this section, it is shown that the HETA may be extended to account for additional forcing conditions – namely where a force is in quadrature with a displacement at a physical location, rather than a harmonic of a mode. This is reflective of most practical scenarios where a force is tuned to reach quadrature with the excitation point. Here, such a forcing is termed a quadrature physical forcing, in comparison to the quadrature harmonic forcing considered in §6.3.

6.4.1 HETA with quadrature physical forcing

To formulate the HETA with quadrature physical forces, the excitation points are defined as $\ell \in \mathcal{L}$, whose number of elements is $R_{\mathcal{L}}$; at the excitation point, ℓ, the harmonic components of the forcing is defined as $j \in \mathcal{F}_\ell$, whose number of elements is $R_{\mathcal{F}_\ell}$. Note that it is assumed that the forced harmonics are included in all modes, i.e.

$$\mathcal{F}_\ell \subseteq \bigcap_{i=1}^{N} \mathcal{H}_i \,. \tag{6.46}$$

Consequently, the total number of forcing harmonics, across all excitatioin points, is given by

$$R_\mathcal{F} = \sum_{\ell \in \mathcal{L}} R_{\mathcal{F}_\ell} \,. \tag{6.47}$$

At excitation point, ℓ, the non-zero i^{th} modal forcing can be obtained by introducing the linear modal transform to the physical forcing, and is given by

$$\tilde{p}_{\ell,i} = \phi_{\ell,i} \tilde{f}_\ell(t) \,, \tag{6.48}$$

where $\tilde{\bullet}$ denotes the non-zero harmonic forcing, as discussed in §6.3.3, and $\phi_{\ell,i}$ is the mode-shape of the i^{th} mode at the excitation point, ℓ. Separating into harmonic components, $\tilde{f}_\ell$ can be expressed as

$$\tilde{f}_\ell = \sum_{j \in \mathcal{F}_\ell} \tilde{f}_{\ell,j} = \sum_{j \in \mathcal{F}_\ell} -\tilde{F}_{\ell,j} \sin\left(j\omega t + \tilde{\psi}_{\ell,j}\right) \,, \tag{6.49}$$

where $\tilde{F}_{\ell,j}$ and $\tilde{\psi}_{\ell,j}$ are the amplitude and phase of the harmonic forcing, $\tilde{f}_{\ell,j}$. As such, the modal forcing, $\tilde{p}_{\ell,i}$, may be approximated as a sum of harmonics using Eqs. (6.48) and (6.49), i.e.

$$\tilde{p}_{\ell,i} = \sum_{j \in \mathcal{F}_\ell} -\phi_{\ell,i} \tilde{F}_{\ell,j} \sin\left(j\omega t + \tilde{\psi}_{\ell,j}\right) \,, \tag{6.50}$$

of which the j^{th} harmonic component is given by

$$\tilde{p}_{\ell,i,j} = -\phi_{\ell,i} \tilde{F}_{\ell,j} \sin\left(j\omega t + \tilde{\psi}_{\ell,j}\right) \,. \tag{6.51}$$

The energy transferred via the modal forcing, $\tilde{p}_{\ell,i}$, to the j^{th} harmonic of the i^{th} mode, $u_{i,j}$, can be computed via Eq. (6.14b), given by

$$\tilde{E}_{P\ell,i,j} = -\int_0^T \tilde{p}_{\ell,i} \dot{u}_{i,j} \mathrm{d}t \approx -\pi j \vartheta_{di,j} U_{i,j} \phi_{\ell,i} \tilde{F}_{\ell,j} \,, \tag{6.52}$$

where

$$\vartheta_{di,j} = \cos\left(\tilde{\psi}_{\ell,j} - \bar{\theta}_{i,j}\right) \,. \tag{6.53}$$

The details of this derivation are given in Appendix C. The phase relationships between the external forcing and NNMs is captured by $\vartheta_{di,j}$. As such, the effect of external forcing on energy transfer is captured by the sign of $\vartheta_{di,j}$ – either an energy gain or an energy loss, reflective of the fact that one force may affect modes differently. In contrast, in the case where independent harmonic forces are applied in quadrature with harmonic displacements, as discussed in §6.3, the applied forces *must* lead to forcing energy-gain terms for the enforced harmonics – see Eqs. (6.19b) and (6.20b). As shown in Appendix C, $\vartheta_{di,j}$ may be related to NNM solutions via quadrature conditions; and hence it is seen as a known parameter.

As discussed in §6.3.2, the forcing energy-transfer terms can be separated into forcing energy-transfer coefficients, $E^{\dagger}_{P\ell,i,j}$, and harmonic forcing amplitudes, $\tilde{P}_{\ell,i,j}$, i.e.

$$\tilde{E}_{P\ell,i,j} \approx E^{\dagger}_{P\ell,i,j}\tilde{P}_{\ell,i,j} \,, \tag{6.54}$$

where

$$E^{\dagger}_{P\ell,i,j} = -\pi j \vartheta_{di,j} U_{i,j} \quad \text{and} \quad \tilde{P}_{\ell,i,j} = \phi_{\ell,i}\tilde{F}_{\ell,j} \,. \tag{6.55}$$

Combining the forcing amplitudes for all harmonics of the i^{th} mode gives

$$\tilde{\mathbf{P}}_{\ell,i} = \boldsymbol{\phi}_{\ell,i}\tilde{\mathbf{F}}_{\ell} \,, \tag{6.56}$$

where

$$\tilde{\mathbf{P}}_{\ell,i} = \begin{pmatrix} \tilde{P}_{\ell,i,1} & \tilde{P}_{\ell,i,2} & \dots & \tilde{P}_{\ell,i,j} & \dots & \tilde{P}_{\ell,i,J} \end{pmatrix}^{\mathsf{T}} \,, \tag{6.57a}$$

$$\boldsymbol{\phi}_{\ell,i} = \operatorname{diag}\begin{bmatrix} \phi_{\ell,i} & \phi_{\ell,i} & \dots & \phi_{\ell,i} & \dots & \phi_{\ell,i} \end{bmatrix} \,, \tag{6.57b}$$

$$\tilde{\mathbf{F}}_{\ell} = \begin{pmatrix} F_{\ell,1} & F_{\ell,2} & \dots & F_{\ell,j} & \dots & F_{\ell,J} \end{pmatrix}^{\mathsf{T}} \,. \tag{6.57c}$$

Next, collecting modal forcing amplitudes for all forced modes of the system gives

$$\tilde{\mathbf{P}}_{\ell} = \boldsymbol{\phi}_{\ell}\tilde{\mathbf{F}}_{\ell} \,, \tag{6.58}$$

where

$$\tilde{\mathbf{P}}_\ell = \left(\begin{array}{ccccccc} \tilde{\mathbf{P}}_{\ell,1}^{\intercal} & \tilde{\mathbf{P}}_{\ell,2}^{\intercal} & \dots & \tilde{\mathbf{P}}_{\ell,i}^{\intercal} & \dots & \tilde{\mathbf{P}}_{\ell,N}^{\intercal} \end{array} \right)^{\intercal}, \tag{6.59a}$$

$$\boldsymbol{\phi}_\ell = \left[\begin{array}{ccccccc} \boldsymbol{\phi}_{\ell,1} & \boldsymbol{\phi}_{\ell,2} & \dots & \boldsymbol{\phi}_{\ell,i} & \dots & \boldsymbol{\phi}_{\ell,N} \end{array} \right]^{\intercal}, \tag{6.59b}$$

As discussed in §6.3, the reduced forcing energy coefficient matrix, $\tilde{\mathbf{E}}_{P,\ell}^{\dagger}$, can be formulated via force reduction

$$\tilde{\mathbf{E}}_{P\ell}^{\dagger} = \mathbf{E}_{P\ell}^{\dagger}\mathbf{C}_{P\ell}\,, \tag{6.60}$$

where $\mathbf{E}_{P\ell}^{\dagger}$ is a $\{R_{\mathcal{H}} \times R_{\mathcal{H}}\}$ diagonal matrix with leading diagonal elements, $E_{P\ell,i,j}^{\dagger}$, defined in Eq. (6.55); and the force reduction matrix, $\mathbf{C}_{P\ell}$, may be constructed using a $\{R_{\mathcal{H}} \times R_{\mathcal{H}}\}$ identity matrix and removing columns associated with unforced harmonics.

The forcing energy-transfer terms are then collected with respect to known terms that can be computed via NNM solutions and unknown terms to be solved via HETA, i.e.

$$\tilde{\mathbf{E}}_{F\ell}^{\dagger}\tilde{\mathbf{F}}_\ell = \mathbf{E}_{P\ell}^{\dagger}\mathbf{C}_{P\ell}\boldsymbol{\phi}_\ell\tilde{\mathbf{F}}_\ell\,, \tag{6.61}$$

where $\tilde{\mathbf{E}}_{F\ell}^{\dagger} = \mathbf{E}_{P\ell}^{\dagger}\mathbf{C}_{P\ell}\boldsymbol{\phi}_\ell$, measuring $\{R_{\mathcal{H}} \times R_{\mathcal{F}_\ell}\}$, and $\tilde{\mathbf{F}}_\ell$ is a vector, measuring $\{R_{\mathcal{F}_\ell} \times 1\}$.

For each excitation point, ℓ, the matrix $\tilde{\mathbf{E}}_{F\ell}^{\dagger}$ and vector $\tilde{\mathbf{F}}_\ell$ may be constructed using the procedure outlined above. The direct collection of them across all excitation points gives

$$\tilde{\mathbf{E}}_{F}^{\dagger} = \left(\begin{array}{ccccccc} \tilde{\mathbf{E}}_{F1}^{\dagger} & \tilde{\mathbf{E}}_{F2}^{\dagger} & \dots & \tilde{\mathbf{E}}_{F\ell}^{\dagger} & \dots & \tilde{\mathbf{E}}_{FR_{\mathcal{L}}}^{\dagger} \end{array} \right), \tag{6.62a}$$

$$\tilde{\mathbf{F}} = \left(\begin{array}{ccccccc} \tilde{\mathbf{F}}_{1}^{\intercal} & \tilde{\mathbf{F}}_{2}^{\intercal} & \dots & \tilde{\mathbf{F}}_{\ell}^{\intercal} & \dots & \tilde{\mathbf{F}}_{R_{\mathcal{L}}}^{\intercal} \end{array} \right)^{\intercal}, \tag{6.62b}$$

where $\tilde{\mathbf{E}}_{F}^{\dagger}$ is a $\{R_{\mathcal{H}} \times R_{\mathcal{F}}\}$ matrix, and $\tilde{\mathbf{F}}$ is a $\{R_{\mathcal{F}} \times 1\}$ vector.

Other energy-transfer terms, i.e. damping and nonlinear energy-transfer terms, $E_{Di,j}$ and $E_{Ni,j}$, are the same as those defined in §6.3, and they can be constructed in the same form as $\mathbf{E}_{D}^{\dagger}$ and $\mathbf{E}_{N}^{\dagger}$ respectively via Eqs. (6.28a) and (6.28d).

As such, for the excitation scenario with quadrature physical forces, the energy balancing expressions can be formulated by considering the energy balancing principle across all harmonics of all modes, given by

$$\mathbf{E}_{D}^{\dagger} + \tilde{\mathbf{E}}_{F}^{\dagger}\tilde{\mathbf{F}} + \mathbf{E}_{N}^{\dagger}\hat{\boldsymbol{\theta}} = \mathbf{0}\,, \tag{6.63}$$

which consists of $R_{\mathcal{H}}$ equations with $R_{\mathcal{H}} + R_{\mathcal{F}}$ unknowns, i.e. $R_{\mathcal{H}}$ phase-shifts and $R_{\mathcal{F}}$ forcing amplitudes. To obtain a determined (solvable) problem, extra $R_{\mathcal{F}}$ constraints can be introduced by considering the quadrature conditions, leading to phase-shift constraints, similar to the discussions in §6.3.3.

To construct phase-shift constraints, the displacement at excitation point, ℓ, is written y_ℓ and may be expressed as a sum of the modal displacements

$$y_\ell = \sum_{i=1}^{N} \phi_{\ell,i} q_i \, . \tag{6.64}$$

Considering the modal displacement as a sum of harmonic components, as in Eq. (6.16), gives

$$y_\ell = \sum_{i=1}^{N} \sum_{j \in \mathcal{H}_i} \phi_{\ell,i} u_{i,j} \, , \tag{6.65}$$

and hence the j^{th} harmonic of the physical displacement y_ℓ may be written

$$y_{\ell,j} = \sum_{i=1}^{N} \phi_{\ell,i} u_{i,j} \, . \tag{6.66}$$

Here as $y_{\ell,j}$ represents the harmonic displacement which is in quadrature with the forcing, it may be written as a sinusoid with amplitude $Y_{\ell,j}$ and phase $\tilde{\psi}_{\ell,j}$, i.e.

$$Y_{\ell,j} \cos\left(j\omega t + \tilde{\psi}_{\ell,j}\right) = \sum_{i=1}^{N} \phi_{\ell,i} U_{i,j} \cos\left(j\omega t + \theta_{i,j}\right) \, , \tag{6.67}$$

where Eq. (6.18) has been used to express $u_{i,j}$ as a sinusoid and where $\theta_{i,j} = \bar{\theta}_{i,j} + \hat{\theta}_{i,j}$.

If the j^{th} harmonic of the force is in quadrature with $y_{\ell,j}$, then the phase, $\tilde{\psi}_{\ell,j}$, of $y_{\ell,j}$ must be equal for both the NNM and the forced case. To find how this leads to a constraint between the modal phase-shift terms, the time- and phase-dependent components of Eq. (6.67) may be separated by first writing

$$\begin{aligned} Y_{\ell,j} \left[\cos\left(j\omega t\right) \cos\left(\tilde{\psi}_{\ell,j}\right) - \sin\left(j\omega t\right) \sin\left(\tilde{\psi}_{\ell,j}\right)\right] = \\ \sum_{i=1}^{N} \phi_{\ell,i} U_{i,j} \left[\cos\left(j\omega t\right) \cos\left(\theta_{i,j}\right) - \sin\left(j\omega t\right) \sin\left(\theta_{i,j}\right)\right] \, . \end{aligned} \tag{6.68}$$

From this, the $\cos(j\omega t)$ and $\sin(j\omega t)$ components may be balanced to give the relationships

$$Y_{\ell,j}\cos\left(\tilde{\psi}_{\ell,j}\right) = \sum_{i=1}^{N}\phi_{\ell,i}U_{i,j}\cos\left(\theta_{i,j}\right) , \tag{6.69a}$$

$$Y_{\ell,j}\sin\left(\tilde{\psi}_{\ell,j}\right) = \sum_{i=1}^{N}\phi_{\ell,i}U_{i,j}\sin\left(\theta_{i,j}\right) . \tag{6.69b}$$

The displacement amplitude $Y_{\ell,j}$ may now be removed by dividing Eq. (6.69b) by Eq. (6.69a) to give

$$\tan\left(\tilde{\psi}_{\ell,j}\right) = \frac{\sum_{i=1}^{N}\phi_{\ell,i}U_{i,j}\sin\left(\theta_{i,j}\right)}{\sum_{i=1}^{N}\phi_{\ell,i}U_{i,j}\cos\left(\theta_{i,j}\right)} . \tag{6.70}$$

If the phase, $\tilde{\psi}_{\ell,j}$, is equal for both the NNM and forced case, it therefore follows that Eq. (6.70) may be satisfied for both $\theta_{i,j} = \bar{\theta}_{i,j} + \hat{\theta}_{i,j}$ (i.e. forced responses) and $\theta_{i,j} = \bar{\theta}_{i,j}$ (i.e. NNMs). With the smallness assumption of phase-shifts, it leads to

$$\frac{\left[\sum_{i=1}^{N}\phi_{\ell,i}U_{i,j}\sin\left(\bar{\theta}_{i,j}\right)\right] + \left[\sum_{i=1}^{N}\phi_{\ell,i}U_{i,j}\cos\left(\bar{\theta}_{i,j}\right)\hat{\theta}_{i,j}\right]}{\left[\sum_{i=1}^{N}\phi_{\ell,i}U_{i,j}\cos\left(\bar{\theta}_{i,j}\right)\right] - \left[\sum_{i=1}^{N}\phi_{\ell,i}U_{i,j}\sin\left(\bar{\theta}_{i,j}\right)\hat{\theta}_{i,j}\right]} = \frac{\sum_{i=1}^{N}\phi_{\ell,i}U_{i,j}\sin\left(\bar{\theta}_{i,j}\right)}{\sum_{i=1}^{N}\phi_{\ell,i}U_{i,j}\cos\left(\bar{\theta}_{i,j}\right)} . \tag{6.71}$$

This restriction represents how the quadrature condition (the applied forcing is *in quadrature with a displacement at a physical location*) imposes a constraint between the phase-shifts of the modal harmonics. It may be simplied to

$$\sum_{i=1}^{N}\sum_{n=1}^{N}\phi_{\ell,i}\phi_{\ell,n}U_{i,j}U_{n,j}\cos\left(\bar{\theta}_{i,j} - \bar{\theta}_{n,j}\right)\hat{\theta}_{i,j} = 0 . \tag{6.72}$$

In this case, each harmonic of each forcing location will be associated with an unknown forcing amplitude, but will also lead to an additional constraint given by Eq. (6.72). For the case where multi-point, multi-harmonic forces are applied, such phase constraints introduce as many constraints as the number of unknown forcing amplitudes, $R_{\mathcal{F}}$, which may be expressed

$$\mathbf{C}_{\theta}\hat{\boldsymbol{\theta}} = \mathbf{0} , \tag{6.73}$$

where $\mathbf{C}_\theta$ denotes the phase constraint matrix, similar to that in Eq. (6.32). Note that, in the case discussed in §6.3, where quadrature harmonic forcing is considered, the phase constraint matrix restricts zero phase-shifts to the enforced harmonics; however, here, the phase constraint matrix enforces relationships between harmonic phase-shifts.

Therefore, the number of unknowns ($R_\mathcal{H}$ phase-shifts and $R_\mathcal{F}$ forcing amplitudes) matches the number of equations (given by the energy balancing, i.e. Eq. (6.63), and the phase constraints, i.e. Eq. (6.73)). Combining Eqs. (6.63) and (6.73), the harmonic-level energy-transfer analysis with quadrature physical forcing may be constructed in the same form as Eq. (6.35), i.e.

$$\mathbf{v} = \mathbf{A}^{-1}\mathbf{B}\,. \tag{6.74}$$

where

$$\mathbf{A} = \begin{bmatrix} \mathbf{E}_N^\dagger & \tilde{\mathbf{E}}_F^\dagger \\ \mathbf{C}_\theta & \mathbf{0} \end{bmatrix}, \quad \mathbf{B} = \begin{pmatrix} -\mathbf{E}_D^\dagger \\ \mathbf{0} \end{pmatrix}, \quad \mathbf{v} = \begin{pmatrix} \hat{\boldsymbol{\theta}} \\ \tilde{\mathbf{F}} \end{pmatrix}. \tag{6.75}$$

This allows the phase-shifts of all harmonics, $\hat{\boldsymbol{\theta}}$, and the physical forcing amplitudes, $\tilde{\mathbf{F}}$, to be computed via known parameters obtained from NNM solutions.

6.4.2 Example 2: a quadrature physical forcing case

To formulate the HETA for a quadrature physical forcing scenario, the two-mode beam model, schematically shown in Fig. 6.2, is again considered. Here a two-harmonic physical force is considered, given by

$$f(t) = F_1 \cos(\varOmega t) + F_2 \cos(3\varOmega t)\ , \tag{6.76}$$

which is applied to the part-span position at $L_1 = 0.1L$, such that the equations of motion are written

$$\ddot{q}_1 + d_1\dot{q}_1 + \omega_{n1}^2 q_1 + N_{q1}(q_1, q_2) = \phi_{\ell,1} f(t), \tag{6.77a}$$
$$\ddot{q}_2 + d_2\dot{q}_2 + \omega_{n2}^2 q_2 + N_{q2}(q_1, q_2) = \phi_{\ell,2} f(t), \tag{6.77b}$$

where the nonlinear forces are given by Eq. (6.10). The parameters of the system are the same as those considered in §6.2.3 and §6.3.4, given in Table 6.1. Each modal displacement, q_i, is approximated by three harmonics, namely the odd-numbered harmonics up to the

5^{th} order, i.e.

$$\mathcal{H}_1 = \{1,\, 3,\, 5\}\,, \qquad \mathcal{H}_2 = \{1,\, 3,\, 5\}\,, \tag{6.78}$$

such that

$$q_1 \approx u_{1,1} + u_{1,3} + u_{1,5}\,, \quad q_2 \approx u_{2,1} + u_{2,3} + u_{2,5}\,. \tag{6.79}$$

As with the example demonsrated in §6.3.4, firstly the known energy-transfer coefficients are assembled into vector or matrix forms. Using Eqs. (6.20a), (6.26a) and (6.28a), the vector of damping energy-transfer terms, $E_{Di,j}$, is given by

$$\mathbf{E}_D^\dagger = \begin{pmatrix} E^\dagger_{D1,1} \\ E^\dagger_{D1,3} \\ E^\dagger_{D1,5} \\ E^\dagger_{D2,1} \\ E^\dagger_{D2,3} \\ E^\dagger_{D2,5} \end{pmatrix} = \begin{pmatrix} \pi\omega d_1 U_{1,1}^2 \\ 9\pi\omega d_1 U_{1,3}^2 \\ 25\pi\omega d_1 U_{1,5}^2 \\ \pi\omega d_2 U_{2,1}^2 \\ 9\pi\omega d_2 U_{2,3}^2 \\ 25\pi\omega d_2 U_{2,5}^2 \end{pmatrix}. \tag{6.80}$$

The diagonal matrix of forcing energy coefficients, whose leading elements, $E^\dagger_{P\ell,i,j}$, are defined by Eq. (6.55), is given by

$$\mathbf{E}^\dagger_{P\ell} = \begin{bmatrix} E^\dagger_{P\ell,1,1} & 0 & 0 & 0 & 0 & 0 \\ 0 & E^\dagger_{P\ell,1,3} & 0 & 0 & 0 & 0 \\ 0 & 0 & E^\dagger_{P\ell,1,5} & 0 & 0 & 0 \\ 0 & 0 & 0 & E^\dagger_{P\ell,2,1} & 0 & 0 \\ 0 & 0 & 0 & 0 & E^\dagger_{P\ell,2,3} & 0 \\ 0 & 0 & 0 & 0 & 0 & E^\dagger_{P\ell,2,5} \end{bmatrix}, \tag{6.81}$$

The force reduction matrix, $\mathbf{C}_{P\ell}$, the modeshape coefficient matrix, $\boldsymbol{\phi}_\ell$, and the non-zero forcing amplitude vector, $\tilde{\mathbf{F}}$, may be obtained via equations from Eq. (6.55) to Eq. (6.60).

These are given by

$$\mathbf{C}_{P\ell} = \begin{bmatrix} 1 & 0 & 0 & 0 \\ 0 & 1 & 0 & 0 \\ 0 & 0 & 0 & 0 \\ 0 & 0 & 1 & 0 \\ 0 & 0 & 0 & 1 \\ 0 & 0 & 0 & 0 \end{bmatrix}, \ \boldsymbol{\phi}_\ell = \begin{bmatrix} \phi_{\ell,1} & 0 \\ 0 & \phi_{\ell,1} \\ \phi_{\ell,2} & 0 \\ 0 & \phi_{\ell,2} \end{bmatrix}, \ \tilde{\mathbf{F}}_\ell = \begin{pmatrix} F_1 \\ F_2 \end{pmatrix}. \tag{6.82}$$

Using Eq. (6.61), the matrix of forcing energy-transfer coefficients, $\tilde{\mathbf{E}}_F^\dagger$, is written

$$\tilde{\mathbf{E}}_{F\ell}^\dagger = \mathbf{E}_{P\ell}^\dagger \mathbf{C}_{P\ell} \boldsymbol{\theta}_\ell = \begin{bmatrix} \phi_{\ell,1} E^\dagger_{P\ell,1,1} & 0 \\ 0 & \phi_{\ell,1} E^\dagger_{P\ell,1,3} \\ 0 & 0 \\ \phi_{\ell,2} E^\dagger_{P\ell,2,1} & 0 \\ 0 & \phi_{\ell,2} E^\dagger_{P\ell,2,3} \\ 0 & 0 \end{bmatrix}, \tag{6.83}$$

Next, as in §6.3, the matrix of nonlinear energy-transfer coefficients may be obtained using Eqs. (6.24c), (6.26d) and (6.28d), i.e.

$$\mathbf{E}_N^\dagger = \begin{bmatrix} E^{\dagger(1,1)}_{N1,1} & E^{\dagger(1,3)}_{N1,1} & E^{\dagger(1,5)}_{N1,1} & E^{\dagger(2,1)}_{N1,1} & E^{\dagger(2,3)}_{N1,1} & E^{\dagger(2,5)}_{N1,1} \\ E^{\dagger(1,1)}_{N1,3} & E^{\dagger(1,3)}_{N1,3} & E^{\dagger(1,5)}_{N1,3} & E^{\dagger(2,1)}_{N1,3} & E^{\dagger(2,3)}_{N1,3} & E^{\dagger(2,5)}_{N1,3} \\ E^{\dagger(1,1)}_{N1,5} & E^{\dagger(1,3)}_{N1,5} & E^{\dagger(1,5)}_{N1,5} & E^{\dagger(2,1)}_{N1,5} & E^{\dagger(2,3)}_{N1,5} & E^{\dagger(2,5)}_{N1,5} \\ E^{\dagger(1,1)}_{N2,1} & E^{\dagger(1,3)}_{N2,1} & E^{\dagger(1,5)}_{N2,1} & E^{\dagger(2,1)}_{N2,1} & E^{\dagger(2,3)}_{N2,1} & E^{\dagger(2,5)}_{N2,1} \\ E^{\dagger(1,1)}_{N2,3} & E^{\dagger(1,3)}_{N2,3} & E^{\dagger(1,5)}_{N2,3} & E^{\dagger(2,1)}_{N2,3} & E^{\dagger(2,3)}_{N2,3} & E^{\dagger(2,5)}_{N2,3} \\ E^{\dagger(1,1)}_{N2,5} & E^{\dagger(1,3)}_{N2,5} & E^{\dagger(1,5)}_{N2,5} & E^{\dagger(2,1)}_{N2,5} & E^{\dagger(2,3)}_{N2,5} & E^{\dagger(2,5)}_{N2,5} \end{bmatrix}, \tag{6.84}$$

where the elements in this matrix may be computed using Eq. (6.20c).

The phase-shift constraints, defined in Eq. (6.72), may be assembled into matrix form as Eq. (6.73), where the matrix of phase-shift constraint coefficients, $\mathbf{C}_\theta$, and vector of phase-shifts, $\hat{\boldsymbol{\theta}}$, are given

$$\mathbf{C}_\theta = \begin{bmatrix} C_{\theta 1,1} & 0 & 0 & C_{\theta 2,1} & 0 & 0 \\ 0 & C_{\theta 1,3} & 0 & 0 & C_{\theta 2,3} & 0 \end{bmatrix}, \tag{6.85a}$$

$$\hat{\boldsymbol{\theta}} = \begin{pmatrix} \hat{\theta}_{11} & \hat{\theta}_{13} & \hat{\theta}_{15} & \hat{\theta}_{21} & \hat{\theta}_{23} & \hat{\theta}_{25} \end{pmatrix}^\intercal, \tag{6.85b}$$

where

$$
\begin{aligned}
C_{\theta 1,1} &= \phi_{\ell,1}^2 U_{1,1}^2 + \phi_{\ell,1}\phi_{\ell,2} U_{1,1} U_{2,1} \cos\left(\bar{\theta}_{1,1} - \bar{\theta}_{2,1}\right), \\
C_{\theta 2,1} &= \phi_{\ell,2}^2 U_{2,1}^2 + \phi_{\ell,2}\phi_{\ell,1} U_{2,1} U_{1,1} \cos\left(\bar{\theta}_{2,1} - \bar{\theta}_{1,1}\right), \\
C_{\theta 1,3} &= \phi_{\ell,1}^2 U_{1,3}^2 + \phi_{\ell,1}\phi_{\ell,2} U_{1,3} U_{2,3} \cos\left(\bar{\theta}_{1,3} - \bar{\theta}_{2,3}\right), \\
C_{\theta 2,3} &= \phi_{\ell,2}^2 U_{2,3}^2 + \phi_{\ell,2}\phi_{\ell,1} U_{2,3} U_{1,3} \cos\left(\bar{\theta}_{2,3} - \bar{\theta}_{1,3}\right).
\end{aligned}
$$

Combining equations from Eq. (6.80) to Eq. (6.85), the energy transfer analysis may be formulated in the form as Eq. (6.74). Therefore, the unknowns, i.e. the physical forcing amplitudes, $\tilde{\mathbf{F}}_\ell$, and the phase-shifts, $\hat{\boldsymbol{\theta}}$, may be computed. Here the results obtained from the HETA are compared with the forced responses obtained via the force appropriation technique, proposed in [90].

Figure 6.8 shows the solved parameters, i.e. physical forcing amplitudes, $|F_1|$ and $|F_2|$, and harmonic phase-shifts, i.e. $\hat{\theta}_{1,1}$, $\hat{\theta}_{1,3}$, $\hat{\theta}_{1,5}$, $\hat{\theta}_{2,1}$, $\hat{\theta}_{2,3}$ and $\hat{\theta}_{2,5}$. In all panels of Fig. 6.8, the predicted results obtained via HETA are shown as solid blue lines whilst the simulated results obtained using force appropriation are shown as red lines with dots. The forcing amplitudes obtained from both techniques are indistinguishable – see panels (a) and (e) in Fig. 6.8. Excellent agreement is generally achieved between analytical predictions and numerical simulations for most phase-shifts. Some discrepency lies in the prediction of $\hat{\theta}_{1,3}$ near the region where a strong internal resonance is shown between two linear modes (the *loop* region in panels (a) and (e)). This discrepancy may arise from the large phase-shift in this region, whilst this technique is derived based on the small phase-shift assumption. Nonetheless, the numerical results indicate a drastic change in the sign of phase-shift from positive to negative or vice versa, which is also captured by the results obtained from HETA. The other discrepancy lies in the prediction of $\hat{\theta}_{2,1}$ near the natural frequency region, however, the trend over response frequency is again captured in good agreement.

In addition, it can be observed that some harmonics, i.e. $u_{1,3}$, $u_{1,5}$ and $u_{2,5}$, exhibit large harmonic phase-shifts near the internally resonant region. However, these harmonics have negligible amplitudes, as such their effect on the overall response is still minimal. In contrast, the fundamental components, i.e. $u_{1,1}$ and $u_{2,3}$, which show large-amplitude and significant effect on the responses, have small phase-shifts along the predicted branch. As with that discussed in §6.3.4, tracking the evolutions of phase-shifts can estimate the applicability of energy balancing analysis when using NNMs to interpret forced responses.

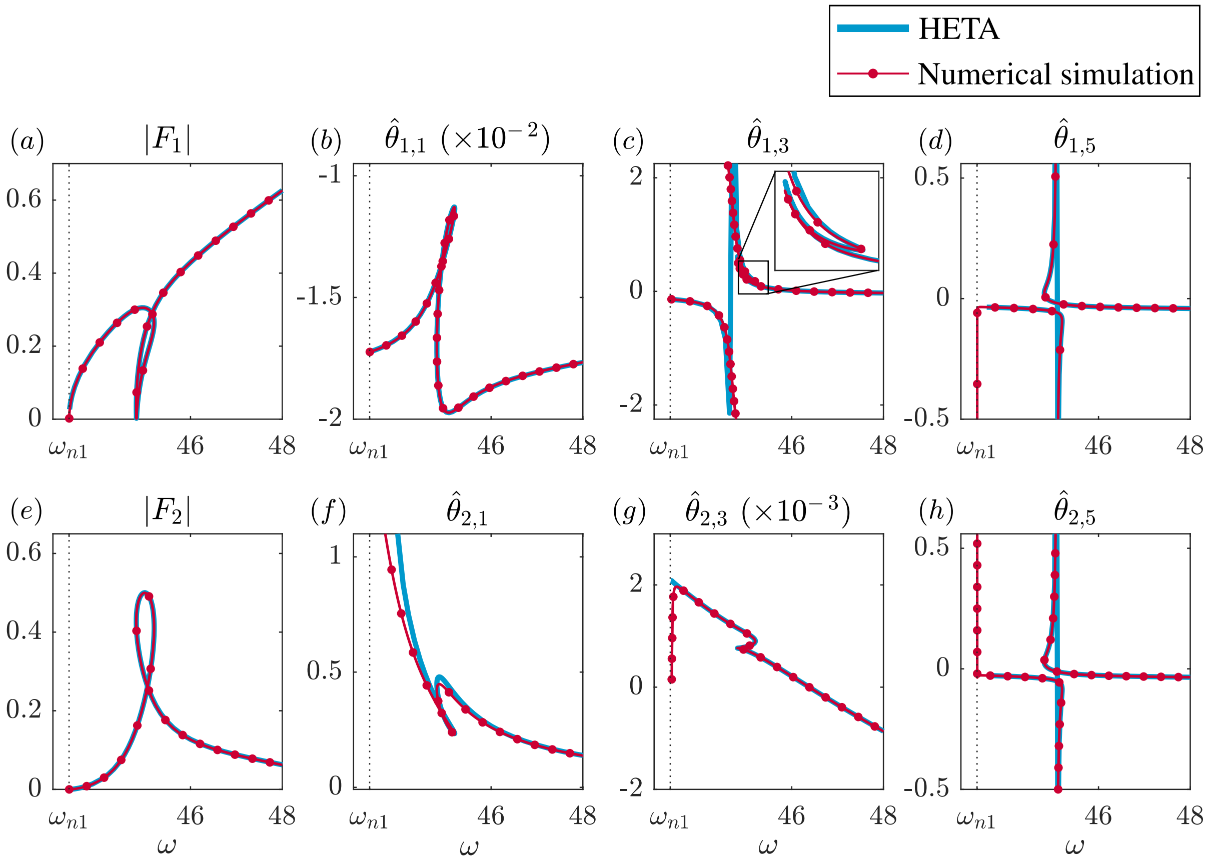

Fig. 6.8 Comparison between the predictions of HETA (using a three-harmonic approximation for each mode) and the numerically-simulated forced responses. (a) and (e) The response frequency, ω, against the forcing amplitudes F_1 and F_2 respectively. (b), (c), (d), (f), (g) and (h) The response frequency, ω, against the phase-shift parameters, $\hat{\theta}_{1,1}$, $\hat{\theta}_{1,3}$, $\hat{\theta}_{1,5}$, $\hat{\theta}_{2,1}$, $\hat{\theta}_{2,3}$ and $\hat{\theta}_{2,5}$ respectively. In all panels, the blue lines represent analytically-predicted values (using the NNM data), the red lines (with dots) represent the numerical results and the dotted-black line denotes the first linear natural frequency.

In practice, force appropriation has been extensively employed in nonlinear modal tests to identify NNMs via forced responses [89, 90, 162, 163, 144]. To achieve this, a limited number of actuators are tuned to exhibit quadrature with the displacement at each excitation point, similar to the example considered in this section. This cannot satisfy the perfect forcing condition (all harmonics of all modes are forced in quadrature) and must lead to deviations between NNMs and forced resonances; such deviations, as demonstrated previously, can be captured by harmonic phase-shifts. In the example presented in Fig. 6.8, the internally resonant region can be accurately captured via force appropriation, which is indicated by the small phase-shifts of large-amplitude fundamental components. This means that the energy balancing analysis, proposed in this chapter, can also be used to aid nonlinear modal tests in designing an appropriate number of excitations and their arrangement based on the criterion of small phase-shifts.

6.4.3 Example 3: isola prediction

Determining the existence of the isolated FRCs, or isolas, is of great importance in the analysis of nonlinear responses [107, 141, 142]; one example lies in the application of a vibration absorber such as a NLTMD, where isolas can significantly affect the vibration suppression performance, as discussed in §2.3.1. Using the energy balancing analysis to predict the existence of isolas has proven to be an efficient method [141]. However, as discussed using examples in Fig. 6.3*b*, when responses contain multiple significant harmonics, predicting the existence of isolas can be challenging – a key motivation for the study in this chapter. In this section, an improved and more robust method is demonstrated in predicting the existence of isolas using the proposed energy balancing analysis.

For comparison, the example system, considered in §6.2, is revisited. The nonlinear beam is modelled by a two-mode model, described by Eqs. (6.9) and (6.10), where the parameters are given in Table 6.1. A mono-point, single-harmonic forcing, expressed by Eq. (6.8), is applied to the part-span position at $L_1 = 0.2L$, the same excitation scenario as the case in Fig. 6.3*b*. Note that the lower-amplitude forcing, denoted by the dashed green line in Fig. 6.3*b*, represents the case where the modal-level energy-transfer analysis is unable to capture the existence of isola.

To formulate the HETA, each mode is approximated by three harmonics, i.e. the odd-numbered harmonics up to the 5th order, the same as considered in §6.4.2. Therefore, the formulation, in this example, is equivalent to that given in §6.4.2 with $F_2 = 0$, and hence it is not re-constructed here. The solved parameters, i.e. forcing amplitude, F_1, and phase-shifts, $\hat{\theta}_{1,1}$, $\hat{\theta}_{1,3}$, $\hat{\theta}_{1,5}$, $\hat{\theta}_{2,1}$, $\hat{\theta}_{2,3}$ and $\hat{\theta}_{2,5}$, are shown as blue lines in Fig. 6.9. In panel (a), the predicted forcing amplitudes, solved via the single-harmonic META, are shown as a green line in comparison with that obtained via the multi-harmonic HETA. Near the natural frequency, the difference between results obtained via the META and HETA is indistinguishable; as response frequency increases, the discrepancy between the two lines grows, indicating an increasing significance of the harmonics.

Considering a forcing amplitude of $F_1 = 0.18$, the HETA predicts one intersection, also shown in Fig. 6.3*b* (the existence of an isola is not captured); whilst the META predicts three intersections, labelled by solid dots and marked by (i), (ii), and (iii) in each

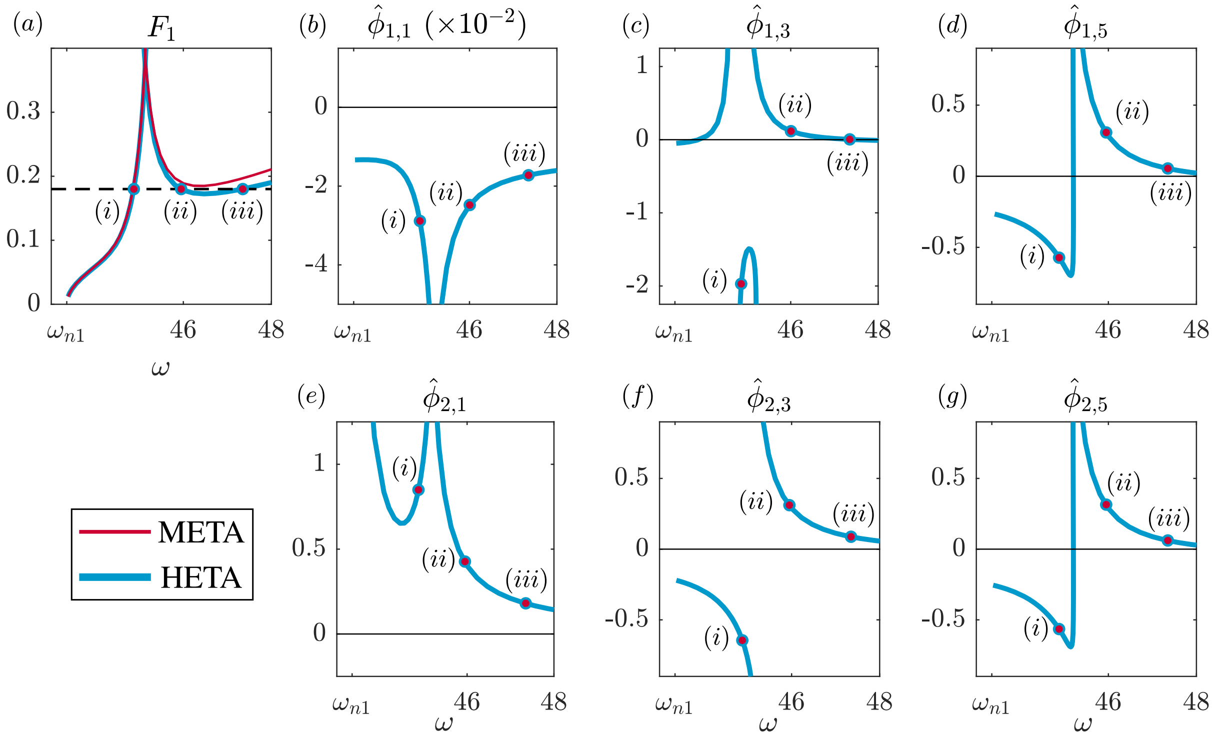

Fig. 6.9 Predicting the existence of an isola using Harmonic-level Energy-Transfer Analysis (HETA). The HETA-predicted forcing amplitude and phase-shifts are shown as blue lines in each panel; the META-predicted forcing amplitude is shown as a red line for comparison in panel (*a*). Considering a forcing amplitude of $F_1 = 0.18$, denoted by a dashed line in panel (*a*), the resonant crossing points on the NNM branch are labelled by solid dots and marked by (*i*), (*ii*) and (*iii*).

panel of Fig. 6.9. This indicates that there are three resonant crossing points between the backbone curve and forced responses. The perturbations, from NNM solutions to resonances, for these three predictions can be evaluated by referring to the phase-shifts from panels (*b*) to (*g*). In each panel, it is shown that the phase-shift at point (*i*) is the largest of the three, whilst that at point (*iii*) is the smallest. Thus, it can be expected that the largest perturbation, from an NNM solution to a resonance, occurs at point (*i*), and the smallest one is at point (*iii*).

To verify these results, the forced responses of the beam system are computed via numerical continuation and shown as red lines in the left panel of Fig. 6.10, along with which the backbone curve is shown as a blue line. Three HETA-predicted crossing points on the backbone curve are likewise denoted by solid dots, whilst the numerically obtained resonances are labelled by '×'. It can be observed that the resonances, predicted via the HETA, show great agreement with the numerical simulations, capturing the

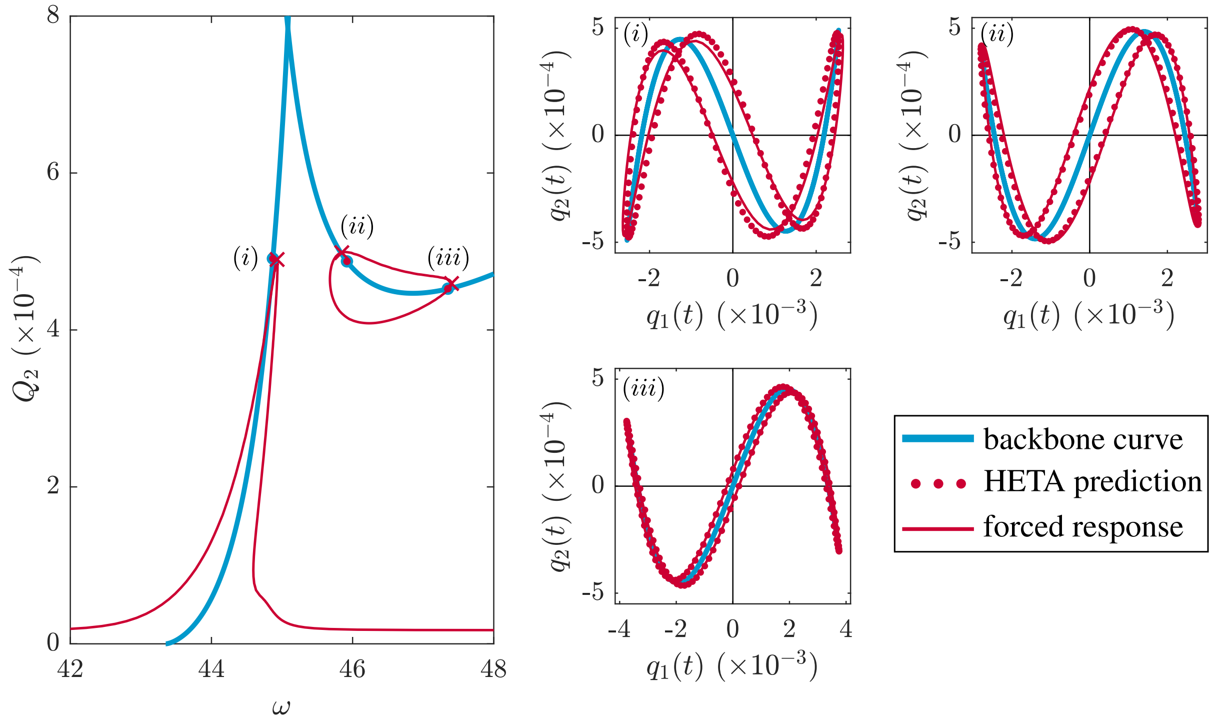

Fig. 6.10 Verification and comparison of the HETA-predicted results using forced responses. In the left panel, the forced responses of the beam system with $F_1 = 0.18$ is computed via numerical continuation and shown as red lines. The HETA-predicted crossing points on the NNM branch are shown as solid dots, denoted by (*i*), (*ii*) and (*iii*); whilst the numerically obtained resonances are labelled by '×' signs. In the right panels, the time-parameterised responses for crossing points on the backbone curve, the HETA-predicted resonances and the numerically obtained resonances are compared.

resonances on both the primary response curve and the isola. To aid comparison, the corresponding time-parameterised responses for the NNM solutions, HETA-predicted resonances (accommdating the NNM solutions with predicted phase-shifts), and the numerically obtained resonances are shown in the right-hand panels. In these panels, the perturbations from NNM solutions to resonances are accurately quantified by the phase-shifts – HETA-predicted responses well match the numerically computed resonances.

In this example, predicting the existence of an isola is considered via the HETA. Results show that the HETA can accurately predict all the resonant crossing points between the backbone curve and forced responses, showing an improved accuracy when compared with the META. The perturbations from crossing points on the backbone curve to the resonances are also shown to be accurately quantified by the phase-shifts. This provides an approximation of the forced response by accommodating the NNM solutions with predicted phase-shifts.

6.5 Summary

From an energy-based perspective, studies in this chapter have extended the scope of undamped and unforced periodic responses, considered in previous chapters, to forced and damped scenarios. This was achieved by considering the energy balancing analysis, across multiple harmonics of modal components in an NNM, to establish the relationships between NNMs and forced responses. The proposed method has demonstrated its applicability, efficiency, and robustness in using NNMs to interpret forced resonances when the smallness assumption of phase-shifts is satisfied.

In §6.2, an overview was given of the mechanism of energy balancing during periodic responses of a nonlinear system – the balancing of net energy transfer (arising from nonlinearity, external forcing, and damping) in and out of the system. Based on this mechanism, the proposed mode-level energy-transfer analysis in [139] has been demonstrated in predicting forced responses to highlight its applicability and limitations. Due to a single-harmonic assumption, it can be constructed in an analytical framework that allows for efficient and accurate prediction only when harmonic contributions are negligible; however, inaccurate and even erroneous predictions have also been observed when harmonics show a significant effect on the responses.

In §6.3, the limitations arising from the single-harmonic assumption have been overcome by constructing the multi-harmonic energy-transfer analysis; in addition, the semi-analytical framework preserves the computational efficiency. This energy balancing analysis was established by viewing forced responses as phase-shift perturbations from NNMs. Combining the energy balancing principle with force reduction and phase-shift constraints, a closed-form solution has been analytically derived. With known inputs of NNM solutions, the proposed method has shown its applicability and efficiency in predicting resonances when compared to numerical simulations.

In §6.4, the multi-harmonic energy balancing technique has been extended to more practical scenarios where the excitations are in quadrature with displacements at physical locations. The predicted results were compared to that achieved via force appropriation, where a great agreement can be generally achieved. As such quadrature forcing scenarios are extensively used in nonlinear modal tests via force appropriation, the proposed method can guide the positioning of actuators in experiment designs.

Also in §6.4, the proposed method has been demonstrated in predicting an isola that contains multiple significant harmonics. It outperforms the single-harmonic method and shows an improved accuracy and robustness – the locations of resonances and the deviations from NNMs to resonances were both accurately predicted.

In implementing this technique, the applicability and accuracy of the proposed method can be directly evaluated via the computed harmonic phase-shifts (the perturbations from NNMs to forced responses). By accommodating the known NNMs with phase-shifts, an approximation of forced responses can be obtained, which could be used for further studies, e.g. stability and bifurcation analysis. Owing to the semi-analytical framework, this technique can be easily extended to account for more complex scenarios, e.g. multiple harmonics of multiple modes of NNMs, and multiple forcing harmonics at multiple locations, without adding much computational effort.

Chapter 7

Understanding targeted energy transfer using backbone curves

In this chapter:

- An overview of Targeted Energy Transfer (TET) is given to establish the relationships between key features of TET and backbone curves. It also highlights the use of backbone curves in interpreting damped transient responses.
- The backbone curve topology, required to realise TET, is interpreted from a symmetry-breaking perspective. By exploring the bifurcation scenarios, such a required backbone curve can be identified from other backbone curve topologies.
- Based on the mechanism of symmetry breaking, an analytical method is proposed to identify the physical parameter conditions in order to realise TET in a structure-NES system.
- The uncovered symmetry-breaking mechanism is verified and demonstrated using a nonlinear beam system.

Publications related to this work:

D. Hong, T. L. Hill, S. A. Neild, 2021. Understanding targeted energy transfer from a symmetry breaking perspective, *Proceedings of the Royal Society A: Mathematical, Physical and Engineering Sciences*, 477(2251) 20210045.

7.1 Introduction

Nonlinear normal modes, or backbone curves, represent the underlying conservative dynamics of a nonlinear system and are widely used in nonlinear modal analysis of damping devices, e.g. the Nonlinear Energy Sink (NES) [216, 45, 46], and flexible structures, e.g. the cables [129], beams [36–38], and micro-electromechanical systems [264, 116, 124]. Some examples have also been studied in previous chapters.

One important reason that underpins the extensive applications of backbone curves lies in the connections between backbone curves and forced periodic responses, established via the energy balancing analysis – see Ref. [139] and Chapter 6. Using this method, backbone curves can be employed for efficient analysis of complex forced periodic behaviours, e.g. detecting the existence of isolas [107, 141, 142], predicting forced responses [262, 137], interpreting the significance of NNMs in forced responses [143, 140], to name a few.

In addition, as discussed in §2.2.3, connections between the backbone curves and damped transient responses can be established through the concept of resonant capture – for weakly coupled nonlinear systems, the transient responses can be locked in the neighbourhood of backbone curves [57, 146]. Using this mechanism, experimental tests can make use of free damped responses to identify backbone curves [90]; conversely, the conceptually simpler and computationally cheaper backbone curves can be used to interpret complex damped transient behaviours. One important application lies in the so-called Targeted Energy Transfer (TET) [57, 146, 206]. The concept of TET relates to the irreversible transfer of energy from one component to another. Building on the concept of resonant capture, many studies have employed an NNM-based framework to investigate TET, see §2.3.1 for a survey.

In engineering practice, making use of TET, the NES is extensively employed for vibration suppression by irreversibly absorbing the vibration from the primary system. In the geometric sense, the essential asymmetry, i.e. mass and potential asymmetry between the primary system and NES, leads to localised NNMs (at the primary system and the NES respectively), which bring about TET [205, 265, 266]. Such an asymmetry is also a practical prerequisite as the energy-dissipating device (the NES) is usually designed to be a much smaller size when compared to the primary system. To explore the fundamental mechanism that underpins the required asymmetry, this chapter employs a symmetry-breaking perspective to trace how the required conditions stem from a perfect symmetric case. This study builds upon the concept of resonant capture and uses backbone curves to interpret damped transient TET. From insights obtained in previous chapters on backbone curve topologies, the necessary backbone curves, as well as parameter conditions, for the realisation of TET are identified. To achieve this, the rest of this chapter is organised as follows.

In §7.2, an overview of the TET phenomenon is given by considering a classic example system that consists of a linear primary system and a nonlinearisable NES. Using time-domain responses, the key features of TET are presented – the occurrence of irreversible energy transfer when the initial energy is above a critical level. Next, based on the concept of resonant capture, it will be demonstrated how these features of damped transient responses can be understood by considering the underlying conservative backbone curves.

In §7.3, discussions continue on the example system (a linear primary system with a nonlinearisable NES). The study here first introduces a symmetrised model, from which the essentially asymmetric example system is interpreted from a symmetry-breaking perspective. The backbone curve topology, underpinning the existence of TET, is then studied by considering how it may be viewed as an evolution from a symmetric case. Discussions in this section reveal how the bifurcation splitting, induced by symmetry breaking, governs the features of TET.

In §7.4, the example system is extended to a general two-mode case. From insights obtained in previous sections, the backbone curve topologies are explored from a symmetry-breaking perspective. By accounting for bifurcation scenarios, the necessary backbone curve topology (which underpins the realisation of TET), found in §7.3, is identified from other topologies. Additionally, analytical modal parameter conditions are derived to distinguish the system that exhibits TET from others.

The achievements will then be demonstrated using two example systems. The first example is a structure-NES system where the primary system is not necessarily linear and the NES is not necessarily nonlinearisable – a generalisation of that considered in §7.3. By mapping the modal parameter conditions to physical parameters, the realisation of TET in the structure-NES system is investigated. Approximate analytical conditions are derived to determine the required parameters of the NES in order to exhibit TET. The second example system is a real physical nonlinear beam system. This example is used to verify and demonstrate the uncovered symmetry-breaking mechanism in the realisation of TET. It will be shown how symmetry breaking leads to the required backbone curves; additionally, numerical simulations are presented to verify the existence of TET.

Finally, this chapter is closed with a summary in §7.5.

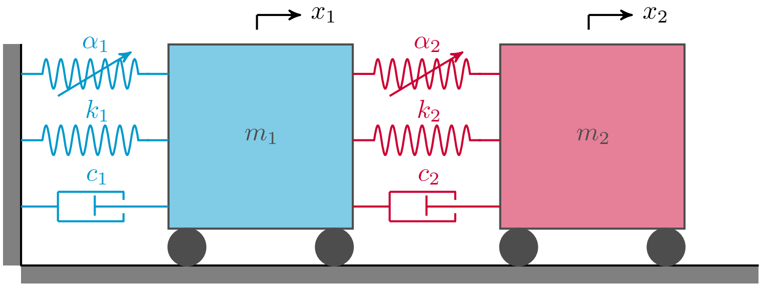

Fig. 7.1 A schematic diagram of a primary system, shown in blue, with a Nonlinear Energy Sink (NES), shown in red. The primary system, with mass value m_1, has displacement x_1 and is grounded by a linear spring, a cubic nonlinear spring and a damper, with coefficients k_1, α_1, and c_1 respectively. The NES, with mass value m_2, has displacement x_2 and is attached to the primary system by a linear spring, a cubic nonlinear spring and a damper, with coefficients k_2, α_2, and c_2 respectively.

7.2 Targeted Energy Transfer

As discussed in §2.3.1 and §7.1, the TET phenomenon represents the nonlinear behaviour where the energy is transferred irreversibly from the energy-imparted component to another component during transient responses when the energy input is above a critical value [57, 146, 206]. In this section, an overview of the realisation and features of TET is given, highlighting the connections between the damped transient responses (capturing TET) and the underlying conservative periodic responses, i.e. backbone curves.

To study TET, the example system that consists of a primary system and a NES is considered. The NES is attached to the primary system and for the energy to flow from the primary system to the NES, from which the energy is dissipated. In line with much of the literature [57, 146, 45], the primary system is modelled here as a mass-spring oscillator that captures the targeted mode of the full system. Schematically shown in Fig. 7.1, this primary system (shown in blue), has mass value m_1, displacement x_1, and is grounded by a linear spring, a linear damper, and a cubic nonlinear spring with coefficients k_1, c_1, and α_1 respectively. The NES (shown in red) is represented as the second mass with mass values, m_2, where $m_2 \ll m_1$, and displacement x_2. This device is attached to the primary system via a linear spring, a linear damper, and a cubic nonlinear spring with coefficients k_2, c_2, and α_2 respectively. The dynamics of the system can be described by the equations of motion

$$m_1\ddot{x}_1 + c_1\dot{x}_1 + c_2\left(\dot{x}_1 - \dot{x}_2\right) + k_1x_1 + k_2\left(x_1 - x_2\right) + \alpha_1x_1^3 + \alpha_2\left(x_1 - x_2\right)^3 = 0\,, \tag{7.1a}$$

$$m_2\ddot{x}_2 + c_2\left(\dot{x}_2 - \dot{x}_1\right) + k_2\left(x_2 - x_1\right) + \alpha_2\left(x_2 - x_1\right)^3 = 0\,, \tag{7.1b}$$

Table 7.1 Parameters of the example system, schematically shown in Fig. 7.1.

m_1	m_2	k_1	k_2	α_1	α_2	c_1	c_2
1	0.05	1	0	0	1	0.005	0.005

where $\dot{\bullet}$ and $\ddot{\bullet}$ represent the first and second time-derivatives of displacement, i.e. velocity and acceleration respectively. Many studies of TET consider a linear primary system, with $\alpha_1 = 0$, and a NES with $k_2 = 0$ [57, 146, 45]. [1] This *classic* case is first considered here for demonstration; whilst the more general case, where the primary system consists of nonlinearity, $\alpha_1 \neq 0$, and where the NES has a linear spring component, $k_2 \neq 0$, will be considered in later sections. Such a general case is reflective of more practical application scenarios, e.g. a nonlinear beam with a NES [267], a drill-string system with a NES [268], as well as in experimental setups [136, 269]. Here, the example system has parameters given in Table 7.1. Note that, the NES has a much smaller mass value than the primary system $m_2/m_1 = 0.05$ – a practical requirement in design that the damping device is much smaller than the system it is protecting.

To study the phenomenon of TET, the primary system is given a non-zero initial velocity (whilst the system is in equilibrium and the velocity of the NES is zero), representing an energy impulse to the primary system. Given an initial velocity of the primary system, the time-domain responses of the system can be computed via inbuilt ODE solvers in Matlab. When $\dot{x}_1(0) = 0.1$, the time histories of the primary system and NES are presented in Fig. 7.2*a*. From the top panel, it can be observed that the responses are dominated by the primary system, i.e. the responses over time of the primary system are much larger than that of the NES. In addition to the displacement evolutions over time, the dominancy of the primary system can also be observed from an energy-based perspective by considering the instantaneous energy ratio in the NES, defined as

$$\begin{aligned} E_{\text{ins,NES}} &= \frac{E_{\text{NES}}}{E_{\text{P}} + E_{\text{NES}}} \\ &= \frac{\frac{1}{2}m_2\dot{x}_2^2 + \frac{1}{2}k_2\left(x_2 - x_1\right)^2 + \frac{1}{4}\alpha_2\left(x_2 - x_1\right)^4}{\frac{1}{2}m_1\dot{x}_1^2 + \frac{1}{2}k_1x_1^2 + \frac{1}{4}\alpha_1x_1^4 + \frac{1}{2}m_2\dot{x}_2^2 + \frac{1}{2}k_2\left(x_2 - x_1\right)^2 + \frac{1}{4}\alpha_2\left(x_2 - x_1\right)^4}, \end{aligned} \tag{7.2}$$

where E_{P} and E_{NES} denote the instantaneous energy of the primary system and NES respectively. In this case, the time-evolution of $E_{\text{ins,NES}}$ is shown in the bottom panel of

---

[1] The differences between a NES and a NLTMD (considered in Chapter 3) should be noted: unlike a NES, a NLTMD has a linear spring, with which the eigenfrequency of the NLTMD can be *tuned* to a target mode of the full system.

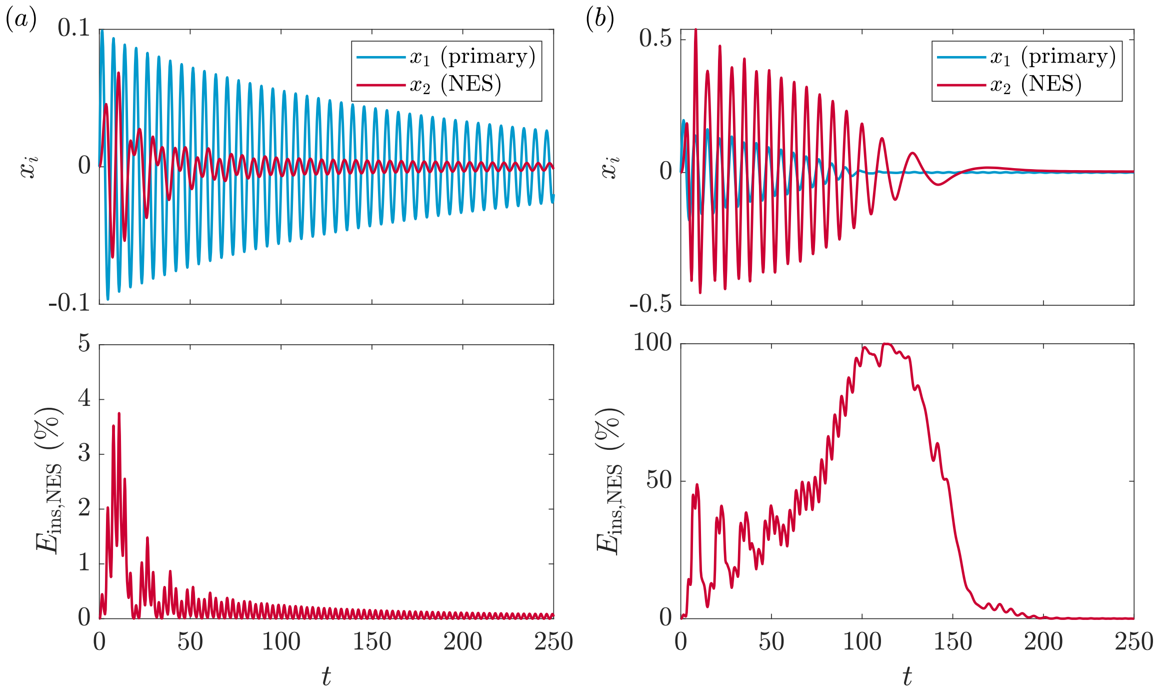

Fig. 7.2 Reponses and energy transfer in the time domain for the example system, represented by Fig. 7.1, with parameters listed in Table 7.1. Response histories for the primary system and NES (top panels), and instantaneous energy carried by the NES (bottom panels) with an initial velocity of $\dot{x}_1(0) = 0.1$ and $\dot{x}_1(0) = 0.2$ in the primary system, shown in panels (*a*) and (*b*) respectively.

Fig. 7.2*a*, where only a very limited amount of energy (less than five percent of the total energy) is transferred to the NES over time.

Next, the initial velocity is increased from $\dot{x}_1(0) = 0.1$ to $\dot{x}_1(0) = 0.2$, and again the response histories of the two components and the instantaneous energy ratio carried by the NES are computed and shown in Fig. 7.2*b*. In contrast to the low-initial-velocity case in Fig. 7.2*a*, significant differences are observed. For this high-initial-velocity case, the time-domain responses are dominated by the NES – it has larger-amplitude responses than the primary system; likewise, a more significant energy ratio can be seen in the NES – see the bottom panel of Fig. 7.2*b*, where, in addition, a more complex phenomenon can be observed. Based on the time-domain response features, the high-initial-velocity responses may be divided into the following stages [45]:

1. **Nonlinear beating** (0 → 50s): for the first stage, the energy is transferring back and forth between the primary system and the NES, seen from the oscillation of $E_{\text{ins,NES}}$ in the bottom panel of Fig. 7.2*b*.

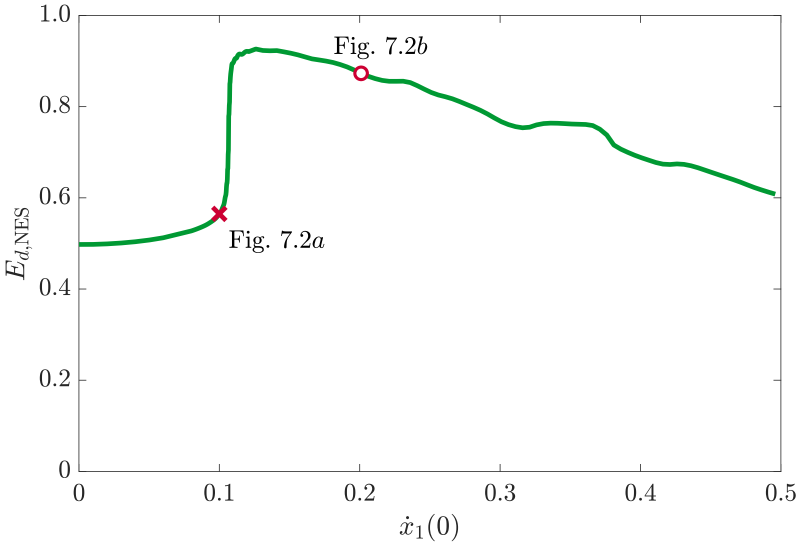

Fig. 7.3 Energy ratio dissipated by the NES with respect to a varied initial velocity in the primary system for the example system with parameters listed in Table 7.1. Two example cases, studied above via Fig. 7.2, are labelled by '×' and '○' respectively.

2. **Resonant capture, or resonant decay** (50 → 120s): following the nonlinear beating, the energy is irreversibly transferred to the NES, until almost all energy is localised in the NES.
3. **Escape** (after about 120s): in the final stage, the majority of the remaining energy is returned back to the primary system, when the total energy has already decayed to a low level.

Shown in the bottom panel of Fig. 7.2*b*, for this high-initial-velocity case, the energy, imparted to the primary system, is transferred irreversibly to the NES during transient responses of resonant capture, or resonant decay.

Indeed, whether the majority of the initial energy impulse remains in the primary system, shown in Fig. 7.2*a*, or is transferred to the NES, Fig. 7.2*b*, is determined by a critical energy level [57, 45, 147]. To find this critical value, one can track the energy dissipation by the NES with respect to a varied initial impulse. Firstly, the energy dissipated by the NES over the responses can be defined as

$$E_{d,\mathrm{NES}} = \left. \frac{c_2 \int_0^T \left(\dot{x}_2 - \dot{x}_1\right)^2 \mathrm{d}t}{c_2 \int_0^T \left(\dot{x}_2 - \dot{x}_1\right)^2 \mathrm{d}t + c_1 \int_0^T \dot{x}_1^2 \mathrm{d}t} \right|_{T \to \infty}, \tag{7.3}$$

Note that, to compute $E_{d,\text{NES}}$, the infinite upper limit T is approximated to a finite value such that the total energy in the system is decayed to less than 1% of the initial value. In Fig. 7.3, the critical energy level can be clearly seen – the steep transition seen around $\dot{x}_1(0) = 0.11$; whilst the low- and high-initial-velocity cases, studied above, are located on either side of this critical energy level.

In summary, when the initial energy impulse in the primary system is below the critical level, the majority of the energy remains in the primary system with little being transferred to the NES. Conversely, when the initial energy impulse in the primary system is above the critical level, the majority of energy may be irreversibly transferred to the NES. The above-critical-value case is related to the realisation of TET [57, 146], characterised by the three-stage nonlinear transient phenomenon.

Up to this point, it has been demonstrated how the realisation of TET can be captured by the time-domain responses and time-evolution of energy localisations, see Fig. 7.2. Additionally, this damped transient phenomenon can also be captured by the underlying conservative periodic dynamics, or backbone curves. Their relationship, termed resonant capture, has been investigated in [216, 45] – when TET occurs, the transient responses are locked in the neighbourhood of NNM manifolds. This relationship is further explored here to demonstrate how the key features of TET, namely the critical energy level and the behaviour of irreversible energy transfer, link to backbone curves.

To achieve this, the backbone curves of the example system are computed via numerical continuation [99]. They are then mapped to the initial velocity space[2], $(\dot{x}_2(0),\ \dot{x}_1(0))$, shown as solid lines in Fig. 7.4*a* – both of the primary backbone curves show $1:1$ synchronous, or Fourier-real, responses with one in-phase, $S^{+}_{\mathcal{R},1}$, and the other one anti-phase, $S^{-}_{\mathcal{R},1}$.[3] Note that, besides the primary branches where the system exhibits 1:1 responses, tongue branches where the system shows $m : n$ resonance $(m, n \in \mathbb{Z}^{+})$ can also be observed, see the *loop* regions in the embedded plot of Fig. 7.4*a*. As will be shown in the following, the resonant capture, observed in the example case in Fig. 7.2*b*, is related

---

[2] A backbone curve in the initial velocity space denotes the projection when all modes achieve their maximum velocities. As the NES system only has synchronous, or Fourier-real, backbone curves, the maximum velocities are reached when all modes pass through the equilibrium position. As such, the energy in the system consists of only kinetic energy without potential energy. This energy composition is similar to the initial conditions considered in this chapter where an initial velocity is given to the primary system when the system is at equilibrium; therefore, such a projection is termed the initial velocity space.

[3] The $1:1$ Fourier-real backbone curves, $S^{\pm}_{\mathcal{R},1}$, are equivalent to that termed $1:1$ synchronous backbone curves, $S^{\pm}_{1,2}$, in Chapters 3 and 4. To see how the Fourier-real and -complex terminologies generalise the synchronous and asynchronous ones, the interested reader is directed to Chapter 5.

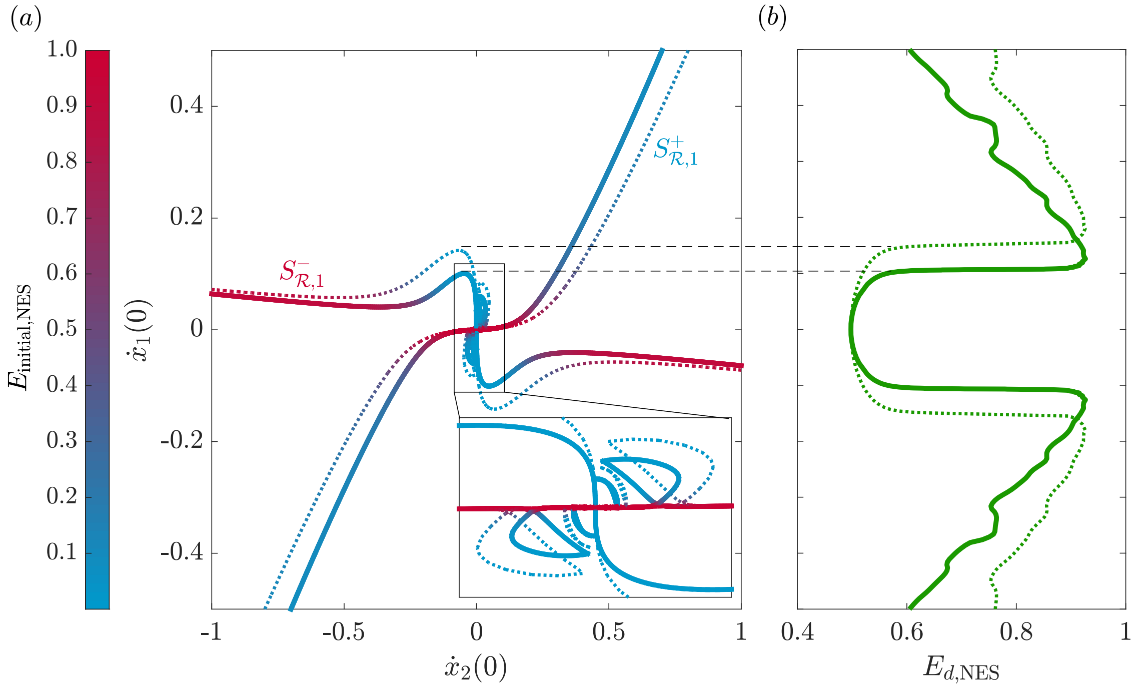

Fig. 7.4 Critical energy level, in the targeted energy transfer, captured by the backbone curves of the example system, shown in Fig. 7.1, where all parameters aside from α_2 are given in Table 7.1, and where $\alpha_2 = 1$ and $\alpha_2 = 0.5$ for the solid and dotted lines respectively. (*a*) Backbone curves in the initial velocity space $(\dot{x}_2(0), \dot{x}_1(0))$. The colour scale, representing the backbone curves, shows the energy in the NES, scaled by total energy in the system. (*b*) Energy ratio dissipated by the NES with a varied initial energy, indicated by an initial velocity, $\dot{x}_1(0)$, in the primary system.

to fundamental, or 1 : 1, resonant capture that is locked in the neighbourhood of the primary branches. It is such a case that will be further explored in the following, whilst for other types of resonant capture, the interested reader may refer to [45]. Additionally, in Fig. 7.4*a*, these backbone curves are shown using a colour scale representing the energy in the NES, scaled by the total energy in the system, for the solutions passing through the equilibrium, i.e.

$$E_{\text{initial,NES}} = \left[\frac{1/2 \cdot m_2 \dot{x}_2^2}{1/2 \cdot m_1 \dot{x}_1^2 + 1/2 \cdot m_2 \dot{x}_2^2} \right]_{t=0} . \tag{7.4}$$

In this figure, the energy localisation in the primary system is denoted in blue on the colour scale; whilst that in the NES is denoted in red. Consequently, the topology of the primary backbone curves can be characterised, considering the energy localisation:

1. Fourier-real, anti-phase backbone curve, $S^-_{\mathcal{R},1}$: at low energy levels, the energy is localised in the primary system (blue), whilst at high energy levels, the energy is localised in the NES (red).
2. Fourier-real, in-phase backbone curve, $S^+_{\mathcal{R},1}$: at low energy levels, the energy is localised in the NES (red), whilst at high energy levels, the energy is localised in the primary system (blue).

To establish the links between the backbone curve topology and the features of TET, the total energy ratio dissipated by the NES for a varied initial velocity, computed via Eq. (7.3), is presented in Fig. 7.4*b* (in comparison to the backbone curves in panel (*a*)). It can be seen that the critical energy level, determining whether TET can be achieved or not, is related to the *fold* on $S^-_{\mathcal{R},1}$, denoted by the dashed line. Besides the example system, whose backbone curves are shown as solid lines, another case where $\alpha_2 = 0.5$ is also shown in Fig. 7.4 using dotted lines, where again, the critical energy level is related to the fold. It will be demonstrated in §7.3 that the generation of this fold may be seen as the result of bifurcation splitting due to symmetry breaking.

In addition to the existence of a critical energy level, another feature of TET lies in the irreversible energy transfer during transient resonant capture. To demonstrate the relationships between backbone curves and this behaviour, the time-domain responses in Fig. 7.2 are first projected to the initial velocity space where $x_1(t) = 0$ (when $\dot{x}_1 > 0$). Using these examples, the NES responses with an initial energy impulse below the critical level (Fig. 7.2*a*) and that above the critical level (Fig. 7.2*b*) are shown as red dots in Fig. 7.5*a* and 7.5*b* respectively. These dots are connected via solid red lines to indicate the path of the decaying response (with initial states labelled '×'). Next, combining the transient response decays (Fig. 7.5) and the energy localisation features of backbone curves (Fig. 7.4), the link between the irreversibility of the TET phenomenon and the backbone curves can be explained, namely,

1. When the initial energy in the primary system is below the critical energy level, the transient response of the system is locked by and decays down $S^-_{\mathcal{R},1}$ (Fig. 7.5*a*), which exhibits energy localisation in the primary system at low energy levels (Fig. 7.4*a*). As such, the majority of the energy input remains in the primary system over time with very limited amount being transferred to the NES, as the example in Fig. 7.2*a*.
2. When the initial energy in the primary system is above the critical energy level, following the nonlinear beating, the resonant capture represents transient responses

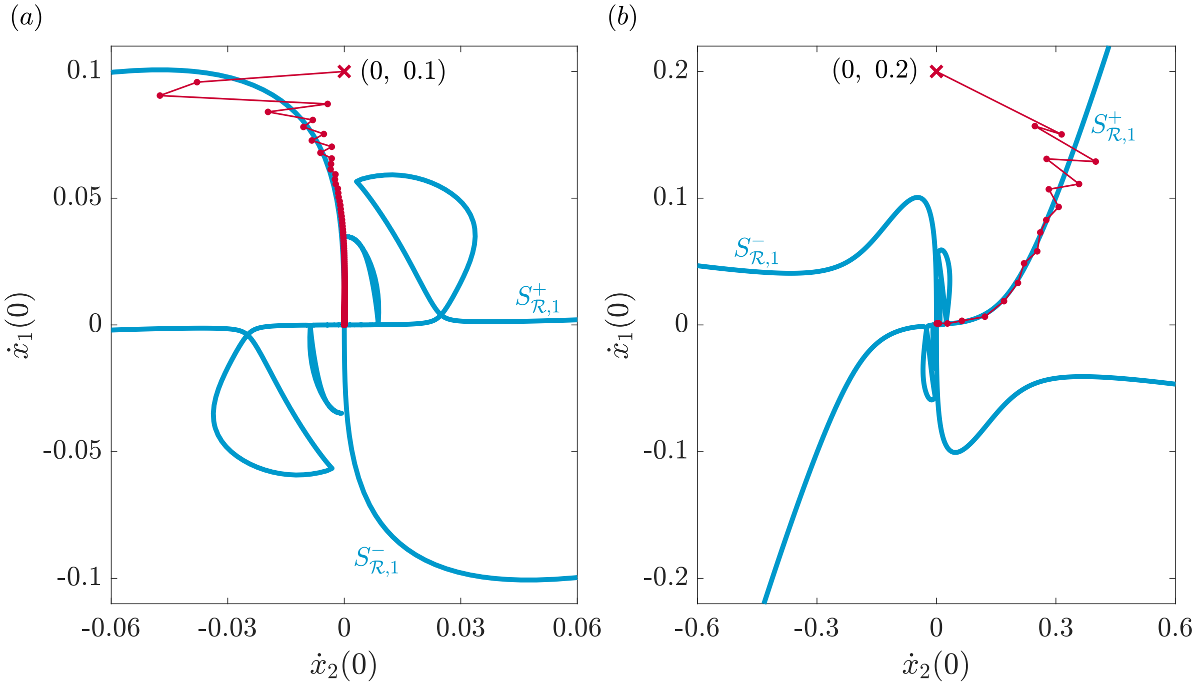

Fig. 7.5 Resonant decay captured by the backbone curves for the example system, shown in Fig. 7.1, where all parameters are given in Table 7.1. The backbone curves of the system are shown as solid blue lines; the initial conditions with non-zero velocity in the primary system are marked by '×'; and resonant decays are represented by extreme values, where $x_1 = 0$ (when $\dot{x}_1 > 0$), as red dots, and connected by thin-red lines to indicate the decaying path. (*a*) Resonant decay of the system when an initial velocity, $\dot{x}_1(0) = 0.1$, is in the primary system, where the time histories are shown in Fig. 7.2*a*. (*b*) Resonant decay of the system when an initial velocity, $\dot{x}_1(0) = 0.2$, is in the primary system, where the time histories are shown in Fig. 7.2*b*.

that are locked by and decaying down $S^+_{\mathcal{R},1}$ (Fig. 7.5*b*). Note that, in this case, the response decays down the fundamental branch, exhibiting the feature of 1 : 1 resonant capture, without triggering subharmonic resonant captures. As indicated by the energy localisation characteristics of $S^+_{\mathcal{R},1}$ in Fig. 7.4*a*, resonant decay down $S^+_{\mathcal{R},1}$ relates to change of energy from the primary system, at high energy levels, to the NES, at low energy levels. Therefore, the resonant decay exhibits irreversible energy transfer from the primary system to the NES, as observed in Fig. 7.2*b*.

The example here shows the connections between features of TET and backbone curves. To assist in understanding this connection through the use of backbone curves, it is useful to consider the system in its modal representation as this domain is normally used in backbone curve analysis [79, 31, 130, 245]. In addition, using the modal representative also allows symmetry of the system to be identified via coefficients of the nonlinear term – as demonstrated in Chapters 3 to 5; this assists the analysis of TET from a symmetry-breaking perspective.

The dynamics of the two-mass system can be transformed from the physical coordinates, given by Eq. (7.1), to the modal domain by introducing linear modal transform (i.e. Eq. (3.11)). Consequently, the modal equations of motion can be derived

$$\ddot{q}_1 + d_1\dot{q}_1 + d_{12}\dot{q}_2 + \omega_{n1}^2 q_1 + \mathit{\Psi}_4 q_1^3 + 3\,\mathit{\Psi}_1 q_1^2 q_2 + \mathit{\Psi}_3 q_1 q_2^2 + \mathit{\Psi}_2 q_2^3 = 0\,, \tag{7.5a}$$

$$\ddot{q}_2 + d_{12}\dot{q}_1 + d_2\dot{q}_2 + \omega_{n2}^2 q_2 + \mathit{\Psi}_1 q_1^3 + \mathit{\Psi}_3 q_1^2 q_2 + 3\,\mathit{\Psi}_2 q_1 q_2^2 + \mathit{\Psi}_5 q_2^3 = 0\,, \tag{7.5b}$$

where ω_{n1} and ω_{n2} are the first and second linear natural frequencies, d_1, d_2, and d_{12} denote modal damping coefficients, and $\mathit{\Psi}_i$ represent coefficients of the nonlinear terms. As the underlying conservative system is equivalent to the two-mass oscillator considered in Chapter 3, these $\mathit{\Psi}_i$ are defined by expressions (3.13) with $\alpha_3 = 0$. In this example case, where the NES does not have a linear spring, i.e. $k_2 = 0$, the modeshape matrix, given in Eq. (3.11), is an anti-diagonal matrix, i.e. $\phi_{11} = 0$ and $\phi_{22} = 0$. As such, $x_1 = \phi_{12}q_2$ and $x_2 = \phi_{21}q_1$, which means the responses in the primary system and the NES, x_1 and x_2, are exactly captured by modal coordinates, q_2 and q_1, respectively. Therefore, in the *initial modal velocity space* $(\dot{q}_1(0),\ \dot{q}_2(0))$, the primary backbone curves are topologically equivalent to those shown in Fig. 7.4*a*, and may be described:

1. Fourier-real, anti-phase backbone curve, $S^-_{\mathcal{R},1}$: at low energy levels, the energy is localised in q_2 (the primary system), whilst at high energy levels, the energy is localised in q_1 (the NES).
2. Fourier-real, in-phase backbone curve, $S^+_{\mathcal{R},1}$: at low energy levels, the energy is localised in q_1, whilst at high energy levels, the energy is localised in q_2,

and as expected, such backbone curve topology captures the features of TET using the modal representative of the system.

Through investigations for TET in applications to a NES, the *damped transient responses* of nonlinear systems are shown to be captured by the backbone curves via the mechanism of resonant capture.[4] As such, it provides a method to account for the realisation of TET – by identifying the required backbone curve topology that locks the transient responses, during which the energy is irreversibly transferred from the primary system to the NES. Nonetheless, with the required backbone curves identified, a practical-relevant issue can

---

[4] Note that, this is compared to that considered in Chapter 6, where the connections between *forced damped periodic responses* and backbone curves are established.

arise – how is such backbone curve topology mapped to the physical parameters of the system?

As demonstrated in §7.1, the essential asymmetry brings about backbone curves with such energy localisation properties that lead to TET [205, 265, 266]. By looking at how such backbone curve topology evolves from a symmetric case due to symmetry breaking, the essential asymmetry will be interpreted in the following studies. From this symmetry-breaking perspective, the required physical parameters will also be identified for the example system in Fig. 7.1. In addition, using the insights, the realisation of TET (through symmetry breaking) will be presented in a nonlinear beam system.

7.3 Relating targeted energy transfer to symmetry breaking

In this section, the example two-mass system, which consists of a linear primary system ($\alpha_1 = 0$) and a nonlinearisable NES ($k_2 = 0$), is used to demonstrate the TET phenomenon from a symmetry-breaking perspective. This is achieved by introducing a symmetrised model – a degenerated model of the example system. This section provides a geometric perspective to interpret TET and, in addition, offers a quantitative method to distinguish the systems that exhibit TET from general nonlinear systems, detailed in §7.4.

As demonstrated in §7.2, backbone curves can capture damped transient responses where TET occurs. Here, to compute backbone curves, i.e. unforced undamped periodic solution branches, the damping terms in Eq. (7.5) are first removed to give the equations of motion for the underlying conservative system, i.e.

$$\ddot{q}_1 + \omega_{n1}^2 q_1 + \Psi_4 q_1^3 + 3\nu \Psi_1 q_1^2 q_2 + \Psi_3 q_1 q_2^2 + \nu \Psi_2 q_2^3 = 0\,, \tag{7.6a}$$

$$\ddot{q}_2 + \omega_{n2}^2 q_2 + \nu \Psi_1 q_1^3 + \Psi_3 q_1^2 q_2 + 3\nu \Psi_2 q_1 q_2^2 + \Psi_5 q_2^3 = 0\,, \tag{7.6b}$$

where coefficients of nonlinear terms are given by

$$\Psi_1 = \phi_{21}^3 \phi_{12} \alpha_2\,, \quad \Psi_2 = \phi_{21} \phi_{12}^3 \alpha_2\,, \quad \Psi_3 = 3\phi_{21}^2 \phi_{12}^2 \alpha_2\,, \quad \Psi_4 = \phi_{21}^4 \alpha_2\,, \quad \Psi_5 = \phi_{12}^4 \alpha_2\,, \tag{7.7}$$

and where Ψ_1 and Ψ_2 are multiplied by ν, i.e. a ‘symmetry-breaking’ parameter with $0 \leqslant \nu \leqslant 1$. The case with $\nu = 1$ represents the underlying conservative dynamics of the system and is termed the *original model*. As demonstrated in Chapter 3, a system with non-zero Ψ_1 and Ψ_2 is dynamically asymmetric and only has mixed-mode backbone curves with imperfect bifurcations; instead, a dynamically symmetric system has zero Ψ_1 and Ψ_2. For the original model of the system, it should be highlighted that no parameter combinations of the example system can lead to $\Psi_1 = \Psi_2 = 0$, see expressions (7.7). Therefore, to relate this essentially asymmetric model to symmetry breaking, a corresponding *symmetrised model* is introduced by enforcing $\nu = 0$ whilst the other modal parameters remain unchanged. As such, the original model may be seen as an evolution from the symmetrised model due to symmetry breaking, (i.e. where ν becomes non-zero). Whilst introducing the parameter ν is artificial, and cannot be realised in the original two-mass system, it allows the symmetry to be continued directly in a single parameter. Thus, the physically unobtainable gap of symmetry can be filled to identify the symmetry-breaking mechanism that leads to the realisation of TET. In addition, as will be shown in §7.4.2, the uncovered symmetry-breaking mechanism can be applied beyond the specific two-mass systems considered here.

To find the backbone curves via Eq. (7.6), the harmonic balance method is used. Firstly, one can observe that the backbone curves for the two-mass oscillator exhibit synchronous responses, see Figs. 7.4 and 7.5, and Refs. [169, 136]; it means that the phase relationships between modal coordinates are either in-phase or anti-phase. In this case, the modal solution is approximated by its leading-order term, i.e. the fundamental harmonic, given by

$$q_i \approx u_i = U_i \cos\left(\omega_{ri} t\right), \tag{7.8}$$

where u_i denotes the fundamental component of q_i, and where U_i and ω_{ri} represent the amplitude and response frequency of u_i respectively. Note that this solution is equivalent to that given by Eq. (3.5) with assumed phase relationships (either in-phase or anti-phase) substituted.

Next, considering the case where TET is realised via fundamental resonant capture, the response frequencies of the two modal coordinates are assumed to be equal, namely, $\omega_{r1} = \omega_{r2} = \omega$. With modal responses in expression (7.8) substituted into equations of motion (7.6), and the non-resonant terms removed, the expressions for computing backbone curves may be obtained after some algebraic manipulations, given by

$$4\left(\omega_{n1}^2 - \omega^2\right) U_1 + 3\,\Psi_4 U_1^3 + 3\,\Psi_3 U_1 U_2^2 + 3\nu p\left(\Psi_2 U_2^3 + 3\,\Psi_1 U_1^2 U_2\right) = 0\,, \tag{7.9a}$$

$$4\left(\omega_{n2}^2 - \omega^2\right) U_2 + 3\,\Psi_5 U_2^3 + 3\,\Psi_3 U_1^2 U_2 + 3\nu p\left(\Psi_1 U_1^3 + 3\,\Psi_2 U_1 U_2^2\right) = 0\,, \tag{7.9b}$$

where $p = +1$ and -1, denote in-phase and anti-phase relationships between two modal coordinates respectively. As the system is equivalent to that considered in Chapter 3, the derivations of backbone curves are not given here, instead some key results are directly presented. For details of derivations, the reader is directed to Chapter 3.

7.3.1 Backbone curves of the symmetrised model

Firstly, the symmetrised case where $\nu = 0$ is considered. In this case, two nontrivial solution sets may be found with respect to either

$$\begin{aligned} &(a)\ S_1\text{: } U_1 \neq 0 \text{ and } U_2 = 0, \text{ and } S_2\text{: } U_1 = 0 \text{ and } U_2 \neq 0; \\ \text{or } &(b)\ S^{\pm}_{\mathcal{R},1}\text{: } U_1 \neq 0 \text{ and } U_2 \neq 0, \end{aligned}$$

where S_1 and S_2 denote single-mode backbone curves, whilst $S^{+}_{\mathcal{R},1}$ and $S^{-}_{\mathcal{R},1}$ represent in-phase and anti-phase backbone curves respectively (also known as mixed-mode backbone curves). Analytical frequency-amplitude expressions for S_1, S_2 and $S^{\pm}_{\mathcal{R},1}$ are given by Eqs. (3.22), (3.23) and (3.24) respectively in §3.4.1.

In symmetric cases, these mixed-mode backbone curves may be seen as solution branches bifurcating from the single-mode backbone curves via Bifurcation Points (BPs). Here, the bifurcation on S_1 is denoted BP1; whilst that on S_2 is denoted BP2. The frequency-amplitude expressions of these bifurcations have also been derived in §3.4.1, they are given by

$$\text{BP1 on } S_1: \quad \omega^2 = \frac{\Psi_4\omega_{n2}^2 - \Psi_3\omega_{n1}^2}{\Psi_4 - \Psi_3}, \quad U_1^2 = \frac{4\left(\omega_{n2}^2 - \omega_{n1}^2\right)}{3\left(\Psi_4 - \Psi_3\right)}, \tag{7.10a}$$

$$\text{BP2 on } S_2: \quad \omega^2 = \frac{\Psi_3\omega_{n2}^2 - \Psi_5\omega_{n1}^2}{\Psi_3 - \Psi_5}, \quad U_2^2 = \frac{4\left(\omega_{n2}^2 - \omega_{n1}^2\right)}{3\left(\Psi_3 - \Psi_5\right)}. \tag{7.10b}$$

Note that, these branch points can exist when the frequency-amplitude relationships are associated with real positive amplitude and frequency, i.e.

$$\text{existence of BP1 on } S_1: \quad \Psi_4 - \Psi_3 > 0, \tag{7.11a}$$

$$\text{existence of BP2 on } S_2: \quad \Psi_3 - \Psi_5 > 0. \tag{7.11b}$$

Using conditions (7.11), the bifurcation scenarios and the backbone curve topologies of the example system can be determined by coefficients of the nonlinear terms (7.7). After some algebraic manipulation, it is revealed that BPs can exist on both S_1 and S_2 when

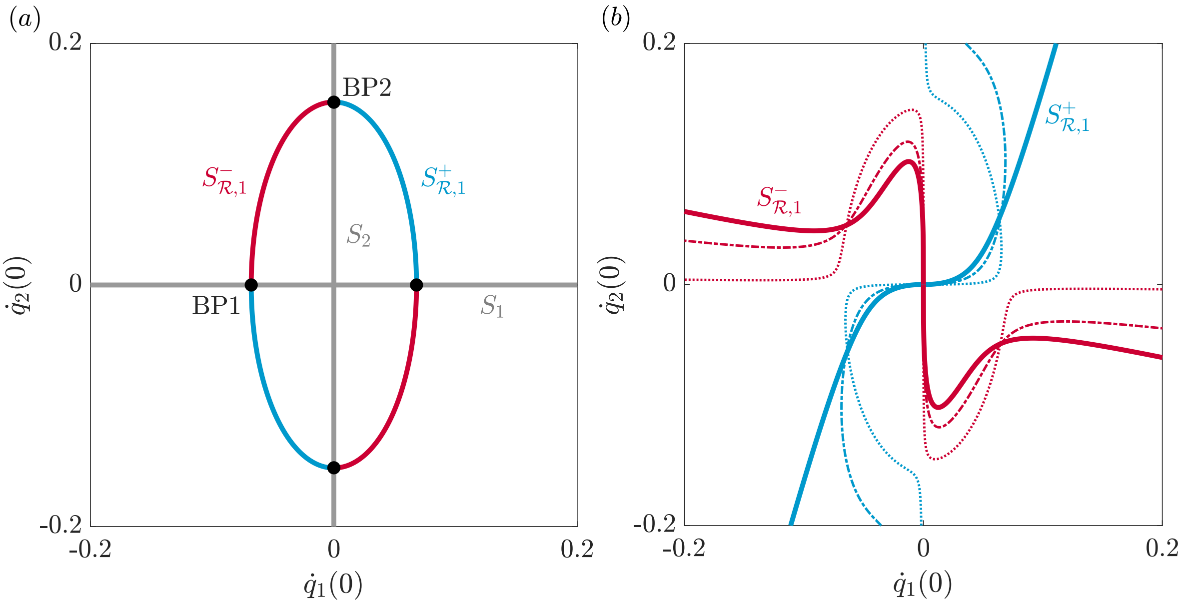

Fig. 7.6 Symmetry-breaking interpretation of the backbone curves that capture the realisation of targeted energy transfer for the example system with parameters given in Table 7.1. (*a*) Backbone curves for the symmetrised model in the initial modal velocity space $(\dot{q}_1(0), \dot{q}_2(0))$. The single-mode backbone curves, S_1 and S_2, are denoted by grey lines. The in-phase and anti-phase backbone curves, $S^{+}_{\mathcal{R},1}$ and $S^{-}_{\mathcal{R},1}$, are denoted by blue and red curves respectively. The bifurcation points are denoted by black dots, labelled BP1 and BP2. (*b*) Evolutions of backbone curves due to symmetry breaking in the initial modal velocity space $(\dot{q}_1(0), \dot{q}_2(0))$. The backbone curves for the example system are shown by solid curves. Two intermediate asymmetric cases, with $\nu = 0.05$ and $\nu = 0.5$, are shown by dotted and dot-dashed curves respectively.

$m_2 < m_1/3$, which can usually be satisfied for the application of a NES, where the NES is a small mass compared to the primary system ($m_2 \ll m_1$). The backbone curves for the symmetrised model of the example system, with parameters given in Table 7.1, are shown in Fig. 7.6*a* in the initial modal velocity space, $(\dot{q}_1(0),\ \dot{q}_2(0))$, – two single-mode backbone curves, S_1 and S_2, are connected by mixed-mode backbone curves, $S^{\pm}_{\mathcal{R},1}$, via BPs.

7.3.2 Backbone curves of the asymmetric model

Following the symmetrised case, the asymmetric case with non-zero Ψ_1 and Ψ_2 is now considered. Due to non-zero Ψ_1 and Ψ_2, single-mode backbone curves, S_1 and S_2, are no longer exist, instead, only mixed-mode backbone curves can be found. The frequency-amplitude relationships can be obtained by rearranging Eqs. (7.9a) and (7.9b), which gives

$$\omega^2 = \omega_{n1}^2 + \frac{3}{4}\left[\Psi_4 U_1^3 + \Psi_3 U_2^2 U_1 + p\nu\left(\Psi_2 U_2^3 + 3\,\Psi_1 U_1^2 U_2\right)\right] U_1^{-1}, \tag{7.12a}$$

$$\begin{aligned} 0 = &\left(-3p\nu\,\Psi_2 U_1^{-1}\right) U_2^4 + 3\left(\Psi_5 - \Psi_3\right) U_2^3 + \left[9p\nu\left(\Psi_2 - \Psi_1\right) U_1\right] U_2^2 + \\ &\left[4\omega_{n2}^2 - 4\omega_{n1}^2 + 3\left(\Psi_3 - \Psi_4\right) U_1^2\right] U_2 + 3p\nu\,\Psi_1 U_1^3. \end{aligned} \tag{7.12b}$$

Here, the backbone curves for the original asymmetric case ($\nu = 1$), as well as two intermediate asymmetric cases ($\nu = 0.5$ and $\nu = 0.05$), are computed via Eq. (7.12) and shown in Fig. 7.6*b* for comparison to the symmetrised case ($\nu = 0$) in panel (*a*). Figure 7.6 shows how the backbone curve topology for the original model may be seen as an asymmetric evolution from that in panel (*a*) due to symmetry breaking – it splits the bifurcation points on single-mode backbone curves, S_1 and S_2, and results in one in-phase and one anti-phase backbone curve, $S_{\mathcal{R},1}^{+}$ and $S_{\mathcal{R},1}^{-}$.

As demonstrated in §7.2 for the two-mass system, the backbone curve topology captures the key features of TET, i.e. the critical energy level and resonant capture (where the irreversible energy transfer occurs). From a symmetry-breaking perspective, the generation of backbone curve topology that underpins the realisation of TET may be understood via Fig. 7.6:

1. **the generation of the critical-energy-level-related fold on $S_{\mathcal{R},1}^{-}$**: the critical energy level, shown in Fig. 7.4*b*, is captured by the fold on $S_{\mathcal{R},1}^{-}$. The generation of this fold may be seen as the result of BP2 (on S_2) splitting due to symmetry breaking, shown in Fig. 7.6.

2. **the generation of the irreversible-energy-transfer-related backbone curve, $S_{\mathcal{R},1}^{+}$**: TET triggered by fundamental resonant capture represents resonant decay follows the in-phase backbone curve, $S_{\mathcal{R},1}^{+}$, which exhibits energy localisation in q_2 at high energy levels, and in q_1 at low energy levels. This transition of energy localisation, an analogue to the irregularity-caused modal veering [37, 270, 137], may be seen as a result of bifurcation splitting caused by symmetry breaking.

Introducing a symmetrised model through parameter ν, the realisation of TET is interpreted using backbone curves from a symmetry-breaking perspective. This provides a mechanism to understand how the backbone curves of a structure-NES system, which exhibits TET, may evolve from the symmetric case – two single-mode backbone curves interconnected by two mixed-mode backbone curves via bifurcation points. By understanding how the simpler, symmetric case is related to the asymmetric case exhibiting

TET, the fundamental properties leading to TET may be studied in greater detail and, therefore, it can provide a method to differentiate a system that exhibits TET from others.

Studies in this section have focused on a two-mass system where the primary system is linear and the NES has no linear component ($\alpha_1 = 0$ and $k_2 = 0$); whilst, in the following section, the example system is extended to general two-mode cases, among which the systems that exhibit TET are identified.

7.4 Identifying systems that exhibit TET

In §7.3, the special backbone curves that underpin the realisation of TET have been investigated. Due to parameter restrictions, the example system exhibits *only* one backbone curve topology, presented in Fig. 7.6. However, in practice, a system may exhibit different backbone curve topologies due to different bifurcation scenarios, for example, the symmetric cases considered in Chapters 3, 4, and 5. In this section, the special case is extended to a general two-mode system by removal of the parameter restrictions; by investigating the bifurcation scenarios, the required backbone curve topology to exhibit TET is identified from general cases. Note that discussions here focus on TET realised via 1 : 1 Fourier-real resonant capture; thus, they serve as a direct extension to the case considered in previous sections.

For such a general case, its backbone curve topology is investigated again from a symmetry-breaking perspective by studying the asymmetric evolutions of backbone curves. It is recalled that the backbone curve topology for a symmetric case is governed by its bifurcation conditions, determined by expressions (7.11). In this case, there are four different bifurcation conditions, namely

$$\begin{aligned}
&\text{with both BP1 and BP2}: && \Psi_4 - \Psi_3 > 0 \quad \text{and} \quad \Psi_3 - \Psi_5 > 0\,, && \text{(7.13a)}\\
&\text{with BP1 and without BP2}: && \Psi_4 - \Psi_3 > 0 \quad \text{and} \quad \Psi_3 - \Psi_5 < 0\,, && \text{(7.13b)}\\
&\text{without BP1 and with BP2}: && \Psi_4 - \Psi_3 < 0 \quad \text{and} \quad \Psi_3 - \Psi_5 > 0\,, && \text{(7.13c)}\\
&\text{without both BP1 and BP2}: && \Psi_4 - \Psi_3 < 0 \quad \text{and} \quad \Psi_3 - \Psi_5 < 0\,. && \text{(7.13d)}
\end{aligned}$$

Four corresponding backbone curve topologies can be computed via Eqs. (3.22), (3.23) and (3.24) and shown in Fig. 7.7*a*, where the vertical axis, i.e. $\Psi_3 - \Psi_5 = 0$, denotes the critical condition for existence of BP2, whilst the horizontal axis, i.e. $\Psi_4 - \Psi_3 = 0$, denotes that for the existence of BP1. Note that backbone curves shown in the initial

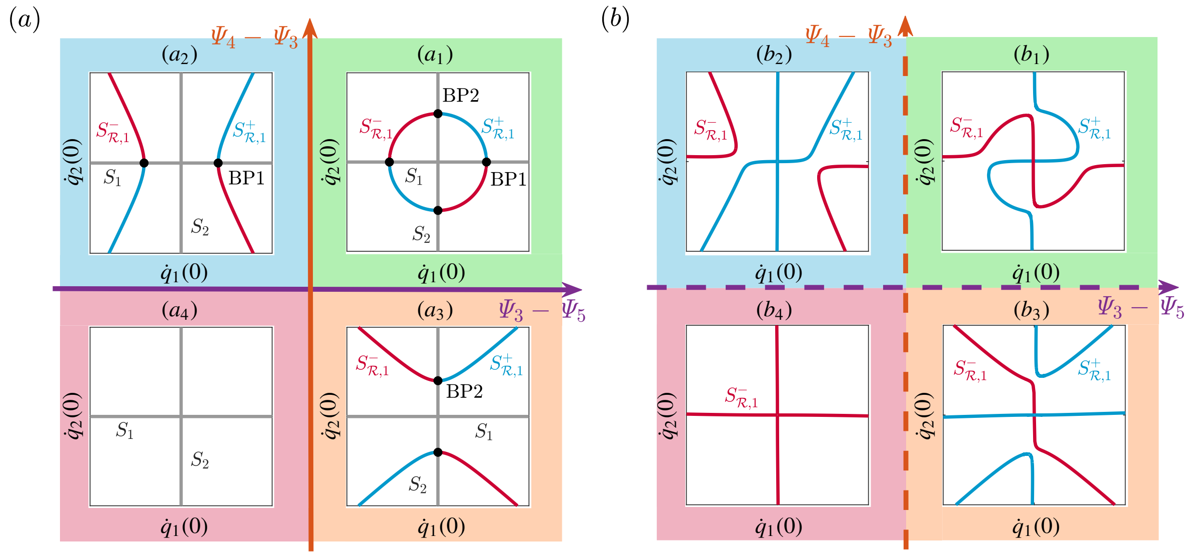

Fig. 7.7 Evolutions of backbone curve topologies due to symmetry breaking. (a) Backbone curve topologies in initial modal velocity space, $(\dot{q}_1(0), \dot{q}_2(0))$, for the symmetrised model with $\nu = 0$. The axes denote the critical boundaries for the existence of bifurcations, defined by Eq. (7.11). The single-mode backbone curves, S_1 and S_2, are shown as grey lines, the in-phase and anti-phase backbone curves, $S^+_{\mathcal{R},1}$ and $S^-_{\mathcal{R},1}$, are shown as blue and red curves respectively. Bifurcations on S_1 and S_2 are denoted by black dots, labelled BP1 and BP2 respectively. (a_1) (the first quadrant) S_1 and S_2 are connected by $S^+_{\mathcal{R},1}$ and $S^-_{\mathcal{R},1}$ via BP1 and BP2. (a_2) (the second quadrant) $S^+_{\mathcal{R},1}$ and $S^-_{\mathcal{R},1}$ bifurcate from S_1 via BP1. (a_3) (the fourth quadrant) $S^+_{\mathcal{R},1}$ and $S^-_{\mathcal{R},1}$ bifurcate from S_2 via BP2. (a_4) (the third quadrant) Two single-mode backbone curves, S_1 and S_2, without bifurcations. (b) Backbone curve topologies in initial modal velocity space, $(\dot{q}_1(0), \dot{q}_2(0))$, for asymmetric cases perturbed from symmetrised model with $\nu = 0.05$. Backbone curve topologies in panels $(b_1) \rightarrow (b_4)$ may be seen as evolutions from those in panel (a), due to symmetry breaking.

velocity space in Fig. 7.7 may be seen as a mapping of that in the frequency-amplitude plot [143]. The advantages of presenting backbone curves in the initial velocity space lie in two aspects: it has a direct connection to the initial state, or initial energy, of the primary system; the fold of the backbone curve can be directly related to the critical energy level, a key feature of the targeted energy transfer.

For any system in the first quadrant, it exhibits a backbone curve topology that S_1 and S_2 are interconnected by $S^{\pm}_{\mathcal{R},1}$ via BP1 and BP2. The structure-NES system, with $\alpha_1 = 0$ and $k_2 = 0$, has a symmetrised model locating in this quadrant, as discussed in §7.3.1. In addition to this case, three other cases, i.e. with BP1 and without BP2 (the second quadrant), without BP1 and with BP2 (the fourth quadrant), and without both BP1 and BP2 (the third quadrant), may also be identified. For any system in the second or the fourth quadrant, it has backbone curves in panels (a_2) or (a_3) – the mixed-mode backbone curves, $S^{\pm}_{\mathcal{R},1}$, bifurcate from the single-mode backbone curve, S_1 or S_2, and extend to higher energy levels. Whilst for a system in the third quadrant, only two single-mode backbone curves, S_1 and S_2, are observed, as neither BP1 nor BP2 exists, see panel (a_4). As with parameter changes, the system may cross the axes (boundaries), leading to a change in backbone curve topology. For example, when the system crosses the axis from the first quadrant to the second quadrant, the bifurcations, denoted BP2, degenerate to infinite frequency and amplitude, leading to a change of backbone curve topology from panels (a_1) to (a_2).

Symmetry breaking is then introduced to the symmetric case to study the asymmetric evolutions of these backbone curves. The backbone curves for an asymmetric case may be computed via Eq. (7.12). With $\nu = 0.05$, the asymmetric evolutions of the symmetric examples (in Fig. 7.7*a*) are shown in Fig. 7.7*b*. Note that, for asymmetric cases, the axes are used to approximately demonstrate the evolution of backbone curve topologies, rather than the exact boundaries. Panel (b_1) shows the same topology as that for the example system in Fig. 7.6*b*. Whilst for those in panels (b_2) and (b_3), the split of bifurcations results in two primary backbone curves (passing through the origin) and one isolated backbone curve. In panel (b_4), the two single-mode backbone curves, S_1 and S_2, in panel (a_4), evolve to mixed-mode backbone curves, $S^{-}_{\mathcal{R},1}$.

For these asymmetric cases in Fig. 7.7*b*, aside from the backbone curves in panel (b_1), which show the same topology as those seen in the example system considered in previous sections, other backbone curve topologies, in panels $(b_2) \rightarrow (b_4)$, exhibit fundamentally different features in energy localisation. With an initial energy in q_1 (or q_2), systems with backbone curves shown in panels $(b_2) \rightarrow (b_4)$ do not show the necessary energy localisation features in backbone curves to exhibit TET, and hence energy remains in q_1 (or q_2) without being transferred to the other mode.

From this symmetry-breaking perspective, to identify the system that exhibits TET from general systems is to distinguish the backbone curve topology shown in panel (b_1) from all cases in Fig. 7.7*b*. This can also be achieved by tracing the degenerated symmetric cases where these asymmetric cases are evolved from, i.e. by distinguishing the symmetric topology in panel (a_1) from those in Fig. 7.7*a*.

In the following sections, these insights are used to identify TET in nonlinear systems. The first example (in §7.4.1) is an extension of that considered in previous discussions, namely a general structure-NES system where α_1 and k_2 are not necessarily zero. In this case, the required physical parameters to realise TET are derived. The other example (in §7.4.2) is a nonlinear beam system, where it will be demonstrated how symmetry breaking leads to the realisation of TET.

7.4.1 Identifying the structure-NES system that exhibits TET

The discussions above focused on identifying the TET-required backbone curves for a general two-mode system in the modal domain, without considering the physical parameter conditions to realise TET. To relate the modal parameter conditions (7.13) to physical parameter conditions, the two-mass oscillator, shown in Fig. 7.1, is again considered but the parameter restrictions, i.e. $\alpha_1 = 0$ and $k_2 = 0$, used in §7.2 and §7.3, are removed to account for a more general case. This generically asymmetric case is explored by considering its evolution from the symmetrised case, via symmetry breaking. Using this technique, the special backbone curve topology (i.e. Fig. 7.6, or Fig. 7.7a_1) can be identified, which allows the physical parameter conditions, leading to TET, to be determined.

Considering non-zero k_2 and α_1, the modeshape matrix, $\mathbf{\Phi}$, is no longer anti-diagonal[5], and the coefficients of nonlinear terms, Ψ_i, are instead given by expressions (3.13) (this general case exhibits the same underlying conservative system as the NLTMD-inspired system considered in Chapter 3). Without the parameter restrictions, this general case can exhibit more complex backbone curve topologies than that considered in §7.2 and §7.3, where the symmetrised model exhibits *only* one backbone curve topology (Fig. 7.6). To explore these, the existence of BPs is considered for the symmetrised model using conditions (7.13). There are two critical boundaries for the existence of bifurcatioins, namely, $\Psi_4 - \Psi_3 = 0$ and $\Psi_3 - \Psi_5 = 0$ (the axes of Fig. 7.7). To find these two boundaries, combining expressions (7.11), (3.13) and (3.12) reveals

critical boundary, $f_1(m_1,\ m_2,\ k_1,\ k_2,\ \alpha_1,\ \alpha_2)$, for the existence of BP1:

$$\Psi_4 - \Psi_3 = 0: \ \frac{\alpha_{2,\mathrm{crit}}}{\alpha_{1,\mathrm{crit}}} = -\frac{(P_1P_2 + P_3)\,P_4}{(P_5P_2 + P_6)\,(P_2 + P_7)^2}, \tag{7.14a}$$

critical boundary, $f_2(m_1,\ m_2,\ k_1,\ k_2,\ \alpha_1,\ \alpha_2)$, for the existence of BP2:

---

[5] In this case, the physical displacement of the primary system, x_1, is no longer exactly represented by the second modal coordinate, q_2; likewise, the displacement of the NES, x_2, is no longer exactly captured by q_1. Nonetheless, an accurate approximation to this is still achieved if k_2 is sufficiently small. In addition, it will be demonstrated in the following that a sufficiently small k_2 is necessary in order to exhibit TET. Thus, the following discussions continue to consider the backbone curve topology in the modal domain.

Table 7.2 Backbone curve topologies for the symmetrised model in regions of Fig. 7.8.

Region	Symmetric backbone curve topology	Exhibits TET
(a)	with both BP1 and BP2, schematically shown in Fig. 7.7a_1	O
(b_1) and (b_2)	with BP1 and without BP2, schematically shown in Fig. 7.7a_2	X
(c)	with BP2 and without BP1, schematically shown in Fig. 7.7a_3	X
(d)	without both BP1 and BP2, schematically shown in Fig. 7.7a_4	X

$$\Psi_3 - \Psi_5 = 0 : \ \frac{\alpha_{2,\text{crit}}}{\alpha_{1,\text{crit}}} = -\frac{\left(-P_1 P_2 + P_3\right) P_4}{\left(-P_5 P_2 + P_6\right)\left(-P_2 + P_7\right)^2}, \tag{7.14b}$$

where parameters, P_i, are given by

$$\begin{cases} P_1 = 2(k_2 m_2 + k_1 m_2 - k_2 m_1), \\ P_2 = \sqrt{k_2^2(m_1+m_2)^2 - 2k_1k_2(m_1-m_2)m_2 + k_1^2 m_2^2}, \\ P_3 = (k_1 m_2 + k_2 m_2 - k_2 m_1)^2 + 4k_2^2 m_1 m_2, \\ P_4 = 4k_2^2 m_2^3, \\ P_5 = 2\left[(k_1+k_2)m_2^2 + k_2 m_1^2 - (k_1 - 2k_2)m_1 m_2\right], \\ P_6 = P_3(m_1+m_2), \\ P_7 = (k_1-k_2)m_2 - k_2 m_1. \end{cases} \tag{7.15}$$

Expressions (7.14) map the boundaries from the modal parameter space to the physical parameter space, $(m_1, m_2, k_1, k_2, \alpha_1, \alpha_2)$. In addition, as with the axes ($\Psi_4 - \Psi_3$ and $\Psi_3 - \Psi_5$) of Fig. 7.7 that divide the *modal parameter space* into regions, f_1 and f_2 also divide the *physical parameter space* into regions, distinguishing the existence of BPs and topologies of backbone curves.

To demonstrate this, it is useful to project the boundaries, f_1 and f_2, to the subspace, $(k_2,\ \alpha_2)$, i.e. the NES-parameter space. Therefore, it allows considering the parameter conditions on the NES in order to exhibit TET in practical design. Here, a primary system with $m_1 = 1$, $k_1 = 1$, and $\alpha_1 = 1$ is considered, and the NES has a mass value of $m_2 = 0.05$. Using expressions (7.14), the space $(k_2,\ \alpha_2)$ may be divided into several major regions[6], labelled (a), (b_1), (b_2), (c), and (d) in Fig. 7.8, where these regions are shaded using the same colour schema as that in Fig. 7.7.

---

[6] Some small regions, and regions related to negative coefficients of nonlinear terms, do not exhibit the topology of interest and are not considered here.

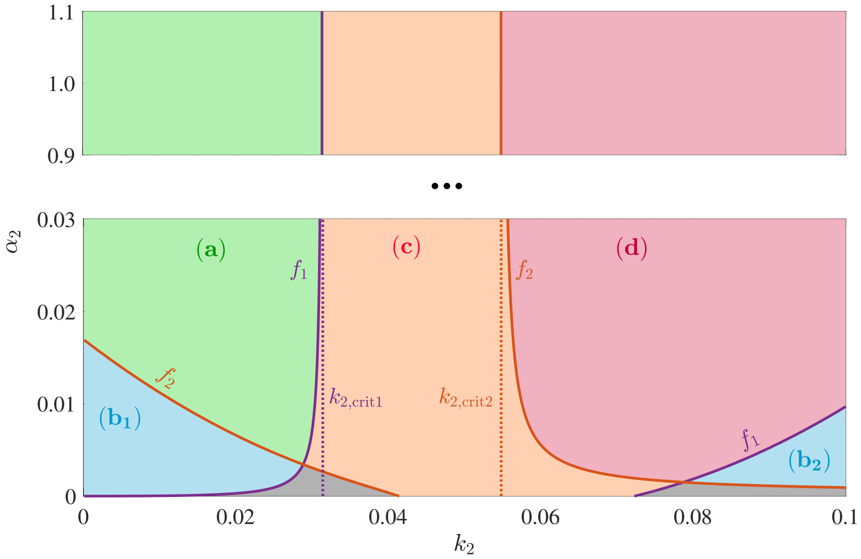

Fig. 7.8 Divisions of the NES-parameter space, $(k_2,\ \alpha_2)$, considering the existence of bifurcations on backbone curves for the symmetrised model with $m_1 = 1$, $k_1 = 1$ and $\alpha_1 = 1$. Solid purple and brown curves denote the critical boundaries for the existence of branch points, defined by expressions (7.14). Asymptotes of the boundaries, denoted by dotted lines, are defined by expressions (7.16). These boundaries divide the space into five major regions, labelled with (a), (b_1), (b_2), (c) and (d). Backbone curve topologies for the symmetrised model in these regions are correspondingly described in Table 7.2 and shown in panels of Fig. 7.7a. Backbone curves and numerical simulations for example systems in each region are shown in Fig. 7.9.

In this figure, the purple and brown lines denote f_1 and f_2 respectively; the dotted purple and brown lines represent asymptotic lines of f_1 and f_2 respectively, given by

$$\text{asymptotic line of } f_1 : \quad k_{2,\text{crit1}} = \frac{\left[3\left(m_1 - m_2\right) - 2\sqrt{3m_1m_2}\right] k_1 m_2}{3\left(m_1 + m_2\right)^2}, \tag{7.16a}$$

$$\text{asymptotic line of } f_2 : \quad k_{2,\text{crit2}} = \frac{\left[3\left(m_1 - m_2\right) + 2\sqrt{3m_1m_2}\right] k_1 m_2}{3\left(m_1 + m_2\right)^2}, \tag{7.16b}$$

denoting critical linear stiffness values of the NES.

The backbone curve topologies for the symmetrised model in these regions are given in Table 7.2 with respect to these shown in Fig. 7.7a. Using these divisions, the backbone curve topologies for the original model may be approximately classfied, along with which the existence of TET is evaluated:

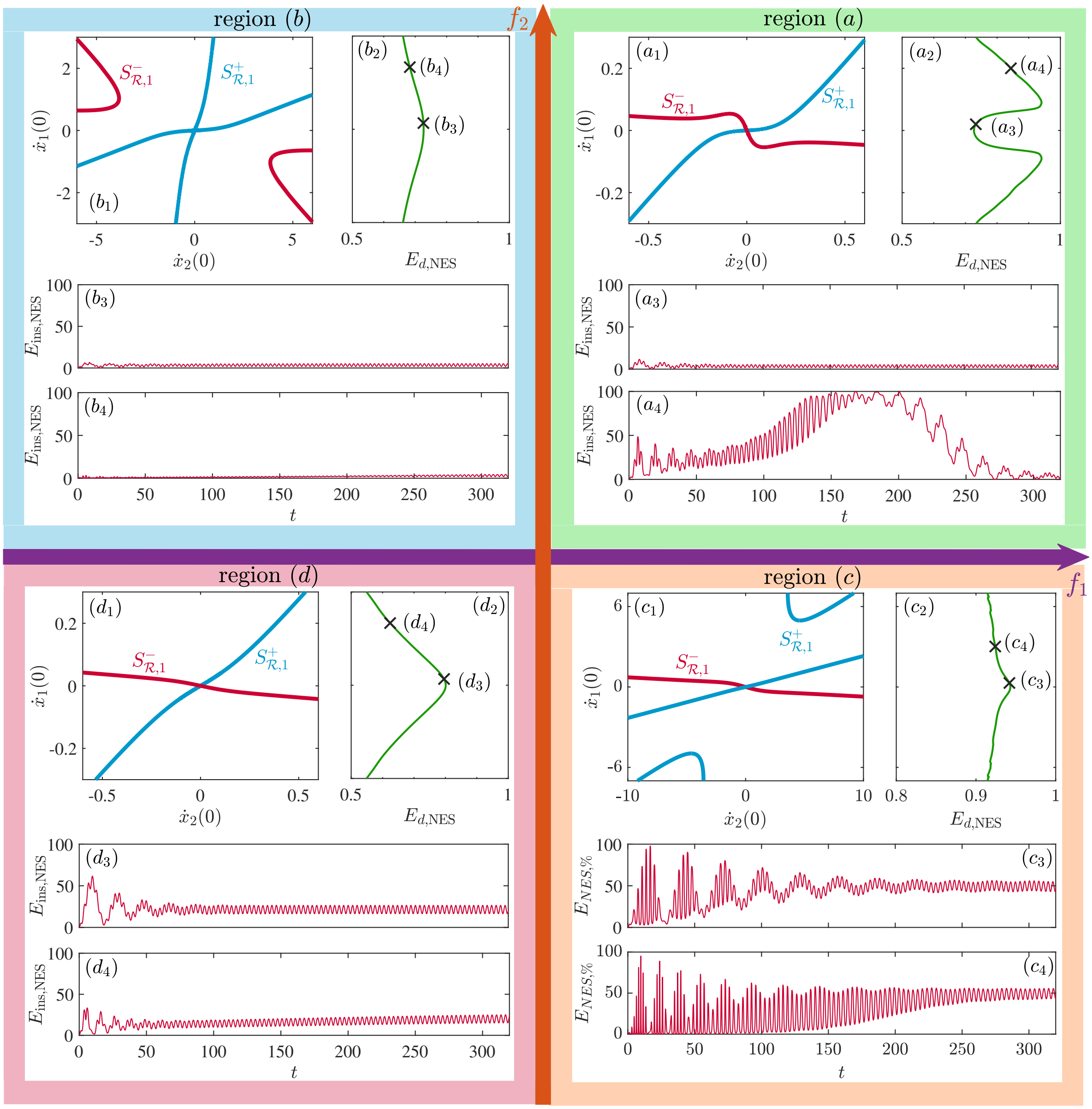

Fig. 7.9 Backbone curves and energy transfer characteristics of example systems with $m_1 = 1$, $m_2 = 0.05$, $k_1 = 1$,$\alpha_1 = 1$ and $c_1 = c_2 = 0.005$, in Fig. 7.8. The figure is divided by boundaries, f_1 and f_2, into four regions, with respect to that in the same colour scheme in Fig. 7.8 – region (a) the first quadrant; regions (b_1) and (b_2) the second quadrant; region (c) the fourth quadrant and region (d) the third quadrant. Backbone curves of the example system are shown in panel $(\bullet_1)$; the energy ratio dissipated by the NES with respect to a varied $\dot{x}_1(0)$ is presented in panel $(\bullet_2)$; Instantaneous energy in the NES over time with respect to two example initial conditions (a low- and a high-initial velocity labelled '×') are shown in panels $(\bullet_3)$ and $(\bullet_4)$.

1. **region** *(a)*: In this region, an example system with $k_2 = 0.02$ and $\alpha_2 = 1$ is first considered – the backbone curves of this system are shown in panel (a_1) in the first quadrant of Fig. 7.9. The energy ratio dissipated by the NES, with respect to the initial velocity in the primary system, is shown in panel (a_2), where a critical energy level may be seen, similar to that in Fig. 7.4b. The instantaneous energy carried by the NES with $\dot{x}_1(0)$ below the critical energy level (panel (a_3)) and above the critical energy level (panel (a_4)), again, show the same features as those seen in the example system (Fig. 7.2). Capturing the key features of TET, this region, shaded in green in Figs. 7.8 and 7.9, represents the physical parameter conditions to exhibit TET. It should be noted that, as α_2 increases, the critical energy level decreases. This can be explained by the symmetrised backbone curves where the amplitude of BP2 (associated with the critical energy level) is decreased with an increasing α_2.
2. **region** *(b)*: Decreasing α_2 from the example case in region (a), the system crosses f_2 and moves to region (b_1). In this region, a example system with $k_2 = 0.02$ and $\alpha_2 = 0.005$ is presented in the second quadrant of Fig. 7.9. The corresponding backbone curves are shown in panel (b_1), whose topology is fundamentally different to that in region (a). In addition to two primary backbone curves (passing through the origin), one isolated backbone curve may be observed. Such a backbone curve topology, indeed, can be seen as evolved from that shown in Fig. 7.7a_2. When applying the primary system with an initial velocity, the energy dissipated by the NES is presented in panel (b_2), where no critical energy level may be seen. Two example cases, denoted (b_3) and (b_4) in panel (b_2), are shown in the bottom panels – the instantaneous energy in the NES over time; they both indicate that very limited energy can be transferred to the NES as the initial energy level varies. Likewise, in region (b_2) of Fig. 7.8, similar backbone curve topologies and energy transferring features can be observed.
3. **region** *(c)*: By increasing k_2, the system in region (a) can cross the boundary, f_1, and moves to region (c) – see Fig. 7.8. An example with $k_2 = 0.05$ amd $\alpha_2 = 0.005$ is presented in the fourth quarant of Fig. 7.9. Its backbone curves, in panel (c_1), are asymmetric evolutions of those shown in Fig. 7.7a_3. Like the system in region (b) of Fig. 7.8, systems in region (c) exhibit two primary backbone curves and one isolated backbone curve. Note that, in these two cases, the isolated backbone curves can vanish with infinite frequency and amplitude, for details of the conditions, the interested reader is directed to discussions in Chapter 3. For the example in

region (c), the energy ratio dissipated by the NES is shown in panel (c_2) – more energy may be dissipated by the NES for a low $\dot{x}_1(0)$ than a high value. When $\dot{x}_1(0) = 0.3$, a strong oscillation of energy between the primary system and the NES may be seen from panel (c_3). Whilst, as $\dot{x}_1(0)$ increases to 3, the instantaneous energy in the NES (panel (c_4)) indicates a trend of energy transferring from the primary system to the NES, but it is less efficient than the example system in region (a). Even though the system in this region exhibits some similarity to that in region (a), key features of TET are not present, e.g. a critical energy level and the energy localisation in the primary system for low initial velocity cases.

4. **region** (d): A further increment of the linear stiffness of the NES leads the system to region (d). An example system with $k_2 = 0.07$ and $\alpha_2 = 1$ is shown in the third quadrant of Fig. 7.9. The backbone curves are shown in panel (d_1), whilst the energy ratio dissipated by the NES is presented in panel (d_2). In this region, like those in regions (b) and (c), no critical energy level can be seen. Shown in panels (d_3) and (d_4) are the instantaneous energy carried by the NES over time for a low- and high-initial-energy cases respectively. It is observed again that limited amount of energy can be transferred to the NES, and less is transferred if k_2 is further increased.

Comparing the examples in region (a) and (b_1), the existence of region (b_1) characterises the minimum degree of nonlinearity necessary for the system to exhibit TET, shown as boundary f_2 and described by expression (7.14b). Whilst the existence of the boundary f_1 denotes the requirement of a small linear stiffness in the NES, quantified by the asymptotic line of f_1, i.e. $k_{2,\text{crit}1}$, and described by expression (7.16a). It should also be noted that, in the case of a linear primary system (i.e. $\alpha_1 = 0$), the two boundaries, f_1 and f_2, degenate as they are no longer defined – see Eqs. (7.14). However, the asymptotes, given by Eqs. (7.16), can still be solved as they are only dependent on the underlying linear system; they quantify the required maximum value of linear stiffness in the NES – only those below this value can exhibit TET – a quantifiable ‘non-linearisability’ as reported in the literature [57, 146, 45].

Even though these boundaries are obtained based on the symmetrised model, they classify the fundamentally different behaviours (shown in Fig. 7.9) and allow one to identify the approximate parameter conditions (region (a) in Fig. 7.8) where a system may exhibit TET.

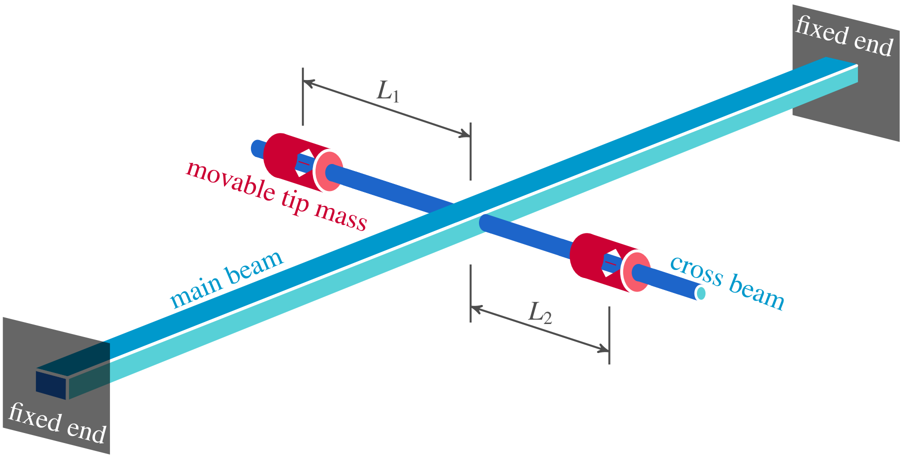

Fig. 7.10 A schematic diagram of the beam system that consists of a main beam and a cross-beam. The main beam has two fixed ends; a cross-beam is welded at the mid-span position of the main beam; and two movable tip masses are attached to the cross-beam with set screws.

Table 7.3 Parameters of the nonlinear beam ROM with symmetric and asymmetric layouts, reported in [137]. The underlying conservative dynamics of the ROM is given by Eq. (4.14) with restoring force defined by Eq. (4.15).

	ω_{n1}	ω_{n2}	Ξ_1	Ξ_2	Ξ_3	Ξ_4
symmetric layout	101.938	105.859	-0.749	2.653	-362.117	-0.147
asymmetric layout	101.744	104.634	15.126	0.406	179.984	0.0985
	Ψ_1	Ψ_2	Ψ_3	Ψ_4	Ψ_5	
symmetric layout	-90.968	0.653	$2.997 \cdot 10^5$	$1.509 \cdot 10^8$	$2.558 \cdot 10^5$	
asymmetric layout	$3.438 \cdot 10^7$	$2.332 \cdot 10^6$	$2.708 \cdot 10^7$	$1.325 \cdot 10^8$	$8.535 \cdot 10^5$	

7.4.2 Identifying TET in a beam system

In this section, another example (a nonlinear beam) is considered to demonstrate the realisation of TET induced by symmetry breaking. The beam model is schematically depicted in Fig. 7.10 – the main beam (with a rectangular cross section) has two fixed ends and is joined to a cross-beam (with a circular cross section) at the mid-span position; two additional movable concentrated masses are attached to the cross-beam. The length, width, and height of the main beam are 1000 mm, 12 mm, and 6 mm, respectively; whilst the length and diameter of the cross-beam are 400 mm and 12 mm respectively. The distances between the centres of the tip masses to the axis of the main beam are denoted L_1 and L_2 respectively. By adjusting the positions of two tip masses, the torsional inertia can be changed; in addition, they also govern the layout symmetry, namely, the system is symmetric when $L_1 = L_2$ whilst asymmetric when $L_1 \neq L_2$.

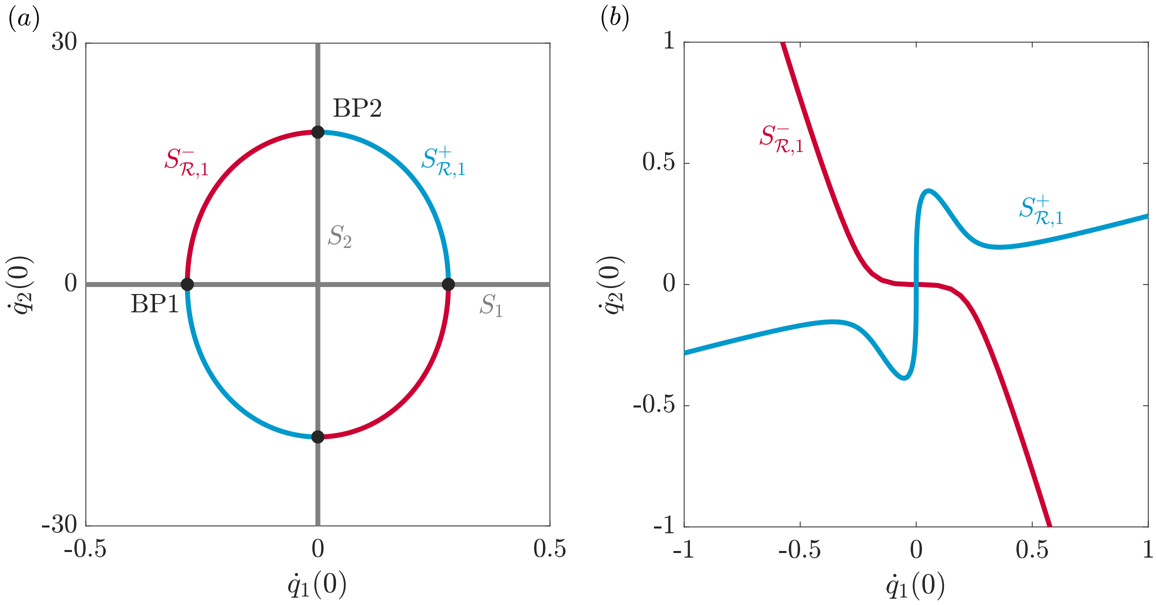

Fig. 7.11 Backbone curves of the nonlinear beam model in the initial modal velocity space, $(\dot{q}_1(0),\ \dot{q}_2(0))$. (*a*) Backbone curves for the symmetric layout with $L_1 = L_2$. (*b*) Backbone curves for the asymmetric layout with $L_1 \neq L_2$.

Such a beam system has been considered in [271, 144] to investigate the effect of geometric nonlinearity via theoretical and experimental studies. The tip masses were tuned such that the system exhibits strongly coupled bending and torsion modes with closely spaced eigenfrequencies – this gives rise to significant 1 : 1 modal interactions. In [137], the symmetry-breaking induced nonlinear modal veering was considered based on a reduce-order model (ROM) derived via the implicit condensation and expansion method [106]. Here, the two-mode ROM derived in [137] is used, which captures modal interactions between the first bending mode, q_1, and the first torsion mode, q_2. Note that this example aims to use a real physical system to demonstrate that symmetry breaking can lead to TET, rather than provide a detailed study on the beam system. Therefore, the modelling is not given here, but the interested reader is directed to [137] for details.

The ROM can be described by equations of motion in the same form as Eq. (4.14) with nonlinear restoring forces defined by Eq. (4.15). In order to investigate the effect of symmetry breaking, two layouts of the beam system are considered with respect to a symmetric layout where $L_1 = L_2 = 177.5$ mm, and an asymmetric layout where $L_1 = 182$ mm and $L_2 = 0.95L_1 = 172.9$ mm. For these two cases, the parameters of the equations of motion are given in Table 7.3, obtained during reduced-order modelling.

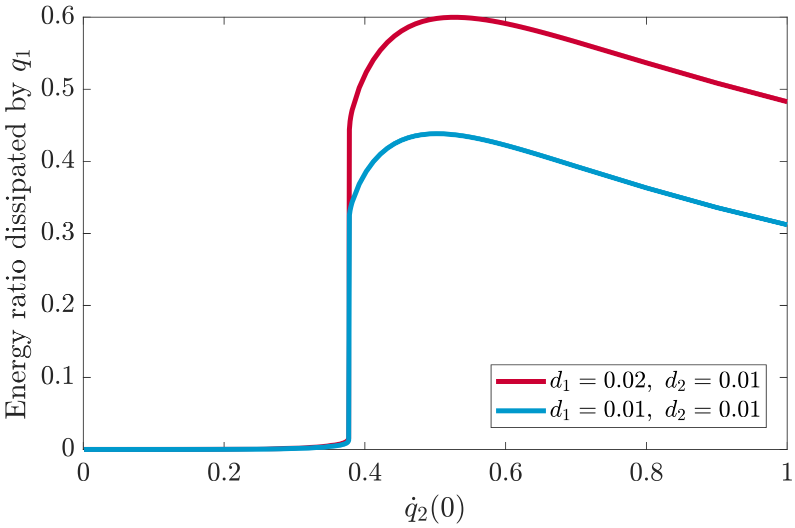

Fig. 7.12 Energy ratio dissipated by q_1 with respect to a varied initial velocity in q_2 for the asymmetric nonlinear beam system.

One can find that, for the symmetric case, $\Psi_1 \approx 0$ and $\Psi_2 \approx 0$, in line with the definition of symmetry given in §7.3.1.

With coefficients of nonlinear terms, Ψ_i, for the symmetric layout, it can be found that the system satisfies parameter conditions (7.11); therefore, it is expected that, on each single-mode backbone curve (emerging from the eigenfrequency), there is one bifurcation leading to mixed-mode backbone curves. Consequently, symmetry breaking introduced by asymmetric positioning of the tip masses can lead to the required backbone curve topology for the realisation of TET. These analytical results are then verified via numerical continuation – the computed backbone curves for the symmetric and asymmetric layouts are shown in Figs. 7.11*a* and 7.11*b* respectively in the initial modal velocity space, $(\dot{q}_1(0),\ \dot{q}_2(0))$. The backbone curves indeed show topological similarity to that in Fig. 7.6.

A varied initial impulse energy is then imparted in q_2, i.e. an initial velocity in q_2, to consider the energy dissipation of two modes. The numerical simulation results are shown in Fig. 7.12 for two damping cases where the two modes have the same linear modal damping $d_1 = d_2$, and where $d_1 = 2d_2$. In both cases, when the initial energy impulse is lower than the critical level, $\dot{q}_2(0) \approx 0.38$, the energy input is concentrated in q_2 without transferring to q_1 – similar to the below-critical-value case considered in §7.2. Meanwhile, when the initial energy input is above the critical level, a significant increment of energy is shown to be transferred to q_1 where it is subsequently dissipated. The energy ratio dissipated by q_1 is shown to be dependent on the relative damping of modes and a further increment of transferred energy can be expected if d_1 increases.

From the simulated results, one can conclude that the asymmetric nonlinear beam system indeed exhibits TET. Such a nonlinear behaviour is captured by its backbone curve topology, shown in Fig. 7.11*b* – an asymmetric evolution from that in Fig. 7.11*a*. Results in this section verify and demonstrate the uncovered symmetry-breaking mechanism in the realisation of TET.

7.5 Summary

Based on the concept of resonant capture, studies in this chapter made use of backbone curves to interpret damped transient responses. Particularly, this chapter used backbone curves to understand the nonlinear phenomenon of TET, where the vibration energy is irreversibly transferred from one component to the other during transient responses. From a symmetry-breaking perspective, the required backbone curves to realise TET have been identified. The uncovered symmetry-breaking mechanism, as well as the required parameter conditions, were demonstrated via examples and can be used to aid practical designs.

In §7.2, an overview of TET was given to highlight its features and establish its connections to the underlying conservative backbone curves. It was demonstrated that the features of TET, namely, the critical energy level and irreversible energy transfer, are both captured by the energy localisation properties of backbone curves. This underpins the applicability of backbone curves in interpreting TET – the fundamental idea of studies in §7.3 and §7.4.

In §7.3, the required backbone curves to realise TET were interpreted from a symmetry-breaking perspective. Using this method, the features of TET were shown to be governed by symmetry-breaking induced bifurcation splitting. The bifurcation splitting generates a fold on the backbone curve that determines the critical energy level; in addition, it leads to a backbone curve with energy localisation transiting from one mode to the other mode, capturing the irreversible energy transfer. Therefore, studies in this section uncovered the symmetry-breaking mechanism to realise TET, and provided a method to identify TET via backbone curve topologies.

In §7.4, by extending the example system that was considered in previous sections to general cases, the necessary backbone curves, found in §7.3, were distinguished from other cases. The required modal parameter conditions were also derived analytically for practical use.

Lastly, two example systems were used to demonstrate the achievements. The first example was the structure-NES system, where the physical parameter conditions were identified to realise TET. These parameter conditions are characterised by a maximum level of linear stiffness and a minimum level of nonlinear stiffness of the NES device. The second example was a nonlinear beam system, where the identified symmetry-breaking mechanism was verified and demonstrated. In breaking the symmetric layout, the necessary backbone curves to achieve TET were found; additionally, simulation results also verified the existence of TET.

Chapter 8

Conclusions and furture work

In this thesis, nonlinear phenomena that emerge from modal interactions have been investigated. This has generated theoretical insights into the mechanisms that underpin the nonlinear behaviours, which can aid practical designs and analysis of engineering systems. In this chapter, a summary of the achievements is presented, along with the corresponding conclusions; additionally, some potential avenues of future research are also discussed.

8.1 Conclusions

Synchronous NNMs and isolated backbone curves

Chapter 3 began by giving an overview of the geometric features of Nonlinear Normal Modes (NNMs) that emerge from modal interactions, particularly, with an emphasis on the synchronous motions.

Next, a two-mass chain oscillator was considered to present the existence of isolated backbone curves. When the system has a symmetric layout, it was demonstrated that there exists a bifurcation on the primary backbone curve, leading to synchronous backbone curves, in line with a vast body of literature. It was shown that, as with the breaking of the symmetric layout, the bifurcation splits and leads to the existence of isolated backbone curves. Additionally, the study revealed that the bifurcation, indicative of a symmetric system, can be preserved under certain parameter conditions. As such, it meant that a physically asymmetric system may act equivalently to a symmetric one, and the corresponding parameter conditions are termed having *dynamic symmetry* in this thesis.

Using these insights, a two-mass oscillator with an asymmetric layout, in the form of a primary system with a nonlinear tuned mass damper attached, was considered to investigate the conditions for the existence of isolated backbone curves. The physical parameter conditions to have dynamic symmetry were derived analytically which, as discussed above, led the asymmetric system to exhibit backbone curves with a bifurcation leading to mixed-mode synchronous backbone curves. In practice, the parameter optimisation (linear parameters of the NLTMD) for vibration suppression performance is not in line with the conditions for dynamic symmetry. As such, optimising the NLTMD breaks these conditions and leads to the emergence of isolated backbone curves. Based on the optimised NLTMD system, the evolutions of backbone curves in the nonlinear parameter space (to be optimised parameters) were then explored. It was found that the parameter space can be divided into several regions, within which the backbone curves show equivalent topologies, whilst the boundaries define the emergence and annihilations of isolated backbone curves. Those conditions were then derived analytically which govern the existence of isolated backbone curves.

Chapter 3 presented the following key points:

- The dynamics of an asymmetric system can act equivalently to a symmetric system when conditions for dynamic symmetry are satisfied. This highlights the connections between these two vastly different systems yet also provides a method to study asymmetric systems.
- The conditions for the existence of isolated backbone curves are derived, which also distinguish the backbone curve topologies in the parameter space. The existence of isolated backbone curves can be reliably and efficiently determined using these analytical conditions.

Asynchronous NNMs and phase-varying backbone curves

In Chapter 4, the concept of NNMs was firstly revisited by extending the synchronous NNMs, considered in Chapter 3, to include asynchronous NNMs. Their difference was highlighted by referring to the phase relationships between interacting modes: the synchronous NNMs are characterised by phase relationships that are either in-phase or anti-phase (either 0 or π); whilst for asynchronous NNMs, the phase relationships can be an arbitrary value (neither 0 nor π). A special case of asynchronous NNM that has been reported in the literature is the out-of-unison NNM (whirling motions) whose phase relationship is $\pi/2$, whilst the more general case was investigated in this chapter.

To achieve this, the existence of general asynchronous NNMs was demonstrated using a single-mass, two-mode system from a symmetry-breaking perspective. It was shown that, with the breaking of the symmetric layout, the special out-of-unison NNMs can be transformed into general asynchronous NNMs. Further analytical derivations revealed that these asynchronous NNMs are on a backbone curve that exhibits phase-amplitude coupling – the phase relationships between modal components are varying along the backbone curve. As such, this new class of nonlinear periodic behaviour was defined as a *phase-varying backbone cuvre*, distinguishing from the commonly observed phase-fixed ones. Next, the existence of phase-varying backbone curves in common engineering structures was demonstrated using a cable model. An additional support was attached to the cable near one end to mimic the engineering practice of installing a grounded device for vibration suppression. It was shown that the support can break the symmetric layout and transform the out-of-unison backbone curve into phase-varying ones.

Based on the results, the conclusions of Chapter 4 are as follows:

- The general asynchronous NNMs may be seen as evolutions of special out-of-unison NNMs due to symmetry breaking. A family of such general asynchronous NNMs formulates a phase-varying backbone curve, which represents a new class of nonlinear behaviours.
- The existence of phase-varying backbone curves, and their accompanying general asynchronous NNMs, highlights the importance of determining phase relationships in computing nonlinear responses, of which a key implication is the use of harmonic balancing method.

Topological mappings of backbone curves

In Chapter 5, discussion began by extending the $1:1$ internal resonance, considered in Chapters 3 and 4, to general $m:n$ cases using a motivating example of a pinned-pinned beam. This was achieved by accounting for the geometric features in the complex plane (the Fourier components in an NNM) with the proposed terminology, namely the Fourier-real and Fourier-complex NNMs. The Fourier-real NNMs denote the generalisation of synchronous NNMs – both modal coordinates are composed of real Fourier components; whilst the Fourier-complex NNMs are genearlised asynchronous NNMs – one mode is composed of real Fourier components and the other mode consists of complex Fourier components. In this beam example, an intricate topology of internal resonances was found that consists of four mixed-mode backbone curves; in addition, two of these backbone curves show similar response frequencies and amplitudes. An extra computational cost was needed to determine the whole picture of internal resonance, and hence, Chapter 5 employed an analytical method to overcome this challenge and provide a method for efficient and robust determination of internal resonance.

To achieve this, a general two-mode symmetric system was considered. Analytical derivations revealed that, in the neighbourhood of a primary backbone curve, the internal resonance can be approximately captured by the Mathieu equation. The solution sets of the Mathieu equation are associated with the Fourier-real and Fourier-complex generalisations given above. It was shown that the mixed-mode backbone curves (emerging from internal resonances) exist in pairs with one Fourier-real and one Fourier-complex type. Additionally, the bifurcations leading to these mixed-mode backbone curves were derived, which are governed by Hill's determinants. Using these insights, the convergence and divergence of bifurcation pairs were explored to account for the existence of internal resonances. It was found that the convergence of bifurcations leads to phase-unlocked resonances due to undetermined phase relationships; whilst the divergence of bifurcations annihilates the correlated internal resonance. A further analytical study revealed that the existence of internal resonances is governed by two parameter conditions, namely the eigenfrequency ratio and nonlinear parameter ratio.

Discussions then extended to the asymmetric case to investigate the symmetry-breaking effect on internal resonances. The asymmetric evolutions of internal resonances were derived, which are captured by a non-homogeneous extended Mathieu equation. Symmetry-breaking induced bifurcation splitting/remaining phenomena, observed throughout the thesis, were shown to be governed by the non-homogeneous terms.

Based on the achievements, the conclusions of Chapter 5 can be drawn:

- Backbone curves can show intricate topologies due to the existence of internal resonance. Based on geometric features, these backbone curves exist in pairs with one Fourier-real and one Fourier-complex type. The convergence of these backbone curves brings about phase-unlocked resonances whilst the divergence of them leads to the annihilation of internal resonances.
- Analytical studies gain an in-depth understanding of the mechanism that governs the features of internal resonances. They also provide a rigorous and efficient method for determining the existence and locations of internal resonances. This can aid the designs of relevant engineering systems when specific types of internal resonances are exploited or eliminated.

Interpreting forced periodic responses using backbone curves

Chapter 6 began by giving an overview of the energy balancing mechanism at the system level, to that at the mode level and harmonic level. From this energy-based perspective, the relationships between backbone curves and forced periodic responses were established. Based on a single-harmonic assumption, the applicability and limitations of energy balancing analysis were demonstrated in predicting forced responses. The results showed that it yielded accurate predictions when harmonic contributions are negligible, however, it showed inaccurate and even incorrect predictions when harmonic contributions are significant. As harmonic contributions in the responses are challenging to know beforehand, the single-harmonic energy balancing method may not give robust and reliable predictions. To overcome the limitations, whilst preserving the computational efficiency, Chapter 6 employed a semi-analytical framework to establish the multi-harmonic energy balancing method.

By viewing forced responses as phase-shift perturbations from NNMs, the proposed method was formulated by combining the energy balancing mechanism with force reductions and quadrature constraints. With known inputs of NNM solutions, the formulas gave rise to closed-form solutions which can be used to compute the required forcing amplitudes and harmonic-phase shifts from NNMs to forced responses. The technique has been demonstrated in a number of examples in comparison with numerical force appropriation, which all showed a strong agreement. Lastly, the technique has been applied in isola prediction, and it outperforms the single-harmonic formulation in accurately capturing the existence of an isola that has multiple significant harmonics.

The conclusions of Chapter 6 can therefore be drawn as follows:

- The harmonics can show significant contributions to nonlinear responses. When applying the energy balancing analysis, it is of great importance to evaluate their significance, or adopt a multi-harmonic formulation, to ensure robust and accurate predictions of forced responses.
- The multi-harmonic energy balancing method is established based on a semi-analytical framework that allows efficient predictions of forced responses with known NNM inputs. The applicability and accuracy of the proposed multi-harmonic energy balancing method can be directly estimated from the computed harmonic phase-shifts.
- The proposed method can be used to aid experimental backbone curve identification in finding an appropriate number of excitation points and their distributions.

Understanding targeted energy transfer using backbone curves

In Chapter 7, the key features of Targeted Energy Transfer (TET) were first demonstrated using a two-mode system that consists of a primary system with a nonlinear energy sink attached. In line with many studies, a linear primary system and a nonlinearisable NES were considered. The irreversible energy transfer and critical energy level were both shown to be captured by the underlying backbone curves. Indeed, it is the mass and potential asymmetry between the primary system and NES that leads to the backbone curves that underpin the transient TET. To explore the realisation of TET, Chapter 7 was devoted to understanding the essential asymmetry from a symmetry-breaking perspective.

To achieve this, a symmetrised model was introduced, which allows the original system to be interpreted as an asymmetric evolution. Therefore, the backbone curves (capturing key features of TET) were interpreted as bifurcation splitting due to symmetry breaking. The bifurcation splitting generates a fold on one backbone curve that governs the critical energy level; whilst it leads the other backbone curve to show energy localisation transiting from one mode to the other, capturing the irreversible energy transfer. Based on the uncovered symmetry-breaking mechanism, the required backbone curves for the realisation of TET can be distinguished from others, and hence, it provides a method to identify systems that exhibit TET.

This method was then demonstrated using two example systems. The first example represents a generalised structure-NES system where the primary structure has a nonlinear spring and the NES has a linear spring. The analytically identified parameter conditions were characterised by a minimum requirement of nonlinear stiffness and a maximum limit of linear stiffness of the NES. The other example was a nonlinear beam system, where the uncovered symmetry-breaking mechanism was verified and demonstrated. In breaking the symmetric layout, the required backbone curves for the realisation of TET were found. Numerical simulations also justified the existence of TET in the nonlinear beam system.

The conclusions of Chapter 7 can therefore be drawn as follows:

- Based on the concept of resonant capture, backbone curves can capture the key features of transient TET, namely the irreversible energy transfer and critical energy level.
- Symmetry breaking represents one mechanism that underpins the realisation of TET and provides a method to identify the system that exhibits TET.

8.2 Future work

This thesis presents theoretical and practical insights into nonlinear behaviours. The work has also revealed many potential paths for future research; these are given as follows.

Modal interactions of high-dimensional systems

In this thesis, modal interactions between two modes have been studied by considering their geometric features. In Chapter 3, the synchronous NNMs and their correlated isolated backbone curves were analytically determined; next, Chapter 4 considered the counterpart – the asynchronous NNMs and phase-varying backbone curves; lastly, Chapter 5 generalised these results for arbitrary $m : n$ two-mode interactions. As two-mode interactions represent the most commonly observed scenarios, the achievements of this thesis can effectively be used to aid modelling, analysis, and designs of nonlinear systems.

However, in literature, higher-dimensional modal interactions have been reported in both experimental and theoretical studies. Further exploration is needed to reveal how the findings in this thesis can be further extended to three-mode interactions and more general cases. There are several scientific questions that can be considered: the mechanism that governs multi-mode interactions; the effect of other non-interacting modes on modal interactions, and in turn, the effect of modal interactions on other non-interacting modes. This can further the understanding of complex nonlinear behaviours in high-dimensional systems and provide practical insights into engineering applications to better handle and exploit these features. One key implication lies in reduced-order modelling, where the selection of the reduced basis is often based on prior knowledge or computational trials. If the general mechanism governing modal interactions can be revealed, it can provide guidance in the reduced basis selection. Furthermore, it may even automate the basis selection to generate a reduced-order model that effectively and efficiently suits different scenarios (different types of modal interactions may occur under different conditions).

Accounting for nonlinear damping in the energy balancing analysis

In Chapter 6, the multi-harmonic energy balancing method was established based on linear modal damping. This case represents many engineering systems that experience geometric nonlinearity, where the damping may be assumed small and linear when compared to the restoring force and external force. In practice, many nonlinear systems can also manifest nonlinear phenomena due to nonlinear damping, for example, bolted joints and rubber damping devices. As these systems are usually operating under cyclic forcing conditions, the energy balancing principle can still be applied, however, with an extension to account for the nonlinear damping effect. This extension is meaningful in terms of studies of nonlinear damping systems as analysis and optimisations of such systems are typically associated with computationally expensive simulations. The semi-analytical[1], multi-harmonic framework can significantly ease the computational burden whilst preserving the required accuracy, especially when considering multi-harmonic responses in the presence of non-smooth damping.

Optimising the vibration suppression performance of a NLTMD

In this thesis, conditions for the existence of isolated backbone curves have been analytically derived. These can directly be used in parameter optimisation of structure-NLTMD systems to eliminate the existence of isolated backbone curves. Even though the existence of isolated backbone curves and their correlated isolas can show significant impact, in practice, the damping devices are often optimised to achieve the best performance in vibration suppression, rather than target eliminating the existence of isolas. In this case, how to reliably guarantee the non-existence of isolas whilst achieving the best performance needs further study. This can be realised by employing the energy balancing analysis in the resonance analysis of NLTMD systems. Firstly, the energy balancing analysis can reliably predict the existence of isolas, as demonstrated in Chapter 6. Next, it can be used to predict amplitudes of resonant responses for any given forcing amplitude, therefore, it can be used to evaluate the vibration suppression performance. Hence, a nonlinear generalised equal-peak optimisation can potentially be formulated based on this technique.

Targeted energy transfer

In this thesis, Targeted Energy Transfer (TET) has been studied in a number of example systems in Chapter 7. In line with much literature, these examples exhibit TET via irreversible energy transfer that is locked in the neighbourhood of synchronous, or Fourier-real, backbone curves. Likewise, as the counterpart of synchronous backbone curves, asynchronous backbone curves may also attract irreversible energy transfer if they are stable. In this case, the irreversible energy transfer can direct energy from one mode to the other via whirling-like motions. This can outperform the classic TET in cases where whirling motions are more favorable to the primary systems than in-phase/anti-phase

---

[1] The extension to nonlinear damping case may require extra assumptions to retain this semi-analytical framework.

motions. However, more detailed studies on the applicability, advantages, and efficiency are needed.

Another avenue of future research is on the realisation of TET without adding peripheral devices, e.g. without an additional nonlinear energy sink. In Chapter 7, the realisation of TET was explored based on the symmetry-breaking mechanism. As demonstrated via the nonlinear beam example, TET was realised by adjusting the distribution of tip masses, which breaks the symmetric layout without additional devices. This indicates the potential to realise in-built TET behaviours in a nonlinear system via deliberate adjustment of the layout. This can be of great significance in optimising nonlinear systems by achieving a more predictable system as energy input in either mode can end up localised in a particular mode due to TET. Therefore, this optimising methodology may allow for a long-lasting design since potential failures of the system can be more reliably estimated based on the energy localised mode. However, a trade-off between the breaking of a regular layout and a better performance needs to be considered; in addition, how such in-built TET can be realised in more general nonlinear systems (not necessarily an asymmetric beam) also needs further exploration.

References

[1] G. Griffiths, Technology and applications of autonomous underwater vehicles, Vol. 2, CRC Press, 2002.

[2] N. Fischer, D. Hughes, P. Walters, E. M. Schwartz, W. E. Dixon, Nonlinear rise-based control of an autonomous underwater vehicle, IEEE Transactions on Robotics 30 (4) (2014) 845–852. doi:10.1109/TRO.2014.2305791.

[3] T. T. Soong, B. F. Spencer Jr., Supplemental energy dissipation: state-of-the-art and state-of-the-practice, Engineering Structures 24 (3) (2002) 243 – 259. doi:10.1016/S0141-0296(01)00092-X.

[4] B. Drew, A. R. Plummer, M. N. Sahinkaya, A review of wave energy converter technology, Proceedings of the Institution of Mechanical Engineers, Part A: Journal of Power and Energy 223 (8) (2009) 887–902. doi:10.1243/09576509JPE782.

[5] J. Davidson, R. Costello, Efficient nonlinear hydrodynamic models for wave energy converter design—a scoping study, Journal of Marine Science and Engineering 8 (1). doi:10.3390/jmse8010035.

[6] Z. Lu, B. Huang, Z. Wang, Y. Zhou, Experimental comparison of dynamic behavior of structures with a particle damper and a tuned mass damper, Journal of Structural Engineering 144 (12) (2018) 04018211. doi:10.1061/(ASCE)ST.1943-541X.0002213.

[7] S. Elias, R. Rupakhety, D. De Domenico, S. Olafsson, Seismic response control of bridges with nonlinear tuned vibration absorbers, Structures 34 (2021) 262–274. doi:10.1016/j.istruc.2021.07.066.

[8] J. R. Ahlquist, J. M. C. no, H. Climent, R. deDiego, J. deAlba, Assessment of nonlinear structural response in a400mgvt, in: Proceedings of the 28th International Modal Analysis Conference (IMAC), Jacksonville, FL, USA, Springer, New York, NY, 2010. doi:10.1007/978-1-4419-9834-7_101.

[9] W.-S. Lee, W.-C. Sue, C.-F. Lin, C.-J. Wu, The strain rate and temperature dependence of the dynamic impact properties of 7075 aluminum alloy, Journal of Materials Processing Technology 100 (1) (2000) 116–122. doi:10.1016/S0924-0136(99)00465-3.

[10] Y.-K. Wen, Method for random vibration of hysteretic systems, Journal of the Engineering Mechanics Division 102 (2) (1976) 249–263. doi:10.1061/JMCEA3.0002106.

[11] W. Lacarbonara, F. Vestroni, Nonclassical responses of oscillators with hysteresis, Nonlinear Dynamics 32 (3) (2003) 235–258.

[12] Material rate dependence and mesh sensitivity in localization problems, Computer Methods in Applied Mechanics and Engineering 67 (1) (1988) 69–85. doi:10.1016/0045-7825(88)90069-2.

[13] M. Conner, D. Tang, E. Dowell, L. Virgin, Nonlinear behavior of a typical airfoil section with control surface freeplay: a numerical and experimental study, Journal of Fluids and Structures 11 (1) (1997) 89–109. doi:10.1006/jfls.1996.0068.

[14] J. Panchal, H. Benaroya, Review of control surface freeplay, Progress in Aerospace Sciences 127 (2021) 100729. doi:10.1016/j.paerosci.2021.100729.

[15] E. P. Petrov, D. J. Ewins, Analytical Formulation of Friction Interface Elements for Analysis of Nonlinear Multi-Harmonic Vibrations of Bladed Disks , Journal of Turbomachinery 125 (2) (2003) 364–371. doi:10.1115/1.1539868.

[16] J. Yuan, F. El-Haddad, L. Salles, C. Wong, Numerical Assessment of Reduced Order Modeling Techniques for Dynamic Analysis of Jointed Structures With Contact Nonlinearities, Journal of Engineering for Gas Turbines and Power 141 (3), 031027. doi:10.1115/1.4041147.

[17] C. C. Cheng, J. Y. Wang, Free vibration analysis of a resilient impact damper, International Journal of Mechanical Sciences 45 (4) (2003) 589 – 604. doi:10.1016/S0020-7403(03)00116-4.

[18] K. Li, A. P. Darby, An experimental investigation into the use of a buffered impact damper, Journal of Sound and Vibration 291 (3 - 5) (2006) 844 – 860. doi:10.1016/j.jsv.2005.06.043.

[19] E. P. Petrov, D. J. Ewins, Advanced Modeling of Underplatform Friction Dampers for Analysis of Bladed Disk Vibration, Journal of Turbomachinery 129 (1) (2006) 143–150. doi:10.1115/1.2372775.

[20] F. Afonso, J. Vale, Éder Oliveira, F. Lau, A. Suleman, A review on non-linear aeroelasticity of high aspect-ratio wings, Progress in Aerospace Sciences 89 (2017) 40–57. doi:10.1016/j.paerosci.2016.12.004.

[21] H. B. Khaniki, M. H. Ghayesh, M. Amabili, A review on the statics and dynamics of electrically actuated nano and micro structures, International Journal of Non-Linear Mechanics 129 (2021) 103658. doi:10.1016/j.ijnonlinmec.2020.103658.

[22] M. Patil, D. Hodges, On the importance of aerodynamic and structural geometrical nonlinearities in aeroelastic behavior of high-aspect-ratio wings, Journal of Fluids and Structures 19 (7) (2004) 905–915. doi:10.1016/j.jfluidstructs.2004.04.012.

[23] D. S. Nguyen, E. Halvorsen, G. U. Jensen, A. Vogl, Fabrication and characterization of a wideband MEMS energy harvester utilizing nonlinear springs, Journal of Micromechanics and Microengineering 20 (12) (2010) 125009. doi:10.1088/0960-1317/20/12/125009.

[24] A. Z. Hajjaj, M. A. Hafiz, M. I. Younis, Mode coupling and nonlinear resonances of mems arch resonators for bandpass filters, Scientific reports 7 (1) (2017) 1–7.

[25] Nonlinear Dynamics and Its Applications in Micro- and Nanoresonators, Vol. ASME 2008 Dynamic Systems and Control Conference, Parts A and B of Dynamic Systems and Control Conference. `doi:10.1115/DSCC2008-2406`.

[26] D. Tang, E. Dowell, Nonlinear aeroelasticity in rotorcraft, Mathematical and Computer Modelling 18 (3) (1993) 157–184. `doi:10.1016/0895-7177(93)90110-K`.

[27] M. Cartmell, Introduction to Linear, Parametric, and Nonlinear Vibrations., Chapman and Hall, Berlin, Germany, 1990.

[28] L. Jezequel, C. H. Lamarque, Analysis of non-linear dynamical systems by the normal form theory, Journal of Sound and Vibration 149 (3) (1991) 429–459. `doi:10.1016/0022-460X(91)90446-Q`.

[29] P. Glendinning, Stability, instability and chaos: an introduction to the theory of nonlinear differential equations, Vol. 11, Cambridge university press, 1994.

[30] D. J. Wagg, S. A. Neild, Nonlinear Vibration with Control., Springer-Verlag, Berlin, Germany, 2009. `doi:10.1007/978-3-319-10644-1`.

[31] G. Kerschen, M. Peeters, J. C. Golinval, A. F. Vakakis, Nonlinear normal modes, part i: A useful framework for the structural dynamicist, Mechanical Systems and Signal Processing 23 (1) (2009) 170–194. `doi:10.1016/j.ymssp.2008.04.002`.

[32] C. Pierre, D. Jiang, S. Shaw, Nonlinear normal modes and their application in structural dynamics, Mathematical Problems in Engineering Article ID 10847 (2006) 15 pp. `doi:10.1155/MPE/2006/10847`.

[33] A. H. Nayfeh, B. Balachandran, Modal interactions in dynamical and structural systems, Applied Mechanics Reviews 42 (11S) (1989) S175–S201.

[34] A. I. Manevich, L. I. Manevitch, The Mechanics of Nonlinear Systems with Internal Resonances, World Scientific, 2005. `doi:10.1142/p368`.

[35] J. Macdonald, Multi-modal vibration amplitudes of taut inclined cables due to direct and/or parametric excitation, Journal of Sound and Vibration 363 (2016) 473–494. `doi:10.1016/j.jsv.2015.11.012`.

[36] R. Lewandowski, On beams membranes and plates vibration backbone curves in cases of internal resonance, Meccanica 31 (3) (1996) 323–346.

[37] W. Lacarbonara, H. N. Arafat, A. H. Nayfeh, Non-linear interactions in imperfect beams at veering, International Journal of Non-Linear Mechanics 40 (7) (2005) 987–1003. `doi:10.1016/j.ijnonlinmec.2004.10.006`.

[38] S. A. Emam, A. H. Nayfeh, Non-linear response of buckled beams to 1:1 and 3:1 internal resonances, International Journal of Non-Linear Mechanics 52 (2013) 12–25. `doi:10.1016/j.ijnonlinmec.2013.01.018`.

[39] S. Chang, A. K. Bajaj, C. M. Krousgrill, Non-linear vibrations and chaos in harmonically excited rectangular plates with one-to-one internal resonance, Nonlinear dynamics 4 (5) (1993) 433–460.

[40] W. Zhang, M. Zhao, Nonlinear vibrations of a composite laminated cantilever rectangular plate with one-to-one internal resonance, Nonlinear Dynamics 70 (1) (2012) 295–313.

[41] O. Thomas, C. Touzé, A. Chaigne, Non-linear vibrations of free-edge thin spherical shells: modal interaction rules and 1: 1: 2 internal resonance, International Journal of Solids and Structures 42 (11-12) (2005) 3339–3373.

[42] M. Amabili, Internal resonances in non-linear vibrations of a laminated circular cylindrical shell, Nonlinear Dynamics 69 (3) (2012) 755–770.

[43] G. Habib, T. Detroux, R. Viguié, G. Kerschen, Nonlinear generalization of den hartog's equal-peak method, Mechanical Systems and Signal Processing 52-53 (2015) 17–28. doi:10.1016/j.ymssp.2014.08.009.

[44] G. Gatti, Fundamental insight on the performance of a nonlinear tuned mass damper, Meccanica 53 (1-2) (2018) 111–123. doi:10.1007/s11012-017-0723-0.

[45] G. Kerschen, Y. S. Lee, A. F. Vakakis, D. M. McFarland, L. A. Bergman, Irreversible passive energy transfer in coupled oscillators with essential nonlinearity, SIAM Journal on Applied Mathematics 66 (2) (2005) 648–679.

[46] A. F. Vakakis, O. V. Gendelman, L. A. Bergman, D. M. McFarland, G. Kerschen, Y. S. Lee, Nonlinear Targeted Energy Transfer in Mechanical and Structural Systems., Vol. 156, Springer Science & Business Media, 2008.

[47] A. F. Vakakis, L. I. Manevitch, Y. V. Mikhlin, V. N. Pilipchuk, A. A. Zevin, Normal modes and localization in nonlinear systems, Springer, 2001.

[48] A. H. Nayfeh, B. Balachandran, Applied nonlinear dynamics: analytical, computational, and experimental methods, John Wiley & Sons, 2008.

[49] G. W. Hill, On the part of the motion of the lunar perigee which is a function of the mean motions of the sun and moon, Acta Mathematica 8 (none) (1900) 1 – 36. doi:10.1007/BF02417081.

[50] G. VON GROLL, D. EWINS, The harmonic balance method with arc-length continuation in rotor/stator contact problems, Journal of Sound and Vibration 241 (2) (2001) 223–233. doi:10.1006/jsvi.2000.3298.

[51] T. Detroux, L. Renson, L. Masset, G. Kerschen, The harmonic balance method for bifurcation analysis of large-scale nonlinear mechanical systems, Computer Methods in Applied Mechanics and Engineering 296 (1) (2015) 18 – 38. doi:10.1016/j.cma.2015.07.017.

[52] L. Guillot, A. Lazarus, O. Thomas, C. Vergez, B. Cochelin, A purely frequency based floquet-hill formulation for the efficient stability computation of periodic solutions of ordinary differential systems, Journal of Computational Physics 416 (2020) 109477. doi:10.1016/j.jcp.2020.109477.

[53] C. Hodges, Confinement of vibration by structural irregularity, Journal of sound and vibration 82 (3) (1982) 411–424.

[54] C. Pierre, E. Dowell, Localization of vibrations by structural irregularity, Journal of Sound and Vibration 114 (3) (1987) 549–564.

[55] R. Langley, N. Bardell, P. Loasby, The optimal design of near-periodic structures to minimize vibration transmission and stress levels, Journal of Sound and Vibration 207 (5) (1997) 627–646. `doi:10.1006/jsvi.1997.1116`.

[56] L. Caracoglia, N. Jones, In-plane dynamic behavior of cable networks. part 2: prototype prediction and validation, Journal of Sound and Vibration 279 (3) (2005) 993–1014. `doi:10.1016/j.jsv.2003.11.059`.

[57] O. Gendelman, L. I. Manevitch, A. F. Vakakis, R. M'Closkey, Energy Pumping in Nonlinear Mechanical Oscillators: Part I—Dynamics of the Underlying Hamiltonian Systems , Journal of Applied Mechanics 68 (1) (2000) 34–41. `doi:10.1115/1.1345524`.

[58] B. Vaurigaud, L. Manevitch, C.-H. Lamarque, Passive control of aeroelastic instability in a long span bridge model prone to coupled flutter using targeted energy transfer, Journal of Sound and Vibration 330 (11) (2011) 2580 – 2595. `doi:10.1016/j.jsv.2010.12.011`.

[59] N. E. Wierschem, S. A. Hubbard, J. Luo, L. A. Fahnestock, B. F. Spencer, D. M. McFarland, D. D. Quinn, A. F. Vakakis, L. A. Bergman, Response attenuation in a large-scale structure subjected to blast excitation utilizing a system of essentially nonlinear vibration absorbers, Journal of Sound and Vibration 389 (2017) 52 – 72. `doi:10.1016/j.jsv.2016.11.003`.

[60] E. Sarrouy, J.-J. Sinou, Non-linear periodic and quasi-periodic vibrations in mechanical systems-on the use of the harmonic balance methods, Advances in vibration analysis research 21 (2011) 419–34.

[61] G. Chen, L. Tang, Z. Yu, Underlying physics of limit-cycle, beating and quasi-periodic oscillations in thermoacoustic devices, Journal of Physics D: Applied Physics 53 (21) (2020) 215502. `doi:10.1088/1361-6463/ab7a57`.

[62] Z. Feng, P. R. Sethna, Global bifurcation and chaos in parametrically forced systems with one-one resonance, Dynamics and Stability of Systems 5 (4) (1990) 201–225.

[63] S. F. Masri, T. K. Caughey, A Nonparametric Identification Technique for Nonlinear Dynamic Problems, Journal of Applied Mechanics 46 (2) (1979) 433–447. `doi:10.1115/1.3424568`.

[64] G. Kerschen, K. Worden, A. F. Vakakis, J.-C. Golinval, Past, present and future of nonlinear system identification in structural dynamics, Mechanical Systems and Signal Processing 20 (3) (2006) 505–592. `doi:10.1016/j.ymssp.2005.04.008`.

[65] A. H. Nayfeh, The method of normal forms, John Wiley & Sons, 2011.

[66] J. Noël, G. Kerschen, Nonlinear system identification in structural dynamics: 10 more years of progress, Mechanical Systems and Signal Processing 83 (2017) 2–35. `doi:10.1016/j.ymssp.2016.07.020`.

[67] M. Krack, J. Gross, Harmonic balance for nonlinear vibration problems, Vol. 1, Springer, 2019.

[68] J. P. Den Hartog, Mechanical Vibrations. Fourth Edition., McGraw-Hill, New York, 1956.

[69] R. Clough, J. Penzien, Dynamics of Structures, Civil engineering series, McGraw-Hill, 1993.

[70] R. R. CRAIG, M. C. C. BAMPTON, Coupling of substructures for dynamic analyses., AIAA Journal 6 (7) (1968) 1313–1319. doi:10.2514/3.4741.

[71] S. W. Doebling, C. R. Farrar, M. B. Prime, D. W. Shevitz, Damage identification and health monitoring of structural and mechanical systems from changes in their vibration characteristics: a literature review.

[72] D. J. Ewins, Modal testing: theory, practice and application, John Wiley & Sons, 2009.

[73] R. M. Rosenberg, Normal Modes of Nonlinear Dual-Mode Systems, Journal of Applied Mechanics 27 (2) (1960) 263–268. doi:10.1115/1.3643948.

[74] R. M. Rosenberg, The Normal Modes of Nonlinear n-Degree-of-Freedom Systems, Journal of Applied Mechanics 29 (1) (1962) 7–14. doi:10.1115/1.3636501.
URL https://hal.archives-ouvertes.fr/hal-01344457

[75] R. H. Rand, Nonlinear normal modes in two-degree-of-freedom systems, Journal of Applied Mechanics 38 (2) (1971) 561–561. doi:10.1115/1.3408826.

[76] R. Rand, A higher-order approximation for nonlinear normal modes in two-degree-of-freedom systems, International Journal of Non-Linear Mechanics 6 (1971) 545 – 547.

[77] A. F. Vakakis, Analysis and identification of linear and nonlinear normal modes in vibrating systems, Ph.D. thesis, California Institute of Technology (1991).

[78] M. E. King, A. F. Vakakis, An Energy-Based Formulation for Computing Nonlinear Normal Modes in Undamped Continuous Systems, Journal of Vibration and Acoustics 116 (3) (1994) 332–340. doi:10.1115/1.2930433.

[79] A. F. Vakakis, Non-linear normal modes (nnms) and their applications in vibration theory: an overview, Mechanical systems and signal processing 11 (1) (1997) 3–22. doi:10.1006/mssp.1996.9999.

[80] S. Shaw, C. Pierre, Non-linear normal modes and invariant manifolds, Journal of Sound and Vibration 150 (1) (1991) 170 – 173. doi:10.1016/0022-460X(91)90412-D.

[81] S. Shaw, C. Pierre, On nonlinear normal modes, in: Nonlinear Vibrations, Vol. 50, ASME, 1992, pp. 1–5.

[82] S. Shaw, C. Pierre, Normal modes for non-linear vibratory systems, Journal of Sound and Vibration 164 (1) (1993) 85–124. doi:10.1006/jsvi.1993.1198.

[83] S. Shaw, C. Pierre, Normal modes of vibration for non-linear continuous systems, Journal of Sound and Vibration 169 (3) (1994) 319 – 347. doi:10.1006/jsvi.1994.1021.

[84] A. M. Lyapunov, The general problem of the stability of motion, International journal of control 55 (3) (1992) 531–534.

[85] A. H. Nayfeh, S. A. Nayfeh, On Nonlinear Modes of Continuous Systems, Journal of Vibration and Acoustics 116 (1) (1994) 129–136. doi:10.1115/1.2930388.

[86] M. Krack, Nonlinear modal analysis of nonconservative systems: Extension of the periodic motion concept, Computers & Structures 154 (2015) 59–71.

[87] G. Haller, S. Ponsioen, Nonlinear normal modes and spectral submanifolds: existence, uniqueness and use in model reduction, Nonlinear dynamics 86 (3) (2016) 1493–1534.

[88] M. Volvert, G. Kerschen, Phase resonance nonlinear modes of mechanical systems, Journal of Sound and Vibration 511 (2021) 116355. doi:10.1016/j.jsv.2021.116355.

[89] M. Peeters, G. Kerschen, J. Golinval, Dynamic testing of nonlinear vibrating structures using nonlinear normal modes, Journal of Sound and Vibration 330 (3) (2011) 486–509. doi:10.1016/j.jsv.2010.08.028.

[90] M. Peeters, G. Kerschen, J. Golinval, Modal testing of nonlinear vibrating structures based on nonlinear normal modes: Experimental demonstration, Mechanical Systems and Signal Processing 25 (4) (2011) 1227–1247. doi:10.1016/j.ymssp.2010.11.006.

[91] L. Renson, A. Gonzalez-Buelga, D. Barton, S. Neild, Robust identification of backbone curves using control-based continuation, Journal of Sound and Vibration 367 (2016) 145–158. doi:10.1016/j.jsv.2015.12.035.

[92] L. Renson, D. A. W. Barton, S. A. Neild, Experimental tracking of limit-point bifurcations and backbone curves using control-based continuation, International Journal of Bifurcation and Chaos 27 (01) (2017) 1730002. doi:10.1142/S0218127417300026.

[93] W. Szemplinska, The Behaviour of Nonlinear Vibrating Systems: Volume II: Advanced Concepts and Applications to Multi-Degree-of-Freedom Systems, Vol. 12, Springer Science & Business Media, 1990.

[94] R. Lewandowski, Computational formulation for periodic vibration of geometrically nonlinear structures—part 1: Theoretical background, International Journal of Solids and Structures 34 (15) (1997) 1925–1947. doi:10.1016/S0020-7683(96)00127-8.

[95] A. H. Nayfeh, D. T. Mook, P. Holmes, Nonlinear oscillations.

[96] A. H. Nayfeh, C. Chin, S. A. Nayfeh, On Nonlinear Normal Modes of Systems With Internal Resonance, Journal of Vibration and Acoustics 118 (3) (1996) 340–345. doi:10.1115/1.2888188.

[97] E. L. Allgower, K. Georg, Introduction to Numerical Continuation Methods, Society for Industrial and Applied Mathematics, 2003. doi:10.1137/1.9780898719154.

[98] R. Seydel, Practical bifurcation and stability analysis, Vol. 5, Springer Science & Business Media, 2009.

[99] H. Dankowicz, F. Schilder, Recipes for Continuation, Society for Industrial and Applied Mathematics, Philadelphia, PA, 2013. doi:10.1137/1.9781611972573.

[100] M. Peeters, R. Viguié, G. Sérandour, G. Kerschen, J.-C. Golinval, Nonlinear normal modes, part ii: Toward a practical computation using numerical continuation techniques, Mechanical Systems and Signal Processing 23 (1) (2009) 195 – 216, special Issue: Non-linear Structural Dynamics. doi:10.1016/j.ymssp.2008.04.003.

[101] G. Kerschen, M. Peeters, J. C. Golinval, C. Stéphan, Nonlinear modal analysis of a full-scale aircraft, Journal of Aircraft 50 (5) (2013) 1409–1419. doi:10.2514/1.C031918.

[102] R. J. Kuether, M. S. Allen, A numerical approach to directly compute nonlinear normal modes of geometrically nonlinear finite element models, Mechanical Systems and Signal Processing 46 (1) (2014) 1–15. doi:10.1016/j.ymssp.2013.12.010.

[103] L. Renson, J. P. Noël, G. Kerschen, Complex dynamics of a nonlinear aerospace structure: numerical continuation and normal modes, Nonlinear Dynamics 79 (2) (2015) 1293 – 1309. doi:10.1007/s11071-014-1743-0.

[104] L. Renson, G. Kerschen, B. Cochelin, Numerical computation of nonlinear normal modes in mechanical engineering, Journal of Sound and Vibration 364 (2016) 177–206. doi:10.1016/j.jsv.2015.09.033.

[105] J. J. Hollkamp, R. W. Gordon, Reduced-order models for nonlinear response prediction: Implicit condensation and expansion, Journal of Sound and Vibration 318 (4-5) (2008) 1139–1153.

[106] M. P. Mignolet, A. Przekop, S. A. Rizzi, S. M. Spottswood, A review of indirect/non-intrusive reduced order modeling of nonlinear geometric structures, Journal of Sound and Vibration 332 (10) (2013) 2437–2460.

[107] R. J. Kuether, B. J. Deaner, J. J. Hollkamp, M. S. Allen, Evaluation of geometrically nonlinear reduced-order models with nonlinear normal modes, AIAA Journal 53 (11) (2015) 3273–3285. doi:10.2514/1.J053838.

[108] I. Tartaruga, A. Elliott, T. L. Hill, S. A. Neild, A. Cammarano, The effect of nonlinear cross-coupling on reduced-order modelling, International Journal of Non-Linear Mechanics 116 (2019) 7–17. doi:10.1016/j.ijnonlinmec.2019.05.006.

[109] E. Nicolaidou, V. R. Melanthuru, T. L. Hill, S. A. Neild, Accounting for quasi-static coupling in nonlinear dynamic reduced-order models, Journal of Computational and Nonlinear Dynamics 15 (7).

[110] A. Vizzaccaro, A. Givois, P. Longobardi, Y. Shen, J.-F. Deü, L. Salles, C. Touzé, O. Thomas, Non-intrusive reduced order modelling for the dynamics of geometrically nonlinear flat structures using three-dimensional finite elements, Computational Mechanics 66 (6) (2020) 1293–1319.

[111] C. Touzé, A. Vizzaccaro, O. Thomas, Model order reduction methods for geometrically nonlinear structures: a review of nonlinear techniques, Nonlinear Dynamics 105 (2) (2021) 1141–1190.

[112] A. A. Muravyov, S. A. Rizzi, Determination of nonlinear stiffness with application to random vibration of geometrically nonlinear structures, Computers & Structures 81 (15) (2003) 1513 – 1523. doi:10.1016/S0045-7949(03)00145-7.

[113] S. A. Rizzi, A. Przekop, System identification-guided basis selection for reduced-order nonlinear response analysis, Journal of Sound and Vibration 315 (3) (2008) 467–485, eUROMECH colloquium 483, Geometrically non-linear vibrations of structures. doi:10.1016/j.jsv.2007.12.031.

[114] A. Lazarus, O. Thomas, J.-F. Deü, Finite element reduced order models for nonlinear vibrations of piezoelectric layered beams with applications to nems, Finite Elements in Analysis and Design 49 (1) (2012) 35–51.

[115] A. Givois, A. Grolet, O. Thomas, J.-F. Deü, On the frequency response computation of geometrically nonlinear flat structures using reduced-order finite element models, Nonlinear Dynamics 97 (2) (2019) 1747–1781.

[116] A. Frangi, G. Gobat, Reduced order modelling of the non-linear stiffness in mems resonators, International Journal of Non-Linear Mechanics 116 (2019) 211–218. doi:10.1016/j.ijnonlinmec.2019.07.002.

[117] E. Nicolaidou, T. L. Hill, S. A. Neild, Detecting internal resonances during model reduction, Proceedings of the Royal Society A: Mathematical, Physical and Engineering Sciences 477 (2250) (2021) 20210215. doi:10.1098/rspa.2021.0215.

[118] S. Jain, P. Tiso, J. B. Rutzmoser, D. J. Rixen, A quadratic manifold for model order reduction of nonlinear structural dynamics, Computers & Structures 188 (2017) 80–94. doi:10.1016/j.compstruc.2017.04.005.

[119] J. Rutzmoser, D. Rixen, P. Tiso, S. Jain, Generalization of quadratic manifolds for reduced order modeling of nonlinear structural dynamics, Computers & Structures 192 (2017) 196–209. doi:10.1016/j.compstruc.2017.06.003.

[120] S. Jain, P. Tiso, G. Haller, Exact nonlinear model reduction for a von kármán beam: Slow-fast decomposition and spectral submanifolds, Journal of Sound and Vibration 423 (2018) 195–211. doi:10.1016/j.jsv.2018.01.049.

[121] S. Ponsioen, S. Jain, G. Haller, Model reduction to spectral submanifolds and forced-response calculation in high-dimensional mechanical systems, Journal of Sound and Vibration 488 (2020) 115640. doi:10.1016/j.jsv.2020.115640.

[122] Z. Veraszto, S. Ponsioen, G. Haller, Explicit third-order model reduction formulas for general nonlinear mechanical systems, Journal of Sound and Vibration 468 (2020) 115039. doi:10.1016/j.jsv.2019.115039.

[123] A. Vizzaccaro, Y. Shen, L. Salles, J. Blahoš, C. Touzé, Direct computation of nonlinear mapping via normal form for reduced-order models of finite element nonlinear structures, Computer Methods in Applied Mechanics and Engineering 384 (2021) 113957. doi:10.1016/j.cma.2021.113957.

[124] A. Opreni, A. Vizzaccaro, A. Frangi, C. Touzé, Model order reduction based on direct normal form: application to large finite element mems structures featuring internal resonance, Nonlinear Dynamics 105 (2) (2021) 1237–1272.

[125] Y. Shen, A. Vizzaccaro, N. Kesmia, T. Yu, L. Salles, O. Thomas, C. Touzé, Comparison of reduction methods for finite element geometrically nonlinear beam structures, Vibration 4 (1) (2021) 175–204.

[126] A. Vizzaccaro, L. Salles, C. Touzé, Comparison of nonlinear mappings for reduced-order modelling of vibrating structures: normal form theory and quadratic manifold method with modal derivatives, Nonlinear Dynamics 103 (4) (2021) 3335–3370.

[127] H. C. Gilliatt, T. W. Strganac, A. J. Kurdila, An investigation of internal resonance in aeroelastic systems, Nonlinear Dynamics 31 (1) (2003) 1–22.

[128] A. Givois, J.-J. Tan, C. Touzé, O. Thomas, Backbone curves of coupled cubic oscillators in one-to-one internal resonance: bifurcation scenario, measurements and parameter identification, Meccanica 55 (3) (2020) 481–503.

[129] T. L. Hill, A. Cammarano, S. A. Neild, D. J. Wagg, Out-of-unison resonance in weakly nonlinear coupled oscillators, Proceedings of the Royal Society A: Mathematical, Physical and Engineering Science 471 (2173) (2015) 20140659. doi:10.1098/rspa.2014.0659.

[130] A. Cammarano, T. L. Hill, S. A. Neild, D. J. Wagg, Bifurcations of backbone curves for systems of coupled nonlinear two mass oscillator, Nonlinear Dynamics 77 (1-2) (2014) 311–320. doi:10.1007/s11071-014-1295-3.

[131] N. A. Alexander, F. Schilder, Exploring the performance of a nonlinear tuned mass damper, Journal of Sound and Vibration 319 (1-2) (2009) 445–462. doi:10.1016/j.jsv.2008.05.018.

[132] G. Gatti, M. Brennan, On the effects of system parameters on the response of a harmonically excited system consisting of weakly coupled nonlinear and linear oscillators, Journal of Sound and Vibration 330 (18-19) (2011) 4538–4550. doi:10.1016/j.jsv.2011.04.006.

[133] T. Detroux, G. Habib, L. Masset, G. Kerschen, Performance, robustness and sensitivity analysis of the nonlinear tuned vibration absorber, Mechanical Systems and Signal Processing 60-61 (2015) 799–809. doi:10.1016/j.ymssp.2015.01.035.

[134] A. Vakakis, M. King, A. Pearlstein, Forced localization in a periodic chain of non-linear oscillators, International Journal of Non-Linear Mechanics 29 (3) (1994) 429–447. doi:10.1016/0020-7462(94)90013-2.

[135] J. Aubrecht, A. F. Vakakis, Localized and Non-Localized Nonlinear Normal Modes in a Multi-Span Beam With Geometric Nonlinearities, Journal of Vibration and Acoustics 118 (4) (1996) 533–542. doi:10.1115/1.2888332.

[136] G. Kerschen, D. M. McFarland, J. J. Kowtko, Y. S. Lee, L. A. Bergman, A. F. Vakakis, Experimental demonstration of transient resonance capture in a system of two coupled oscillators with essential stiffness nonlinearity, Journal of Sound and Vibration 299 (4-5) (2007) 822–838.

[137] D. A. Ehrhardt, T. L. Hill, S. A. Neild, J. E. Cooper, Veering and nonlinear interactions of a clamped beam in bending and torsion, Journal of Sound and Vibration 416 (2018) 1 – 16. doi:10.1016/j.jsv.2017.11.045.

[138] E. Emaci, T. A. Nayfeh, A. F. Vakakis, Numerical and experimental study of nonlinear localization in a flexible structure with vibro-impacts, ZAMM - Journal of Applied Mathematics and Mechanics / Zeitschrift für Angewandte Mathematik und Mechanik 77 (7) (1997) 527–541. doi:10.1002/zamm.19970770712.

[139] T. L. Hill, A. Cammarano, S. A. Neild, D. J. Wagg, Interpreting the forced responses of a two-degree-of-freedom nonlinear oscillator using backbone curves, Journal of Sound and Vibration 349 (2015) 276–288. doi:10.1016/j.jsv.2015.03.030.

[140] M. Cenedese, G. Haller, How do conservative backbone curves perturb into forced responses? a melnikov function analysis, Proceedings of the Royal Society A: Mathematical, Physical and Engineering Sciences 476 (2234) (2020) 20190494. doi:10.1098/rspa.2019.0494.

[141] T. L. Hill, S. A. Neild, A. Cammarano, An analytical approach for detecting isolated periodic solution branches in weakly nonlinear structures, Journal of Sound and Vibration 379 (2016) 150–165. doi:10.1016/j.jsv.2016.05.030.

[142] T. Detroux, J.-P. Noël, L. N. Virgin, G. Kerschen, Experimental study of isolas in nonlinear systems featuring modal interactions, PLOS ONE 13 (3) (2018) 1–25. doi:10.1371/journal.pone.0194452.

[143] T. L. Hill, A. Cammarano, S. A. Neild, D. A. W. Barton, Identifying the significance of nonlinear normal modes, Proceedings of the Royal Society A: Mathematical, Physical and Engineering Sciences 473 (2199) (2017) 20160789. doi:10.1098/rspa.2016.0789.

[144] L. Renson, T. L. Hill, D. A. Ehrhardt, D. A. W. Barton, S. A. Neild, Force appropriation of nonlinear structures, Proceedings of the Royal Society A: Mathematical, Physical and Engineering Sciences 474 (2214) (2018) 20170880. doi:10.1098/rspa.2017.0880.

[145] Y. Sun, A. Vizzaccaro, J. Yuan, L. Salles, An extended energy balance method for resonance prediction in forced response of systems with non-conservative nonlinearities using damped nonlinear normal mode, Nonlinear Dynamics 103 (4) (2021) 3315–3333.

[146] A. F. Vakakis, O. Gendelman, Energy pumping in nonlinear mechanical oscillators: part ii—resonance capture, J. Appl. Mech. 68 (1) (2001) 42–48.

[147] D. D. Quinn, O. Gendelman, G. Kerschen, T. P. Sapsis, L. A. Bergman, A. F. Vakakis, Efficiency of targeted energy transfers in coupled nonlinear oscillators associated with 1: 1 resonance captures: Part i, Journal of Sound and Vibration 311 (3-5) (2008) 1228–1248.

[148] T. Sapsis, A. F. Vakakis, O. V. Gendelman, L. A. Bergman, G. Kerschen, D. Quinn, Efficiency of targeted energy transfers in coupled nonlinear oscillators associated with 1: 1 resonance captures: Part ii, analytical study, Journal of Sound and Vibration 325 (1-2) (2009) 297–320.

[149] J. Wright, J. Cooper, M. Desforges, Normal-mode force appropriation—theory and application, Mechanical Systems and Signal Processing 13 (2) (1999) 217–240. doi:10.1006/mssp.1998.1214.

[150] B. J. Schwarz, M. H. Richardson, Experimental modal analysis, CSI Reliability week 35 (1) (1999) 1–12.

[151] B. Peeters, C. Ventura, Comparative study of modal analysis techniques for bridge dynamic characteristics, Mechanical Systems and Signal Processing 17 (5) (2003) 965–988. doi:10.1006/mssp.2002.1568.

[152] J. Brownjohn, F. Magalhaes, E. Caetano, A. Cunha, Ambient vibration re-testing and operational modal analysis of the humber bridge, Engineering Structures 32 (8) (2010) 2003–2018. doi:10.1016/j.engstruct.2010.02.034.

[153] P. Avitabile, Modal testing: a practitioner's guide, John Wiley & Sons, 2017.

[154] J.-N. Juang, R. S. Pappa, An eigensystem realization algorithm for modal parameter identification and model reduction, Journal of Guidance, Control, and Dynamics 8 (5) (1985) 620–627. doi:10.2514/3.20031.

[155] B. Peeters, H. Van der Auweraer, P. Guillaume, J. Leuridan, The polymax frequency-domain method: a new standard for modal parameter estimation?, Shock and Vibration 11 (3-4) (2004) 395–409.

[156] P. Van Overschee, B. De Moor, Subspace identification for linear systems: Theory—Implementation—Applications, Springer Science & Business Media, 2012.

[157] M. Platten, J. Wright, G. Dimitriadis, J. Cooper, Identification of multi-degree of freedom non-linear systems using an extended modal space model, Mechanical Systems and Signal Processing 23 (1) (2009) 8–29, special Issue: Non-linear Structural Dynamics. doi:10.1016/j.ymssp.2007.11.016.

[158] M. F. Platten, J. R. Wright, J. E. Cooper, G. Dimitriadis, Identification of a nonlinear wing structure using an extended modal model, Journal of Aircraft 46 (5) (2009) 1614–1626. doi:10.2514/1.42024.

[159] U. Fuellekrug, D. Goege, Identification of weak non-linearities within complex aerospace structures, Aerospace Science and Technology 23 (1) (2012) 53–62, 35th ERF: Progress in Rotorcraft Research. doi:10.1016/j.ast.2011.04.012.

[160] L. Chun-Lin, A tutorial of the wavelet transform, NTUEE, Taiwan 21 (2010) 22.

[161] M. Feldman, Hilbert transform in vibration analysis, Mechanical Systems and Signal Processing 25 (3) (2011) 735–802. doi:10.1016/j.ymssp.2010.07.018.

[162] S. Peter, R. I. Leine, Excitation power quantities in phase resonance testing of nonlinear systems with phase-locked-loop excitation, Mechanical Systems and Signal Processing 96 (2017) 139–158. doi:10.1016/j.ymssp.2017.04.011.

[163] V. Denis, M. Jossic, C. Giraud-Audine, B. Chomette, A. Renault, O. Thomas, Identification of nonlinear modes using phase-locked-loop experimental continuation and normal form, Mechanical Systems and Signal Processing 106 (2018) 430–452. doi:10.1016/j.ymssp.2018.01.014.

[164] J. Sieber, B. Krauskopf, Control based bifurcation analysis for experiments, Nonlinear Dynamics 51 (3) (2008) 365–377.

[165] G. Abeloos, F. Müller, E. Ferhatoglu, M. Scheel, C. Collette, G. Kerschen, M. Brake, P. Tiso, L. Renson, M. Krack, A consistency analysis of phase-locked-loop testing and control-based continuation for a geometrically nonlinear frictional system, Mechanical Systems and Signal Processing 170 (2022) 108820. doi:10.1016/j.ymssp.2022.108820.

[166] L. Renson, A. Shaw, D. Barton, S. Neild, Application of control-based continuation to a nonlinear structure with harmonically coupled modes, Mechanical Systems and Signal Processing 120 (2019) 449–464. doi:10.1016/j.ymssp.2018.10.008.

[167] G. Quintana, J. Ciurana, Chatter in machining processes: A review, International Journal of Machine Tools and Manufacture 51 (5) (2011) 363 – 376. doi:10.1016/j.ijmachtools.2011.01.001.

[168] Y. S. Lee, A. F. Vakakis, L. A. Bergman, D. M. McFarland, G. Kerschen, Triggering mechanisms of limit cycle oscillations in a two degree-of-freedom wing flutter model, in: ASME 2005 International Design Engineering Technical Conferences and Computers and Information in Engineering Conference, American Society of Mechanical Engineers, 2005, pp. 1863 – 1872. doi:10.1115/DETC2005-84687.

[169] G. Kerschen, J. J. Kowtko, D. M. Mcfarland, L. A. Bergman, A. F. Vakakis, Theoretical and experimental study of multimodal targeted energy transfer in a system of coupled oscillators, Nonlinear Dynamics 47 (1-3) (2007) 285–309. doi:10.1007/s11071-006-9073-5.

[170] D. Antonio, D. H. Zanette, D. López, Frequency stabilization in nonlinear micromechanical oscillators, Nature Communications 3 (2012) 806.

[171] M. Febbo, S. P. Machado, Nonlinear dynamic vibration absorbers with a saturation, Journal of Sound and Vibration 332 (6) (2013) 1465–1483. doi:10.1016/j.jsv.2012.11.025.

[172] N. Carpineto, W. Lacarbonara, F. Vestroni, Hysteretic tuned mass dampers for structural vibration mitigation, Journal of Sound and Vibration 333 (5) (2014) 1302–1318. doi:10.1016/j.jsv.2013.10.010.

[173] D. A. W. Barton, S. G. Burrow, L. R. Clare, Energy harvesting from vibrations with a nonlinear oscillator, Journal of Vibration and Acoustics 132 (2) (2010) 021009. doi:10.1115/1.4000809.

[174] P. L. Green, K. Worden, K. Atallah, N. D. Sims, The benefits of duffing-type nonlinearities and electrical optimisation of a mono-stable energy harvester under white gaussian excitations, Journal of Sound and Vibration 331 (20) (2012) 504–4517. doi:10.1016/j.jsv.2012.04.035.

[175] T. T. Soong, S. F. Masri, G. W. Housner, An overview of active structural control under seismic loads, Earthquake Spectra 7 (3) (1991) 483 – 505. doi:10.1193/1.1585638.

[176] J. Q. Sun, M. R. Jolly, M. A. Norris, Passive, adaptive and active tuned vibration absorbers—a survey, Journal of Mechanical Design 117 (B) (1995) 234 – 242.

[177] L. Kela, P. Vähäoja, Recent studies of adaptive tuned vibration absorbers/neutralizers, Applied Mechanics Reviews 62 (6) (2009) 1 – 9. doi:10.1115/1.3183639.

[178] Z. Lu, Z. Wang, Y. Zhou, X. Lu, Nonlinear dissipative devices in structural vibration control: A review, Journal of Sound and Vibration 423 (9) (2018) 18 – 49. doi:10.1016/j.jsv.2018.02.052.

[179] W. Lin, A. K. Chopra, Earthquake response of elastic sdf systems with non-linear fluid viscous dampers, Earthquake Engineering and Structural Dynamics 31 (9) (2002) 1623 – 1642. doi:10.1002/eqe.179.

[180] S. J. Dyke, B. F. Spencer Jr., M. K. Sain, J. D. Carlson, Modeling and control of magnetorheological dampers for seismic response reduction, Smart Materials and Structures 5 (5) (1996) 565 – 575.

[181] B. F. Spencer Jr., S. J. Dyke, M. K. Sain, J. D. Carlson, Phenomenological model for magnetorheological dampers, Journal of Engineering Mechanics 123 (3).

[182] D. L. Guo, H. Y. Hu, J. Q. Yi, Neural network control for a semi-active vehicle suspension with a magnetorheological damper, Journal of Vibration and Control 10 (3) (2006) 461 – 471. doi:10.1177/1077546304038968.

[183] L. Chen, L. Sun, Steady-state analysis of cable with nonlinear damper via harmonic balance method for maximizing damping, Journal of Structural Engineering 143 (2). doi:10.1061/(ASCE)ST.1943-541X.0001645.

[184] E. Gourdon, N. A. Alexander, C. A. Taylor, C. H. Lamarque, S. Pernot, Nonlinear energy pumping under transient forcing with strongly nonlinear coupling: Theoretical and experimental results, Journal of Sound and Vibration 300 (3-5) (2007) 522–551. doi:10.1016/j.jsv.2006.06.074.

[185] H. Frahm, Device for damping vibrations of bodies, uS Patent 0989958 (1911).

[186] R. Rana, T. T. Soong, Parametric study and simplified design of tuned mass dampers, Journal of Sound and Vibration 20 (3) (1998) 193 – 204. doi:10.1016/S0141-0296(97)00078-3.

[187] C.-L. Lee, Y.-T. Chen, L.-L. Chung, Y.-P. Wang, Optimal design theories and applications of tuned mass dampers, Engineering Structures 28 (1) (2006) 43 – 53. doi:10.1016/j.engstruct.2005.06.023.

[188] S. Chakraborty, B. K. Roy, Reliability based optimum design of tuned mass damper in seismic vibration control of structures with bounded uncertain parameters, Probabilistic Engineering Mechanics 26 (2) (2010) 215 – 221. doi:10.1016/j.probengmech.2010.07.007.

[189] Y. Yang, J. M. noa, Y. Altintas, Optimization of multiple tuned mass dampers to suppress machine tool chatter, International Journal of Machine Tools and Manufacture 50 (9) (2010) 834 – 842. doi:10.1016/j.ijmachtools.2010.04.011.

[190] A. Malher, C. Touzé, O. Doaré, G. Habib, G. Kerschen, Flutter control of a two-degrees-of-freedom airfoil using a nonlinear tuned vibration absorber, Journal of Computational and Nonlinear Dynamics 12 (5) (2017) 051016. `doi:10.1115/1.4036420`.

[191] M. Wang, Feasibility study of nonlinear tuned mass damper for machining chatter suppression, Journal of Sound and Vibration 330 (9) (2011) 1917–1930. `doi:10.1016/j.jsv.2010.10.043`.

[192] G. Habib, G. Kerschen, Suppression of limit cycle oscillations using the nonlinear tuned vibration absorber, Proceedings of the Royal Society A: Mathematical, Physical and Engineering Sciences 471 (2015) 20140976. `doi:10.1098/rspa.2014.0976`.

[193] H. N. Abramson, Response curves for a system with softening restoring force, Journal of Applied Mechanics 22 (3) (1955) 434–435.

[194] C. Duan, R. Singh, Isolated sub-harmonic resonance branch in the frequency response of an oscillator with slight asymmetry in the clearance, Journal of Sound and Vibration 314 (1-2) (2007) 12–18. `doi:10.1016/j.jsv.2007.12.040`.

[195] S. Misra, H. Dankowicz, M. R. Paul, Degenerate discontinuity-induced bifurcations in tapping-mode atomic-force microscopy, Physica D: Nonlinear Phenomena 239 (1-2) (2010) 33–43. `doi:10.1016/j.physd.2009.10.001`.

[196] A. H. Nayfeh, D. T. Mook, Nonlinear Oscillations, Physics Textbook., Wiley, Weinheim, Germany, 1995.

[197] L. A. DiBerardino, H. Dankowicz, Accounting for nonlinearities in open-loop protocols for symmetry fault compensation, Journal of Computational and Nonlinear Dynamics 9 (2) (2013) 021002. `doi:10.1115/1.4025193`.

[198] R. J. Kuether, L. Renson, T. Detroux, C. Grappasonni, G. Kerschen, M. S. Allen, Nonlinear normal modes, modal interactions and isolated resonance curves, Journal of Sound and Vibration 351 (2015) 299–310. `doi:10.1016/j.jsv.2015.04.035`.

[199] C. Grenat, S. Baguet, C. H. Lamarque, R. Dufour, A multi-parametric recursive continuation method for nonlinear dynamical systems, Mechanical Systems and Signal Processing 127 (2019) 276–289. `doi:10.1016/j.ymssp.2019.03.011`.

[200] G. Habib, G. Cirillob, G. Kerschen, Uncovering detached resonance curves in single-degree-of-freedom systems, Procedia Engineering 199 (2017) 649–656. `doi:10.1016/j.proeng.2017.09.116`.

[201] G. I. Cirillo, G. Habib, G. Kerschen, R. Sepulchre, Analysis and design of nonlinear resonances via singularity theory, Journal of Sound and Vibration 392 (2017) 295–306. `doi:10.1016/j.jsv.2016.12.044`.

[202] G. Habib, G. I. Cirillo, G. Kerschen, Isolated resonances and nonlinear damping, Nonlinear Dynamics 93 (3) (2018) 979–994. `doi:10.1007/s11071-018-4240-z`.

[203] J. P. Noël, T. Detroux, L. Masset, G. Kerschen, L. N. Virgin, Isolated response curves in a base-excited, two-degree-of-freedom, nonlinear system, in: ASME 2015 International Design Engineering Technical Conferences and Computers and

Information in Engineering Conference, American Society of Mechanical Engineers, 2015. doi:10.1115/DETC2015-46106.

[204] A. Casalotti, A. Arena, W. Lacarbonara, Mitigation of post-flutter oscillations in suspension bridges by hysteretic tuned mass dampers, Engineering Structures 69 (2014) 62–71.

[205] O. Gendelman, Transition of energy to a nonlinear localized mode in a highly asymmetric system of two oscillators, Nonlinear dynamics 25 (1-3) (2001) 237–253.

[206] A. F. Vakakis, Inducing passive nonlinear energy sinks in vibrating systems, Journal of Vibration and Acoustics 123 (3) (2001) 324–332. doi:10.1115/1.1368883.

[207] A. T. Savadkoohi, B. Vaurigaud, C.-H. Lamarque, S. Pernot, Targeted energy transfer with parallel nonlinear energy sinks, part ii: theory and experiments, Nonlinear dynamics 67 (1) (2012) 37–46.

[208] O. Gendelman, G. Sigalov, L. Manevitch, M. Mane, A. Vakakis, L. Bergman, Dynamics of an eccentric rotational nonlinear energy sink, Journal of applied mechanics 79 (1).

[209] G. Sigalov, O. Gendelman, M. Al-Shudeifat, L. Manevitch, A. F. Vakakis, L. Bergman, Resonance captures and targeted energy transfers in an inertially-coupled rotational nonlinear energy sink, Nonlinear dynamics 69 (4) (2012) 1693–1704.

[210] F. Nucera, A. F. Vakakis, D. McFarland, L. Bergman, G. Kerschen, Targeted energy transfers in vibro-impact oscillators for seismic mitigation, Nonlinear Dynamics 50 (3) (2007) 651–677.

[211] O. Gendelman, Analytic treatment of a system with a vibro-impact nonlinear energy sink, Journal of Sound and Vibration 331 (21) (2012) 4599–4608.

[212] G. Habib, F. Romeo, The tuned bistable nonlinear energy sink, Nonlinear Dynamics 89 (1) (2017) 179–196.

[213] J. Zang, Y.-W. Zhang, Responses and bifurcations of a structure with a lever-type nonlinear energy sink, Nonlinear Dynamics 98 (2) (2019) 889–906.

[214] F. Nucera, D. McFarland, L. Bergman, A. Vakakis, Application of broadband nonlinear targeted energy transfers for seismic mitigation of a shear frame: Computational results, Journal of Sound and Vibration 329 (15) (2010) 2973 – 2994. doi:10.1016/j.jsv.2010.01.020.

[215] D. Younesian, A. Nankali, M. E. Motieyan, Application of the nonlinear energy sink systems in vibration suppression of railway bridges, in: ASME 2010 10th Biennial Conference on Engineering Systems Design and Analysis, The American Society of Mechanical Engineers, 2010. doi:10.1115/ESDA2010-24629.

[216] Y. S. Lee, G. Kerschen, A. F. Vakakis, P. Panagopoulos, L. Bergman, D. M. McFarland, Complicated dynamics of a linear oscillator with a light, essentially nonlinear attachment, Physica D: Nonlinear Phenomena 204 (1) (2005) 41 – 69. doi:10.1016/j.physd.2005.03.014.

[217] M. F. Daqaq, R. Masana, A. Erturk, D. Dane Quinn, On the role of nonlinearities in vibratory energy harvesting: a critical review and discussion, Applied Mechanics Reviews 66 (4).

[218] N. Tran, M. H. Ghayesh, M. Arjomandi, Ambient vibration energy harvesters: A review on nonlinear techniques for performance enhancement, International Journal of Engineering Science 127 (2018) 162–185. `doi:10.1016/j.ijengsci.2018.02.003`.

[219] S. Roundy, P. K. Wright, J. M. Rabaey, Energy Scavenging for Wireless Sensor Networks, Springer, Boston, MA, 2004. `doi:10.1007/978-1-4615-0485-6`.

[220] J. A. Paradiso, T. Starner, Energy scavenging for mobile and wireless electronics, IEEE Pervasive Computing 4 (2005) 18 – 27. `doi:10.1109/MPRV.2005.9`.

[221] S. Meninger, J. O. Mur-Miranda, R. Amirtharajah, A. Chandrakasan, J. H. Lang, Vibration-to-electric energy conversion, IEEE Transactions on Very Large Scale Integration (VLSI) Systems 9 (1) (2001) 64 – 76. `doi:10.1109/92.920820`.

[222] P. D. Mitcheson, T. C. Green, E. M. Yeatman, A. S. Holmes, Architectures for vibration-driven micropower generators, Journal of Microelectromechanical Systems 13 (3) (2004) 429 – 440. `doi:10.1109/JMEMS.2004.830151`.

[223] N. E. duToit, B. L. Wardle, S. Kim, Design considerations for mems-scale piezoelectric mechanical vibration energy harvesters, Integrated Ferroelectrics 71 (1) (2005) 121–160. `doi:10.1080/10584580590964574`.

[224] B. P. Mann, N. D. Sims, Energy harvesting from the nonlinear oscillations of magnetic levitation, Journal of Sound and Vibration 319 (1 - 2) (2009) 515 – 530. `doi:10.1016/j.jsv.2008.06.011`.

[225] G. Sebald, H. Kuwano, D. Guyomar, B. Ducharne, Experimental duffing oscillator for broadband piezoelectric energy harvesting, Smart Materials and Structures 20 (102001). `doi:10.1088/0964-1726/20/10/102001`.

[226] L. Gu, C. Livermore, Impact-driven, frequency up-converting coupled vibration energy harvesting device for low frequency operation, Smart Materials and Structures 20 (045004). `doi:10.1088/0964-1726/20/4/045004`.

[227] R. L. Harne, K. W. Wang, A review of the recent research on vibration energy harvesting via bistable systems, Smart Materials and Structures 22 (023001). `doi:10.1088/0964-1726/22/2/023001`.

[228] G. Assanto, G. I. Stegeman, M. Sheik-Bahae, E. VanStryland, Coherent interactions for all-optical signal processing via quadratic nonlinearities, IEEE journal of quantum electronics 31 (4) (1995) 673–681.

[229] J. M. Hales, S. Zheng, S. Barlow, S. R. Marder, J. W. Perry, Bisdioxaborine polymethines with large third-order nonlinearities for all-optical signal processing, Journal of the American Chemical Society 128 (35) (2006) 11362–11363.

[230] J. F. Rhoads, S. W. Shaw, K. L. Turner, J. Moehlis, B. E. DeMartini, W. Zhang, Generalized parametric resonance in electrostatically actuated microelectrome-

chanical oscillators, Journal of Sound and Vibration 296 (4) (2006) 797–829. doi:10.1016/j.jsv.2006.03.009.

[231] J. F. Rhoads, S. W. Shaw, K. L. Turner, R. Baskaran, Tunable Microelectromechanical Filters that Exploit Parametric Resonance, Journal of Vibration and Acoustics 127 (5) (2005) 423–430. doi:10.1115/1.2013301.

[232] P. Warnitchai, Y. Fujino, T. Susumpow, A non-linear dynamic model for cables and its application to a cable-structure system, Journal of Sound and Vibration 187 (4) (1995) 695 – 712. doi:10.1006/jsvi.1995.0553.

[233] R. Lewandowski, Solutions with bifurcation points for free vibration of beams: an analytical approach, Journal of sound and vibration 177 (2) (1994) 239–249.

[234] A. H. Nayfeh, P. F. Pai, Linear and Nonlinear Structural Mechanics, Wiley-Interscience, 2004.

[235] R. H. Rand, Lecture notes on nonlinear vibrations, Dept. Theoretical and Applied Mechanics, Cornell University, Ithaca, NY, 2005.

[236] D. J. Higham, N. J. Higham, MATLAB guide, SIAM, 2016.

[237] D. A. Ehrhardt, T. L. Hill, S. A. Neild, Experimentally measuring an isolated branch of nonlinear normal modes, Journal of Sound and Vibration 457 (2019) 213 – 226. doi:10.1016/j.jsv.2019.06.006.

[238] H. Yabuno, T. Kashimura, T. Inoue, Y. Ishida, Nonlinear normal modes and primary resonance of horizontally supported jeffcott rotor, Nonlinear Dynamics 66 (3) (2011) 377–387.

[239] S. A. Neild, D. J. Wagg, Applying the method of normal forms to second-order nonlinear vibration problems, Proceedings of the Royal Society A: Mathematical, Physical and Engineering Science 467 (2128) (2011) 1141–1163. doi:10.1098/rspa.2010.0270.

[240] W. Lacarbonara, Nonlinear normal modes for damage detection., Springer, New York, 2013.

[241] T. Asami, O. Nishihara, Closed-form exact solution to H_∞ optimization of dynamic vibration absorbers (application to different transfer functions and damping systems), Journal of Vibration and Acoustics 125 (3) (2003) 398–405. doi:10.1098/rspa.2010.0270.

[242] S. Nielsen, S. Krenk, Whirling motion of a shallow cable with viscous dampers, Journal of Sound and Vibration 265 (2) (2003) 417 – 435. doi:10.1016/S0022-460X(02)01455-4.

[243] B. M. Pacheco, Y. Fujino, A. Sulekh, Estimation curve for modal damping in stay cables with viscous damper, Journal of Structural Engineering 119 (6) (1993) 1961–1979. doi:10.1061/(ASCE)0733-9445(1993)119:6(1961).

[244] S. Krenk, Vibrations of a taut cable with an external damper, Journal of Applied Mechanics 67 (4) (2000) 772–776.

[245] S. A. Neild, A. R. Champneys, D. J. Wagg, T. L. Hill, A. Cammarano, The use of normal forms for analysing nonlinear mechanical vibrations, Philosophical Transactions of the Royal Society A: Mathematical, Physical and Engineering Sciences 373 (2051) (2015) 20140404. `doi:10.1098/rsta.2014.0404`.

[246] C. Touzé, Normal form theory and nonlinear normal modes: Theoretical settings and applications, Springer Vienna, Vienna, 2014, pp. 75–160. `doi:10.1007/978-3-7091-1791-0_3`.

[247] M. Nahon, Dynamics and control of a novel radio telescope antenna, in: Modeling and Simulation Technologies Conference and Exhibit, 1999, p. 4120.

[248] R. Msallam, S. Dequidt, R. Causse, S. Tassart, Physical model of the trombone including nonlinear effects. application to the sound synthesis of loud tones, Acta Acustica united with Acustica 86 (4) (2000) 725–736.

[249] M. Ducceschi, C. Touzé, Modal approach for nonlinear vibrations of damped impacted plates: Application to sound synthesis of gongs and cymbals, Journal of Sound and Vibration 344 (2015) 313–331.

[250] D. Cao, S. Leadenham, A. Erturk, Internal resonance for nonlinear vibration energy harvesting, The European Physical Journal Special Topics 224 (14) (2015) 2867–2880.

[251] F. Mangussi, D. H. Zanette, Internal resonance in a vibrating beam: a zoo of nonlinear resonance peaks, PloS one 11 (9) (2016) e0162365.

[252] R. Lewandowski, Computational formulation for periodic vibration of geometrically nonlinear structures—part 2: Numerical strategy and examples, International Journal of Solids and Structures 34 (15) (1997) 1949–1964. `doi:10.1016/S0020-7683(96)00126-6`.

[253] L. Ruby, Applications of the mathieu equation, American Journal of Physics 64 (1) (1996) 39–44.

[254] I. Kovacic, R. Rand, S. Mohamed Sah, Mathieu's equation and its generalizations: overview of stability charts and their features, Applied Mechanics Reviews 70 (2).

[255] A. Lazarus, O. Thomas, A harmonic-based method for computing the stability of periodic solutions of dynamical systems, Comptes Rendus Mécanique 338 (9) (2010) 510–517.

[256] E. I. Butikov, Analytical expressions for stability regions in the ince–strutt diagram of mathieu equation, American Journal of Physics 86 (4) (2018) 257–267. `doi:10.1119/1.5021895`.

[257] G. Kotowski, Lösungen der inhomogenen mathieuschen differentialgleichung mit periodischer störfunktion beliebiger frequenz (mit besonderer berücksichtigung der resonanzlösungen), ZAMM - Journal of Applied Mathematics and Mechanics / Zeitschrift für Angewandte Mathematik und Mechanik 23 (4) 213–229. `doi:10.1002/zamm.19430230405`.

[258] J. Kim, J.-G. Hong, J. Chung, Nonlinear dynamic modeling and response analysis of a rotor–blade system with whirling motion, Nonlinear Dynamics 98 (2) (2019) 953–970.

[259] N. Saeed, On the steady-state forward and backward whirling motion of asymmetric nonlinear rotor system, European Journal of Mechanics - A/Solids 80 (2020) 103878. doi:10.1016/j.euromechsol.2019.103878.

[260] R. J. Kuether, M. S. Allen, J. J. Hollkamp, Modal substructuring of geometrically nonlinear finite element models with interface reduction, AIAA Journal 55 (5) (2017) 1695–1706. doi:10.2514/1.J055215.

[261] Y. Sun, J. Yuan, A. Vizzaccaro, L. Salles, Comparison of different methodologies for the computation of damped nonlinear normal modes and resonance prediction of systems with non-conservative nonlinearities, Nonlinear Dynamics 104 (4) (2021) 3077–3107.

[262] A. Shaw, T. Hill, S. Neild, M. Friswell, Periodic responses of a structure with 3:1 internal resonance, Mechanical Systems and Signal Processing 81 (2016) 19–34. doi:10.1016/j.ymssp.2016.03.008.

[263] T. L. Hill, Modal interactions in nonlinear systems (2016). doi:10.13140/RG.2.1.2720.9368.

[264] W. Xie, H. Lee, S. Lim, Nonlinear dynamic analysis of mems switches by nonlinear modal analysis, Nonlinear dynamics 31 (3) (2003) 243–256.

[265] O. Gendelman, Y. Starosvetsky, M. Feldman, Attractors of harmonically forced linear oscillator with attached nonlinear energy sink i: description of response regimes, Nonlinear Dynamics 51 (1-2) (2008) 31–46.

[266] Y. Starosvetsky, O. Gendelman, Strongly modulated response in forced 2dof oscillatory system with essential mass and potential asymmetry, Physica D: Nonlinear Phenomena 237 (13) (2008) 1719–1733.

[267] M. Kani, S. Khadem, M. Pashaei, M. Dardel, Vibration control of a nonlinear beam with a nonlinear energy sink, Nonlinear Dynamics 83 (1-2) (2016) 1–22.

[268] R. Viguié, G. Kerschen, J.-C. Golinval, D. McFarland, L. Bergman, A. Vakakis, N. Van de Wouw, Using passive nonlinear targeted energy transfer to stabilize drill-string systems, Mechanical Systems and Signal Processing 23 (1) (2009) 148–169.

[269] A. Lund, S. J. Dyke, W. Song, I. Bilionis, Identification of an experimental nonlinear energy sink device using the unscented kalman filter, Mechanical Systems and Signal Processing 136 (2020) 106512.

[270] V. Gattulli, M. Lepidi, Localization and veering in the dynamics of cable-stayed bridges, Computers & Structures 85 (21-22) (2007) 1661 – 1678. doi:10.1016/j.compstruc.2007.02.016.

[271] L. Renson, D. Ehrhardt, D. Barton, S. Neild, J. Cooper, Connecting nonlinear normal modes to the forced response of a geometric nonlinear structure with closely spaced modes, Proc. of the ISMA, Leuven, Belgium, 19–21 September (2016) 2775–2785.

Appendix A

List of coefficients

Parameters of the zero discriminant for determining the existence of isolated backbone curves in Chapter 3

$$
\begin{aligned}
g_3 =& -19683\left(\phi_{11}^2+\phi_{12}^2\right)^4\left(\phi_{11}\delta_{11}+\phi_{12}\delta_{12}\right)^2\left(\phi_{11}\delta_{12}-\phi_{12}\delta_{11}\right)^6, && \text{(A.1)}\\
g_5 =& -19683\left(\delta_{11}^2+\delta_{12}^2\right)^4\left(\phi_{11}\delta_{11}+\phi_{12}\delta_{12}\right)^2\left(\phi_{11}\delta_{12}-\phi_{12}\delta_{11}\right)^6, && \text{(A.2)}\\
g_4 =& -19683P\left(\phi_{11}\delta_{12}-\phi_{12}\delta_{11}\right)^6, && \text{(A.3)}
\end{aligned}
$$

where

$$
\begin{aligned}
P =& \left(2\phi_{11}^6-8\phi_{11}^4\phi_{12}^2-\frac{2}{3}\phi_{11}^2\phi_{12}^4-\frac{4}{27}\phi_{12}^6\right)\delta_{11}^6\\
&+\left(2\phi_{12}^6-8\phi_{11}^2\phi_{12}^4-\frac{2}{3}\phi_{11}^4\phi_{12}^2-\frac{4}{27}\phi_{11}^6\right)\delta_{12}^6\\
&+\left(28\phi_{11}^5\phi_{12}-\frac{88}{3}\phi_{11}^3\phi_{12}^3-\frac{4}{9}\phi_{11}\phi_{12}^5\right)\delta_{11}^5\delta_{12}\\
&+\left(28\phi_{11}\phi_{12}^5-\frac{88}{3}\phi_{11}^3\phi_{12}^3-\frac{4}{9}\phi_{11}^5\phi_{12}\right)\delta_{11}\delta_{12}^5\\
&+\left(-8\phi_{11}^6+90\phi_{11}^4\phi_{12}^2-\frac{404}{9}\phi_{11}^2\phi_{12}^4-\frac{2}{3}\phi_{12}^6\right)\delta_{11}^4\delta_{12}^2\\
&+\left(-8\phi_{12}^6+90\phi_{11}^2\phi_{12}^4-\frac{404}{9}\phi_{11}^4\phi_{12}^2-\frac{2}{3}\phi_{11}^6\right)\delta_{11}^2\delta_{12}^4 && \text{(A.4)}\\
&+\left(-\frac{88}{3}\phi_{11}^5\phi_{12}+\frac{3536}{27}\phi_{11}^3\phi_{12}^3-\frac{88}{3}\phi_{12}^5\phi_{11}\right)\delta_{11}^3\delta_{12}^3,
\end{aligned}
$$

and where $\delta_{11} = \phi_{11} - \phi_{21}$ and $\delta_{12} = \phi_{12} - \phi_{22}$.

Nonlinear parameters of the equations of motion for the single-mass, two-mode system in Chapter 4

The equations of motion for the single-mass, two-mode system in the physical domain are given by Eq. (4.3), where the parameters of $\mathbf{N_x}$ are defined as

$$\begin{aligned}
\beta_1 &= \frac{k_2 \cos(\delta) \sin^2(\delta)}{2L_2}, \\
\beta_2 &= -\frac{\left[3\cos^2(\delta) - 1\right] \sin(\delta)\, k_2}{2L_2}, \\
\beta_3 &= -\frac{L_1 L_3 k_2 \cos(\delta) \left[3\cos^2(\delta) - 2\right] + L_3 L_2 k_1 - L_1 L_2 k_3}{2L_1 L_2 L_3}, \\
\beta_4 &= \frac{k_2 \sin(\delta) \cos^2(\delta)}{2L_2}, \\
\gamma_1 &= -\frac{\left[5\cos^2(\delta) - 1\right] \sin^2(\delta)\, k_2}{8L_2^2}, \\
\gamma_2 &= \frac{k_2 \sin(\delta) \cos(\delta) \left[5\cos^2(\delta) - 3\right]}{2L_2^2}, \\
\gamma_3 &= -\frac{15L_1^2 L_3^2 k_2 \cos^2(\delta) \left[\cos^2(\delta) - 1\right] + 2L_3^2 L_2^2 k_1 + 2L_1^2 L_3^2 k_2 + 2L_1^2 L_2^2 k_3}{4L_1^2 L_2^2 L_3^2}, \\
\gamma_4 &= -\frac{k_2 \cos(\delta) \sin(\delta) \left[5\cos^2(\delta) - 2\right]}{2L_2^2}, \\
\gamma_5 &= \frac{\cos^2(\delta)\, L_1^2 L_3^2 k_2 \left[5\cos^2(\delta) - 4\right] + L_3^2 L_2^2 k_1 + L_1^2 L_2^2 k_3}{8L_1^2 L_2^2 L_3^2}.
\end{aligned} \tag{A.5}$$

Using linear modal transform, Eq. (4.3) can be mapped to the modal domain, given by Eq. (4.4), where the parameters of $\mathbf{N_q}$ are given by

$$\begin{aligned}
\mathit{\Xi}_1 =& \left(3\beta_1\phi_{12} + \beta_2\phi_{22}\right)\phi_{11}^2 + 2\left(\beta_2\phi_{12} + \beta_3\phi_{22}\right)\phi_{11}\phi_{21} + \left(\beta_3\phi_{12} + 3\beta_4\phi_{22}\right)\phi_{21}^2, \\
\mathit{\Xi}_2 =& \left(3\beta_1\phi_{11} + \beta_2\phi_{21}\right)\phi_{12}^2 + 2\left(\beta_2\phi_{11} + \beta_3\phi_{21}\right)\phi_{12}\phi_{22} + \left(\beta_3\phi_{11} + 3\beta_4\phi_{21}\right)\phi_{22}^2, \\
\mathit{\Xi}_3 =& 3\left[\beta_1\phi_{11}^3 + \beta_2\phi_{11}^2\phi_{21} + \beta_3\phi_{11}\phi_{21}^2 + \beta_4\phi_{21}^3\right], \\
\mathit{\Xi}_4 =& 3\left[\beta_1\phi_{12}^3 + \beta_2\phi_{12}^2\phi_{22} + \beta_3\phi_{12}\phi_{22}^2 + \beta_4\phi_{22}^3\right], \\
\mathit{\Psi}_1 =& \left(4\gamma_1\phi_{12} + \gamma_2\phi_{22}\right)\phi_{11}^3 + \left(3\gamma_2\phi_{12} + 2\gamma_3\phi_{22}\right)\phi_{11}^2\phi_{21}
\end{aligned}$$

$$
\begin{aligned}
&+ \left(2\gamma_3\phi_{12} + 3\gamma_4\phi_{22}\right)\phi_{11}\phi_{21}^2 + \left(\gamma_4\phi_{12} + 4\gamma_5\phi_{22}\right)\phi_{21}^3, \qquad \text{(A.6)}\\
\Psi_2 =& \left(4\gamma_1\phi_{11} + \gamma_2\phi_{21}\right)\phi_{12}^3 + \left(3\gamma_2\phi_{11} + 2\gamma_3\phi_{21}\right)\phi_{12}^2\phi_{22}\\
&+ \left(2\gamma_3\phi_{11} + 3\gamma_4\phi_{21}\right)\phi_{12}\phi_{22}^2 + \left(\gamma_4\phi_{11} + 4\gamma_5\phi_{21}\right)\phi_{22}^3,\\
\Psi_3 =& 2\left[\left(6\gamma_1\phi_{12}^2 + 3\gamma_2\phi_{12}\phi_{22} + \gamma_3\phi_{22}^2\right)\phi_{11}^2 + \left(6\gamma_5\phi_{22}^2 + 3\gamma_4\phi_{12}\phi_{22} + \gamma_3\phi_{12}^2\right)\phi_{21}^2\right.\\
&\left.+ \left(3\gamma_2\phi_{12}^2 + 4\gamma_3\phi_{12}\phi_{22} + 3\gamma_4\phi_{22}^2\right)\phi_{11}\phi_{21}\right],\\
\Psi_4 =& 4\left[\gamma_1\phi_{11}^4 + \gamma_2\phi_{11}^3\phi_{21} + \gamma_3\phi_{11}^2\phi_{21}^2 + \gamma_4\phi_{11}\phi_{21}^3 + \gamma_5\phi_{21}^4\right],\\
\Psi_5 =& 4\left[\gamma_1\phi_{12}^4 + \gamma_2\phi_{12}^3\phi_{22} + \gamma_3\phi_{12}^2\phi_{22}^2 + \gamma_4\phi_{12}\phi_{22}^3 + \gamma_5\phi_{22}^4\right].
\end{aligned}
$$

Appendix B

A nonlinear beam model

In this section, a nonlinear beam with two immovable ends in the axial direction is considered. From Refs. [252, 30, 52], the equation of motion for this beam can be described by a von Kármán model, given by

$$\rho A \frac{\partial^2 w(x,t)}{\partial t^2} + EI \frac{\partial^4 w(x,t)}{\partial x^4} - N(t) \frac{\partial^2 w(x,t)}{\partial x^2} = 0\,, \tag{B.1}$$

where parameters ρ, A, E, I and N denote the density, cross-sectional area, Young's modulus, second moment of area and axial force of the beam, respectively; and where $w(x,t)$ represents the transverse deflection at axial position x at time t, and $N(t)$ is the dynamic tension, given by

$$N(t) = \frac{EA}{2L} \int_0^L \left(\frac{\partial w(x,t)}{\partial x} \right)^2 \mathrm{d}x\,, \tag{B.2}$$

which leads to nonlinear terms in Eq. (B.1).

The nonlinear beam is expanded via the Galerkin method. Using its underlying linear modes to separate the space and time dependence of the transverse deflection gives

$$w(x,t) = \sum_{i=1}^{\infty} \phi_i(x) q_i(t)\,, \tag{B.3}$$

where $\phi_i(x)$ denotes the i^{th} modeshape at axial position x, and $q_i(t)$ is the i^{th} modal displacement over time. Substituting Eq. (B.3) into Eqs. (B.1) and (B.2), it leads to

$$\rho A \left(\sum_{i=1}^{\infty} \phi_i \ddot{q}_i \right) + EI \left(\sum_{i=1}^{\infty} \phi_i^{''''} q_i \right) - \frac{EA}{2L} \left[\int_0^L \left(\sum_{i=1}^{\infty} \phi_i^{'} q_i \right)^2 \mathrm{d}x \right] \left(\sum_{i=1}^{\infty} \phi_i^{''} q_i \right) = 0\,, \tag{B.4}$$

where $\phi_i^{'}$, $\phi_i^{''}$ and $\phi_i^{''''}$ denote the first, second and fourth derivative of ϕ_i, with respect to x, respectively; $\ddot{q}_i$ is the second derivative of q_i with respect to t, namely the modal acceleration. Next, multiplying Eq. (B.4) by the modephase of the n^{th} modal coordinate, ϕ_n, and intergrating over the length of the beam reveals

$$\begin{aligned} \rho A \left[\sum_{i=1}^{\infty} \left(\int_o^L \phi_i \phi_n \mathrm{d}x \right) \ddot{q}_i \right] + EI \left[\sum_{i=1}^{\infty} \left(\int_o^L \phi_i^{''''} \phi_n \mathrm{d}x \right) q_i \right] \\ - \frac{EA}{2L} \left[\sum_{i=1}^{\infty} \sum_{j=1}^{\infty} \sum_{k=1}^{\infty} \left(\int_0^L \phi_i^{'} \phi_j^{'} \mathrm{d}x \right) \left(\int_0^L \phi_k^{''} \phi_n \mathrm{d}x \right) q_i q_j q_k \right] = 0\,. \end{aligned} \tag{B.5}$$

Recalling the orthogonal relationships of the underlying linear modes gives

$$\int_0^L \phi_i \phi_n \mathrm{d}x = 0 \quad \text{and} \quad \int_0^L \phi_i^{''''} \phi_n \mathrm{d}x = 0 \quad \text{when} \quad i \neq n\,. \tag{B.6}$$

With these orthogonal conditions, Eq. (B.5) can be reduced to

$$\begin{aligned} \rho A \left(\int_o^L \phi_n^2 \mathrm{d}x \right) \ddot{q}_i + EI \left(\int_o^L \phi_n^{''''} \phi_n \mathrm{d}x \right) q_i \\ - \frac{EA}{2L} \left[\sum_{i=1}^{\infty} \sum_{j=1}^{\infty} \sum_{k=1}^{\infty} \left(\int_0^L \phi_i^{'} \phi_j^{'} \mathrm{d}x \right) \left(\int_0^L \phi_k^{''} \phi_n \mathrm{d}x \right) q_i q_j q_k \right] = 0\,. \end{aligned} \tag{B.7}$$

Equation (B.7) can then be rearranged as

$$\ddot{q}_n + \omega_{nn}^2 q_n + \left(\sum_{i=1}^{\infty} \sum_{j=1}^{\infty} \sum_{k=1}^{\infty} \mu_{i,j,k,n} q_i q_j q_k \right) = 0\,, \tag{B.8}$$

where

$$\omega_{nn} = \frac{EI \left(\int_o^L \phi_n^{''''} \phi_n \mathrm{d}x \right)}{\rho A \left(\int_o^L \phi_n^2 \mathrm{d}x \right)} \quad \text{and} \quad \mu_{i,j,k,n} = \frac{E \left(\int_0^L \phi_i^{'} \phi_j^{'} \mathrm{d}x \right) \left(\int_0^L \phi_k^{''} \phi_n \mathrm{d}x \right)}{2L\rho \left(\int_o^L \phi_n^2 \mathrm{d}x \right)}\,. \tag{B.9}$$

Equation (B.8) represents the conservative (i.e. undamped and unforced) motions for the n^{th} mode. To find the natural frequency, ω_{nn}, and coefficients of nonlinear terms, $\mu_{i,j,k,n}$, linear modeshapes are required from the underlying linear system. The modeshapes can be obtained from finite element analysis, or alternatively, by employing an analytical approach.

Here, a pinned-pinned beam is considered to demonstrate how analytical approch is implimented. Firstly, the underlying linear system can be obtained by the removal of nonlinear terms associated with dynamic axial force, i.e.

$$\rho A\left[\sum_{i=1}^{\infty}\left(\int_{o}^{L}\phi_i\phi_n\mathrm{d}x\right)\ddot{q}_i\right]+EI\left[\sum_{i=1}^{\infty}\left(\int_{o}^{L}\phi_i^{''''}\phi_n\mathrm{d}x\right)q_i\right]=0\,. \tag{B.10}$$

For the underlying linear system, the modal parameters can be determined from the boundary conditions. In this case, considering the pinned-pinned boundary conditions gives

$$w|_{x=0}=0,\quad \left.\frac{\partial^2 w}{\partial x^2}\right|_{x=0}=0,\quad w|_{x=L}=0,\quad \left.\frac{\partial^2 w}{\partial x^2}\right|_{x=L}=0. \tag{B.11}$$

With these boundary conditions, the natural frequency and modephase can be obtained from Eq. (B.10), i.e.

$$\omega_{nn}=\left(\frac{n\pi}{L}\right)^2\sqrt{\frac{EI}{\rho A}},\quad \text{and}\quad \phi_n(x)=\sin\left(n\pi\frac{x}{L}\right)\,. \tag{B.12}$$

Substituting Eq. (B.12) back to Eqs. (B.8) and (B.9), a pinned-pinned beam with a two-mode truncation can be obtained

$$\ddot{q}_1+\omega_{n1}^2q_1+\Psi_4q_1^3+\Psi_3q_2^2q_1=0\,, \tag{B.13}$$

$$\ddot{q}_2+\omega_{n2}^2q_2+\Psi_5q_2^3+\Psi_3q_1^2q_2=0\,, \tag{B.14}$$

where

$$\Psi_3=\mu_{1,2,2,1}+\mu_{2,1,2,1}+\mu_{2,2,1,1},\quad \Psi_4=\mu_{1,1,1,1},\quad \Psi_5=\mu_{2,2,2,2}\,. \tag{B.15}$$

Appendix C

Computing the energy-transfer terms

In Chapter 6, the energy balancing for the j^{th} harmonic of the i^{th} mode is given by

$$E_{Di,j} + E_{Pi,j} + E_{Ni,j} = 0\,, \tag{C.1}$$

which shows the relationship between the damping, forcing and nonlinear energy-transfer terms, where these terms are computed using

$$E_{Di,j} = \int_0^T \left[d_i \dot{q}_i\right] \dot{u}_{i,j} \mathrm{d}t\,, \tag{C.2a}$$

$$E_{Pi,j} = -\int_0^T \left[p_i(t)\right] \dot{u}_{i,j} \mathrm{d}t\,, \tag{C.2b}$$

$$E_{Ni,j} = \int_0^T \Big[N_{qi}(\mathbf{q})\Big] \dot{u}_{i,j} \mathrm{d}t\,. \tag{C.2c}$$

It is now shown that these terms may be written as linear functions of the forcing amplitudes, $P_{i,j}$, and phase-shifts, $\hat{\theta}_{i,j}$, which are assumed to be unknown and to be solved via the energy balancing analysis.

Damping energy-transfer term

Substituting the harmonic expansion of the modal velocities, from Eq. (6.18), into the expression for the damping energy loss, Eq. (C.2a), gives

$$E_{Di,j} = \int_0^T \left[d_i \sum_{k\in\mathcal{H}_i} \dot{u}_{i,k}\right] \dot{u}_{i,j} \mathrm{d}t\,. \tag{C.3}$$

Noting that $\dot{u}_{i,0} = 0$ and that

$$\int_0^T \dot{u}_{i,k}\dot{u}_{i,j}\mathrm{d}t = 0\,, \qquad \text{when: } k \neq j\,, \tag{C.4}$$

Eq. (C.3) may be simplified to

$$E_{Di,j} = d_i \int_0^T \dot{u}_{i,j}^2 \mathrm{d}t\,. \tag{C.5}$$

Substituting the expression for $\dot{u}_{i,j}$, from Eq. (6.18), into Eq. (C.5) then gives

$$E_{Di,j} = d_i \int_0^T \left[-j\omega U_{i,j} \sin\left(j\omega t + \bar{\theta}_{i,j} + \hat{\theta}_{i,j}\right)\right]^2 \mathrm{d}t\,, \tag{C.6a}$$

$$= \pi j^2 \omega d_i U_{i,j}^2\,, \tag{C.6b}$$

where $T = 2\pi\omega^{-1}$ has been used.

Note that the linear modal damping is considered here, whilst a discussion on nonlinear damping can be found in [145].

Forcing energy-transfer term

Substituting the harmonic expansion of external forcing, Eq. (6.17), into the expression for the forcing energy loss, Eq. (C.2b), gives

$$E_{Pi,j} = -\int_0^T \left[\sum_{k\in\mathcal{H}_i} p_{i,k}\right] \dot{u}_{i,j}\mathrm{d}t\,. \tag{C.7}$$

Noting that

$$\int_0^T p_{i,k}\dot{u}_{i,j}\mathrm{d}t = 0\,, \qquad \text{when: } k \neq j\,, \tag{C.8a}$$

$$\text{and:} \qquad \int_0^T p_{i,0}\dot{u}_{i,j}\mathrm{d}t = 0\,, \qquad \text{for all } j\,, \tag{C.8b}$$

Eq. (C.7) is simplified to

$$E_{Pi,j} = -\int_0^T p_{i,j}\dot{u}_{i,j}\mathrm{d}t\,. \tag{C.9}$$

The harmonic forcing, $p_{i,j}$ and velocity, $\dot{u}_{i,j}$, are assumed as

$$p_{i,j} = -P_{i,j} \sin\left(j\omega t + \psi_{i,j}\right), \tag{C.10a}$$

$$\begin{aligned} \dot{u}_{i,j} &= -j\omega U_{i,j} \sin\left(j\omega t + \theta_{i,j}\right) \\ &= -j\omega U_{i,j} \sin\left(j\omega t + \bar{\theta}_{i,j} + \hat{\theta}_{i,j}\right). \end{aligned} \tag{C.10b}$$

where $P_{i,j}$ and $\psi_{i,j}$ are the amplitude and phase of the forcing respectively. Substituting the expressions for $p_{i,j}$ and $\dot{u}_{i,j}$ into Eq. (C.9), gives

$$\begin{aligned} E_{Pi,j} &= \int_0^T \left[-P_{i,j} \sin\left(j\omega t + \psi_{i,j}\right)\right] \times \\ &\qquad \left[j\omega U_{i,j} \sin\left(j\omega t + \bar{\theta}_{i,j} + \hat{\theta}_{i,j}\right)\right] \mathrm{d}t\,, \end{aligned} \tag{C.11a}$$

$$\approx -\pi j P_{i,j} U_{i,j} \cos\left(\psi_{i,j} - \bar{\theta}_{i,j}\right), \tag{C.11b}$$

where it has been assumed that the phase-shift, $\hat{\theta}_{i,j}$, is small. The phase difference, $\psi_{i,j} - \bar{\theta}_{i,j}$, accounts for the effect of external forcing on harmonic $u_{i,j}$ – either an energy gain or an energy loss.

For the case where quadrature harmonic forcings are considered, i.e. §6.3, the phase of the harmonic forcing, $\psi_{i,j}$, may be assumed to be equal the phase of the velocity, $\bar{\theta}_{i,j}$. This further simplifies Eq. (C.11) to

$$E_{Pi,j} \approx -\pi j P_{i,j} U_{i,j}\,. \tag{C.12}$$

Assuming the displacement amplitude, $U_{i,j}$, is known but the forcing amplitude, $P_{i,j}$, is unknown, the forcing energy term may be separated into the known, $E^{\dagger}_{Pi,k}$, and unknown, $P_{i,k}$, components, i.e.

$$E_{Pi,j} \approx P_{i,j} E^{\dagger}_{Pi,j}\,, \qquad \text{where:} \quad E^{\dagger}_{Pi,j} = -\pi j U_{i,j}\,, \tag{C.13}$$

where the dagger, $\bullet^{\dagger}$, denotes a known term.

Whilst, for the case where quadrature physical forcings are considered, as in §6.4, the phase relationship between the external forcing and the harmonic can be determined using the phase constraints Eq. (6.70) with the substitution of $\theta_{i,j} = \bar{\theta}_{i,j}$, i.e.

$$\tan\left(\psi_{\ell,j}\right) = \frac{\sum_{i=1}^{N} \phi_{\ell,i} U_{i,j} \sin\left(\bar{\theta}_{i,j}\right)}{\sum_{i=1}^{N} \phi_{\ell,i} U_{i,j} \cos\left(\bar{\theta}_{i,j}\right)} \,. \tag{C.14}$$

In this context, the phase difference, $\psi_{i,j} - \bar{\theta}_{i,j}$, can be evaluated using the NNM solutions; therefore, it can be seen as a known parameter.

Nonlinear energy-transfer term

As with the forcing energy-loss term, the known and unknown components must be separated in the nonlinear energy-loss term, Eq. (6.14c). Before considering the (unknown) phase-shifts, $\hat{\theta}_{i,j}$, the responses are divided into the NNM responses (assumed to be known) and the perturbations (assumed to be unknown) – i.e. $q_i = \bar{q}_i + \hat{q}_i$ where, as previously, $\bar{q}_i$ represents the NNM response and where $\hat{q}_i$ is the perturbation to the i^{th} modal displacement due to the forcing. Following this, the vector of modal displacements may be written $\mathbf{q} = \bar{\mathbf{q}} + \hat{\mathbf{q}}$, and the harmonics are written $u_{i,j} = \bar{u}_{i,j} + \hat{u}_{i,j}$. Substituting these into the nonlinear energy-loss term, Eq. (6.14c), leads to

$$E_{Ni,j} = \int_0^T \left[N_{qi}\left(\bar{\mathbf{q}} + \hat{\mathbf{q}}\right)\right] \left[\dot{\bar{u}}_{i,j} + \dot{\hat{u}}_{i,j}\right] \mathrm{d}t \,. \tag{C.15}$$

Assuming the perturbation terms are small, the Taylor series expansion may be applied to the nonlinear force to give

$$E_{Ni,j} \approx \int_0^T \left[N_{qi}\left(\bar{\mathbf{q}}\right) + \left(\sum_{n=1}^{N} \left[\frac{\mathrm{d}N_{qi}}{\mathrm{d}q_n}\right]_{\mathbf{q}=\bar{\mathbf{q}}} \hat{q}_n\right)\right] \times \left[\dot{\bar{u}}_{i,j} + \dot{\hat{u}}_{i,j}\right] \mathrm{d}t \,, \tag{C.16}$$

which may be expanded out to

$$\begin{aligned} E_{Ni,j} \approx \int_0^T & \left[N_{qi}\left(\bar{\mathbf{q}}\right) \dot{\bar{u}}_{i,j}\right] + \left[N_{qi}\left(\bar{\mathbf{q}}\right) \dot{\hat{u}}_{i,j}\right] \\ & + \left[\left(\sum_{n=1}^{N} \left[\frac{\mathrm{d}N_{qi}}{\mathrm{d}q_n}\right]_{\mathbf{q}=\bar{\mathbf{q}}} \hat{q}_n\right) \dot{\bar{u}}_{i,j}\right] \\ & + \left[\left(\sum_{n=1}^{N} \left[\frac{\mathrm{d}N_{qi}}{\mathrm{d}q_n}\right]_{\mathbf{q}=\bar{\mathbf{q}}} \hat{q}_n\right) \dot{\hat{u}}_{i,j}\right] \mathrm{d}t \,. \end{aligned} \tag{C.17}$$

As the unperturbed response represents an NNM, the first term in the integral of Eq. (C.17) represents the net energy transfer due to the nonlinear coupling of an NNM response. As an NNM cannot exhibit a net energy transfer, it follows that

$$\int_0^T N_{qi}\left(\bar{\mathbf{q}}\right)\dot{\bar{u}}_{i,j}\mathrm{d}t = 0\,. \tag{C.18}$$

Assuming that the perturbations, $\hat{q}_n$ and $\hat{u}_{i,j}$, are small it also follows that the final term in the integral of Eq. (C.17) is negligible. Therefore, Eq. (C.17) may be further approximated to

$$E_{Ni,j} \approx \int_0^T \left[N_{qi}\left(\bar{\mathbf{q}}\right)\dot{\hat{u}}_{i,j}\right] + \left[\left(\sum_{n=1}^{N}\left[\frac{\mathrm{d}N_{qi}}{\mathrm{d}q_n}\right]_{\mathbf{q}=\bar{\mathbf{q}}}\hat{q}_n\right)\dot{\bar{u}}_{i,j}\right]\mathrm{d}t\,. \tag{C.19}$$

The perturbations, $\hat{q}_n$ and $\hat{u}_{i,j}$, are now written in terms of the phase-shifts, $\hat{\theta}_{i,j}$. To achieve this, Eq. (6.18) is used to write the j^{th} harmonic of the i^{th} mode as

$$\begin{aligned} u_{i,j} = \bar{u}_{i,j} + \hat{u}_{i,j} &= U_{i,j}\cos\left(j\omega t + \bar{\theta}_{i,j} + \hat{\theta}_{i,j}\right), & \text{(C.20a)}\\ &= U_{i,j}\cos\left(j\omega t + \bar{\theta}_{i,j}\right)\cos\left(\hat{\theta}_{i,j}\right) & \text{(C.20b)}\\ &\quad -U_{i,j}\sin\left(j\omega t + \bar{\theta}_{i,j}\right)\sin\left(\hat{\theta}_{i,j}\right), & \\ &\approx \bar{u}_{i,j} - U_{i,j}\sin\left(j\omega t + \bar{\theta}_{i,j}\right)\hat{\theta}_{i,j}\,, & \text{(C.20c)} \end{aligned}$$

where it has been assumed that $\hat{\theta}_{i,j}$ is small. It therefore follows that

$$\hat{u}_{i,j} \approx -U_{i,j}\sin\left(j\omega t + \bar{\theta}_{i,j}\right)\hat{\theta}_{i,j} = \frac{1}{j\omega}\dot{\bar{u}}_{i,j}\hat{\theta}_{i,j}\,, \tag{C.21}$$

and hence the perturbation terms in Eq. (C.19) may be written

$$\dot{\hat{u}}_{i,j} \approx \frac{1}{j\omega}\ddot{\bar{u}}_{i,j}\hat{\theta}_{i,j}\,, \quad \text{and} \quad \hat{q}_n = \sum_{k\in\mathcal{H}_n}\frac{\hat{\theta}_{n,k}}{k\omega}\dot{\bar{u}}_{n,k}\,. \tag{C.22}$$

Substituting these into Eq. (C.19) gives

$$\begin{aligned} E_{Ni,j} &\approx \int_0^T \left[\sum_{n=1}^{N}\frac{\partial N_{qi}}{\partial q_n}\left(\sum_{k\in\mathcal{H}_n}\frac{\hat{\theta}_{n,k}}{k\omega}\dot{\bar{u}}_{n,k}\right)\right]\dot{\bar{u}}_{i,j}\mathrm{d}t + \frac{\hat{\theta}_{i,j}}{j\omega}\int_0^T N_{qi}\left(\bar{\mathbf{q}}\right)\ddot{\bar{u}}_{i,j}\mathrm{d}t\,. & \text{(C.23a)}\\ &\approx \left[\sum_{n=1}^{N}\sum_{k\in\mathcal{H}_n}\frac{\hat{\theta}_{n,k}}{k\omega}\left(\int_0^T\frac{\partial N_{qi}}{\partial q_n}\dot{\bar{u}}_{n,k}\dot{\bar{u}}_{i,j}\mathrm{d}t\right)\right] + \frac{\hat{\theta}_{i,j}}{j\omega}\int_0^T N_{qi}\left(\bar{\mathbf{q}}\right)\ddot{\bar{u}}_{i,j}\mathrm{d}t\,. & \text{(C.23b)} \end{aligned}$$

As with the forcing energy-loss term, this may be separated into the known components (i.e. the NNM responses) and unknown components (the phase-shifts) as follows

$$E_{Ni,j} \approx \sum_{n=1}^{N} \sum_{k \in \mathcal{H}_n} E_{Ni,j}^{\dagger(n,k)} \hat{\theta}_{n,k} \,, \tag{C.24}$$

where the known component is written

$$E_{Ni,j}^{\dagger(n,k)} = \begin{cases} \dfrac{1}{k\omega} \displaystyle\int_0^T \dfrac{\partial N_{qi}}{\partial q_n} \dot{\bar{u}}_{i,j} \dot{\bar{u}}_{n,k} \mathrm{d}t \,, \\ \qquad\qquad\qquad \text{when: } \{i,j\} \neq \{n,k\} \,, \\ \dfrac{1}{j\omega} \displaystyle\int_0^T \dfrac{\partial N_{qi}}{\partial q_i} \dot{\bar{u}}_{i,j}^2 \mathrm{d}t \\ \qquad + \dfrac{1}{j\omega} \displaystyle\int_0^T N_{qi} \ddot{\bar{u}}_{i,j} \mathrm{d}t \,, \\ \qquad\qquad\qquad \text{when: } \{i,j\} = \{n,k\} \,. \end{cases} \tag{C.25}$$

As previously discussed, the dagger, $\bullet^{\dagger}$, denotes a known term.